Theoretical and Experimental Investigations of Isotope Shift

Christopher W.P. Palmer

The Queen's College
Oxford

Abstract of thesis submitted for the degree of

Doctor of Philosophy

Hilary Term 1982

This thesis is concerned with the measurement and interpretation of isotope shifts. The first part describes an experimental determination of isotope shifts in the $4s^2\ ^1S_0 - 4s5s\ ^1S_0$ transition of neutral calcium. This measurement was performed using the method of Doppler-free two-photon absorption spectroscopy in an atomic beam of the natural mixture of calcium isotopes. The laser was stabilized and scanned by means of an external, pressure-swept etalon, and its scan was calibrated by recording the transmission fringes of the laser through a confocal etalon, 2 m in length. This calibration etalon was stabilized with reference to an I_2-stabilized Helium-Neon laser. The isotope shifts of all the stable isotopes of calcium were measured; the results are believed to be free from systematic error and so the standard deviations are derived from the scatter of the results.

A	Isotope Shift $\delta\nu^{A-44}$/MHz
40	-1169.99(28)
42	-563.66(7)
43	-263.67(6)
46	534.34(70)
48	1023.50(7)

These results are compared with other accurate measurements of isotope shifts in calcium by laser spectroscopy, by means of the King plot. All the measurements are consistent except for the only odd isotope ^{43}Ca, which, in this transition, unlike those in the other experiments, is free from hyperfine structure. The best values of the isotope shifts are thus determined by a least squares procedure. The mass and field shifts are separated using the values of $\delta\langle r^2\rangle$ determined from muonic isotope shifts, and this leads to more accurate values of $\delta\langle r^2\rangle$.

The second part of the thesis concerns the interpretation of anomalous isotope shifts in samarium. Pairs of spectral lines had been found for which the shifts of even-even isotopes did not lie on a straight line on a King plot. These deviations are interpreted as evidence for the insufficiency of first-order perturbation theory for the treatment of isotope shifts in a number of levels of the samarium spectrum. By comparing shifts in transitions connecting these levels with shifts in transitions connecting levels for which first-order perturbation theory appears to be a good approximation, values of off-diagonal matrix elements are found. These are not required to be unreasonably large to explain the observed deviations.

THEORETICAL AND EXPERIMENTAL INVESTIGATIONS OF ISOTOPE SHIFT

BY

CHRISTOPHER W.P. PALMER

A Thesis submitted in part fulfilment
of the requirements for the degree of
Doctor of Philosophy
at the University of Oxford

The Queen's College
Oxford

February
1982

Acknowledgments

The work described in this thesis was carried out within the Atomic Physics Group of the Clarendon Laboratory, Oxford, and would not have been possible without the advice and encouragement of all the other members of the group throughout this project. I must, however, give particular thanks to a number of people: to my supervisor Dr G.K. Woodgate, for suggesting the experiments to me in the first place, for guiding me through it and for his helpful criticism of this thesis; to Dr D.N. Stacey, who contributed greatly to the work described in Chapter 8, in many hours of joint grappling with conceptual difficulties, and also suggested the method of analysis described in Appendix B; to Dr J. Nicol, who, on sabbatical leave from James Cook University of North Queensland, helped me to build the apparatus and find out how to use it; to Dr P.E.G. Baird for teaching me how to operate dye lasers, keeping the ring laser running while the experiment was done and for his patience in putting right my mistakes; to Mr C.W. Goodwin for his continuous practical assistance and infallible provision of alternatives to red wax; and to Dr R.C. Thompson for his guidance with computing. I would also like to thank my typists, Mrs D.J. Adam and Miss F. Chandler, for a great deal of fast and accurate typing. Finally I would like to thank Miss J.J. Smith for references to Donne and Milton.

TABLE OF CONTENTS

		Page
INTRODUCTION		1
CHAPTER 1	Methods of Investigating Nuclear Charge Distributions	
1.1	Introduction	4
1.2	Distributions in Nuclei	4
1.3	Electron Scattering and Muonic Atoms	11
1.4	Optical Isotope Shifts	19
1.5	Other Isotope Shift Measurements in Calcium	29
CHAPTER 2	Theory of Two-Photon Absorption	
2.1	Introduction	32
2.2	Assumptions in the Theory	33
2.3	The Hamiltonian, and Perturbation Theory	35
2.4	Two-photon Absorption in the Absence of Hyperfine Structure	40
2.5	The Effect of Hyperfine Structure	52
2.6	The Effect of Laser Bandwidth and transit time	57
2.7	Evaluation of the Two-photon rate for Calcium	61
CHAPTER 3	The Atomic Beam	
3.1	Introduction	64
3.2	The Atomic Beam Oven	65
3.3	The Vacuum System	68
3.4	Calculation of Number Density	70
3.5	The Detection of the Fluorescence	78
3.6	The Focussing Lenses	82
3.7	Background Light	88

CHAPTER 4 The Laser System

4.1 Introduction 90

4.2 The Dye Lasers 90

4.3 Calibration of the Scan 94

4.4 Other Optical Components 100

4.5 The Method of Running 104

CHAPTER 5 Computer Analysis of Results

5.1 Introduction 108

5.2 Analysis of the first fitting program 109

5.3 Discussion of Fitting Procedure 113

5.4 The Calibration and Plotting Programs 116

5.5 The Fitting Program 119

5.6 The Function-generating Subroutine 129

CHAPTER 6 Results

6.1 Introduction 132

6.2 The Line Profile 132

6.3 Isotope Shifts 136

CHAPTER 7 Discussion of Results

7.1 Introduction 150

7.2 Comparison of Isotope Shifts using the King Plot 150

7.3 The Second-Order Hyperfine Shift 154

7.4 Values of $\delta\langle r^2\rangle$ for the stable Calcium Isotopes 160

CHAPTER 8 Anomalous Isotope Shifts in Samarium

8.1 Introduction 166

8.2 Description of the Experimental Results 167

8.3 Two-level Mixing 172

Chapter 8, cont.

8.4 Discussion 183

APPENDIX A 189

APPENDIX B 200

APPENDIX C 205

APPENDIX D 215

REFERENCES 217

INTRODUCTION

The work described in this thesis falls into two distinct parts. The major part is concerned with an experiment to measure isotope shift in atomic calcium, and the interpretation of these and other experimental results in calcium. The final Chapter is concerned with the interpretation of some anomalies in isotope shifts in samarium (Griffith et al., 1979, 1981). I shall defer further description of this part of my work until Chapter 8; in the remainder of this Introduction I shall briefly describe the background to the calcium experiment.

The primary motivation for measuring isotope shifts in calcium is the possibility of extracting from the measurements information about the nuclear charge distributions of the different isotopes. Jackson (1979) has summarized the reasons for interest in the calcium isotopes by nuclear physicists in her introductory talk at the conference "What do we know about the radial shape of nuclei in the calcium region?":- calcium provides the first long sequence of stable isotopes; they have a magic proton number ($Z = 20$) and span the gap between the neutron magic numbers $N = 20$ to $N = 28$. This allows us to study the following basic nuclear properties: the effects of shell closure, the change in the distribution of a fixed number of protons as the number of neutrons is increased, and the change in neutron and matter distributions as the neutron number increases. It could be added that the total number of nucleons (40-48) is sufficiently small to permit calculation of nuclear properties using fundamental nucleon-nucleon interactions, as well as interactions containing phenomenological parameters, and also the calculation of very important correlation effects not included in a lowest order Hartree-Fock calculation.

The contribution of optical isotope shifts, muonic atom isotope shifts and elastic electron scattering to this programme is the determination

of charge distributions - that is, primarily, proton distributions (although see section 1.3)-since these leptonic probes interact only with the nuclear charge. Optical spectroscopy is capable of determining the isotope shift of unstable isotopes, and the spins and nuclear moments of odd isotopes, both stable and unstable. This is an important contribution since it is very difficult to obtain any other information about nucleon distributions in these nuclei, and one parameter of the charge distribution can by this means be quite accurately determined.

Hyperfine structure, although providing additional information about nuclear spins and moments, is somewhat of a hindrance from the point of view of accurate isotope shift measurements. This is because firstly, the measurement of the centre of gravity of the hyperfine structure is more difficult than the measurement of a single peak position, and secondly, if there are nearby levels there is the possibility of an additional isotope shift due to the hyperfine interaction in second order perturbation theory. Because of this, and in view of the fact that another experiment measuring isotope shifts and hyperfine structures in the calcium intercombination line was then in progress (Bergmann et al., 1980), it was decided to measure isotope shifts only, in a transition without hyperfine structure. This requires a transition obeying the selection rule $J = 0 \rightarrow J = 0$, which is forbidden for all one-photon transitions; this suggests the use of two-photon spectroscopy. This method has many advantages: the spectra are easy to interpret, with little likelihood of power shifts (cf. saturation spectroscopy) and, most importantly, it is a Doppler-free technique. It requires, however, a laser operating at half the frequency interval between the two levels, capable of being scanned smoothly and supplying at least several tens of milliwatts of power.

Now the groundstate of calcium is $4s^2\ ^1S_0$; the lowest excited $J = 0$ even-parity state (two-photon transitions cause no change in parity) is $4s5s\ ^1S_0$, at 33317 cm^{-1}, so that the required wavelength is 600 nm, which is

close to the peak of the tuning range of one of the strongest dyes used in tunable dye lasers, Rhodamine 6G. Commercial dye lasers operating at this wavelength using Rhodamine 6G were readily available in 1978 at the start of this work.

Thus the outline of the experiment is as follows: a narrow bandwidth dye laser operating at 600 nm is focussed into a vacuum system containing a vapour of free calcium atoms. As the laser is slowly scanned, two-photon absorption to the $4s5s\ ^1S_0$ state takes place; the light emitted as these atoms cascade back to the ground state is detected. This signal, which shows peaks due to the different isotopes in the natural mixture of calcium, together with information which calibrates the scan of the laser, enables the isotope shifts to be determined.

The description of the work is divided into chapters as follows: Chapter 1 contains an outline of the theory of isotope shifts and their interpretation and information already discovered, from optical isotope shifts and other experiments, concerning charge distributions in calcium isotopes. In Chapter 2 the theory of two-photon absorption is presented, and possible absorption rates in calcium calculated. Chapter 3 describes the construction of the atomic beam of calcium, and Chapter 4 the laser system, and calibration of the laser scan. Chapter 5 contains a description of the method used to extract the results, using computer analysis of digitally recorded data. In Chapter 6 the results are presented, which are discussed in Chapter 7, together with other recent isotope shift data.

CHAPTER 1

METHODS OF INVESTIGATING NUCLEAR CHARGE DISTRIBUTIONS

1.1 Introduction

In this Chapter, I shall briefly review the different distributions in nuclei and then describe how one important distribution, the charge distribution, is measured. In section 1.2 I shall discuss the question of nuclear distributions, and the information that can be obtained from leptonic probes, and in section 1.3 I shall describe in slightly more detail how this analysis is performed in the case of electron scattering and muonic X-rays, with reference to light atoms in general and calcium in particular. The other leptonic probe of the nucleus is of course provided by the atomic electrons; and so in section 1.4 I shall describe the theory of the isotope shift in spectral lines and its interpretation in terms of nuclear properties. Earlier isotope shift work in calcium is reviewed briefly in section 1.5. This Chapter, therefore, describes the motivation for performing an accurate measurement of isotope shifts in a new transition in calcium, and provides the necessary background information for the interpretation of the results.

•

1.2 Distributions in Nuclei

The fact that nuclei consist of two types of particle, each with significant internal structure on a length scale not much smaller than that of the nucleus, makes their description substantially more complicated than that of atoms. In the atom, of course, there is just one type of particle, the electron, and the length scale of its apparent internal structure, the

Compton wavelength $\hbar/mc$, is $1/\alpha$ times smaller than the atomic length scale, the Bohr radius.

The simplest distributions in the nuclear ground state $|0\rangle$ are the proton and neutron densities

$$\rho_p(\underline{r}) = \langle 0 | \sum_{\text{protons}} \delta(\underline{r}_i - \underline{r}) | 0 \rangle$$

$$\rho_n(\underline{r}) = \langle 0 | \sum_{\text{neutrons}} \delta(\underline{r}_i - \underline{r}) | 0 \rangle$$

and the matter density

$$\rho_m = \rho_n + \rho_p \ .$$

These are simply calculated from a theoretical wavefunction by taking the indicated expectation values; however they do not correspond to distributions directly calculable from any experimental method. For this reason a very large number of different types of scattering experiment is used in an attempt to map different distributions in the nucleus; for a review of the many different techniques used to study calcium nuclei the reader is referred to the Proceedings of a recent International Discussion Meeting "What do we know about the radial shape of nuclei in the Calcium Region?"*. I shall only discuss the use of leptonic probes to determine the charge distribution. This ignores the so-called "magnetic electron scattering" (op. cit. and Sick et al., 1977), which determines distributions of valence nucleons in non-spin-zero nuclei.

Thus we are considering three types of experiment: firstly the measurement of cross sections for elastic electron scattering from spin-zero

---

* Proceedings of the International Discussion Meeting, held at Kernforschungszentrum, Karlsruhe, May 1979.
Edited by H. Rebel, H.J. Gils and G. Schatz, Institüt fur Angewandtekern-physik, Kfk., Karlsruhe.

nuclei, secondly the measurement of absolute transition energies and isotope shifts of X-rays emitted by muonic atoms, and thirdly the measurement of isotope shifts in electronic transitions, by either X-ray or optical spectroscopy. All of these involve the interaction of a lepton with the nucleus, and this interaction is purely electromagnetic in character. Thus by studying the behaviour of the lepton it is possible to infer the electromagnetic structure of the nucleus. There are two important simplifications that can be made. Firstly the effect of nuclear states other than the ground state is often very small. In optical spectroscopy such an effect is negligible, and in muonic atom spectroscopy it leads to the 'nuclear polarization' corrections. Although large compared with experimental error in that case, they can be roughly computed, and the uncertainties in this computation are generally small compared with the effects of the finite size of the nucleus, although each nucleus must be treated as a separate case. Secondly we ignore the effects of multipole moments other than the charge distribution. This is exact for spin-zero nuclei; for nuclei with spin these moments lead to hyperfine structure in electronic or muonic spectroscopy, which serves to complicate the analysis, while not changing the basic effect of the finite charge distribution. In the case of electron scattering, these multipole moments lead to additional scattering, and greatly complicate the extraction of the charge form factor. (The scattering angle and momentum transfer dependence of the scattering from these higher multipole moments is, however, used in the magnetic electron scattering referred to above.)

To sum up, then, experimental results for all these leptonic probes are determined by the nuclear ground state charge distribution; this statement is exact for spin-zero nuclei and in the case of non spin-zero nuclei the effect of other electromagnetic properties of the nucleus can be allowed for in some experiments. In the remainder of this section I shall discuss the charge distribution and contributions to it from the "theoretical" dis-

tributions ρ_n and ρ_p. In the next section I shall discuss electron scattering and muonic atoms, and in section 1.4 I shall turn to the main subject of this thesis, isotope shifts.

Clearly, since protons are charged and neutrons are not, a first approximation to the charge distribution ρ_c is the point proton distribution ρ_p. However we know that the proton is an extended object with an rms charge radius of $\sim$0.8 fm, and a roughly Gaussian charge distribution. Chandra and Sauer (1976) fitted experimental data with a model for the charge distribution of the proton consisting of a sum of three Gaussians:

$$F_p(r) = \sum_i \frac{\theta_i}{(\pi r_i^{3/2})} \exp -(r^2/r_i^2); \qquad \sum \theta_i = 1$$

with a mean square charge radius of

$$\langle r^2 \rangle_p = \sum_i \frac{3\theta_i}{2} r_i^2 = 0.775 \text{ fm}^2.$$

Defining the symbol $\otimes$ to denote a convolution, we have, to this approximation,

$$\rho_c = \rho_p \otimes F_p$$

(N.B. this implies that the normalization of ρ_c is the same as ρ_p, that is

$$\int \rho_c d^3\underline{r} = Z .$$

Thus ρ_c is the charge density in electron charges per unit volume).

It turns out that to this approximation it is necessary to consider two additional contributions to ρ_c. The first is from the charge distribution of the neutron; although the neutron has no net charge, it has a charge distribution with a net positive charge on the inside surrounded by a sphere of negative charge extending to $\sim$0.7 fm. Chandra and Sauer also parameterized

the neutron distribution as a similar sum of Gaussians with two terms $\theta_1 = +1$, $r_1^2 = 0.469$ fm^2 and $\theta_2 = -1$, $r_2^2 = 0.546$ fm^2. This gives the mean square charge radius as

$$\langle r^2 \rangle_n = -0.116 \text{ fm}^2 .$$

The second contribution to the charge distribution is from the spin-orbit interaction of the nucleons. It is well known, from the shell model of nuclei, that nucleons have a considerable interaction between their spin and orbital angular momenta; the origin of this interaction is in the nucleon-nucleon interaction, and not in the electromagnetic interaction as in atoms. Thus in a partly filled subshell of specified n and ℓ there will be a preferred relative orientation between spin and orbital angular momenta; specifically, in a less than half filled subshell, all the nucleons will have their $\underline{\ell}$ and $\underline{s}$ parallel, coupled to give $j = \ell + \frac{1}{2}$. This is the situation between neutron numbers 20 and 28; 20 is a closed shell configuration, and the next eight neutrons go into the $1f_{7/2}$ shell.

This allows us to understand the origin of this contribution to the charge distribution. The nucleon is a moving magnetic dipole $\underline{\mu}$; the neutron, for example, has $\underline{\mu} = 2\mu_n \mu_N \underline{s}$, where μ_n is the magnetic moment in nuclear magnetons, and μ_N is the nuclear magneton $e\hbar/2m_p$. In virtue of its motion this moving magnetic moment appears in the nuclear centre of mass frame to have an electric dipole moment

$$\underline{\mu}_e \simeq \frac{1}{c^2} \underline{v} \times \underline{\mu}$$

and so there is a polarization density

$$\underline{P} = \frac{1}{c^2} \underline{v} \times \underline{\mu} \, \rho_n .$$

This can be seen from the transformation properties of electromagnetic fields. $\underline{E}$ and $c\underline{B}$ transform as a second rank tensor under Lorentz transformations, as do $c\underline{D}$ and $\underline{H}$. Now

$$c\underline{D} = c\varepsilon_0 \underline{E} + c\underline{P} = \frac{1}{c\mu_0} \underline{E} + c\underline{P}$$

and

$$\underline{H} = \frac{1}{c\mu_0} c\underline{B} - \underline{M}$$

and so $c\underline{P}$ and $-\underline{M}$ also transform as a second rank tensor. By transforming from the moving frame, where there is just a magnetization $\underline{M}$, to the stationary frame, we find a polarization

$$\underline{P} = \frac{1}{c^2} \underline{v} \times \underline{M} .$$

But $\underline{M} = \rho_n \underline{\mu}$ and so this is equivalent to the above equation. The charge density is given by $-\underline{\nabla}.\underline{P}$, and for a spherically symmetric vector field $\underline{P}$,

$$\underline{\nabla}.\underline{P} = \frac{1}{r^2} \frac{d}{dr} (r \underline{r} .\underline{P}).$$

Thus we find

$$\rho_{\ell s} = (\frac{\hbar}{mc})^2 \mu_n \underline{\ell}.\underline{s} \frac{1}{r^2} \frac{d}{dr} (r \rho_n) \quad .$$

a result first obtained by Bertozzi *et al.* (1972). This is a single nucleon (neutron in this case) contribution to the charge distribution, and so here ρ_n refers to the density of neutrons in the $n\ell j$ subshell $\rho_n(n\ell j)$. Thus the total charge density produced through the spin orbit effect by neutrons is

$$\rho_{\ell s} = (\frac{\hbar}{mc})^2 \mu_n \sum_{n\ell j} \underline{\ell} . \underline{s} \frac{1}{r^2} \frac{d}{dr} (r \rho_n(n\ell j))$$

with a similar sum for protons.

Now $\underline{\ell}.\underline{s} = \frac{1}{2}\ell$ for $j = \ell+\frac{1}{2}$, $2\ell+2$ nucleons

$= -\frac{1}{2}(\ell+1)$ for $j = \ell-\frac{1}{2}$, 2ℓ nucleons

and so the sum over both values of j, assuming the same radial wavefunction, vanishes, leaving only the contribution from unclosed ℓ-shells. In calcium all the ℓ-shells are filled for the proton distribution, while the eight neutrons added between ^{40}Ca and ^{48}Ca go into the $1f_{7/2}$ subshell, leaving the $1f_{5/2}$ subshell empty. Thus in calcium there is only an effect from valence neutrons, which is why I have been discussing neutrons throughout.

Strictly speaking, because spherical symmetry was invoked in the derivation it is only true for filled j-subshells, but it is invariably used for partly filled subshells also.

Putting together the three contributions, we find

$$\rho_c = \rho_p \otimes F_p + \rho_n \otimes F_n + \rho_{\ell s}.$$

Bertozzi et al. also calculated the effect of these additional contributions to the mean square charge radius:-

$$\langle r^2 \rangle \approx \langle r_p^{\,2} \rangle + \langle r^2 \rangle_p + \frac{N}{Z} \langle r^2 \rangle_n + \frac{N(n\ell j)}{Z} \ell \mu_n \left(\frac{\hbar}{mc}\right)^2$$

where $\langle r_p^{\,2} \rangle$ is the mean square radius of the point proton distribution, $\langle r^2 \rangle_p$ and $\langle r^2 \rangle_n$ are the proton and neutron mean square radii and $N(n\ \ell\ j)$ is the number of valence neutrons in the $n\ell_{\ell+\frac{1}{2}}$ subshell. In the case of ^{48}Ca

$N = 28$ $\qquad N(1f_{7/2}) = 8$

$Z = 20$ $\qquad \ell = 3$

and using

$\mu_n = -1.79$ n.m. $\qquad \langle r^2 \rangle_n = -0.116$ fm^2

we find the effect of the neutrons on $\delta\langle r^2\rangle^{40-48}$ is 0.046 fm^2 from the neutron form factor and 0.110 fm^2 from the spin orbit effect. The observation that ^{48}Ca has a slightly smaller charge radius than ^{40}Ca, or at least a very closely similar one, does not imply that the proton distribution has shrunk. I shall return to this point in Chapter 7 when the results of this experiment are used to derive values for $\delta\langle r^2\rangle$.

1.3 Electron Scattering and Muonic Atoms

Within the plane wave Born approximation, the differential cross section for elastic electron scattering from a spin-zero nucleus is

$$\frac{d\sigma}{d\Omega} = \left.\frac{d\sigma}{d\Omega}\right)_{Mott} |F(q)|^2 \qquad (1)$$

where $\left.\frac{d\sigma}{d\Omega}\right)_{Mott}$ is the point charge scattering cross section calculated by Mott and $F(q)$ is the form factor. It is $F(q)$ which contains all the information about the nucleus:-

$$F(q) = \int \rho_c(\underline{r})\, e^{i\underline{q}.\underline{r}}\, d^3\underline{r} \qquad (2)$$

where $\underline{q}$ is the momentum transfer

$$\hbar\underline{q} = \underline{p}' - \underline{p}$$

between the incident and scattered electron. Note that the Z-dependence of the point charge scattering cross section is contained in F(q), because of the normalization of ρ_c.

Going beyond the first Born approximation does not change the essential physics - a quantity derived from the experimental data is the

Fourier transform of the charge distribution. Thus, because we can take data only up to some finite momentum transfer q_{max} we have a problem that appears in similar forms in other branches of science, e.g. radio astronomy, of determining a function from incomplete knowledge of its Fourier transform.

Initially some model, such as a two-parameter Fermi distribution, was taken and the parameters varied to give the best fit to the data. As more data, at higher momentum transfers, were obtained, more and more parameters were needed to give a good fit. The disadvantages of model fitting were considered by Sick (1974). The major problem is that one has no realistic estimate of the error in the resulting $\rho_c(r)$, since the only error estimate one has is in the model parameters; there is no way of telling what error is introduced by the particular limitations of the model itself. Furthermore, the model may introduce correlations between different parts of the distributions, because of its particular form, which are potentially misleading in that a parameter introduced to give a certain freedom to the model may in fact affect the distribution in other ways as well.

In this paper Sick introduced a "model independent" method of analysis, the sum-of-Gaussians method. He pointed out that while there is no truly model-independent way of analysing the data, one has constraints on possible $\rho_c(r)$; for example because of the finite extent of the proton one does not expect to find structure in $\rho_c(r)$ on a length scale smaller than 0.8 fm. In fact theoretical calculations generally show no structure below a rather larger limit, and a fundamental argument based on an upper limit for $d^2\rho_p/dr^2$ can be constructed to explain this. The second point is that it is desirable to make every parameter in the model-independent model affect the charge density over a particular range of r only, in order that the true precision in determining ρ_c at that point can be discovered, and not connected to ρ_c at other points. This leads naturally to the sum-of-Gaussians (SOG) model:-

$$\rho_c(r) = \frac{Ze}{2\pi^{3/2}\gamma^3} \sum_{i=1}^{N} \frac{Q_i}{1+2R_i^2/\gamma^2} [\exp -(r-R_i)^2/\gamma^2 + \exp-(r+R_i)^2/\gamma^2]$$

where normalization requires $\sum Q_i = 1$.

The width of each Gaussian is the same and fixed, for reasons explained above. In calcium, for example, Sick has used R_G ($= \gamma\sqrt{3/2}$, the rms radius of each Gaussian) fixed at 1.45 fm (Sick et al., 1979). The R_i are random, subject to a pre-determined density along the r-axis e.g. two per fm up to some maximum, and one per fm beyond that up to an outer limit. For this set of R_i the Q_i are determined by a least squares fit to the data. This is repeated many times, with different randomly generated sets of R_i. All those resulting distributions for which the fit to the cross sections is better than some criterion constitute the range of possible distributions, and so the envelope of these distributions determines the model independent error limit on ρ_c, while the best such distribution gives the most likely form for ρ_c.

This is not the only method of analysing electron scattering data independently of model. In the same year Dreher et al. (1974) introduced the Fourier Bessel expansion. By making the weak assumption that the charge density is zero outside some radius one can obtain the charge density as a Fourier series whose coefficients are determined by the form factor. Because of the spherical symmetry, however, the functions in the expansion are not sines and cosines but spherical Bessel functions

$$\rho_c(r) = \sum a_\nu j_0(q_\nu r) \tag{3}$$

where

$$a_\nu = \frac{1}{2\pi}\frac{q_\nu^2}{R} F(q_\nu)$$

$$q_\nu = \frac{\pi\nu}{R} \quad .$$

At very large q the form factor is determined by the proton form factor, and so an estimate of the contribution of form factor values above

q_{max} can be made, and the associated error - the completeness error - gives a model-independent error band to the $\rho_c(r)$.

Having briefly described the methods used for analysis, we now consider what electron scattering can tell us about charge distributions. Firstly an experimental point: to measure a cross section certain geometrical factors are involved - effective size of detector, number of scatterers per unit area of beam, etc. These result in a normalization uncertainty in the measured cross sections, that is they can all be scaled by some number near one. If sufficient data, to sufficiently high q, are available the data will "normalize themselves" through a sum rule in the Fourier-Bessel coefficients:-

$$F(q=0) = \int \rho_c(r)\, d^3\underline{r} = Z \qquad \text{from (2)}$$

$$= \sum 2\,(-)^{\nu+1} F(q_\nu) \qquad \text{from (3).}$$

However, to use this we also need data at very small momentum transfer - small scattering angles - and these are very difficult to obtain. These cross sections at small scattering angles also contribute most of the information to the measurement of mean square charge radii:-

$$\langle r^2 \rangle = 2R^2 \sum (-)^{\nu+1} \left(1 - \frac{6}{(\pi\nu)^2}\right) F(q_\nu)$$

in the Fourier-Bessel method of analysis. Because of the decreasing nature of $F(q_\nu)$, the first few form-factor values contribute most to this summation. Thus we see the problems of normalization and cross sections at small q are related, and that they combine to make $\langle r^2 \rangle$ hard to measure accurately.

Secondly we consider the limitation on the analysis due to finite q_{max}. High q form factor values are determined by small scale structure in the charge density distribution, and this is exemplified by the determination of $\rho_c(r=0)$. By Fourier inversion of equation 2

$$\rho_c(0) = \frac{1}{2\pi^2} \int F(q)\, q^2\, dq$$

and so to determine $\rho_c(0)$ we need good absolute normalization, and a sufficiently high q_{max} that contributions from the unmeasured region are negligible. Because F(q) oscillates, the contributions to the integrand are successively postive and negative - in ^{40}Ca this led to a discrete ambiguity in $\rho_c(0)$ depending on whether the form factor was extrapolated to converge to zero, or cross zero and then converge from the other side. This has now been resolved by new data (Sick et al., 1979) at higher q.

It should be pointed out that in calcium at least the q_{max} limitation is one of measuring the small cross sections involved. The paper just referred to used a 500 MeV electron beam, and so the maximum possible momentum transfer, neglecting the electron mass, is 1000 MeV/c, giving q of 5 fm^{-1}; however the cross section reaches the current limit of sensitivity at 3.7 fm^{-1}. The result of this new, high momentum transfer, data is that $\rho_c(r)$ for ^{40}Ca is well determined even at the centre of the nucleus, as shown in Fig. 1.1, which is taken from Sick et al. (1979). (This analysis also used muonic data - see below.)

We now turn to the measurement of X-rays emitted by muonic atoms to see in what way they supplement the information about the nuclear charge distribution. A muonic atom is created when a nucleus in a solid target captures a muon from a muon beam. The lifetime of the muon (2 μs), and the decay rates of excited muonic states (e.g. 2p state has a lifetime of 4.8 x 10^{-17} s) are such that the muon is quite likely to transfer to its lowest energy level before decaying, and so such a target in a muon beam is a source of X-ray lines.

Neglecting for the moment all relativistic effects, and the effects of finite nuclear size and screening by the electrons, the muonic atom is hydrogen-like. Thus, to this approximation, the energy levels are

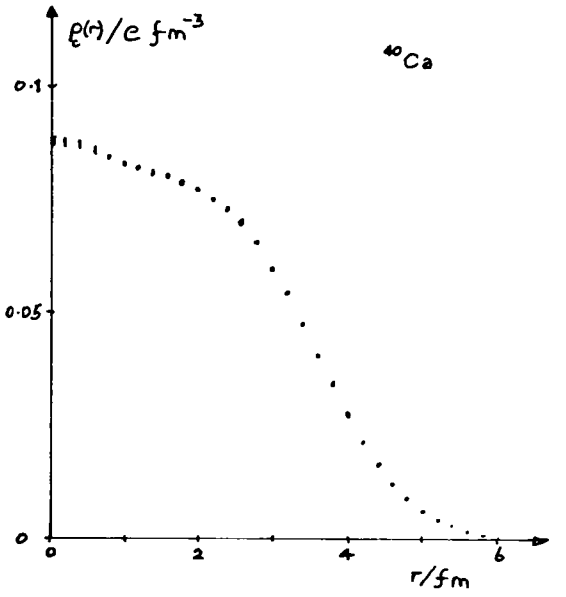


FIGURE 1.1 Charge Density of ^{40}Ca
(from Sick et al, 1979).
The uncertainty due to statistical and incompleteness errors is shown where it is larger than the thickness of the pen line.

$$E_n = -Z^2 \left(\frac{m_\mu}{m_e}\right) \frac{R}{n^2}$$

and so the energy of the X-ray emitted in the 2p-1s transition, the most frequently studied, is

$$2.11\ Z^2 \text{ keV}$$

which for Ca gives 845 KeV (the observed value is 784 KeV). The quantity corresponding to the first Bohr radius is

$$\frac{a_\mu}{Z} = \left(\frac{m_e}{m_\mu}\right) \frac{a_o}{Z} = 256/Z \text{ fm}$$

which for Ca is 13 fm. Thus nuclear size effects are going to be very important, given that the nuclear radius given by $1.2A^{1/3}$ fm is 4.1 fm.

In order to calculate the effect of the finite nuclear size, a perturbation approach starting from zero nuclear size is not going to be very satisfactory: one needs to start with a reasonable charge distribution and solve the Dirac equation for the muon moving in that potential. It was pointed out by Barratt (1970) that for a class of charge distributions including most likely distributions, the transition energy depended on a certain integral over the charge distribution to a very good approximation. Thus the transition energy determines what has come to be known as the Barratt radius $\langle r^k e^{-\alpha r} \rangle$ where k and α are given as functions of Z. For the $2p\ ^2P_{3/2}$-$1s\ ^2S_{1/2}$ transition k is close to 2, and α is small ($\lesssim 0.15$ fm^{-1}), and so for this transition the Barratt radius is similar to the second moment; for example in calcium k = 2.114, α = 0.065 fm^{-1}.

The reason for this model independence can be understood as follows: in first order perturbation theory, the isotope shift of a given level can be written as

$$\Delta E = -e \int \rho_\mu \, \Delta\phi_c \, d^3\underline{r}$$

where ρ_μ is the probability density of the muon, $\psi^{\dagger}\psi$, and $\Delta\phi_c$ is the change in electrostatic potential due to the change in nuclear charge distribution $\Delta\rho_c$. However, interchanging the order of integration (there is of course an integration in ϕ_c) we find

$$\Delta E = e \int \Delta\rho_c \, \phi_\mu \, d^3\underline{r}$$

where ϕ_μ is the electrostatic potential due to the muon, showing that $\Delta E = \Delta\langle\phi_\mu\rangle$ where the average is taken over the charge distribution. For the isotope shift in a transition ϕ_μ is replaced by the change in potential between the two states. Thus the model independence is derived from the fact that for all reasonable nuclear charge distributions, the electrostatic potential set up by the muon distribution is the same, and proportional to $r^k e^{-\alpha r}$. The absolute transition energy therefore determines the Barratt radius, and the isotope shift the change in Barratt radius.

In order to do this, all the other corrections to the energy must be calculated - effect of nuclear motion, nuclear polarization and higher order QED effects. This has been done for nuclei in the calcium region with an uncertainty of about 20 eV for the QED corrections, and 60 eV for the nuclear polarization correction. (The latter is an arbitrarily assigned error of 30% of the correction - see Wohlfahrt et al., 1981).

In order to get an idea of the precision possible with muonic data I shall take as an example the 2p-1s transition in calcium (Wohlfahrt et al., 1978 and 1981). The isotope shifts are small and so targets of separated isotopes have to be used. The absolute transition energy for ^{40}Ca was found to be 784.180(25) KeV, and so the theoretical uncertainty of $\sim$80-100 eV is larger than the experimental error. The transition energy for a Dirac particle in a pure Coulomb field, corrected for nuclear motion to lowest order,

and including α^2 corrections, is

$$\frac{1}{2}\ \frac{Z^2\alpha^2 m_\mu}{1 + m_\mu/M_{Ca}}\ \left(\frac{3}{4} + \alpha^2 Z^2 \frac{15}{64}\right) = 847.256 \text{ KeV}.$$

Higher order QED corrections contribute 5.907 KeV, and nuclear polarization 0.170 KeV, leaving a field shift of -63.076 KeV, which, with a sensitivity factor of -0.1922 fm^k/KeV implies a Barratt radius of 12.123 fm^k. (Note that I am outlining the main contributions to the energy with reference to a point nucleus for the sake of clarity - in the actual calculations reasonable nuclear charge distributions are used at all times, and the Dirac equation solved numerically.) In fact the Barratt radius was found to be 10.879(5) fm^k, where the error does not include the estimated 0.012 fm^k uncertainty due to the nuclear polarization correction.

Wohlfahrt et al. were also able to measure transition energies of other calcium isotopes - ^{42}Ca, ^{43}Ca, ^{44}Ca and ^{48}Ca with similar precision, and ^{46}Ca with rather lower precision (~100 eV) because this very rare isotope could only be obtained in a small sample with 43% ^{46}Ca and 50% ^{40}Ca. We shall consider the isotope shift ^{44}Ca-^{40}Ca. The difference in transition energies is -1.023(13) KeV; note that energy differences are determined with rather smaller error than the absolute transition energies. The theoretical uncertainties are also smaller. This shift is largely composed of a shift due to the change in reduced mass correction:-

$$\Delta E_{mass}^{44-40} = \left(\frac{m_\mu/M_{40} - m_\mu/M_{44}}{1 + m_\mu/M_{44}}\right) E_{40} = 0.202 \text{ KeV}$$

and a shift due to the change in the Barratt radius

$$\Delta E_{field} = \frac{\delta \langle r^k_e - \alpha r \rangle^{44-40}}{C_z}$$

where the sensitivity factor C_z was given above as -0.1922 fm^k/KeV. There

is also a small change in other corrections of 0.014 KeV, giving a field shift of 1.240 KeV, and hence $\delta\langle r^k e^{-\alpha r}\rangle = 0.238\ fm^k$.

Having discussed separately the analysis of data from muonic atoms and electron scattering we must finally discuss the combined analysis of data from both sources. This has been done both by Sick in the paper quoted above (Sick, 1979) and Wohlfahrt et al. (op. cit.). The most obvious way of using the muonic data is to use the Barratt radius as a constraint on the charge density, and consider only $\rho_c(r)$ which have this Barratt radius. Since, as noted earlier, the Barratt radius is similar to a mean square radius, and the mean square radius is determined in electron scattering by form-factor values at low momentum transfer, we find that the information deduced from muonic atoms supplies just that information which is hard to obtain from electron scattering alone.

A second way of combining the two sources of information is by calculating charge distribution differences. These can be calculated from cross section ratios and transition energy differences, both of which are more accurately determined, because of common normalization factors, than information for a single isotope. Some of these $\Delta\rho_c$ for calcium isotopes, taken from Wohlfahrt et al. (1981) are shown in Chapter 7 when the latest experiments determining the charge density are compared. This combined analysis also permits values of $\delta\langle r^2\rangle$ to be deduced, which is very important for the interpretation of optical isotope shifts, to which we now turn.

1.4 Optical Isotope Shifts

It was shown in the last section that the combination of detailed information about ρ_c from electron scattering and the measurement of a single, integral parameter by muonic atoms allowed a combined analysis giving, if sufficient information is available, a very good picture of the charge dis-

tribution. It might be asked why it is then interesting or necessary to measure optical isotope shifts. Part of the answer can be given straight away - the optical isotope shift can be measured with higher precision from a sample containing other isotopes of the element and, more importantly, almost unlimited quantities of other elements, than the muonic isotope shift. However to do justice to the question, it is necessary to go into the theory of isotope shift, which we now proceed to do before returning to the question at the end of the section.

In order to calculate the isotope shift it is sufficient to use a perturbative method, although it may in some cases be necessary to go beyond first order perturbation theory, as we shall see in Chapter 8. Thus we need expressions for the perturbing operators. Consider physically the difference between two atoms, different isotopes of the same element. The only differences between them that appear in the atomic Hamiltonian are the following:-

(i) The nuclei have different masses M_N

(ii) The nuclei have different charge distributions ρ_c

(iii) The nuclei have different spins and multipole moments.

We shall consider each of these in turn.

Firstly we consider the effect of the mass of the nucleus. This enters the Hamiltonian mainly in the kinetic energy of the nucleus. Because the method used to derive the operator in most text-books is only valid as a relation between matrix elements, which is sufficient in first order but might lead to doubt as to the correct procedure in second order, I shall derive the perturbing operator rather carefully, in a non-relativistic approach. Relativistic corrections to this operator have been derived (Stone, 1961, 1963; Bauche and Champeau, 1976) and observed (de Clercq et al., 1981); these are not required for any of this work, and since their dependence on M_N is the same, they are only ever relevant in a comparison of a theoretical calculation of the mass effect with experiment.

We consider therefore an atomic Hamiltonian in an inertial reference frame

$$(4) \qquad H = \frac{P_N^2}{2M_N} + \sum_i \frac{p_i^2}{2m} + V(\underline{r}_i - \underline{r}_N, \underline{r}_i - \underline{r}_j)$$

where the interaction energy is supposed to depend only on relative co-ordinates and velocities. It is usual to work in a reference frame with the nucleus at the origin, and the centre of mass motion separated off. This can be done in two ways: either, first make the transition to quantum mechanics and then change variables, or change variables by performing a classical canonical transformation and then make the transition to quantum mechanics. Both methods yield the same operator; I shall follow the second route.

We want to introduce new position variables

$$(5a) \qquad \text{centre of mass} \qquad \underline{R} = \frac{M_N \underline{r}_N + \sum_i m\underline{r}_i}{M}$$

$$(5b) \qquad \text{relative position} \qquad \underline{r}'_i = \underline{r}_i - \underline{r}_N$$

where M is the atomic mass, $M = M_N + Zm$. This means that we must also change momentum variables in a canonical transformation (see e.g. Goldstein, 1950, Chapter 8). We do this using a transformation function

$$F = \underline{P} \cdot \underline{R} + \sum_i \underline{p}'_i \cdot \underline{r}'_i$$

where $\underline{P}$ and $\underline{p}'_i$ are the momenta conjugate to $\underline{R}$ and $\underline{r}'_i$. The equations of transformation are

$$\bar{q} = \frac{\partial F}{\partial \bar{p}} \qquad p = \frac{\partial F}{\partial q}$$

where p, q and $\bar{p}$, $\bar{q}$ are any conjugate pair of old and new co-ordinates respectively. The first equation is trivial, while the second gives

$$\underline{P}_N = \frac{M_N}{M}\underline{P} - \sum_i \underline{p}_i'$$

$$\underline{p}_i = \frac{m}{M}\underline{P} + \underline{p}_i' \ .$$

Substitution into the Hamiltonian gives the transformed Hamiltonian

$$H = \frac{P^2}{2M} + \sum_i \frac{p_i'^2}{2\mu} + V(\underline{r}_i', \underline{r}_i' - \underline{r}_j') + \frac{1}{2M_N}\sum_{i\neq j} \underline{p}_i' \cdot \underline{p}_j' \tag{6}$$

where $\mu = m/(1 + m/M_N)$. This gives the usual atomic Hamiltonian with the following changes: (a) the additional term $P^2/2M$, which is the centre of mass motion and, in the absence of external fields, is separable from the internal motion and can therefore be ignored; and (b) the replacement of m by μ in the electron kinetic energy term, and the additional term at the end. These last two are responsible for the mass shift. We can write the kinetic energy operator instead as (dropping primes from now on)

$$\sum_i \frac{p_i^2}{2m} + \frac{1}{2M_N} P^2 \qquad \text{where } P = \sum_i \underline{p}_i \ . \tag{7}$$

The first form corresponds to splitting up this second form into its one-electron and two-electron parts, which are responsible for the normal and specific mass shifts respectively. If we write $M_N = AM_u$, where A is the mass in a.m.u. (approximately given by the mass number) and M_u is the mass of the a.m.u., we obtain for the perturbation between two isotopes

$$(H_{A'} - H_A)_{mass} = \frac{1}{2M_u}\left(\frac{1}{A'} - \frac{1}{A}\right) P^2 \ . \tag{8}$$

There are two points to be made about equation 8. The first concerns correc-

tions to the isotope shift operator; in the papers referred to above (Stone, 1961, 1963) Stone derives an electronic Hamiltonian containing other terms dependent on the nuclear mass; these are all of order $\alpha^2 m/M_N$, whereas equation 8 is of order m/M_N. Stone ignores all operators of order $(m/M_N)^2$; however it is clear from his work that any such terms are also relativistic, and hence of order $(\alpha m/M_N)^2$, which is certainly negligible. Thus to an excellent approximation the isotope shift operator is proportional to $\delta(1/M_N)$. The second point concerns the method used to evaluate the expectation value of the operator. It is usual to assume that the one-electron part, the normal mass shift, causes a scaling of the entire spectrum by μ/m. Thus the effect of this term in the isotope shift is

$$NMS^{A'-A} = \left(\frac{\mu^{A'}}{\mu^{A}} - 1\right) \nu(A)$$

where $h\nu(A)$ is the transition energy in isotope A. This gives

$$(9) \qquad NMS^{A'-A} = \left(\frac{1 + m/M_A}{1 + m/M_{A'}} - 1\right) \nu_A = \frac{m}{M_u}\left(\frac{1}{A'} - \frac{1}{A}\right) \frac{\nu_A}{1 + m/M_A}$$

This is only true if the order α^2 magnetic terms in the electronic Hamiltonian are ignored, and Stone also calculates effective isotope shift operators which correct for using this approximation to the expectation value. The $(1 + m/M_A)$ denominator can be ignored therefore since firstly it implies an exactness in the formula that is not really present, and secondly, it is anyway very small. (These statements do not necessarily apply to one-electron atoms.) Since there is always the specific mass shift (SMS) term to be added to the NMS, which cannot be calculated with any degree of precision, equation 9 is really only useful as a guide to the order of magnitude of mass shifts to be expected. In complex spectra it is a rough guide at best, as the SMS can be many times larger.

The second isotope shift effect to be considered is that of the change

in the nuclear charge distribution between isotopes. I shall follow the same procedure of presenting a non-relativistic calculation and referring to the results of more detailed calculation.

The same approach that we used when considering the muonic atom field shift, of considering the nuclear charge interacting with the potential set up by the electrons, is useful here also. Now s-electron wavefunctions are substantially constant over the nuclear volume, and other wavefunctions are very small, and so to a good approximation the potential set up by the electrons is determined by

$$\nabla^2 \varphi_e = \frac{e}{\varepsilon_0} |\psi(0)|^2$$

which, neglecting constants of integration, has the solution

$$\phi_e = \frac{r^2}{6} \frac{e}{\varepsilon_0} |\psi(0)|^2 \quad .$$

Thus the field shift is given by (Rosenthal and Breit, 1932)

$$FS^{A'-A} = Ze \int \Delta\rho_c(\underline{r})\ \phi_e\ d^3\underline{r}$$

or

$$FS^{A'-A} = \frac{4\pi}{3} Z(a_0^3\ |\psi(0)|^2) \frac{\delta\langle r^2\rangle^{A'-A}}{a_0^2} \quad \text{Rydberg's.} \tag{10}$$

Bodmer (1953) was the first to show that when relativistic effects are considered, and without using perturbation theory, the isotope shift is still approximately proportional to $\delta\langle r^2\rangle$, whatever the shape of the nucleus. In very heavy atoms this approximation starts to break down (Seltzer, 1969) but in elements in the calcium region this approximation is excellent. Thus we can summarize this result in the equation

$$FS^{A'-A} = F\ \delta\langle r^2\rangle^{A'-A} \tag{11}$$

where F is proportional to the change in electron density at the nucleus. This leads us to suppose that transitions involving a change of the number of s electrons are most favourable for the observation of large field shifts; this is usually the case, although in complex spectra the re-arrangement of the inner shells between the two states can lead to a large effect even if the two configurations have equal numbers of s-electrons. In the calcium transition studied here ($4s^2$-4s5s) the number of s-electrons is unchanged but the n quantum number changes by one; this too leads to a significant change in electron density.

The third and final isotope-dependent term in the Hamiltonian is the hyperfine interaction. Generally this can be written

$$H_{hf} = \sum_{k=1}^{2I} T_n^k \cdot T_e^k \qquad (12)$$

where T_n^k is a nuclear multipole moment of rank k, and T_e^k an electron operator of rank k. Thus isotopes with zero spin have no hyperfine interaction, and in levels with zero J there is no hyperfine structure. It is well known that in first order H_{hf} leaves unchanged the centre of gravity of the hyperfine structure, and so to this order there is no isotope shift due to this Hamiltonian. However in second order this is not so; the Hamiltonian can couple states of different J, which in second order does lead to shifts of the centre of gravity. This is true for levels with J = 0 as well as other levels - although they show no hyperfine structure they are still subject to the hyperfine interaction, and this can shift the level in second order. We shall make simple calculations of the second order hyperfine interaction in Chapter 7.

To sum up then, the isotope shift in a spectral line, ignoring second-order hyperfine effects which are zero in isotopes with no nuclear spin, and negligibly small in many transitions any way, is given by

$$\delta\nu_{if}^{A'-A} = -M_{if}\left(\frac{1}{A'} - \frac{1}{A}\right) + F_{if}\,\delta\langle r^2\rangle^{A'-A} \quad . \tag{13}$$

I should insert here a word about sign conventions:- $\delta\nu^{A'-A}$ denotes $\nu(A') - \nu(A)$ and so if $A' > A$ this is the usual sign convention that the isotope shift is positive if the higher mass-number isotope has the higher frequency. I shall not always use $A' > A$, but the notation always has the significance just stated. F_{if} is proportional to

$$|\psi_f(0)|^2 - |\psi_i(0)|^2$$

where f and i are the upper and lower states, and so is negative if the upper state has smaller electron density at the nucleus, as is very often the case. M_{if} is approximately given by

$$\frac{1}{2M_u}\left(\langle i|P^2|i\rangle - \langle f|P^2|f\rangle\right);$$

there is no general sign convention established for M since both alternatives have disadvantages; this definition has the states i and f appearing in a different order from the definition of F, but has the advantage that a positive M implies a positive mass shift, and similarly for F.

Equation 13 relies only on the validity of first order perturbation theory since, as noted above, the relativistic corrections to mass shift are also proportional to $\delta(1/M_N)$. It thus indicates the maximum amount of information we can obtain from optical isotope shifts alone. The nuclear properties enter only in the accurately known nuclear mass and the change in mean square charge radius. Thus to determine $\delta\langle r^2\rangle$ it is necessary first to separate the mass and field shifts, by determining M, and secondly find a value for F in order to interpret relative $\delta\langle r^2\rangle$, given by the field shifts themselves, as absolute $\delta\langle r^2\rangle$. Neither of these steps can be performed with isotope shift data in one spectral line alone.

Neither is it possible to gain additional information from another spectral line, because of a relationship between isotope shifts in different spectral lines first discovered by King (1963). Multiplying equation 13 by $(\frac{1}{A} - \frac{1}{A'})$ we find (writing i for if)

$$\delta\sigma_i^{A'-A} = M_i + F_i(\delta\langle r^2\rangle^{A'-A} \frac{A'-A}{AA'})$$

where

$$\delta\sigma_i^{A'-A} = \frac{A'-A}{AA'} \delta\nu_i^{A'-A}$$

and similarly for a spectral line j

$$\delta\sigma_j^{A'-A} = M_j + F_j(\delta\langle r^2\rangle^{A'-A} \frac{A'-A}{AA'}).$$

Eliminating the bracketed term which contains all the dependence on nuclear properties we find

$$\delta\sigma_j^{A'-A} = (M_j - \frac{F_j}{F_i} M_i) + \frac{F_j}{F_i} \delta\sigma_i^{A'-A} \tag{14}$$

showing that the scaled isotope shifts $\delta\sigma$ lie on a straight line with slope $\phi = F_j/F_i$ and intercept $\mu = M_j - \phi M_i$. Thus an additional spectral line introduces two new unknowns, M_j and F_j, and allows only another two constants, ϕ and μ, to be determined.

In heavy atoms, methods for estimating M and F have been developed (Heilig and Steudel, 1974), and these are sufficiently accurate to allow very useful values of $\delta\langle r^2\rangle$ to be obtained. In light atoms these techniques break down completely because the relative size of the mass and field shifts require that the mass shift constant M be determined with very high precision. This can be seen from the following order of magnitude estimate. Consider a transition at 6000Å with an electron density change at the nucleus of one electron a_o^{-3}, and consider the isotope shift between A and A+2.

$$\text{Mass shift} \approx \frac{550}{A^2} \text{ GHz}$$

$$\text{Field shift constant} \approx 5 \times 10^{-3} Z \text{ GHz fm}^{-2}.$$

If we further estimate $\langle r^2 \rangle = 1.44\ A^{2/3}\ \text{fm}^2$,

so that $\delta\langle r^2 \rangle^{A,A+2} = 1.92\ A^{-1/3}\ \text{fm}^2$

this gives a field shift $\approx 10^{-2} Z/A^{1/3}$ GHz.

Thus the ratio of mass and field shifts is a very strong function of Z, and in the region of Z = 20 the field shifts are very small compared with the mass shifts.

Despite this the very great precision with which isotope shifts can be measured, and the high accuracy with which nuclear masses are known mean that $\delta\langle r^2 \rangle$ can be deduced from the measurements with a greater accuracy than using just the electron-scattering and muonic atoms data. The method used is an extension of the idea of combined analysis already used for the muonic and electron scattering data; they have been used to determine $\delta\langle r^2 \rangle$ between all stable isotopes in calcium, and we can use these several pieces of data to determine the constants F and M with sufficient precision to deduce more accurate values of $\delta\langle r^2 \rangle$. In the end this process is limited by the accuracy of the muonic isotope shifts, but a very considerable improvement in accuracy can be achieved.

That in itself might be reason enough for measuring isotope shifts in calcium. However there is another very powerful reason: it is quite possible to measure isotope shifts and hyperfine structures of radioactive isotopes with very small samples in the presence of enormous backgrounds of other elements, and large backgrounds of stable calcium isotopes. This can yield measurements of $\delta\langle r^2 \rangle$, spin, and magnetic and quadrupole moment ratios. This experiment does not include measurements on radioactive isotopes, for the reasons that a two-photon transition does not, because of its dependence on $(\text{power})^2$, give as much signal from a small number of atoms as a one-photon

transition, except at laser powers rather larger than seemed likely in the foreseeable future at the time. The sort of powers available from ring dye lasers at some wavelengths may soon change this view, but it is still very much easier to do a sensitive experiment on a one-photon transition. This does not mean that our experiment does not contribute to the determination of $\delta\langle r^2\rangle$ for unstable isotopes; the very accurate isotope shifts we have been able to measure, and our relative freedom from second order hyperfine effects, means that this information leads, essentially through the King plot, equation 14, to more accurate values of M and F for these other transitions.

1.5 Other Isotope shift measurements in Calcium

The natural abundances of the stable calcium isotopes and the lifetimes of the unstable ones are shown in Table 1.1. It can be seen that all

TABLE 1.1

Abundances and Lifetimes of Calcium Isotopes

A	Lifetime	Abundance
40		96.94%
41	1.3×10^5 y	
42		0.65%
43		0.14%
44		2.08%
45	163 days	
46		0.003%
47	4.54 days	
48		0.19%

isotopes except ^{40}Ca can be considered rare, and this has seriously hampered the measurement of isotope shifts by optical spectroscopy. The isotope shift ^{48}Ca-^{40}Ca was determined by Pery (1954) using separated isotopes in hollow cathode discharge lamps, as part of an investigation of the hyperfine structure of ^{43}Ca (Kelley et al., 1954), in a number of lines in Ca and Ca^+. Further isotope shift work, described briefly in Bruch et al. (1969), together with electron scattering data, for the isotopes ^{42}Ca, ^{44}Ca and ^{48}Ca, showed that the mean square radius increased somewhat between ^{40}Ca and ^{44}Ca, and then decreased again so that ^{48}Ca was roughly the same size as ^{40}Ca.

This striking departure from a steady increase of $\langle r^2 \rangle$ with A stimulated further work, in optical isotope shifts as well as the electron scattering and muonic atoms work already referred to (Sick et al., 1979 and Wohlfahrt et al., 1981). Epstein and Davis (1971) measured isotope shifts in the resonance line, as did Brandt et al. (1978) who also measured for the first time the isotope shift of ^{43}Ca, and also the very rare isotope ^{46}Ca. The latter work used an atomic beam to reduce the Doppler width of the signals; with this, classical spectroscopy had reached its limit in precision and sensitivity.

With the advent of laser spectroscopy, new experiments were carried out, on both stable and unstable isotopes, at a new level of precision. In addition to the work described in this thesis, two experiments have been performed giving very precise isotope shifts in the intercombination line (Bergmann et al., 1980) and the resonance line. The latter experiment is being performed by Schatz and co-workers at Kernforschungszentrum, Karlsruhe, and final results have not yet been published (at December 1981) but progress was reported at the European Conference on Atomic Physics, Heidelberg 1981. Isotope shifts in other transitions have also been determined with less accuracy as a by-product of magnetic resonance studies in the 4s4p $^3P_2$ state (Grundevik et al., 1979) and 3d4s $^1D_2$ state (reported by Aydin, Ertmer and

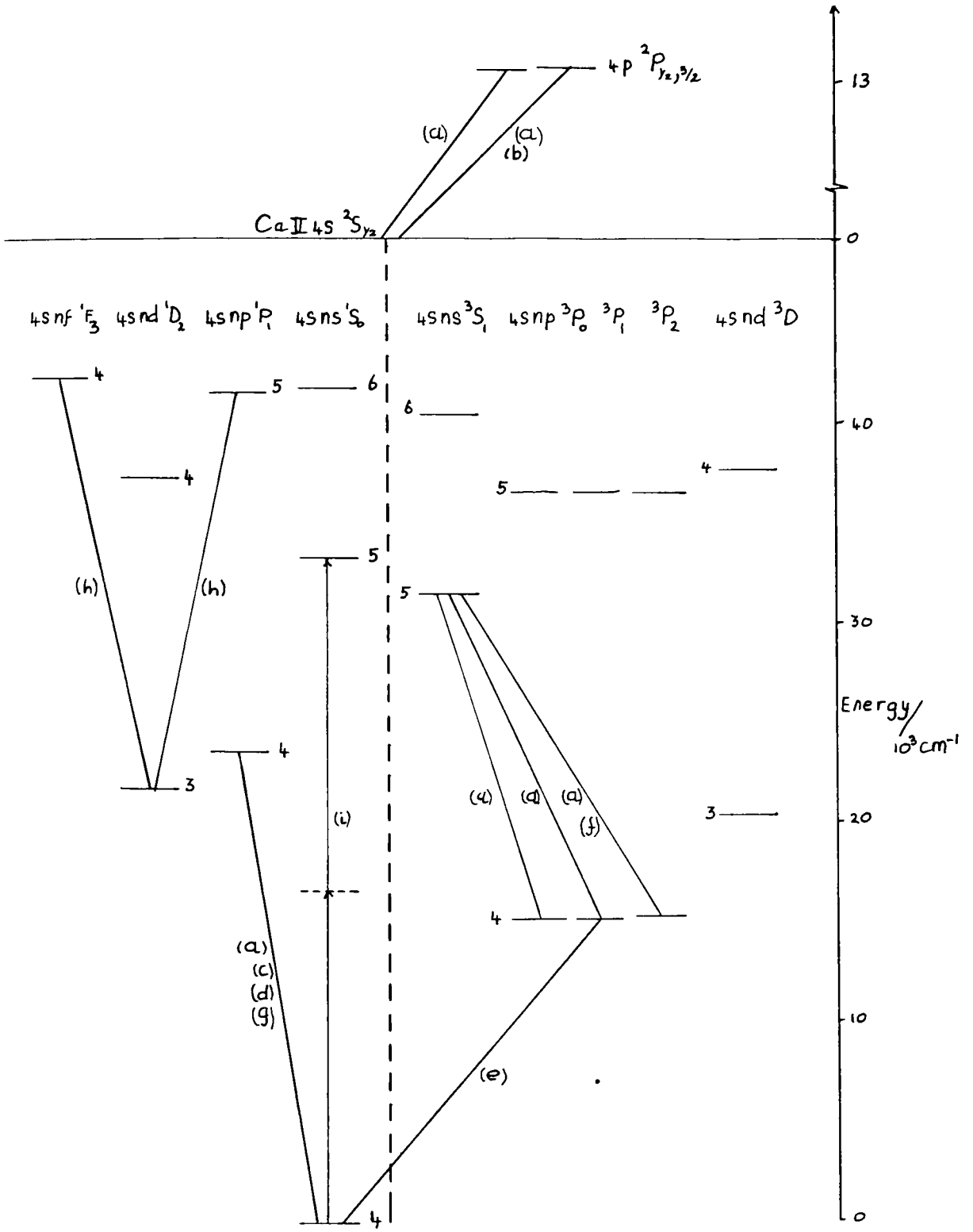


FIGURE 1.2 Term Diagram Showing Measurements of Isotope Shift in Ca.

Key
(a) Pery (1954)
(b) Bruch et al (1969)
(c) Epstein and Davies (1971)
(d) Brandt et al (1978)
(e) Bergmann et al (1980)
(f) Grundevik et al (1979)
(g) Schatz (private communication)
(h) Aydin et al (reported at ECAP 1981)
(i) This work.

Johann, ECAP, Heidelberg, 1981). This information is summarized on a term diagram in Fig. 1.2.

It can be seen from this that for determining $\delta\langle r^2\rangle$ the only experiments to consider are the three most accurate laser spectroscopy experiments, this work, and that on the resonance line and the intercombination line. The field shifts in the two s-p transitions turn out to be about twice as large as in our s-s' transition, and so we require greater accuracy of measurement to achieve the same accuracy in $\delta\langle r^2\rangle$. This is partly compensated however by the narrow linewidth we can obtain due to the small natural width of the upper state, and the absence of hyperfine structure for the isotope ^{43}Ca. The detailed comparison of results from all three experiments will be taken up in Chapter 7.

CHAPTER 2

THEORY OF TWO-PHOTON ABSORPTION

2.1 Introduction

In this chapter I shall present the theory of two-photon absorption by free atoms, with the aim of calculating the excitation rate per atom as a function of laser intensity. The transition of interest, being $J = 0 \rightarrow J = 0$, is the simplest possible case; however I shall present the theory in a rather more general way, for arbitrary J, including the effect of hyperfine structure and considering the angular distribution of the resulting fluorescence. Although this makes sections 2.4 and 2.5 rather lengthy, and not strictly relevant to this particular, very simple, case, I include the calculation because in any other transition it would be necessary. The calculation was performed because of interest in the possibility of measuring isotope shifts in the $4s^2$-$4s4d\ ^1D_2$ transition in calcium which turned out not to be technically feasible at the time; so far as I am aware the expressions for the angular distributions have not been given explicitly elsewhere.

In section 2.2 I shall describe the initial assumptions and approximations that I shall make, and refer to other work that relaxes some of these constraints. The interaction Hamiltonian is presented in section 2.3, and the result of evaluating it in perturbation theory is given in the form of a set of diagram rules. In section 2.4 these rules are applied to the case of two-photon absorption, and expressions for excitation rates calculated, neglecting hyperfine structure; the effect of hyperfine structure in modifying these results is described in section 2.5. In section 2.6 I shall briefly discuss the effects of finite laser band-width and of finite interaction time of the atoms with the laser. In section 2.7 the excitation rate for the

transition of interest in calcium is estimated.

2.2 Assumptions in the theory

The literature on Doppler-free two-photon absorption is now vast and in the presentation of a reasonably simple theory relevant to this experiment a great restriction in scope is called for. I shall, therefore, present the theory of two-photon absorption as it is likely to be used for the determination of level separations in atoms (isotope shifts, hyperfine structures, etc.). This implies the following approximations, which are briefly discussed below.

(i) I shall neglect throughout collisions between atoms.

(ii) I shall only consider the first non-zero order of perturbation theory, which is equivalent to saying that the laser power is, with respect to some criterion, low.

(iii) I shall assume that the initial state of the atoms before interaction with the laser is thermal - in particular that the m_J substates are equally populated and there is no coherence between them.

(iv) I shall assume that there is no near-resonant intermediate state; this assumption is used in various ways. Firstly the hyperfine structure of the intermediate state is neglected, and secondly the Doppler shift of the two beams for an atom moving in the laser field can be ignored.

(v) I shall assume the two laser beams have equal frequency, since only then is the Doppler effect cancelled.

(vi) I shall not consider the Zeeman effect.

Most of these are obviously the conditions that one would try to arrange for the purposes of high-resolution spectroscopy. The question of the effects of higher laser power needs to be considered a little; there are

two effects that one wants to prevent, namely shift and broadening, and their occurrence depends greatly on the presence or otherwise of a resonant intermediate state, and so condition (iv), as well as making the calculation easier, is also important from an experimental point of view. Power broadening is clearly only going to be important when the two-photon excitation rate R is large or comparable with the natural decay rate Γ_f of the upper state. Salour (1978), assuming no near-resonant states for absorption or emission of one photon from either initial or final states, shows that the shift is of order $\sqrt{R\Gamma_f}$. Thus if condition (iv) is satisfied, then so is condition (ii) provided $R \ll \Gamma_f$.

The possibility of doing Doppler-free two-photon absorption was first noted by Vasilenko, Chebotaev and Shishaev (1970), who also pointed out that in general the Doppler-free absorption peak would be superimposed on a Doppler-broadened background from atoms absorbing two photons from the same beam. Cagnac, Grynberg and Biraben (1973) extended the idea to multi-photon Doppler-free spectroscopy, and they also presented formulae for absorption rates, and showed that in some cases, by choice of polarization, the Doppler-broadened background could be eliminated. Most of the results in this chapter are not, of course, new but can be found in that paper, in the recent review by Grynberg and Cagnac (1977) and in the paper by Flusberg et al. (1976). I shall, however, go into the question of angular distribution of the radiation in rather more detail than these authors (Grynberg and Cagnac refer to it) because it can be an important consideration in the design of a suitable geometry, and in the choice of polarizations.

All the work just referred to assumes that the atoms interact with a single occupied mode of the radiation field, and that this mode is in a pure number state. In practice, an approximation to this is given by a laser with a frequency width much less than the natural width of the upper state of the two-photon transition; the question of how the finite bandwidth and interaction time of the laser affect the results is taken up in section 2.6;

until then there is a seventh assumption, that the laser bandwidth is small compared with the natural width. Various authors have considered two-photon absorption without making one or more of the above assumptions. In particular the effect of collisions in broadening the transition has been considered by Berman (1976) and Ben Reuven et al. (1976). Stenholm and Salomaa, in a series of papers (Stenholm and Salomaa, 1975, 1976, 1977, and Salomaa, 1978) have calculated the effects of relaxing conditions (i), (ii), (iv) and (v), in a formalism where collisional damping is introduced phenomenologically. Different authors also employ a variety of calculational methods, including the formalism of the "dressed atom" by Cagnac and Grynberg, and the semi-classical density matrix by Stenholm and Salomaa. I shall use elementary quantum mechanics in my calculation, starting from a Hamiltonian in which the radiation field is quantized; the justification for this very straightforward approach is considered in the next section.

2.3 The Hamiltonian, and Perturbation Theory

In his lecture course 'Atoms in strong resonant fields', Cohen-Tannoudji (1977) considers the example of resonance fluorescence in a laser beam using lowest order QED diagrams - exactly the approach I shall use for two-photon absorption - and using the dressed atom formalism. He shows that neither approach is suitable for calculating, say, the fluorescent spectrum under strong monochromatic excitation. It might reasonably be wondered, then, whether similar objections can be raised to this approach to two-photon absorption; fortunately this is not the case, despite the fact that the frequency does satisfy a resonance criterion ($2\omega = \omega_{if}$) and the field is strong by usual standards. The reason for this is that the important terms in the interaction Hamiltonian between atom and field involve absorption or emission of single photons, and we are restricting the discussion to situations where

there are no single-photon resonances between the atom and the laser field. For this reason our approach is still valid, under the assumptions of section 2.2.

The Hamiltonian for a combined system of atom + radiation field in a box of volume V is

$$H = H_{atom} + H_{field} + H_{int} \tag{1}$$

where H_{atom} is the Hamiltonian of a free atom with eigenstates $|i\rangle$, energy $\hbar\omega_i$:

$$H_{atom}\,|i\rangle = \hbar\omega_i\,|i\rangle. \tag{2}$$

$$H_{field} = \sum_{\underline{k},\lambda} \hbar\omega_{\underline{k}}\, a^{\dagger}_{\underline{k}\lambda} a_{\underline{k}\lambda} \tag{3a}$$

$$H_{int} = \sum_{\underline{k},\lambda} i\hbar\,(g_{\underline{k}\lambda}\, a_{\underline{k}\lambda} - g^{\dagger}_{\underline{k}\lambda}\, a^{\dagger}_{\underline{k}\lambda}). \tag{3b}$$

In equations 3a and 3b $a^{\dagger}_{\underline{k}\lambda}$ is a creation operator for a photon with wave-vector $\underline{k}$ and polarization vector $\underline{\varepsilon}_{\lambda}$, and the summation is over the modes of the radiation field; $a_{\underline{k}\lambda}$ is the corresponding annihilation operator. If we denote by $|n_{\underline{k}\lambda}\rangle$ a state with n photons in mode $\underline{k},\lambda$, then

$$a^{\dagger}|n_{\underline{k},\lambda}\rangle = \sqrt{n_{\underline{k}\lambda} + 1}\;|(n+1)_{\underline{k}\lambda}\rangle$$

$$a\,|n_{\underline{k},\lambda}\rangle = \sqrt{n_{\underline{k}\lambda}}\;|(n-1)_{\underline{k}\lambda}\rangle \quad .$$

Hence in equation 3b we see coupling between states in which the photon number changes by just one, as mentioned above. The operator g, which specifies the strength of this interaction, is given by

$$g_{\underline{k}\lambda} = -\sqrt{\frac{\omega_{\underline{k}}}{2\varepsilon_0 \hbar V}}\ \underline{\varepsilon}_{\underline{k}\lambda}\cdot\underline{D}$$

where $\underline{D}$ is the atomic dipole moment, $\underline{D} = \sum_{\text{electrons}} -e\underline{r} = -e\underline{R}$. Note that while $\underline{D}$ is an operator, $\underline{\varepsilon}$ is a (possibly complex) c-number. There are, of course, higher order terms in the interaction, both single photon terms like the magnetic dipole interaction, and a small two-photon term (see, for example, Loudon, 1973). The question of the correct form of the Hamiltonian, and the relative merits of the length form $\underline{E}.\underline{D}$ and the velocity form $\underline{A}.\underline{p}$ for the electric dipole approximation has been the subject of much discussion. In the case of two-photon absorption, Bunkin (1966) demonstrated the equality of the results obtained using the two interactions, provided the complete sum over intermediate states is retained. If however it is desired to make the single intermediate state approximation, the $\underline{E}.\underline{D}$ form must be used.

We shall use basis states of the form $|i>|\{n_{\underline{k}\lambda}\}>$, where the second term is an infinite product over all the modes of the radiation field; these are eigenstates of the Hamiltonian without H_{int}, with energy

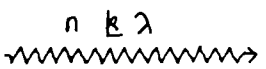
$$\hbar\omega(i,\{n_{\underline{k}\lambda}\}) = \hbar(\omega_i + \sum_{\underline{k}\lambda} n\omega_{\underline{k}}) .$$

In general a subscripted ω (e.g. ω_i) refers to a state of either the atom or the field; which is intended should be clear from the subscript. An ω followed by labels in brackets refers to one of these combined states of atom + field.

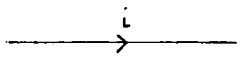
It is now a straightforward piece of quantum mechanics to find the transition rate between a specified initial state, and a specified final state, as a perturbation expansion. In accordance with what has been said above, I shall only consider initial states in which the atom is in a specified state (although I shall have to sum over magnetic substates) and a small number of modes of the radiation field are occupied, with simple number states. More complicated initial conditions are needed to describe real lasers of

course, and this is related to my additional seventh assumption.

Each term in the perturbation expansion can be represented by a diagram, and the rate can be found from the diagram using simple rules. The components of the diagram are as follows.



(i) A zig-zag line representing a multiply-occupied photon mode with wavevector $\underline{k}$ and polarization $\underline{\varepsilon}_\lambda$.



(ii) A straight line indicating an atom in state i.

Interactions are represented by junctions at which the number of photons changes by one and the atom changes state. The arrows indicate the direction of time - loosely the diagram can be thought of as showing the motions of the atom through the interaction, but the angles the lines make with each other have no significance, so this must not be taken too literally.

The diagram rules are as follows.

1) Draw all diagrams consistent with the given initial and final states (or all diagrams up to a given order).

2) The rate for the process is given by

$$2\pi\delta(\omega(\text{initial}) - \omega(\text{final}))|M|^2$$

where M is the sum of the matrix elements for each diagram.

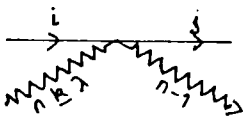
3) The matrix element for a diagram is given by the following factors:

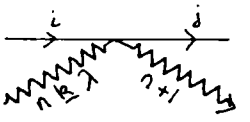
(i) For each internal atom line a factor $i/[\omega(\text{initial}) - \omega(r) + i(\Gamma_r/2)]$, where 'initial' refers to the initial state of atom + field, and 'r' its state at this point of the interaction. Γ_r is the level width of the atomic state in question, given by the sum of rates (both spontaneous and induced) depopulating the level. Within the assumptions

of section 2.2, this is given by the radiative width

$$\Gamma_r = \sum_k A_{rk} .$$

(ii) For each vertex a factor

Absorption  $-\sqrt{n}\ \left(\frac{\omega_{\underline{k}}}{2\varepsilon_0 \hbar V}\right)^{\frac{1}{2}} \langle j|\underline{D}|i\rangle . \underline{\varepsilon}_\lambda$

Emission  $\sqrt{n+1}\ \left(\frac{\omega_{\underline{k}}}{2\varepsilon_0 \hbar V}\right)^{\frac{1}{2}} \langle j|\underline{D}|i\rangle . \underline{\varepsilon}_\lambda^*$

4) For each initially occupied photon state we make the identification

$$\frac{n(\omega_{\underline{k}})}{V} = \frac{I(\omega,\Omega)}{\hbar\omega c}\ d\omega\ d\Omega$$

where I = power/unit area/unit frequency range/unit solid angle, and at the end of the calculation we can integrate over the appropriate source variables ω and Ω. This assumes no phase relation between different frequencies, and so is appropriate for a broad-band thermal source. For a laser beam an alternative form is

$$\frac{n(\omega_{\underline{k}})}{V} = \frac{P(\omega)}{\hbar\omega c}\ d\omega \qquad P(\omega) = \text{power/unit area/unit frequency}$$

since the solid angle of the source is so small; however in this case the assumption of no phase relationship may not be valid. Under our seventh assumption of narrow linewidth we get the simple form

$$\frac{n(\omega_{\underline{k}})}{V} = \frac{P}{\hbar\omega c} \qquad P = \text{power/unit area.}$$

5) For each scattered photon in the final state we must sum the probabilities of its being in all the modes within the solid angle of our detector. (Since in principle this can be as small as we desire, these different modes are in principle distinguishable, and so probabilities and not amplitudes are summed.) We do this by introducing density of states factors $\frac{V}{(2\pi)^3}\frac{\omega^2}{c^3}\, d\omega d\Omega$ for each scattered photon which are integrated over the frequency range and solid angle of detection, or, if the photon is not detected, then over all frequency and solid angle, and summed over polarization.

In the case of only one vertex, these rules reduce to the Fermi Golden Rule

$$\text{Rate} = 2\pi\delta(\omega(i)-\omega(f))\,|\langle f|H_{int}|i\rangle|^2 ,$$

and so they can be seen as a generalization to higher orders of perturbation theory of this well-known rule.

2.4 Two-photon Absorption in the absence of Hyperfine Structure

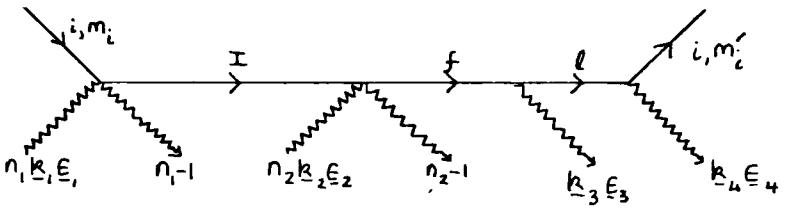
As I mentioned above, this section is made quite lengthy by the calculation of the angular distribution of the fluorescence. The main results are found in equations 12 and 15; the factors $R(k_1 k_2)$ are defined in equation 9.

It is necessary first to establish a symbol convention. The symbol i has up till now denoted a complete set of quantum numbers for a specified substate; it is now necessary to deal with angular sums, so i will sometimes be written i,m_i or i,F,m_F, and so i denotes all other quantum numbers required in addition to those explicitly given, to define completely the indicated

state with angular momentum J_i. In 3-J and 6-J symbols, to avoid unnecessary subscripts, i will be used for J_i. Henceforth an ω with numerical subscript, e.g. ω_1, represents the frequency of a photon with wave-vector $\underline{k}_1$.

It is now a straightforward task to write down the rate of two-photon absorption, with the upper state decaying by two steps to the ground state (from parity considerations, the number of steps must be even) using the two diagrams below.

(4a)



+ diagram with beams 1 and 2 interchanged

The rate for this process is $2\pi\delta(\omega_3 + \omega_4 - \omega_1 - \omega_2)\,|M(m_i m_i')|^2$ where the matrix element M is given by

$$M(m_i m_i') = \sum_{\substack{I m_I \\ m_f m_\ell}} \frac{1}{(2\varepsilon_0 \hbar V)^2} \sqrt{n_1 n_2 \omega_1 \omega_2 \omega_3 \omega_4} \quad \times$$

(4b)

$$\frac{\langle i m_i' | \underline{D}.\underline{\varepsilon}_4^* | \ell m_\ell \rangle \langle \ell m_\ell | \underline{D}.\underline{\varepsilon}_3^* | f m_f \rangle \langle f m_f | \underline{D}.\underline{\varepsilon}_2 | I m_I \rangle \langle I m_I | \underline{D}.\underline{\varepsilon}_1 | i m_i \rangle}{(\omega_1 - \omega_I + i\Gamma_I/2)(\omega_1 + \omega_2 - \omega_f + i\Gamma_f/2)(\omega_1 + \omega_2 - \omega_3 - \omega_\ell + i\Gamma_\ell/2)} \quad + 1 \leftrightarrow 2$$

by application of the rules. The energy of the initial state, ω_i, has been taken to be zero. It is helpful, to avoid repeating steps unnecessarily when hyperfine structure is introduced in section 2.5, to separate this rate into two factors, one of which contains all the atomic matrix elements, and the other contains all the constants, including, for convenience, the reduced matrix elements common to all the diagrams in the sum, that is $\langle f \| D \| \ell \rangle$ and $\langle \ell \| D \| i \rangle$. We write the rate as $C|D(m_i m_i')|^2$ where

$$C = 2\pi\delta(\omega_1+\omega_2-\omega_3-\omega_4)\,\frac{n_1 n_2 \omega_1\omega_2\omega_3\omega_4 e^8}{16\varepsilon_0{}^4\hbar^4 V^4}\,\frac{|\langle f\,||R||\,\ell\rangle|^2|\langle \ell\,||R||\,i\rangle|^2}{[(\omega_1+\omega_2-\omega_f)^2+\Gamma_f^2/4][(\omega_1+\omega_2-\omega_3-\omega_\ell)^2+\Gamma_\ell^2/4]}$$

(5a)

$$D(m_i m_i') = \sum_{\substack{Im_I \\ m_f m_\ell}} \frac{\langle im_i'|\underline{R}.\underline{\varepsilon}_4^*|\ell m_\ell\rangle\langle \ell m_\ell|\underline{R}.\underline{\varepsilon}_3^*|fm_f\rangle\langle fm_f|\underline{R}.\underline{\varepsilon}_2|Im_I\rangle\langle Im_I|\underline{R}.\underline{\varepsilon}_1|im_i\rangle}{\langle i\,||R||\,\ell\rangle\langle \ell\,||R||\,f\rangle(\omega_1-\omega_I+i\Gamma_I/2)} + (1\leftrightarrow 2)\ .$$

(5b)

This is a rate, per atom in the m_i substate, for scattering into the m_i' substate producing photons of specified polarization in a given mode of the radiation field. We now sum over rates which in principle are distinguishable but which in practice we do not distinguish between, as follows:

- We sum over final magnetic substates m_i'.
- Only a fraction $1/(2J_i+1)$ of the atoms are in each initial substate m_i, so we average over initial states m_i.
- We sum over final photon states in solid angle $d\Omega$ and frequency $d\omega$, giving density of states factors.
- If, as is usually the case, there is no high resolution detection of the photons we also sum over their frequencies, by integrating with respect to ω_3 and ω_4.

All these steps are straightforward, including the ω_3 integral (because of the δ-function), except the ω_4 integral, which is of the form

$$\int_0^{\omega_1+\omega_2} \frac{\omega_4^3(\omega_1+\omega_2-\omega_4)^3}{(\omega_4-\omega_\ell)^2+\Gamma_\ell^2/4}\,d\omega_4\ .$$

This can be performed exactly, and the result is a power series in Γ_ℓ/ω_4 and $\Gamma_\ell/(\omega_1+\omega_2-\omega_4)$, both of which are very small ($\sim 10^{-6}$), and so we take only the first term, which is $\omega_\ell^3(\omega_1+\omega_2-\omega_\ell)^3 2\pi/\Gamma_\ell$. Since $\omega_1+\omega_2 \approx \omega_f$ we write the second factor as $(\omega_f-\omega_\ell)^3 = \omega_{f\ell}^3$. Finally we replace n/V by $P/\hbar\omega c$ for

each laser beam, and introduce the Einstein coefficients $A_{f\ell}$ and $A_{\ell i}$, where

$$A_{\ell i} = \frac{4}{3}\frac{\alpha}{c^2}\,\omega_\ell^3\,\frac{|\langle i\,||R||\,\ell\rangle|^2}{2J_\ell + 1}$$

to arrive at the comparatively simple result

$$\begin{aligned}\text{Rate}\,(\underline{\varepsilon}_3 \text{ into } d\Omega_3 \\ \underline{\varepsilon}_4 \text{ into } d\Omega_4) &= \frac{9\pi}{8}\,P_1P_2\,\frac{\alpha^2}{\hbar^2}\,\left(\frac{A_{\ell i}}{\Gamma_\ell}\right)\left(\frac{A_{f\ell}}{\Gamma_f}\right)(2J_f+1)(2J_\ell+1)\;g(\omega_1+\omega_2-\omega_f) \\ &\quad \times \sum_{m_i m_i'}\frac{|D(m_i m_i')|^2}{2J_i+1}\;d\Omega_3\,d\Omega_4 \end{aligned} \tag{6}$$

where $g(\omega)$ is the normalized Lorentzian lineshape function

$$g(\omega) = \frac{\Gamma_f}{2\pi}\,\frac{1}{\omega^2 + \Gamma_f^2/4}$$

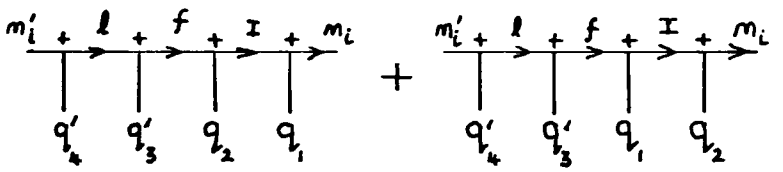
The two bracketed factors A/Γ represent the probability that the upper state will decay by the route we have chosen to observe - they are in fact branching ratios. Since by hypothesis the only decay mechanism is radiative, then if we sum over all possible decays to find the total absorption rate, these factors will sum to 1.

The calculation has implicitly been carried out for a specified velocity class of atoms, and in the atoms' rest frame, so $\omega_1 = \omega_L - \underline{k}_1.\underline{v}$, where ω_L is the laser frequency. Thus if the atom absorbs two oppositely directed photons ($\underline{k}_1 = -\underline{k}_2$) the Doppler shifts in $g(\omega)$ cancel and when we average over the velocity distribution, there is no velocity dependence and so all velocity classes contribute equally. (It may be objected that there is a velocity dependence in ω_1 in the denominator in D; however by hypothesis the denominator is large compared with the Doppler shifts, and so this velocity dependence is negligible. By the same token the term $i\Gamma/2$ is also very small, and henceforth this denominator will be written $\Delta\omega_I$, which denotes $\omega_L - \omega_I$.) On the

other hand if the atom absorbs two photons from the same beam there is a velocity dependence of $g(\omega)$, and so on averaging over the velocity distribution the profile becomes Doppler-broadened and $g(\omega)$ becomes $g_D(\omega)$, where g_D is the appropriate convolution of g with the velocity distribution. In this case the two diagrams in equation 4a with beams 1 and 2 interchanged are identical and so the extra term denoted $1 \leftrightarrow 2$ in equations 4b and 5b is absent. This leads to an additional factor of 1/4 in the Doppler-broadened background rate.

We now turn to the factor D. I shall treat D using the diagram method of angular momentum theory (Brink and Satchler, 1968); rules for manipulating these diagrams are given in Appendix A, and also many other results to which I shall refer. Using the Wigner-Eckart theorem in the form of equation A23 we obtain

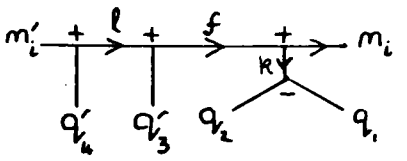
$$D = \sum_I \frac{\langle f \| R \| I \rangle \langle I \| R \| i \rangle}{\Delta\omega_I} \varepsilon_1 \varepsilon_2 \varepsilon_3^* \varepsilon_4^* \tag{7}$$



I have used a notation for the ε's which is slightly abbreviated; each ε_i represents a spherical component labelled by q_i of the corresponding vector $\underline{\varepsilon}_i$, and summation over q_i is understood. Similarly ε_i^* represents the q_i' component of $\underline{\varepsilon}_i^*$, and again the summation is understood.

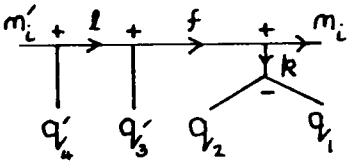
Using equation A16 for the latter halves of the diagrams we obtain for the sum of two diagrams in equation 7

$$\sum_k (2k+1) \begin{Bmatrix} f & i & k \\ 1 & 1 & I \end{Bmatrix} (1 + (-)^k) (-)^{i+f+k}$$



Thus the k = 1 term cancels between the two diagrams; this is the result of $1/\Delta\omega_I$ being a common factor between the two diagrams, that is, of neglecting the velocity dependence of ω_1 and ω_2. This means that in practice the vector (k = 1) term may not totally vanish in the case of a near resonant intermediate state, but certainly will in the case we are considering. This transforms equation 7 into

$$D = \sum_{k=0,2} 2Q_k \sqrt{(2k+1)}\, \varepsilon_1 \varepsilon_2 \varepsilon_3^* \varepsilon_4^* \qquad (8)$$



where $Q_k = \sum_I \frac{\langle f \| R \| I \rangle \langle I \| R \| i \rangle}{\Delta\omega_I} \sqrt{(2k+1)} \begin{Bmatrix} f & i & k \\ 1 & 1 & I \end{Bmatrix} (-)^{i+f+k}$.

Equation 8 expresses the decomposition of the two-photon absorption process into a scalar or isotropic part and a tensor or quadrupolar part. This tensorial reduction was noted by Cagnac, Grynberg and Biraben (1973) and given explicitly by Grynberg and Cagnac (1977) in terms of a tensorial reduction of an effective two-photon operator

$$Q = (\underline{\varepsilon}_1 \cdot \underline{D} \frac{1}{\omega - H_{atom}} \underline{\varepsilon}_2 \cdot \underline{D}) + 1 \leftrightarrow 2 \ .$$

Q_k is the reduced matrix element of the k^{th}-rank tensor part of Q; it is denoted in Grynberg and Cagnac (1977) by $\langle f \| Q^k \| i \rangle$.

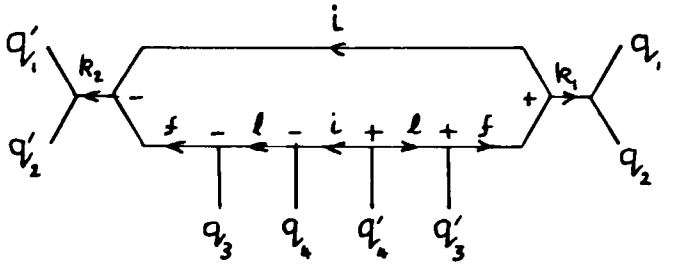
Anticipating the final result we define the partial rates

$$R(k_1,k_2) = 32\pi^3 P_1 P_2 \frac{\alpha^2}{\hbar^2} g(\omega_1 + \omega_2 - \omega_f) \frac{Q_{k_1} Q^*_{k_2}}{2J_i + 1} \qquad (9)$$

Then, combining equations 6, 7 and 8, we find

(10) Rate $\begin{pmatrix} \underline{\varepsilon}_3 \text{ into } d\Omega_3 \\ \underline{\varepsilon}_4 \text{ into } d\Omega_4 \end{pmatrix} = \sum_{k_1 k_2} \frac{9}{64\pi^2}(2J_\ell + 1)(2J_f + 1)\sqrt{(2k_1+1)(2k_2+1)}$ x

$$R(k_1 k_2)\left(\frac{A_{f\ell}A_{\ell i}}{\Gamma_f \Gamma_\ell}\right) \varepsilon_1\varepsilon_1^*\varepsilon_2\varepsilon_2^*\varepsilon_3\varepsilon_3^*\varepsilon_4\varepsilon_4^* \; d\Omega_3 \; d\Omega_4 \quad x$$



Equation 10 expresses the rate for coincidence counting in $d\Omega_3$ and $d\Omega_4$. In practice one usually only detects one photon, or detects both photons not in coincidence, the rate for which is the sum of the two single photon counting rates. Thus we need to sum over the final states of one photon; in order to find the total excitation rate (for calculations to determine whether or not the power broadening is significant) we need to sum over both photons.

Consider first the sum over polarizations; because the two polarization vectors $\underline{\varepsilon}_\lambda$ and $\hat{\underline{k}}$, the unit vector in the direction of propagation $\underline{k}$, form a complete set, we have the relation

(11) $$\sum_\lambda \varepsilon_{q\lambda}\, \varepsilon^*_{q'\lambda} = (-)^q\, \delta(q,-q') - \hat{k}_q \hat{k}_{q'}$$

or in Cartesians

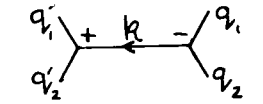
$$\sum_\lambda \varepsilon_{i\lambda}\varepsilon_{j\lambda} = \delta_{ij} - \hat{k}_i \hat{k}_j \; .$$

(δ_{ij} and $\delta(i,j)$ are equivalent forms of the Kronecker delta; the latter form is used when the subscripts would otherwise be confusing.) If we now integrate over all directions of $\hat{\underline{k}}$, the first term in equation 11 gives $4\pi\delta_{ij}$, and the

second term $-\frac{2\pi}{3}\delta_{ij}$ (or $(-)^q\delta(q,-q')$ in sphericals). An arrow on a photon line denotes $(-)^{1+q}\delta(q,-q')$ and so we get the rule:-

To sum over final photon states, join the two photon lines with an arrow, and replace $\varepsilon_q\varepsilon^*_{q'}d\Omega$ by $-8\pi/3$.

To find the total absorption rate we sum over both final photon states using this rule, and simplify the diagram using equation A8 three times. Finally we sum over different decay routes, to yield the result

(12) Total Absorption Rate = $\sum_{k=0,2} R(k,k)$  $\varepsilon_1\varepsilon^*_1\varepsilon_2\varepsilon^*_2$

We note that all the atomic variables are contained in the partial rates R, while the diagram simply connects together the polarization vectors of the lasers. Because of this, diagrams of this sort can be expressed in ordinary vector notation, eliminating the 3-J symbols. Properties of diagrams of this sort, which I term isotropic diagrams, are discussed in Appendix A; here I just quote the two results from equation A27:

Total Absorption rate:-

(13)
$$\begin{aligned} &k = 0 \text{ term} && R(0,0).\tfrac{1}{3}|\underline{\varepsilon}_1\cdot\underline{\varepsilon}_2|^2 \\ &k = 2 \text{ term} && R(2,2).\tfrac{1}{5}T_{ij}(\underline{\varepsilon}_1,\underline{\varepsilon}_2)T_{ij}(\underline{\varepsilon}^*_1,\underline{\varepsilon}^*_2) \end{aligned}$$

where, in Cartesian coordinates,

(14)
$$T_{ij}(\underline{\varepsilon}_1,\underline{\varepsilon}_2) = \tfrac{1}{2}(\varepsilon_{1i}\varepsilon_{2j} + \varepsilon_{2i}\varepsilon_{1j}) - \tfrac{1}{3}\underline{\varepsilon}_1\cdot\underline{\varepsilon}_2\delta_{ij} \quad .$$

Explicitly, the sum gives

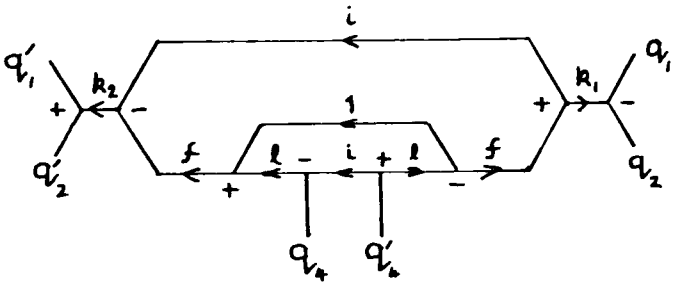
$$R(2,2).\tfrac{1}{5}(\tfrac{1}{2} + \tfrac{1}{2}|\underline{\varepsilon}_1\cdot\underline{\varepsilon}^*_2|^2 - \tfrac{1}{3}|\underline{\varepsilon}_1\cdot\underline{\varepsilon}_2|^2)$$

These results will be discussed shortly; first we calculate the

angular distribution of the photons. Suppose only the second photon $\underline{\varepsilon}_4$ is detected; summing over final states of the first photon $\underline{\varepsilon}_3$ we obtain:-

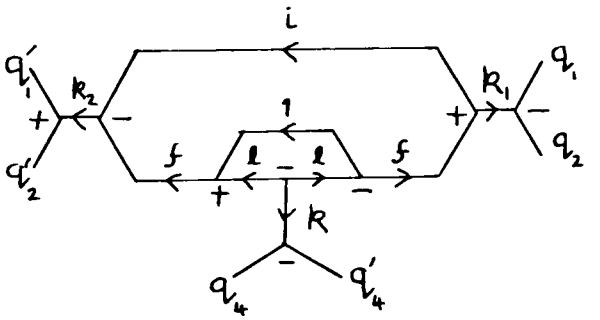
$$\text{Rate } (\underline{\varepsilon}_4 \text{ into } d\Omega_4) = \sum_{k_1 k_2} \frac{3}{8\pi}(2J_\ell+1)(2J_f+1)\sqrt{(2k_1+1)(2k_2+1)}\; R(k_1,k_2)\; x$$

$$\frac{A_{f\ell}}{\Gamma_f}\frac{A_{\ell i}}{\Gamma_\ell}\; \varepsilon_1\varepsilon_1^*\varepsilon_2\varepsilon_2^*\varepsilon_4\varepsilon_4^*\, d\Omega_4$$



We can simplify the diagram by coupling together the two q_4 lines using equation A18, so that the diagram becomes

$$\sum_{k=0,1,2}$$

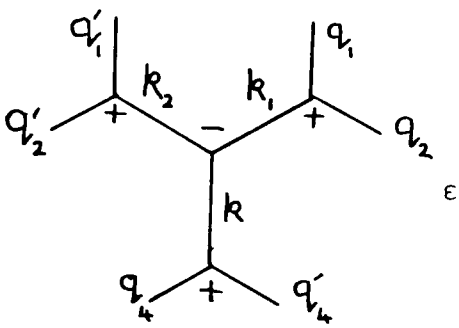


$$(2k+1)(-)^{\ell-i+1}\begin{Bmatrix}\ell & \ell & k\\ 1 & 1 & i\end{Bmatrix}$$

Two applications of the "F_3 box" rule, equation A15 and the definition of the 6-j symbol, equation A12, give the final result:-

$$\text{Rate } (\underline{\varepsilon}_4 \text{ into } d\Omega_4) = \frac{3}{8\pi}(2J_\ell+1)(2J_f+1)\frac{A_{f\ell}}{\Gamma_f}\frac{A_{\ell i}}{\Gamma_\ell}\; x$$

$$\sum_{\substack{k_1 k_2=0,2\\ k=0,1,2}} \sqrt{(2k_1+1)(2k_2+1)}\;(2k+1)(-)^{2f+1+k} R(k_1 k_2) \begin{Bmatrix}\ell & \ell & k\\ 1 & 1 & i\end{Bmatrix}\begin{Bmatrix}\ell & \ell & k\\ f & f & 1\end{Bmatrix}\begin{Bmatrix}f & f & k\\ k_1 & k_2 & i\end{Bmatrix}$$



$$\varepsilon_1\varepsilon_1^*\varepsilon_2\varepsilon_2^*\varepsilon_4\varepsilon_4^*\, d\Omega_4 \,.$$

(15)

In the case that the final state is not the same as the initial state, but different, i' say, then there are small changes to this equation:- the branching ratio is of course changed to the branching ratio $A_{\ell i'}/\Gamma_\ell$, there is an additional sign of $(-)^{i-i'}$ and the i in the first 6-J symbol is changed to i'.

For any particular set of values of k, k_1 and k_2 the isotropic diagram can be evaluated using equations A28-A30. However for many transitions only a small number of diagrams is non-zero, because one or more of the 6-j symbols vanish. These conditions can be expressed by selection rules. I shall consider briefly the selection rules for the non-vanishing of the total rate (equation 9). We have firstly the overall selection rules

$$\Delta J = 0, 1, 2 \quad (0 \not\leftrightarrow 1) \quad \text{No parity change.}$$

Considering the selection rules for the monopole and quadrupole operators separately, we have

Monopole operator $\Delta J = 0$

Quadrupole operator $\Delta J = 0, 1, 2$ $(0 \not\to 0, \tfrac{1}{2} \not\to \tfrac{1}{2}, 0 \not\leftrightarrow 1)$

and so the condition for both terms in equation 9 to be non-zero is:-

Mixed $\Delta J = 0, \quad J \geq 1.$

We shall consider the angular distribution from these three cases separately.

(i) Pure Monopole. Equation 15 reduces to

$$(16) \qquad \text{Rate } (\underline{\varepsilon}_4 \text{ into } d\Omega_4) = \frac{d\Omega_4}{8\pi} \frac{A_{f\ell}}{\Gamma_f} \frac{A_{\ell i}}{\Gamma_\ell} \; R(0,0) . \frac{1}{3} |\underline{\varepsilon}_1 \cdot \underline{\varepsilon}_2|^2$$

showing that the radiation is isotropic and unpolarized. The polarization sum simply multiplies equation 16 by a factor of 2.

(ii) Pure Quadrupole. Equation 15 reduces to three terms, equations 17a to 17c.

$$(17)\qquad \text{Rate } (\underline{\varepsilon}_4 \text{ into } d\Omega_4) = \frac{d\Omega_4}{8\pi} \frac{A_{f\ell}}{\Gamma_f} \frac{A_{\ell i}}{\Gamma_\ell} R(2,2)(B_1 + B_2 + B_3)$$

where

$$(17a)\qquad B_1 = \frac{1}{5} T_{ij}(\underline{\varepsilon}_1, \underline{\varepsilon}_2) T_{ij}(\underline{\varepsilon}_1^*, \underline{\varepsilon}_2^*)$$

$$(17b)\qquad B_2 = \frac{3}{\sqrt{5}} (2J_\ell+1)(2J_f+1)(-)^{2f} \begin{Bmatrix} 1 & 1 & 1 \\ \ell & \ell & i \end{Bmatrix} \begin{Bmatrix} \ell & \ell & 1 \\ f & f & 1 \end{Bmatrix} \begin{Bmatrix} 2 & 2 & 1 \\ f & f & i \end{Bmatrix} \times$$

$$T_{i\ell}(\underline{\varepsilon}_1, \underline{\varepsilon}_2) T_{\ell j}(\underline{\varepsilon}_1^*, \underline{\varepsilon}_2^*) \varepsilon_{ijk}(\underline{\varepsilon}_4 \times \underline{\varepsilon}_4^*)_k$$

$$(17c)\qquad B_3 = 6\sqrt{\frac{3}{7}} (2J_\ell+1)(2J_f+1)(-)^{2f} \begin{Bmatrix} 1 & 1 & 2 \\ \ell & \ell & i \end{Bmatrix} \begin{Bmatrix} \ell & \ell & 2 \\ f & f & 1 \end{Bmatrix} \begin{Bmatrix} 2 & 2 & 2 \\ f & f & i \end{Bmatrix} \times$$

$$T_{ij}(\varepsilon_1, \varepsilon_2) T_{jk}(\underline{\varepsilon}_1^* \varepsilon_2^*) T_{ki}(\varepsilon_4, \varepsilon_4^*) \ .$$

The term B_1 is isotropic and unpolarized, and integrates to give the total rate of equation 9; B_2 vanishes when summed over polarization, but B_3 does not and leads to anisotropy of the fluorescence.

(iii) Mixed term. In this case none of the terms in equation 15 is zero, and the total rate consists of a sum of all terms above in parts (i) and (ii), plus two further terms which are interference terms between the two rates R(0,0) and R(2,2). These interference terms to the rate are

$$\frac{d\Omega_4}{8\pi}\frac{A_{f\ell}A_{\ell i}}{\Gamma_f}\frac{}{\Gamma_\ell}R(0,2).\sqrt{3}(2J_\ell+1)(2J_f+1)(-)^{2f+1}\begin{Bmatrix}\ell & \ell & 2\\ 1 & 1 & i\end{Bmatrix}\begin{Bmatrix}\ell & \ell & 2\\ f & f & i\end{Bmatrix} \times$$

(18)

$$\underline{\varepsilon}_1.\underline{\varepsilon}_2 T_{ij}(\underline{\varepsilon}_1^*\underline{\varepsilon}_2^*)T_{ij}(\varepsilon_4,\varepsilon_4^*) \quad + \text{ complex conjugate .}$$

Very similar, although slightly simpler, expressions can be derived in the same way from equation 10 in the case that the first emitted photon is detected; if the detector responds to both photons then the sum of the two rates is taken. However I do not go into this here, since this is not relevant to the calcium experiment.

In the final part of this section I shall consider the elimination of the Doppler background by choice of polarizations. This was first suggested by Cagnac, Grynberg and Biraben (1973), who noted that if the two laser beams were circularly polarized then the Doppler-broadened component of a transition of the monopole type would be eliminated. In order for the Doppler-free component not to be eliminated as well, the circular polarization of the two beams must be of opposite sense. We now consider if it is generally possible to eliminate the Doppler-broadened component. The total rate for this component is given by equation 12 with $\underline{\varepsilon}_1 = \underline{\varepsilon}_2$, and multiplied by $\frac{1}{4}$.

We look first at the Monopole case. The rate is proportional to $|\underline{\varepsilon}_1.\underline{\varepsilon}_1|^2$; if we write the polarization vector as $\underline{a} + i\underline{b}$ where $\underline{a}$ and $\underline{b}$ are real, $\underline{a}^2 + \underline{b}^2 = 1$ and $\underline{a}.\underline{b} = 0$, then

$$|\underline{\varepsilon}.\underline{\varepsilon}|^2 = (a^2 - b^2)^2$$

and the condition for this to be zero is $\underline{a}^2 = \underline{b}^2 = \frac{1}{2}$, that is left or right circularly polarized light. In order for the Doppler-free signal not to vanish also it is necessary for the return wave to have opposite circular polarization, that is, the direction of rotation of its electric vector must be opposite. Because it is also travelling in the opposite direction its helicity is unchanged. However it is the direction of rotation, not the heli-

city, which is preserved on reflection, and so a suitable retarder must be inserted to change the polarization.

Turning now to the Quadrupole case, the total rate is proportional to

$$1 - \frac{1}{3} |\underline{\varepsilon}_1 \cdot \underline{\varepsilon}_1|^2$$

which is clearly positive definite. Thus it is not possible by choice of polarization to eliminate the Doppler-broadened background for a quadrupole case. If the ground state has $J_i = 0$, so that the upper state has $J_f = 2$, then it is possible to discriminate against the detection of the Doppler-broadened component by choice of polarization, although it is not possible to prevent the absorption from taking place. This can be done by using the circularly polarized laser beams which are used in the Monopole case. Then atoms which absorb both photons from the same beam populate the $m_f = \pm 2$ states, while atoms absorbing one photon from each beam populate the $m_f = 0$ state. Thus the decay of the Doppler-broadened component to a $J = 1$ state is σ-polarized, while that of the Doppler-free component is both σ and π. If a polarizer in front of the detector at right angles to the laser beams is set to pass light polarized parallel to the lasers, the Doppler-broadened background will be eliminated, unless the fluorescence becomes depolarised through scattering, as it may do if it is emitted in a decay to the ground state and the path from interaction region to detector passes through a considerable quantity of the atom under study.

2.5 The Effect of Hyperfine Structure

We now calculate the modification that a nuclear spin I, leading to hyperfine structure levels labelled by F, makes to the results for the total absorption rate and angular distributions calculated in section 2.4. We start

with the atom in substate $|i,F_i>$; a fraction $n(F_i)$ of all atoms will be in this state initially. If, for example, we have atoms coming from an oven in thermal equilibrium at temperature T, and the hyperfine structure is small compared with kT, then $n(F_i)$ is proportional to the statistical weight:

$$n(F_i) = (2F_i+1)/(2J_i+1)(2I+1) .$$

We consider excitation to a specific final substate $|f,F_f>$ - if the h.f.s. is not large compared with the natural width of the upper state, this approximation will fail, and an appropriate sum of diagrams, with different resonance denominators, should be taken before squaring the matrix element. This will modify the lineshape function $g(\omega)$. Since we are assuming no high resolution on the detection we shall sum over the F's of the states ℓ and i in the decay. With these modifications, equation 6 becomes

$$\text{Rate}(\underline{\varepsilon}_3 \text{ into } d\Omega_3 \;\; \underline{\varepsilon}_4 \text{ into } d\Omega_4) = \frac{9\pi}{8} P_1 P_2 \frac{\alpha^2}{\hbar^2}\left(\frac{A_{\ell i}}{\Gamma_\ell}\frac{A_{f\ell}}{\Gamma_f}\right)(2J_f+1)(2J_\ell+1)g(\omega_1+\omega_2-\omega_f) \times \sum_{\substack{m_i \\ F_i' \; m_i'}} \frac{n(F_i)}{2F_i+1} \left|D(F_i m_i, F_i' m_i')\right|^2 \; d\Omega_3 d\Omega_4 \tag{19}$$

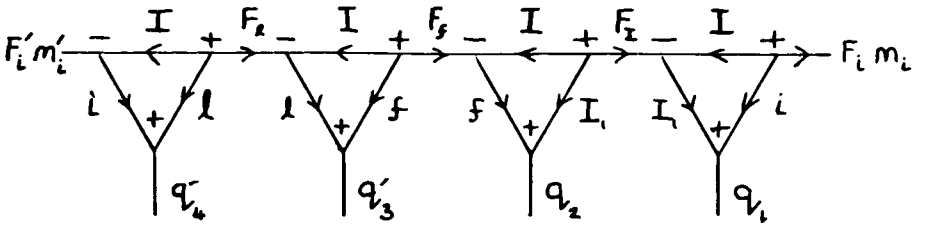
where

$$D(F_i m_i, F_i' m_i') = \sum_{\substack{I_1 F_I m_I \\ m_f F_\ell m_\ell}} \frac{<iF_i'm_i'|\underline{R}.\underline{\varepsilon}_4^*|\ell F_\ell m_\ell><\ell F_\ell m_\ell|\underline{R}.\underline{\varepsilon}_3^*|fF_f m_f><fF_f m_f|\underline{R}.\underline{\varepsilon}_2|I_1 F_I m_I><I_1 F_I m_I|\underline{R}.\underline{\varepsilon}_1|iF_i m_i>}{<i\,||R||\,\ell><\ell\,||R||\,f>\,\Delta\omega_I} + 1 \leftrightarrow 2. \tag{20}$$

Turning equation 20 into diagrams using equation A25 we obtain

$$D(m_i, F_i' m_i') = \sum_{I_1} \frac{\langle f \| R \| I_1 \rangle \langle I_1 \| R \| i \rangle}{\Delta\omega_I} \varepsilon_1 \varepsilon_2 \varepsilon_3^* \varepsilon_4^* \quad x$$

$$\sum_{F_\ell F_I} (2F_i+1)(2F_\ell+1)(2F_f+1)(2F_I+1)$$

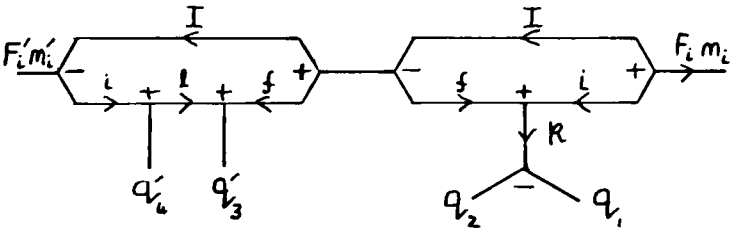


$+ 1 \leftrightarrow 2.$

Using equation A9 twice and then equation A16, this reduces to

$$D = \sum_{k=0,2} 2Q_k \sqrt{2k+1}\, \varepsilon_1 \varepsilon_2 \varepsilon_3^* \varepsilon_4^*$$

(21) $\qquad (2F_i+1)(2F_f+1)$

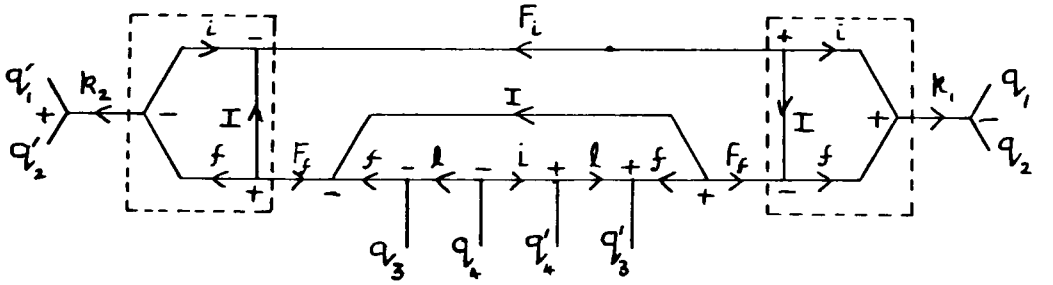


Substituting into equation 19 and using equation A 9 again we obtain

$$\text{Rate}(\underline{\varepsilon}_3 \text{ into } d\Omega_3 \;\; \underline{\varepsilon}_4 \text{ into } d\Omega_4) = \sum_{k_1 k_2} \frac{9}{64\pi^2} (2J_f+1)(2J_\ell+1)(2F_f+1)^2 n(F_i)(2J_i+1) \; x$$

$$\sqrt{(2k_1+1)(2k_2+1)}\; R(k_1 k_2) \left(\frac{A_{f\ell}}{\Gamma_f} \frac{A_{\ell i}}{\Gamma_\ell}\right) \quad x$$

$$\varepsilon_1 \varepsilon_1^* \varepsilon_2 \varepsilon_2^* \varepsilon_3 \varepsilon_3^* \varepsilon_4 \varepsilon_4^* \; d\Omega_3 \; d\Omega_4 \quad x$$

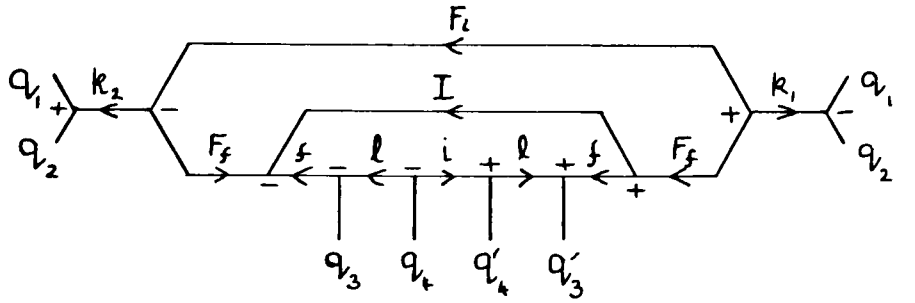


Finally we use the "F_3 box rule" equation A15 on the two regions enclosed in dotted lines, to obtain the analogue of equation 10 in the case of hyperfine structure:-

$$\text{Rate}(\underline{\varepsilon}_3 \text{ into } d\Omega_3 \text{ , } \underline{\varepsilon}_4 \text{ into } d\Omega_4) = \sum_{k_1 k_2} \frac{9}{64\pi^2} R(k_1 k_2) \frac{A_{f\ell}}{\Gamma_f} \frac{A_{\ell i}}{\Gamma_\ell} (2J_f+1)(2J_\ell+1)(2F_f+1)^2 x$$

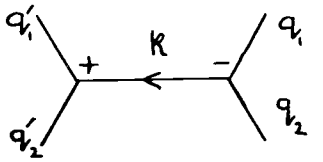
$$(2J_i+1)\sqrt{(2k_1+1)(2k_2+1)}\; n(F_i) \begin{Bmatrix} i & f & k_1 \\ F_f & F_i & I \end{Bmatrix} \begin{Bmatrix} i & f & k_2 \\ F_f & F_i & I \end{Bmatrix} x \tag{22}$$

$$\varepsilon_1 \varepsilon_1^* \varepsilon_2 \varepsilon_2^* \varepsilon_3 \varepsilon_3^* \varepsilon_4 \varepsilon_4^* \; d\Omega_3 \; d\Omega_4$$



Summing over all final states we obtain, after using equation A 8 repeatedly, the following expression for the total rate:

$$\text{Total Absorption Rate} = \sum_{k=0,2} n(F_i)\, R(k,k)\, (2F_f+1)(2J_i+1) \begin{Bmatrix} i & f & k \\ F_f & F_i & I \end{Bmatrix}^2 \tag{23}$$



$$\varepsilon_1 \varepsilon_1^* \varepsilon_2 \varepsilon_2^*$$

As a check on the calculation we note that if $I = 0$, so that $n(F_i) = 1$ and $F_i = i$, $F_f = f$, then equation 23 reduces, as it must, to equation 12. Thus the total absorption rate for a hyperfine component is just $n(F_i)(2F_f+1)(2J_i+1)\begin{Bmatrix} i & f & k \\ F_f & F_i & I \end{Bmatrix}^2$ times the rate in the absence of hyperfine structure (if the transition has pure multipolarity). This gives selection rules for the transitions as follows:

Monopole case $\quad \Delta F = 0$

Quadrupole case $\quad \Delta F = 0, \pm 1, \pm 2, \; 0 \not\to 0, \; \tfrac{1}{2} \not\to \tfrac{1}{2}, \; 0 \not\to 1.$

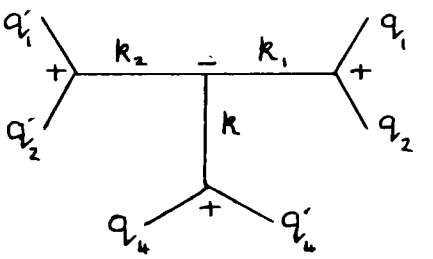
Thus while the multipolarity of the transition is determined by the J's of the initial and final state, specific hyperfine components in a mixed case may be pure monopole or quadrupole.

The angular distributions will also depend on the angular momentum F_f; I shall again do the calculation for the distribution of the second photon $\underline{\varepsilon}_4$ to compare with equation 15.

$$\text{Rate}\,(\underline{\varepsilon}_4 \text{ into } d\Omega_4) = \frac{3}{8\pi}(2J_\ell+1)(2J_f+1)(2F_f+1)^2(2J_i+1)n(F_i)\,\frac{A_{f\ell}}{\Gamma_f}\,\frac{A_{\ell i}}{\Gamma_\ell} \tag{24}$$

$$\times \sum_{\substack{k_1 k_2 = 0,2 \\ k=0,1,2}} \sqrt{(2k_1+1)(2k_2+1)}\,(2k+1)(-)^{1+F_i-i-I} R(k_1 k_2)\varepsilon_1\varepsilon_1^*\varepsilon_2\varepsilon_2^*\varepsilon_4\varepsilon_4^*\,d\Omega_4$$

$$\times \begin{Bmatrix} i & f & k_1 \\ F_f & F_i & I \end{Bmatrix}\begin{Bmatrix} i & f & k_2 \\ F_f & F_i & I \end{Bmatrix}\begin{Bmatrix} 1 & 1 & k \\ \ell & \ell & i \end{Bmatrix}\begin{Bmatrix} f & f & k \\ \ell & \ell & 1 \end{Bmatrix}\begin{Bmatrix} f & f & k \\ F_f & F_f & I \end{Bmatrix}\begin{Bmatrix} F_f & F_f & k \\ k_1 & k_2 & F_i \end{Bmatrix}$$



This has exactly the same form as equation 15, but the additional 6-J symbols make its evaluation rather more difficult. It is easy to verify that if I = 0 it reduces to equation 15, and when integrated over ε_4 it reduces to equation 23. If the final state is not the same as the initial state then the same changes apply, that is i → i' in the third 6-J symbol, and in the phase.

2.6 The effect of Laser bandwidth and transit time

The treatment of two-photon absorption given above rests on a number of assumptions, as described in section 2.2, most of which are likely to be valid for any experiment which aims to do high-resolution spectroscopy. However, there are two assumptions, those of a single mode of the radiation field exciting the transitions, and a very long time of interaction with the field, which will not necessarily be valid, and it is necessary to examine how relaxing these assumptions will affect the results. The first point to note is that most of the development of sections 2.4 and 2.5, which was concerned with angular momenta, selection rules and angular distributions, is still valid since these results stem from the polarization of the lasers, which we can still consider to be well-defined. This is because the temporal behaviour of the electric field is, in principle, quite independent of its vectorial behaviour; we have analyzed in detail how the vectorial behaviour influences the rate while making the simplest possible assumption about the temporal behaviour of the field, and if we now make more general assumptions concerning the temporal behaviour of the field, this will only affect the total rate, not the relative intensities of hyperfine components, or the angular distribution.

We shall continue to assume a certain narrow bandwidth in the laser light, such that

$$\Delta\omega_L \ll \Delta\omega_I$$

where $\Delta\omega_L$ is a measure of the laser bandwidth, and, as in section 2.4, $\Delta\omega_I$ is a resonance denominator. If we consider the partial rates R(k,k) of equation 9, this is equivalent to saying that the atomic response, given by the reduced matrix element $|Q_k|^2$, is constant over the laser bandwidth. This assumption is reasonable in the light of the other assumptions we have made

concerning $\Delta\omega_I$.

We turn first to the dependence of the rate on the laser bandwidth, continuing to assume that the atoms interact with the field for a long time, compared with the lifetime of the upper state. This problem has been studied by Mollow (1968) and Salomaa (1978); however the latter paper makes at the outset the assumption that the two laser beams are mutually uncorrelated, which is clearly not the case in Doppler-free two-photon spectroscopy since both beams are derived from the same laser (although there is a time delay between the two beams of ~2 ns, which may be significant). This assumption simplifies the situation, but of course the important features are thereby lost. We therefore consider only the paper by Mollow.

He works with the interaction Hamiltonian $\frac{e}{m}\,\underline{A}.\underline{p}$, and so for comparison with the results of earlier sections it is convenient to convert his results to those which he would have obtained had he used $\underline{E}.\underline{D}$. For simplicity we consider a $0 \rightarrow 0$ transition; then the expression found above for the total absorption rate is given by equation 12, which can be written

$$(25) \qquad \text{Total absorption rate} = 32\pi^3\frac{\alpha^2}{\hbar^2}\left|\sum_I \frac{R_{fI}R_{Ii}}{\Delta\omega_I}\right|^2 . g(\omega_1+\omega_2-\omega_f)P_1P_2\left|\underline{\varepsilon}_1\cdot\underline{\varepsilon}_2\right|^2$$

where I have used the notation $R_{ij} = \langle i|R|j\rangle$. In order to simplify the situation further, I shall consider only a single laser beam, which reduces the above expression by a factor of 4, as discussed above. We can generalise this expression to the case of a finite bandwidth laser using the method mentioned in section 2.3 of replacing P_1 by $P_1(\omega)\,d\omega$ and integrating over both ω's; however this contains an implicit assumption about the nature of the field correlations. We define an atomic response function

$$(26) \qquad A(\omega) = 8\pi^3\,\frac{\alpha^2}{\hbar^2}\,\left|\sum_I \frac{R_{fI}R_{Ii}}{\omega - \omega_I}\right|^2 \quad .$$

Then equation 25 reduces to

$$(27)\qquad \begin{matrix}\text{Total}\\ \text{Absorption}\\ \text{Rate}\end{matrix} = A(\omega)\int d\omega_1\, d\omega_2\, P(\omega_1)P(\omega_2)g(\omega_f-\omega_1-\omega_2)$$

If we take a specific form for the laser power spectrum $P(\omega)$ we can evaluate the integral in equation 27; an example worked out by Mollow is for the case of a Lorentzian power spectrum with full width at half maximum of Γ_L. With this assumption we obtain

$$(28)\qquad \begin{matrix}\text{Absorption}\\ \text{Rate}\end{matrix} = A(\omega)P^2\frac{\Gamma_f+2\Gamma_L}{2\pi}\cdot\frac{1}{(\omega_f-2\omega)^2+\frac{1}{4}(\Gamma_f+2\Gamma_L)^2}$$

If we examine our assumptions, then we find that this is for the case where the laser light is some sort of statistical mixture of number states - probably, in fact, not a physically realizable model. Mollow calculates the absorption rate for two more reasonable models, chaotic light and a model of an intensity stabilized laser, both with the same power spectrum as in the above calculation. Translating his results to the $\underline{E}.\underline{D}$ interaction, he obtains:-

$$(29)\qquad \begin{matrix}\text{Absorption rate}\\ \text{(Chaotic light)}\end{matrix} = 2A(\omega)P^2\frac{\Gamma_f+2\Gamma_L}{2\pi}\cdot\frac{1}{(\omega_f-2\omega)^2+\frac{1}{4}(\Gamma_f+2\Gamma_L)^2}$$

$$(30)\qquad \begin{matrix}\text{Absorption rate}\\ \text{(Laser light)}\end{matrix} = A(\omega)P^2\frac{\Gamma_f+4\Gamma_L}{2\pi}\cdot\frac{1}{(\omega_f-2\omega)^2+\frac{1}{4}(\Gamma_f+4\Gamma_L)^2}$$

This shows very clearly that the absorption spectrum and the integrated absorption both depend on the statistical nature of the light as well as its power spectrum. The general result derived by Mollow is

$$(31)\qquad \text{Absorption rate} = 4\varepsilon_0^2c^2A(\omega)\frac{1}{2\pi}\int_{-\infty}^{\infty}\exp\left(i\omega_f t-\frac{\Gamma_f}{2}|t|\right)G^{(2)}(0,0;tt)dt$$

where $G^{(2)}$ is the second order correlation function

$$(32) \qquad G^{(2)}(t_1't_2';t_1t_2) = T_r(\rho_F E^{\dagger}(t_1')E^{\dagger}(t_2')E(t_1)E(t_2))$$

where ρ_F is the density operator of the field, and E and $E^{\dagger}$ are the creation and annihiliation parts of the electric field operator. Evaluating equation 32 for the two specific forms of ρ_F gives the results already quoted in equations 29 and 30.

All these results apply to a stationary field, that is one whose statistical properties are independent of time. Although the laser, like many other sources, is stationary, the field seen by any particular atom is not, because it passes through the interaction region in a time ~d/v, where d is a beam diameter and v a thermal speed. Thus the atom sees not a stationary field but a pulse. Mollow gives the probability of two-photon absorption from such a pulse. If we continue to make the narrow-bandwidth assumption in the sense mentioned above, that is the frequency dependence of $A(\omega)$ is neglected over the full range of frequencies to which the atom is exposed in the pulse, then his result for $P_2(t)$, the probability of two-photon absorption, reduces to

$$(33) \qquad P_2(t) = 4\varepsilon_0^2 c^2 A(\omega) \frac{1}{2\pi} \int_0^t \int \exp(i\omega_f(t_2-t_1) - \frac{\Gamma_f}{2}|t_2-t_1|)G^{(2)}(t_1t_1;t_2t_2)dt_1dt_2$$

This clearly gives equation 31 for the rate in the case of a stationary field.

Thus the complete calculation of transit-time effects coupled with laser bandwidth would proceed as follows. It is necessary to know the full two point second-order correlation function $G^{(2)}(\underline{r}_1t_1,\underline{r}_1t_1;\underline{r}_2t_2,\underline{r}_2t_2)$ and the spatial and velocity distribution of the atoms. For a particular velocity and spatial class of atoms, equation 33 is evaluated with $\underline{r}_1 = \underline{r}_0 + \underline{v}t_1$, etc. to find the total absorption of this class per atom. The rate at which these atoms cross the beam then gives the absorption rate from this class. This

is repeated for all other velocity and spatial classes of atoms within the view of the detector.

This is clearly a formidable task of statistical averaging; there is also one further complication. We have considered only one beam; the usual procedure of using a single laser beam reflected onto itself means that the operator for the electric field in the interaction region is roughly $E(t) + E(t-\tau)$ where τ is the round trip time from interaction region to mirror and back, and $E(t)$ is the electric field of one laser beam. This introduces further complexity into the second order correlation function.

If the spectrum were partially resolved it might be necessary to go to these lengths to establish a theoretical profile. In a well-resolved spectrum it is very fortunate that this is not the case; all that is necessary is that the profiles be symmetrical so that their centre is well-defined. The conclusion from this section is that there is considerable uncertainty about the exact rate and spectrum to be expected in our experiment. For the purposes of calculation I shall use the integrated rate given by equation 12; that is I shall use the value given by that equation for the area under the absorption curve. From equations 29 and 30 we see that this is uncertain by at least a factor 2. For the actual rate at line centre it is necessary to replace $g(\omega_f - \omega_1 - \omega_2)$ at line centre by a suitable value taken from an estimate of the true lineshape. The value of $g(0)$ is $2/\pi\Gamma_f$; in the evaluation of the rate I shall replace Γ_f by some value increased by $\sim 2\Gamma_L$. This is also uncertain by a factor of at least 2. The evaluation of the rate for calcium is undertaken in the final section.

2.7 Evaluation of the Two-photon rate for Calcium

The evaluation of the rate for the transition of interest, $4s^2\ {}^1S_0$ - $4s5s\ {}^1S_0$, is made much simpler by the fact that $J_i = J_f = 0$; this means

that only the scalar term contributes to the absorption rate, and the fluorescence is bound to be isotropic and unpolarized. Examination of the term diagram of Fig. 1.2 shows that a further simplification can be made - the approximation of only one intermediate state. Intermediate states must have $J_I = 1$, and apart from the resonance level $4s4p\ ^1P_1$, the only other nearby $J = 1$ level is $4s4p\ ^3P_1$, and the matrix element of this level with the ground state is extremely small because of the selection rule $\Delta S = 0$.

Equation 12 can therefore by written, for $|\underline{\varepsilon}_1 \cdot \underline{\varepsilon}_2|^2 = 1$

$$\text{Absorption Rate} = \frac{32}{9}\pi^3\frac{\alpha^2}{\hbar^2}\, g^*(0)P^2\, \frac{|\langle 4s5s\,^1S \,||R||\, 4s4p\,^1P\rangle\langle 4s4p\,^1P \,||R||\, 4s^2\,^1S\rangle|^2}{(\omega_{4s4p} - \frac{1}{2}\omega_{4s5s})^2}$$

where $g^*(0)$ is the suitably modified lineshape function at line centre. Substituting for the reduced matrix elements in terms of absorption f-values

$$f_{ik} = \frac{2m}{3\hbar}\,\omega_{ik}\,\frac{|\langle i \,||R||\, k\rangle|^2}{2J_k+1}$$

and writing $g^*(0)$ as $2/\pi\Gamma_f^*$ gives

$$\text{(34)}\qquad \text{Absorption Rate} = \frac{3}{\pi^2\Gamma_f^*}\,\frac{\alpha^2}{m^2c^4}\,\frac{\lambda_{iI}\lambda_{If}}{\Delta\bar{\nu}^2}\, f_{iI}f_{If}\, P^2$$

where I have expressed the resonance denominator in wave numbers.

The atomic data for calcium gives

$\lambda_{iI} = 423$ nm
$\lambda_{If} = 1035$ nm
$\Delta\bar{\nu} = 6.99 \times 10^5\ m^{-1}$
} Bashkin and Stoner (1978)

$f_{iI} = 1.75$ Wiese, Smith and Miles (1969).

The transition $4s4p\ ^1P_1 - 4s5s\ ^1S_0$ does not appear in Wiese et al. (op. cit.)

but the corresponding triplet transition does, with an f-value of 0.125. If we take the radial integral to be the same for the singlet transition, we get $f_{If} = 0.074$. Putting $\Gamma_f^* = 6 \times 10^7\ s^{-1}$ (corresponding to a Lorentzian of width 10 MHz) then we obtain

$$\text{Absorption Rate} = 4.7 \times 10^{-6}\ s^{-1}\ (\text{mW mm}^{-2})^2$$

Thus for a laser power of 10 mW focussed to an area of 20 μm radius, the power per unit area is given by 800 mW mm^{-2}, and the corresponding absorption rate by 300 s^{-1}. If the laser power is instead 100 mW, the absorption rate per atom of $3 \times 10^4\ s^{-1}$ is still very small compared with the natural decay rate of the upper state of $\sim 2 \times 10^7\ s^{-1}$, even given the uncertainties in these figures. We therefore anticipate no power-dependent shifts or broadening. (The uncertainty in the f-value does not affect this comparison, since both the absorption rate and the decay rate depend linearly upon it.)

CHAPTER 3

THE ATOMIC BEAM

3.1 Introduction

In this chapter I describe the atomic beam used in the experiment, and make an estimate of the expected signal size. The signal depends on many parameters, some of which, in particular the diameter of the laser beam, affect other characteristics of the experiment - in this case, the linewidth of the signal. In practice, therefore, the design evolved by taking easily attainable values for various parameters such as oven temperature and laser beam diameter, and calculating the resulting signal in order to see if it is sufficient to observe. However, in order to give some idea of the number density of calcium atoms required in the interaction region, we make an initial estimate based on the rate of 300 s^{-1} found in Chapter 2 for two beams of 10 mW focussed to 20 μm radius waists, and suppose that it is required to detect 10^4 photons per second on the peak of a 1% isotope - in other words a signal free from statistical noise, and large compared with a typical dark current. If the collection solid angle for detecting fluorescence is $4 \times 10^{-3}.4\pi$ sr, and we assume 10% detection efficiency then the total number of calcium atoms we require in the interaction region is 8×10^6. We can estimate the interaction volume by taking a cylinder, radius w_o and length equal to twice the confocal parameter $z = \pi w_o^2/\lambda$; thus the interaction volume is roughly $2(\pi w_o^2)^2/\lambda$, which for w_o = 20 μm gives 5×10^{-12} m^3, and so we require a number density of $\sim 1.5 \times 10^{18}$ m^{-3}. The number density corresponding to the vapour pressure curve for Ca is shown in Fig. 3.1.

In section 3.2 I shall describe the atomic beam oven, and in section 3.3 I shall give details of the associated vacuum system. The number density

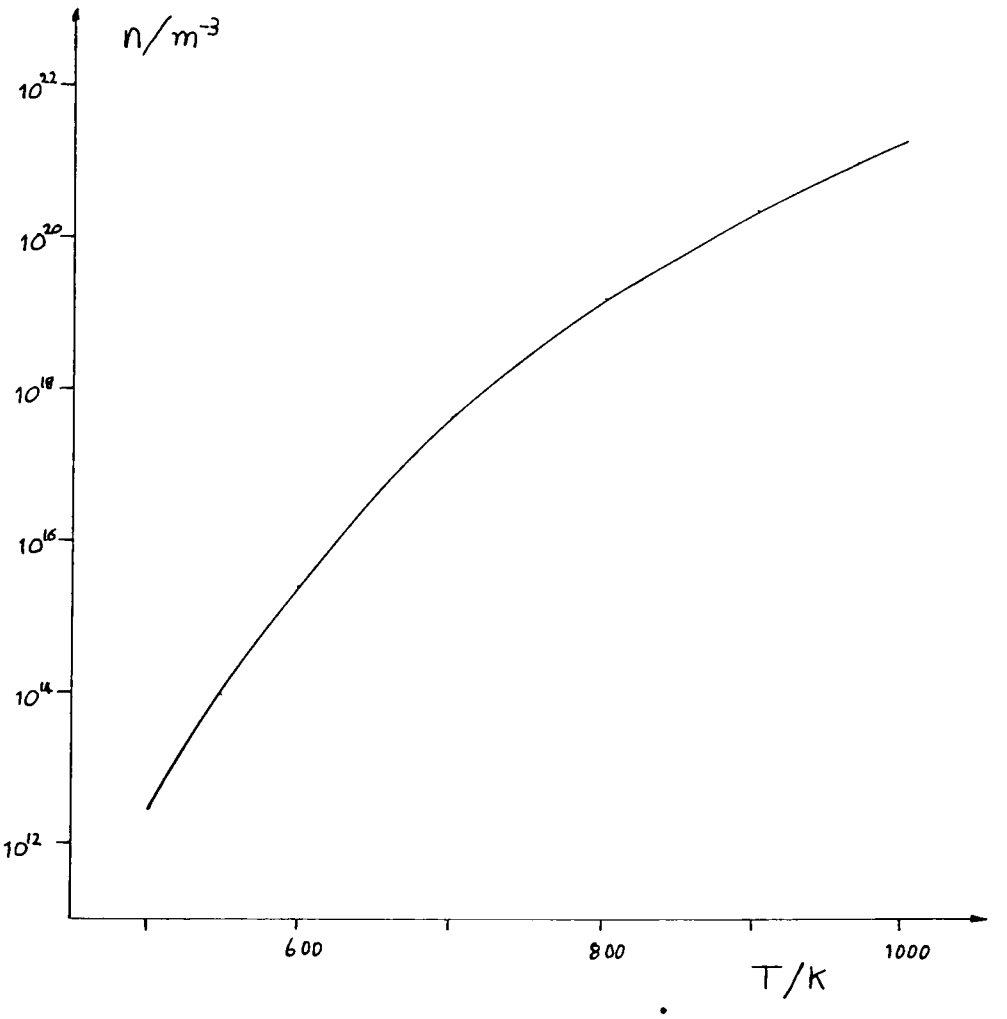
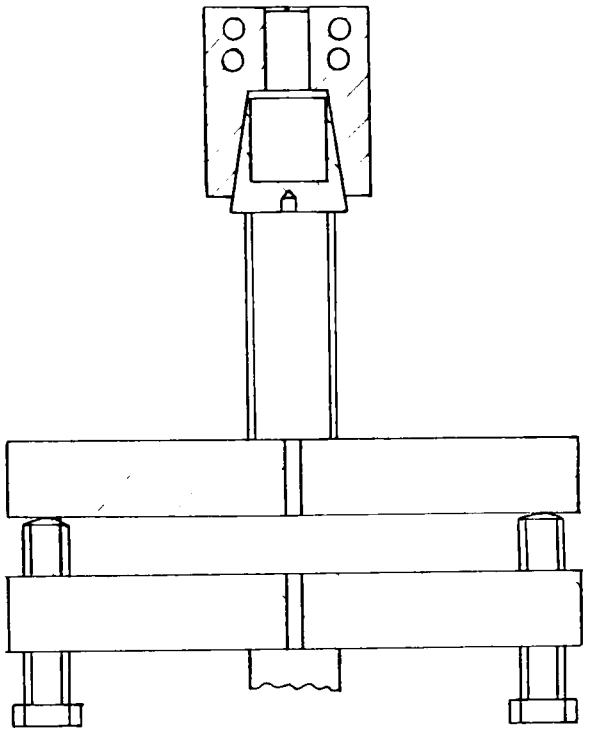


FIGURE 3.1 The number density of Ca atoms in its saturated vapour as a function of temperature.

of calcium atoms in the interaction region is discussed in section 3.4, and in section 3.5 I describe the detection of the fluorescence from the interaction region. In section 3.6 I describe the system of lenses used to focus the laser into the interaction region; in this section also, drawing together the results of the other sections, an estimate of signal size is made. In the final section I discuss the background light, and the steps taken to minimize it.

3.2 The Atomic Beam Oven

It is possible to perform a two-photon absorption experiment in a cell containing a vapour of the element to be studied, but for a metallic element such as calcium it would be necessary to construct some system for preventing the atoms from condensing on the windows of the cell, for example a buffer gas. This would lead to uncertainties about pressure broadening and shifts; although it is very likely that such shifts would be isotope-independent, the very large range of masses of calcium isotopes (^{48}Ca is 20% heavier than ^{40}Ca) means that the distribution of atomic speeds would be different for different isotopes, and there is certainly the possibility of systematic error. It was therefore decided to perform the experiment in an atomic beam with no buffer gas. This is free from the above-mentioned source of systematic error and provides an ideal environment for studying free atoms in the absence of collisions. It is also convenient because provided there is a small amount of collimation of the beam, most of it can be caught on a water-cooled plate and the amount reaching the windows is very small. However the atomic number density that can be achieved is much smaller at the same temperature than in a cell, and so the oven has to be somewhat hotter to compensate for this. If the beam is collimated too much, the number density is further reduced; however since we only require collimation for "cleanli-



Section through AA.

Plan

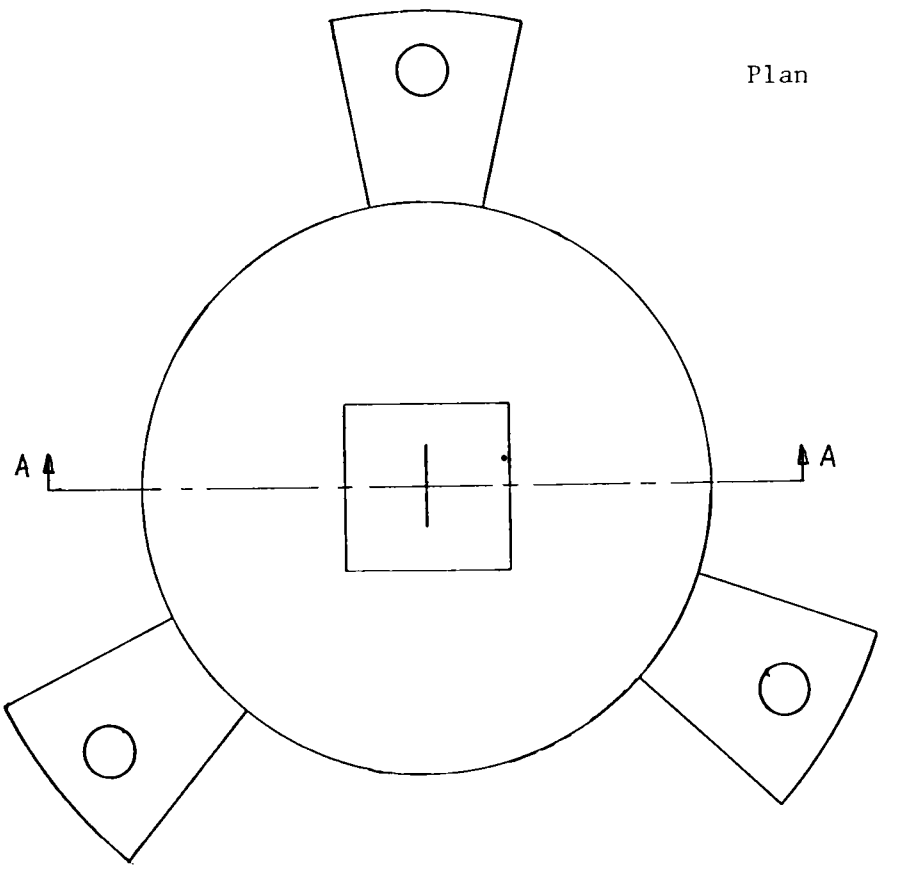


FIGURE 3.2 The Atomic Beam Oven and Levelling Table.

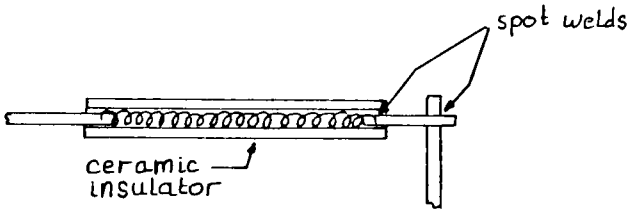
ness" (that is, catching the atoms on our beam catcher plate) and not for any elimination of the Doppler effect, we were able to use a low collimation.

The oven is shown in Fig. 3.2; it was made out of mild steel bar. It consists of a hollowed out conical base, with a volume of about 1 cm^3 for calcium granules, and a heated upper part which rests on the cone. The cone semi-angle was chosen to be 7° - this is a compromise between a sufficiently large angle to make extraction of the base easy for reloading, and a sufficiently shallow angle to locate accurately the upper half of the oven. The slit is 0.6 mm deep, and was cut with a 0.2 mm slitting saw; in use over a period of two years it widened somewhat, particularly at one end. With this slit width and depth the oven needed reloading after about 20 hours at operating temperature.

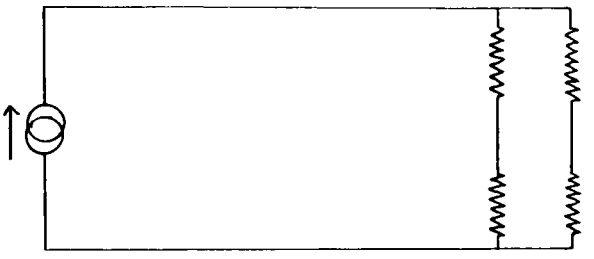
The oven is supported on three hollow thin-walled stainless steel tubes with very low thermal conductivity, 35 mm long, which fit into shallow holes in the base of the cone and in the upper brass table. This table is supported by three levelling screws from the lower brass table allowing small vertical movements and tilt adjustments of the oven inside the vacuum system. The lower brass table is rigidly connected via three steel legs, 108 mm long, to the connecting collar described in the next section. In addition to the height and tilt adjustments of the oven inside the vacuum system, there are also height, tilt and rotation adjustments of the entire vacuum system as described in the next section.

The oven is enclosed in two cylindrical heatshields below and at the side, and one heatshield above, with a rectangular slit over the oven slit. These are made of thin nickel sheet and are supported by a frame of 1 mm nickel wire spot-welded to form a tripod which sits on the upper brass table. The two circular heatshield bases have holes to permit passage of the tripod legs of the oven, and also its thermocouple wires and heater wires.

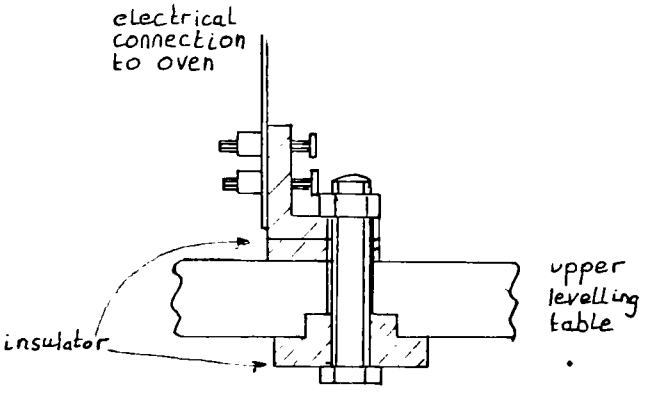
The oven is heated by four coils of 100 μm diameter tungsten wire enclosed in ceramic. Each coil has about 35 turns, and is made by wrapping



Construction of Heater Coils.



Electrical Connection of Heaters.



Section through Clamp.

FIGURE 3.3

the wire, which has previously been annealed by passing it through a flame, around a former of 1 mm tungsten wire held in a collet in a lathe set to about 60 rpm. These coils are connected together in pairs by spot-welding to 1 mm nickel wire inserted into the last coil, and then carefully pushed into the ceramic insulators in the holes of the oven. The free ends of the coils are then spot-welded to lengths of nickel wire which pass down through the lower heat shields to clamps on the upper brass table (see Fig. 3.3). From here copper wire leads to 10 A vacuum seals on the connecting collar described in the next section.

The heaters were powered by a Coutant LB 1000.2 10 A 15 V power supply. This can act as either a current or voltage source with overload protection; we used it as a current source with the voltage limit set at the maximum (15 V). A current of about 8 A was used; the resistance of the heaters was 1.2 Ω per coil and so typical performance was 80 W of electrical heating to provide a temperature of 600°C. This temperature was monitored by a Chromel Alumel thermocouple inserted into a small hole in the base of the oven and held in place by a clamp below the lower brass table. The effective cold junction was the connecting collar and the voltage was measured on a digital voltmeter. The operating temperature as measured by this voltmeter was around 600°C - below 550°C there was very little signal with the available laser power, and above 650°C the stray light from the oven increased rather sharply so that it was not advantageous to increase number density further by increasing the temperature. The number density at this temperature will be discussed in section 3.4 below.

After heating, the spot-welded junctions between the nickel and tungsten wires became rather brittle and when reloading the oven they were sometimes broken. When this happened the entire system of nickel connecting wires and tungsten coils was replaced. Even when no breakages occurred, the heaters still had a finite lifetime; after several weeks of use the resistance of the heaters declined slowly and eventually they had to be replaced because

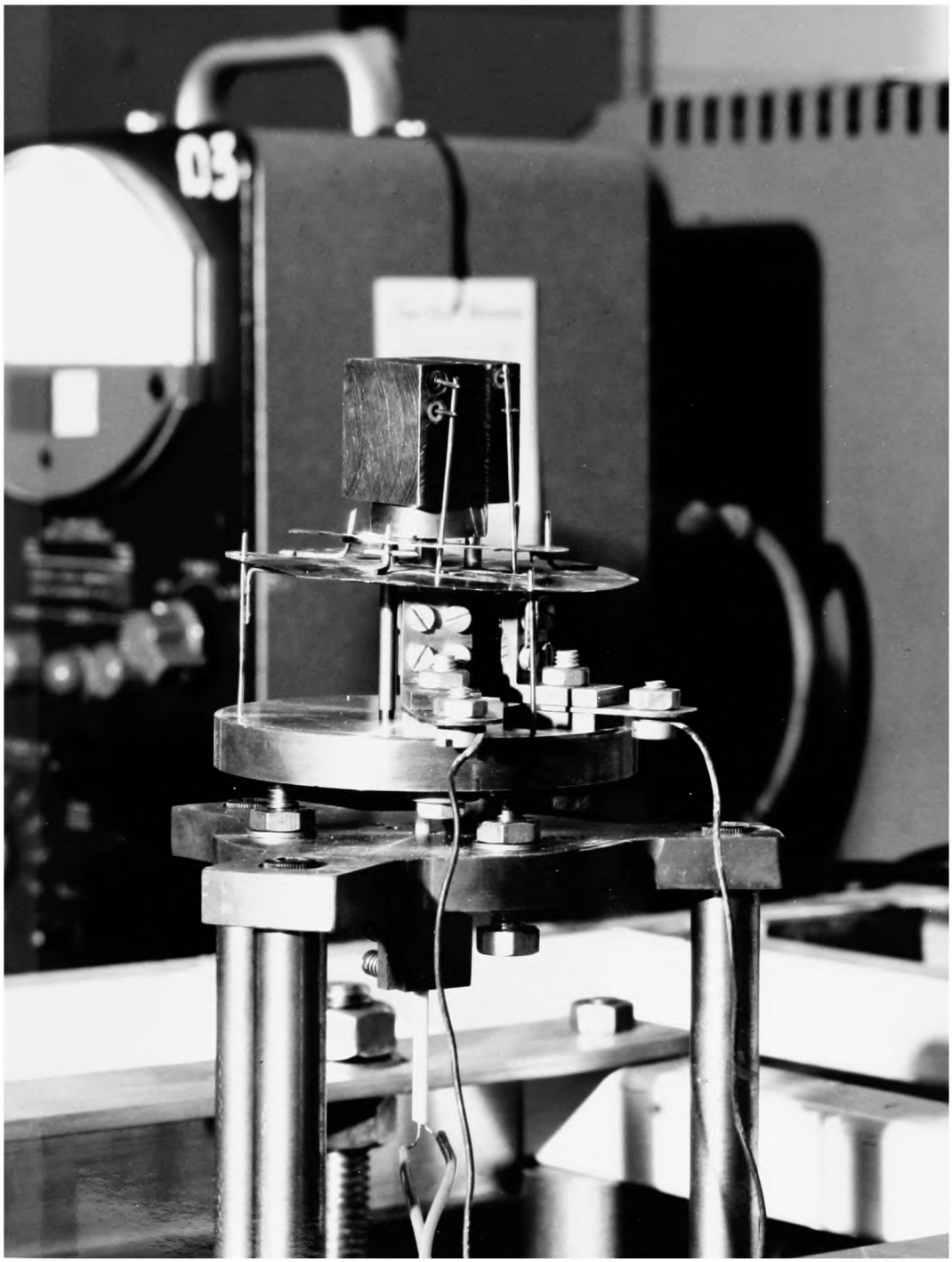
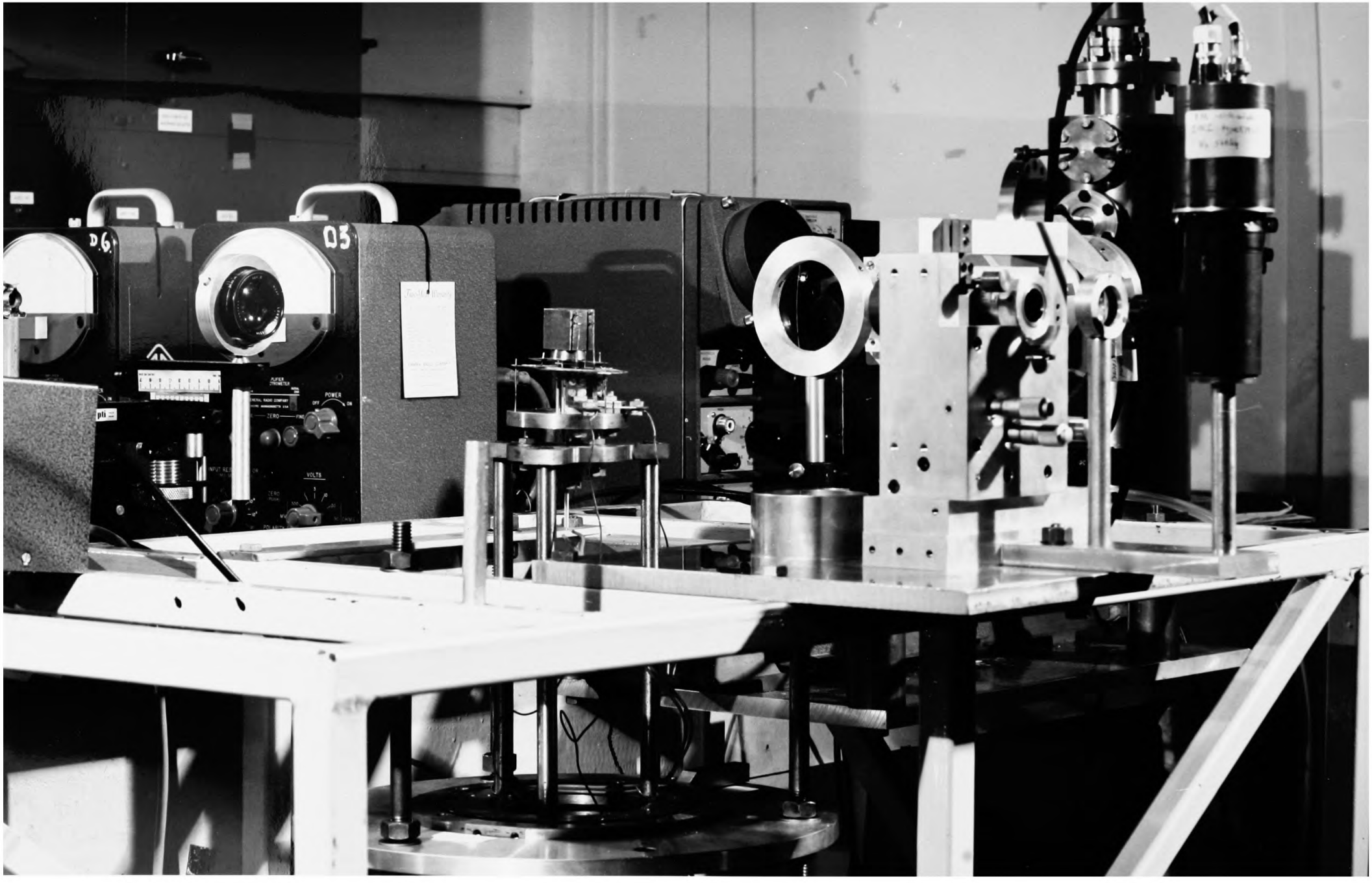


FIGURE 3.4a


D6
03
POWER
OFF
ON
ZERO
FINE
VOLTS

at the maximum current setting of 10 A there was insufficient heating power. I never fully understood why this happened; there was rarely any evidence of turns of the coils sticking together and so lowering the overall resistance - in fact when removed from the oven after use the coils usually looked unchanged. It is possible that the heater coils were partially shorted out by a layer of tungsten deposited on the inside of the ceramic insulator which when exposed to the air was oxidised and so rendered electrically insulating. The ceramic insulators were replaced once, and this certainly increased the observed resistance of the heater coils.

The photographs (Fig. 3.4) show the oven in situ, with the vacuum chamber and heat shields removed. The tripod oven legs are partially hidden behind the clamps taking the electrical connections to the heaters. Below the lower brass table can be seen the clamp holding the thermocouple wires which at this point are enclosed in a twin hole ceramic insulator. The tripod legs of the lower table can be seen going to the connecting collar.

3.3 The Vacuum System

The vacuum system is shown in Fig. 3.5. The oven was contained in a stainless steel can with seven ports. The lower 4" port connected through a connecting collar to an Edwards E02 diffusion pump, with thermoelectrically cooled baffle valve. This collar was supported on a large dural plate which was hung on three threaded rods from a frame resting on the floor. These allowed vertical and tilt motions of the entire vacuum system. The collar was not fixed to the supporting plate but rested in a circular recess and so the entire vacuum system could also be rotated by a "finger" screwed to the top flange of the collar. All these adjustments can be seen in Fig. 3.4b: the "finger" is visible projecting over the supporting plate to the rear. The use of these mechanical adjustments for alignment is described in section

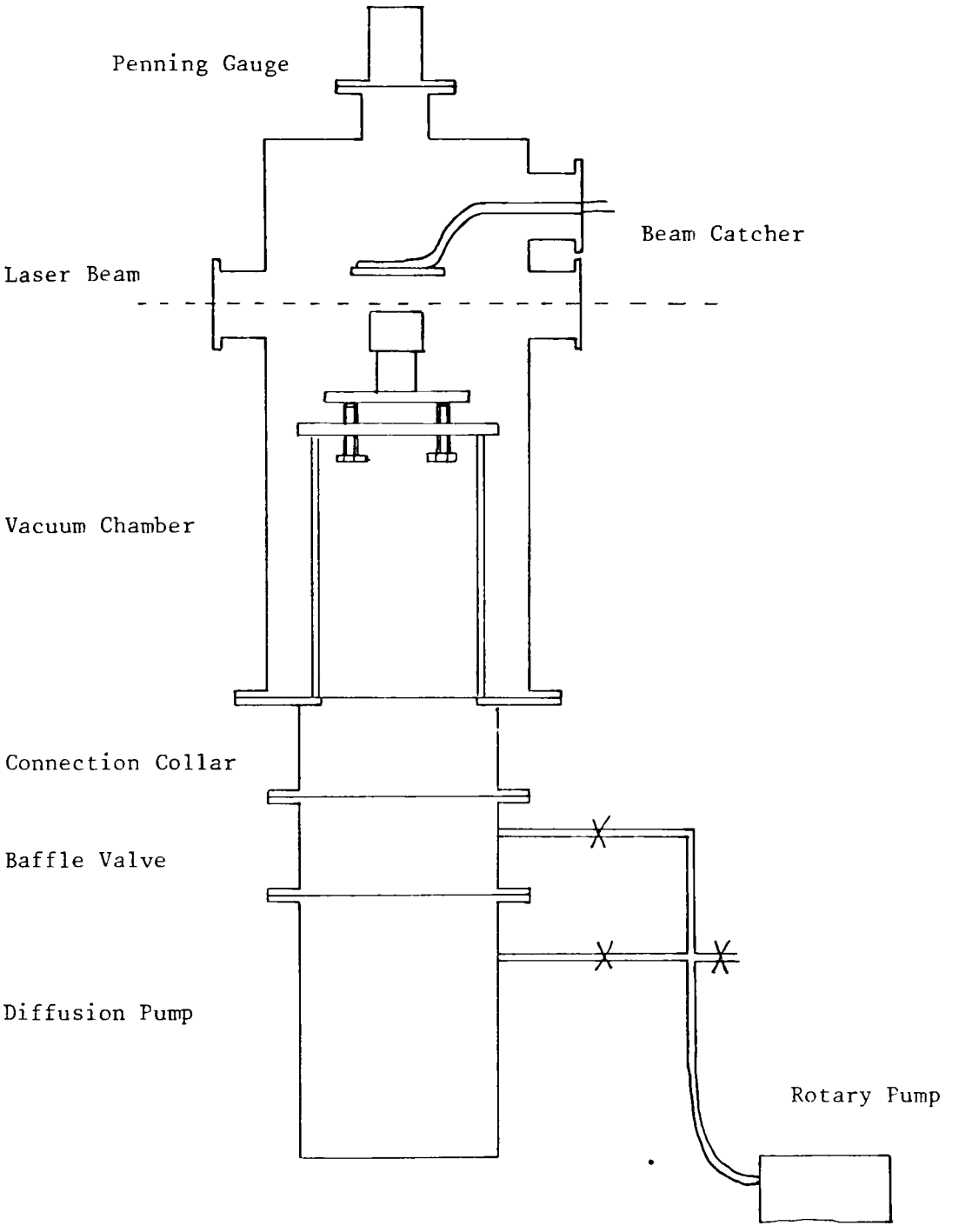


FIGURE 3.5 Schematic Diagram of Vacuum System

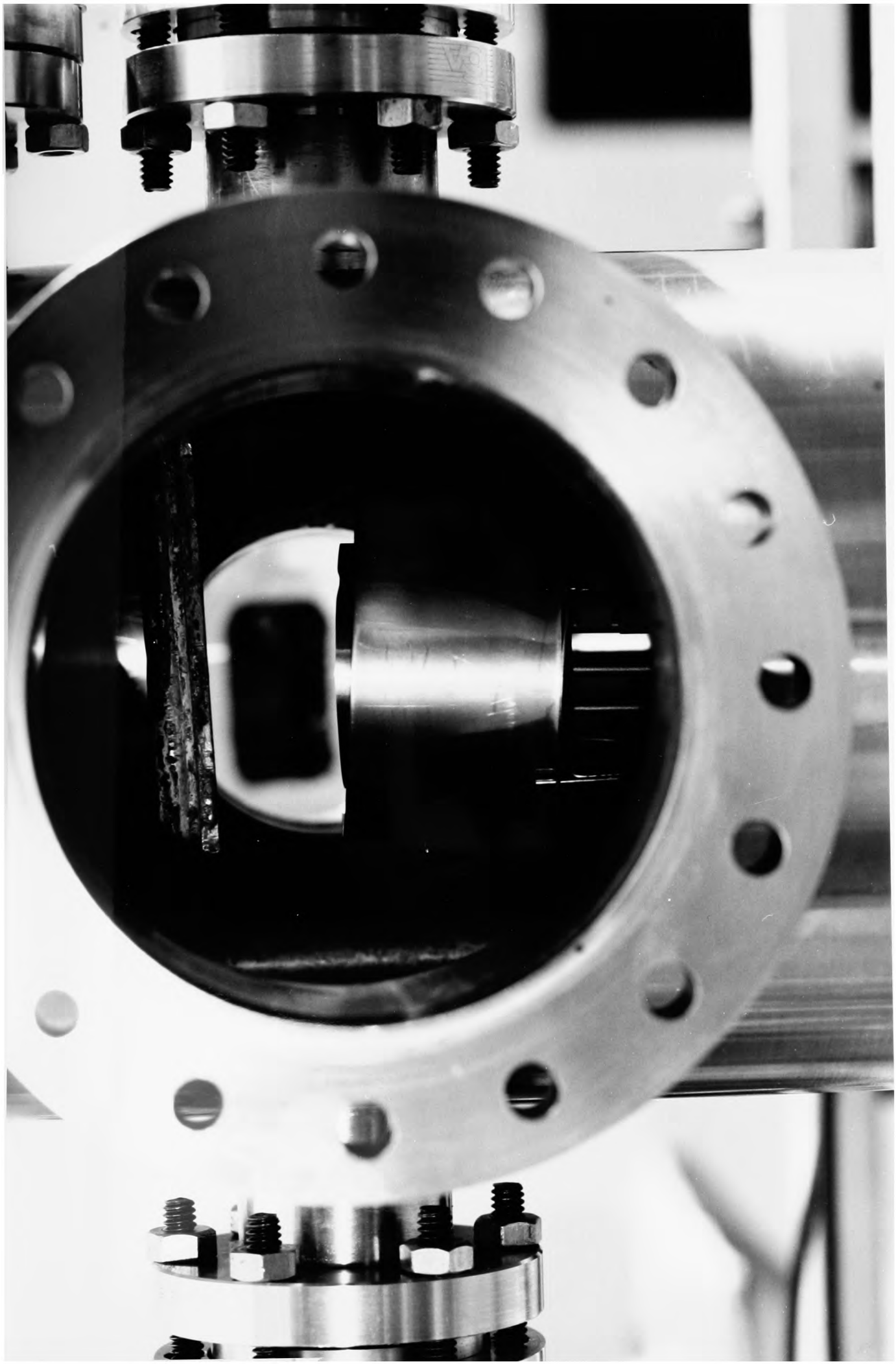
3.6.

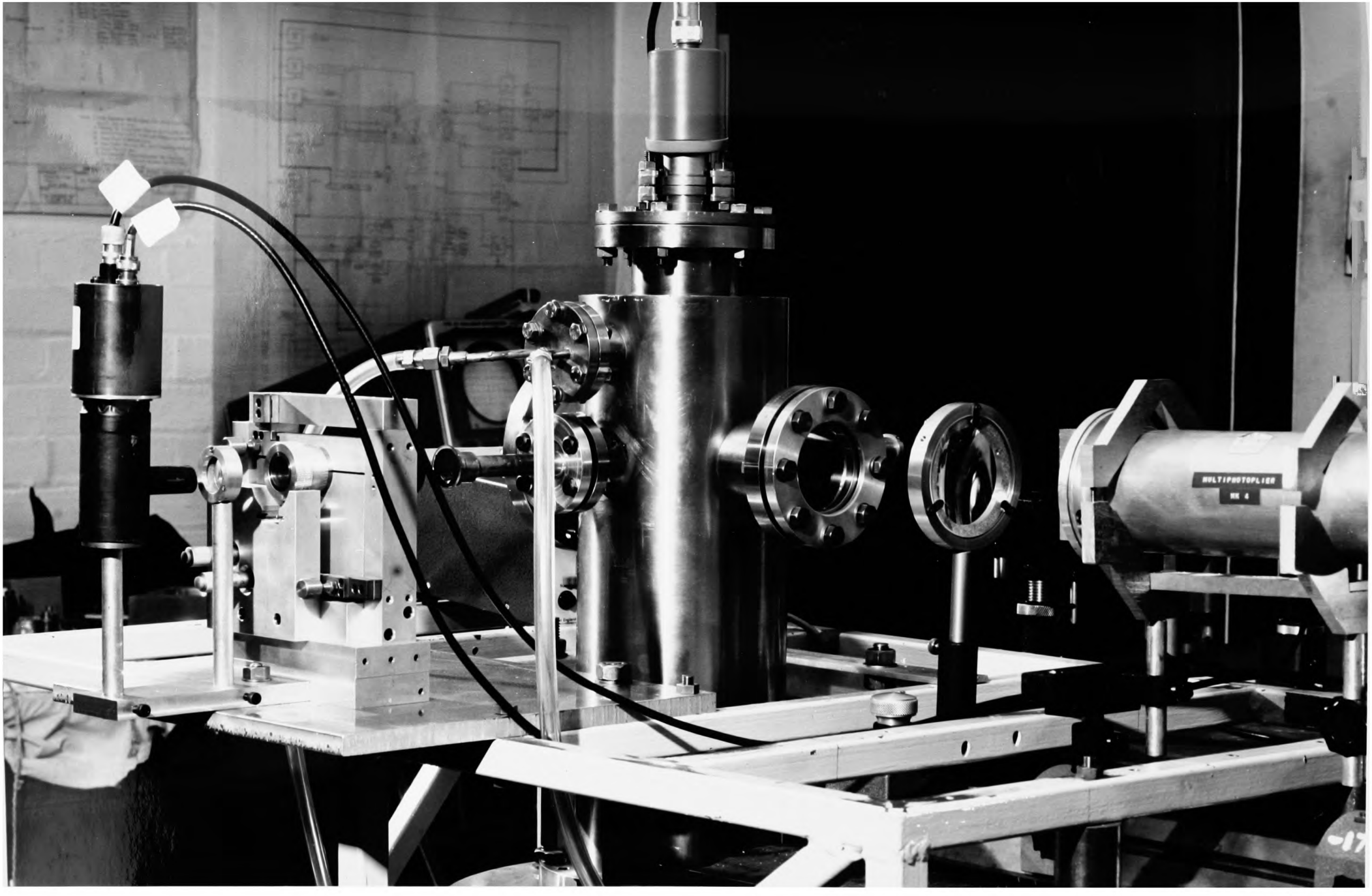
The rotary pump used for roughing out the system and backing the diffusion pump was situated on the floor about six feet from the frame and connected to the vacuum system by flexible polythene tubing. This was to minimize any vibration of the frame due to the pump; since the frame also carried the mirror which reflected the laser beam to form the returning waist it is very important that there should be as little vibration of the frame as possible.

Of the remaining vacuum ports, the upper 3" port carried an Edwards Penning gauge which measured the pressure in the system. This was about 2×10^{-5} torr with the diffusion pump, but when the calcium was heated the pressure fell further to 4×10^{-6} torr indicating gettering by the calcium.

There were three, 1½" ports of which two held windows to admit the laser to the vacuum system, and the third held a water-cooled metal plate which acted as a beam catcher. There was a 2½" port at right angles to these through which the fluorescence was observed, and a large 4" port opposite it which was used as an observation window; normally it was covered with black paper. Fig. 3.6 is a photograph taken through this port (the window has been removed to avoid stray reflections) showing the oven, now clad in its heat shields, and the water-cooled beam catcher above it. The laser window flanges are visible to left and right, with the beam catcher flange above the righthand window. The window through which fluorescence was observed is visible directly behind the oven. Fig. 3.7 is taken from the opposite side of the system and shows on the right the photomultiplier used to monitor the fluorescence, and on the left the mirror reflecting the laser.

It will be seen on this photograph that the laser windows are on stalks to take them further from the interaction region. This minimized the deposit of calcium on these windows, which were only cleaned twice over the whole period of the experiment. The deposit of calcium on the other two windows was more rapid, and these were cleaned each time the oven was reloaded,




MULTIPHOTOPLIER
MK 4

that is after about 20 hours use.

The electrical connections to the oven were made through the connecting collar; these consisted of the two wires taking the heat current, and two wires for the thermocouple. Later an earth wire for the heat shield was introduced to prevent discharge effects in the region between the oven and the heat shield. These are discussed below in section 3.7.

3.4 Calculation of Number Density

In this section I calculate the number density of calcium atoms in the region of interaction with the laser, and their velocity distribution along the laser beam, which determines the lineshape of the Doppler-broadened component of the absorption signal. Two interesting special cases are considered in a brief digression at the end of the section. Ramsey (1963) Chapter II is a general reference for this section.

The calculation assumes the validity of the kinetic theory of effusion; the conditions for this in the case of effusion from a long slit of width w and depth d (see Fig. 3.8) are $w \ll \lambda$ and $d \ll \lambda$, where λ is the atomic mean free path. For angles of effusion near the normal, we can ignore the effect

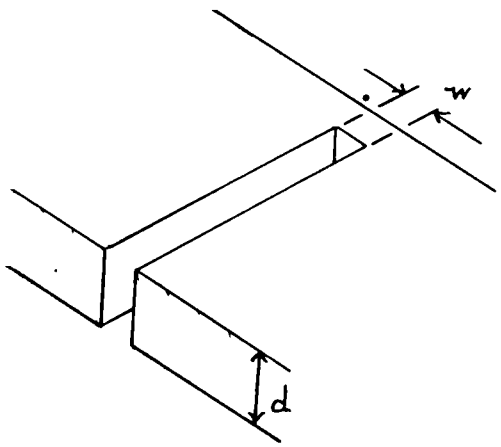


FIGURE 3.8

w ~ 0.2 mm

d ~ 0.6 mm

of the finite slit depth; for angles away from the normal the effusion rate is reduced by a conservation factor (Ramsey, loc. cit.). In our case the conservation factor is close to unity only for a region of a few degrees from

the normal, but the laser beam is situated directly over the slit, and has a diameter of a fraction of a millimetre, and so the conservation factor can be taken to be one.

In this case the situation is that of simple effusion from a slit, and the primary result of the theory is that the rate of effusion of atoms with speeds between c, c + dc in solid angle $d\Omega$ from length $d\ell$ of the slit, width w, is

$$\text{(1)} \qquad \text{Rate} = n\, c\, P(c)\, dc\, \cos\theta\, \frac{d\Omega}{4\pi}\, w\, d\ell$$

where θ is the angle from the normal, and P(c) and n are the speed distribution and number density inside the oven. We require first to turn this rate into a number density at a general point.

The situation is shown in Fig. 3.9; the origin O is at the centre of the slit of length L, with the z axis along the slit and the x axis normal to it. We aim to calculate the number density at P, labelled by Cartesian co-ordinates (x,y,z) or cylindrical co-ordinates (r,ϕ,z). The length $d\ell$ of slit is located at A, distant ℓ from O, while B is the point on the z axis nearest to P. Thus BP = r, and we define AP = s.

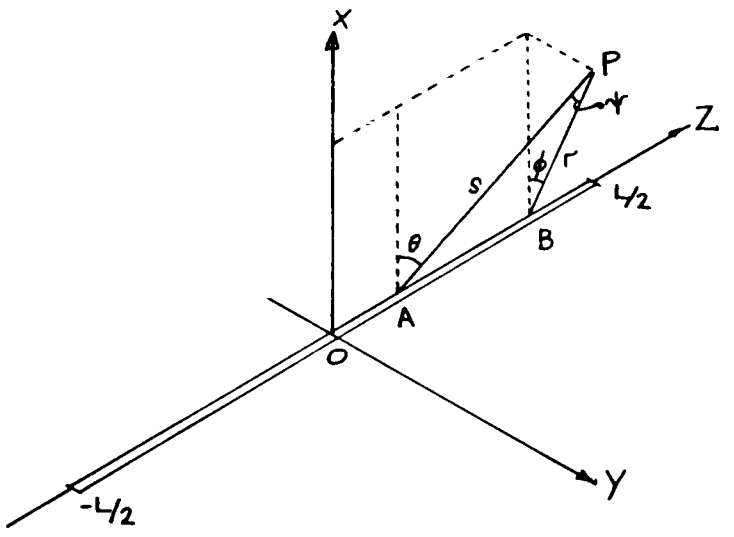


FIGURE 3.9

Consider a small element of volume at P; for the purposes of convert-

ing the flux of equation (1) to a number density we can choose the volume element to be any convenient shape, and so we take it to be an element of a spherical shell centred at A, subtending there an angle $d\Omega$, with thickness ds. Then equation 1 gives the rate at which atoms from length $d\ell$ at A in velocity class dc cross the volume element. The time they take to do so is ds/c, and so the number in the volume element at any instant is

$$n\ P(c)\ \cos\theta\ \frac{d\Omega}{4\pi}\ w\ d\ell\ ds.$$

But the volume of the element is $s^2 ds d\Omega$, and so the number density of atoms from length $d\ell$ at A with speed in c, c+dc is

(2) $$\text{Partial number density} = n\ P(c)\ dc\ \left(\frac{\cos\theta\ w\ d\ell}{4\pi s^2}\right) .$$

Note that the factor in brackets is just the solid angle subtended by the area w $d\ell$ of the slit, at P. Thus the total number density at P is

(3) $$\text{Total number density} = \frac{n\Delta\Omega}{4\pi}$$

where $\Delta\Omega$ is the total solid angle subtended by the slit at P. We define a geometrical factor $G(r,\phi,z) = \Delta\Omega/4\pi$ which connects the number density inside the oven to the number density in the beam at P. .The result of integrating equation 2 is

(4a) $$G(r,\phi,z) = \frac{w\ \cos\phi}{4\pi r}\ (\sin\psi_1 + \sin\psi_2)$$

where

(4b) $$\sin\psi_1 = \frac{\frac{1}{2}L + z}{[r^2 + (\frac{1}{2}L+z)^2]^{\frac{1}{2}}},\quad \sin\psi_2 = \frac{\frac{1}{2}L - z}{[r^2 + (\frac{1}{2}L-z)^2]^{\frac{1}{2}}}$$

(ψ_1 and ψ_2 are the limits of ψ, the angle $A\hat{P}B$, when A is at $\pm L/2$.)

As we noted above, our results are only valid near the normal, and

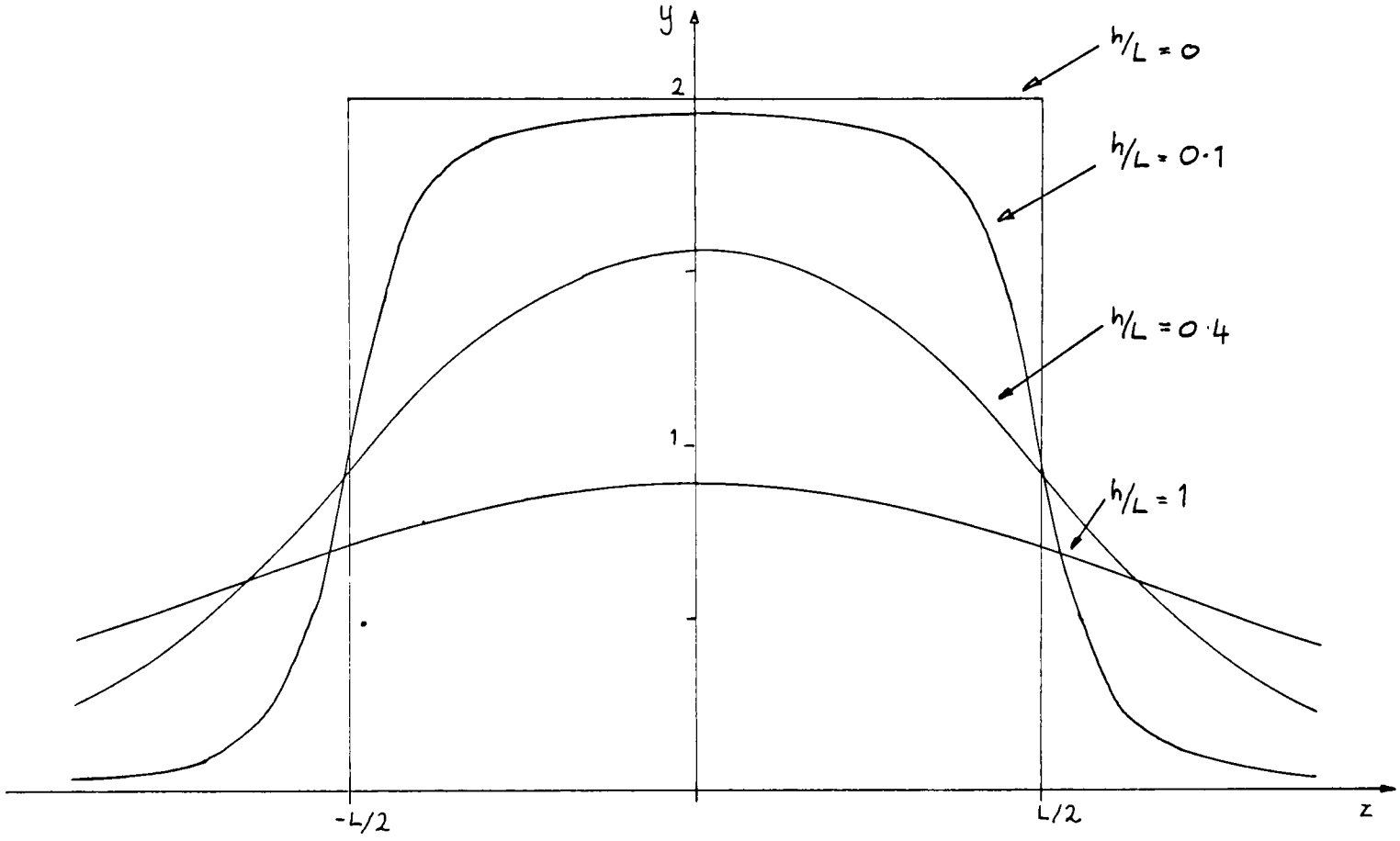


FIGURE 3.10 The Graph shows $y = \sin \psi_1 + \sin\psi_2$ for various values of h/L.

The geometrical factor G is given by

$$G = \frac{w}{4\pi h} y$$

so $\cos\phi = 1$, and we can replace r by h, the height over the slit. Thus we have

$$(5) \qquad G(h,0,z) = \frac{w}{4\pi h}\left\{\frac{\frac{1}{2}L - z}{[h^2 + (\frac{1}{2}L - z)^2]^{\frac{1}{2}}} + \frac{\frac{1}{2}L + z}{[h^2 + (\frac{1}{2}L + z)^2]^{\frac{1}{2}}}\right\}.$$

This function is shown for various values of h/L in Fig. 3.10; in our case L = 10 mm and h ≃ 4 mm, so the appropriate curve is that for h/L = 0.4. We see that the number density is fairly uniform over the region $-L/2 \leq z \leq L/2$, but falls off outside this region. The maximum number density at any given height is at z = 0

$$(6a) \qquad G(h,0,0) = \frac{w}{4\pi h}\,\frac{L}{[h^2 + L^2/4]^{\frac{1}{2}}}$$

while the average over the region $-L/2 \leq z \leq L/2$ is

$$(6b) \qquad \bar{G}(h) = \frac{w}{2\pi L}\,[\sqrt{1 + L^2/h^2} - 1] \ .$$

The uniformity of number density can also be seen by taking the ratio of equations 6a and 6b

$$\frac{\bar{G}(h)}{G(h,0,0)} = \frac{2(1 + L^2/4h^2)^{\frac{1}{2}}}{1 + (1 + L^2/h^2)^{\frac{1}{2}}} = 0.87 \text{ for } h/L = 0.4.$$

The actual value of $\bar{G}$ for w = 0.2 mm, h = 4 mm and L = 10 mm is 5.4×10^{-3}, and so to obtain a number density of 2×10^{18} m^{-3} in the beam we require a number density of 4×10^{20} in the oven, or a temperature of about 600°C.

We now turn to the calculation of the velocity distribution parallel to the slit (that is, along the laser beam). The z-component of the velocity is

$$c_z = c \sin\psi$$

and so

$$P(c)dC = \frac{4\pi c_z^2 \operatorname{cosec}^2\psi}{\pi^{3/2} v_D^3} \exp -\left(\frac{c_z^2 \operatorname{cosec}^2\psi}{v_D^2}\right) |\operatorname{cosec}\psi| \, dc_z$$

where

$$v_D^2 = 2kT/M.$$

Making this substitution in equation 2, and in addition the substitutions

$$\cos\theta = \cos\phi\cos\psi$$

$$d\ell = r \sec^2\psi \, d\psi$$

$$s^2 = r^2\sec^2\psi$$

we find the contribution of length $d\ell$ of slit at A to the number density of velocity class dc_z to be

$$(7) \qquad \frac{n w \cos\phi}{r} \frac{c_z^2 dc_z}{\pi^{3/2} v_D^3} . |\operatorname{cosec}^3\psi| \cos\psi \exp -\left(\frac{c_z^2 \operatorname{cosec}^2\psi}{v_D^2}\right) d\psi .$$

To find the total number density of velocity class dC_z at P we integrate equation 7 over ψ as follows:-

If $|z| > L/2$ integrate from $-\psi_1$ to ψ_2;

$-L/2 \leq z \leq L/2$ and $c_z > 0$, integrate from $-\psi_1$ to 0;

$-L/2 \leq z \leq L/2$ and $c_z < 0$, integrate from 0 to ψ_2.

If we define the number density per unit velocity range to be $N(c_z;r,\phi,z)$, so that

$$\int N \, dc_z = G \, n$$

then the result of integrating equation 7 is

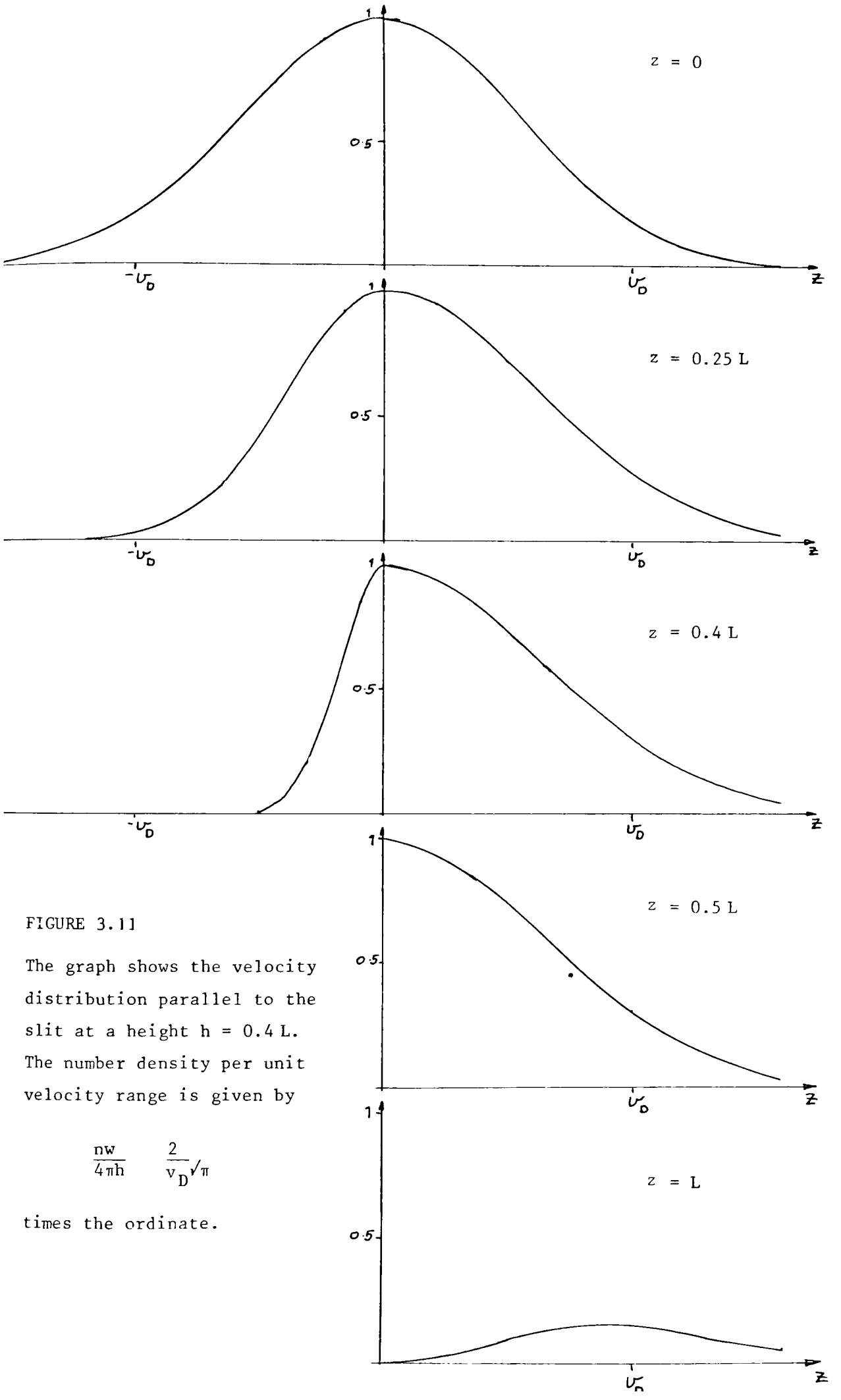


FIGURE 3.11

The graph shows the velocity distribution parallel to the slit at a height h = 0.4 L. The number density per unit velocity range is given by

$$\frac{nw}{4\pi h} \quad \frac{2}{v_D\sqrt{\pi}}$$

times the ordinate.

$$|z| < L/2 \quad N(c_z) = \frac{n w \cos\phi}{4\pi r} \frac{2}{v_D\sqrt{\pi}} \exp\left(\frac{-c_z^2}{v_D^2 \sin^2\psi_1}\right) \quad \text{if } c_z > 0$$

(8a)

$$= \frac{n w \cos\phi}{4\pi r} \frac{2}{v_D\sqrt{\pi}} \exp\left(\frac{-c_z^2}{v_D^2 \sin^2\psi_2}\right) \quad \text{if } c_z < 0$$

(8b)

$$|z| > L/2 \quad N(c_z) = \frac{n w \cos\phi}{4\pi r} \frac{2}{v_D\sqrt{\pi}} \left|\exp\left(\frac{-c_z^2}{v_D^2 \sin^2\psi_1}\right) - \exp\left(\frac{-c_z^2}{v_D^2 \sin^2\psi_2}\right)\right|$$

where, in equation 8b, c_z has the same sign as z, and $N(c_z)$ is zero otherwise. As in the case of equation 5 for the factor G, equation 8 is only valid near the normal, and so we can put

$$\cos\phi = 1 \qquad r = h$$

$$\sin^2\psi_1 = \left[1 + \left(\frac{2h}{L - 2z}\right)^2\right]^{-1} \qquad \sin^2\psi_2 = \left[1 + \left(\frac{2h}{L - 2z}\right)^2\right]^{-1} .$$

The velocity distribution is plotted for h/L = 0.4 and for various values of z in Fig. 3.11; we see that the distribution is nearly symmetrical over the central half of the slit, but becomes very asymmetrical in the region z > L/2.

We now consider the lineshape of the Doppler-broadened component of the absorption. This will vary from point to point within the atomic beam, as the velocity distribution varies. At any point in the beam an atom with a non-zero velocity parallel to the laser will see two laser beams with equal and opposite Doppler shifts. Thus the spectrum of the Doppler-broadened component is symmetrical, having the form of the velocity distribution plus its mirror image in the $c_z = 0$ axis, and so from a general point over the slit the Doppler-broadened component has a spectrum consisting of the sum of two Gaussians with unequal width, and unequal area beneath them. If however we assume that most of the absorption takes place near the centre of the slit, where the laser intensity is greatest, the spectrum of the Doppler-broadened component has approximately the form of a single Gaussian, with width narrower than that appropriate for the oven temperature by a factor

$$\sin\psi = (1 + 4h^2/L^2)^{-\frac{1}{2}}.$$

For h/L = 0.4, this is 0.78, giving a Gaussian FWHM of 1300 MHz for ^{40}Ca at 600°C, for absorption at 600 nm.

We finally digress briefly to consider the relative intensities of the Doppler-free and Doppler-broadened components. We note that away from the slit ($z > \frac{1}{2}L$) the velocity distribution goes to zero at $c_z = 0$. Thus if the laser beams were both focussed into this region the spectrum would have the form of Fig. 3.12.

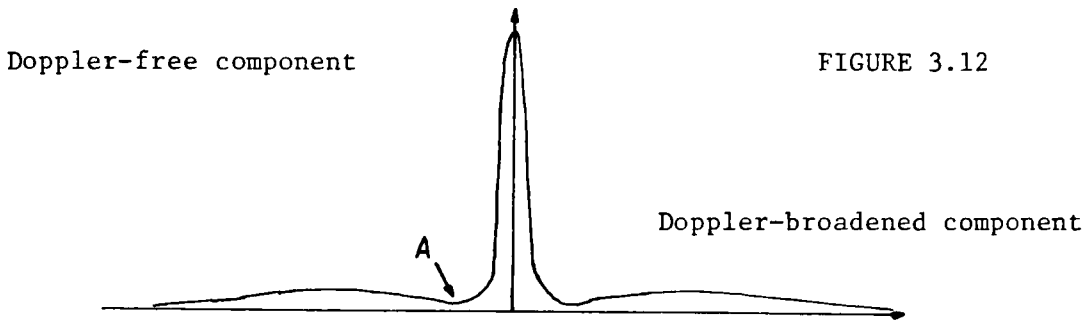


FIGURE 3.12

This means that if the Doppler-broadened component cannot be eliminated by choice of polarization it can be moved away from the Doppler-free component if this is necessary, although at a cost of a loss in signal. This is unlikely to be of any practical use, but if the spectrum contained a peak due to a very rare isotope at the point marked A in Fig. 3.12 which was masked by the noise due to the Doppler-broadened component of the nearby large peak, then it could be advantageous to move the background away. It is more likely however that the resulting loss of signal would more than compensate for the drop in noise. This effect was first noted by Dr. Meisel (private communication).

It is important that this effect is peculiar to the beam geometry, where there is a region in which all the atoms have the same direction of velocity component along the beam. It might be thought that a similar effect could be obtained in a cell by displacing the waists of the two beams longitudinally, so that most of the Doppler-broadened component comes from the

two separated waists while the Doppler-free component comes mostly from the region between the waists. The Doppler background is clearly Gaussian from all points in the laser beam, and the relative intensity of the Doppler-free and Doppler-broadened components can be found by integrating I^2 over the plane perpendicular to the laser beam, where I^2 is $(I_1^2 + I_2^2)$ for the Doppler-broadened component, and $(4I_1I_2)$ for the Doppler-free component. (This method is described in more detail in the next section.) We find, if the waists are at $z = \pm d$, with confocal parameter z_o, then

$$\text{Doppler-broadened component} \sim \frac{P_1^2}{z_o^2 + (z-d)^2} + \frac{P_2^2}{z_o^2 + (z+d)^2}$$

$$\text{Doppler-free component} \sim \frac{8P_1P_2}{2z_o^2 + (z-d)^2 + (z+d)^2}$$

where P_1, P_2 are the powers of the two beams. If we take these equal, then the ratio of intensities is

$$\frac{\text{Doppler-free}}{\text{Doppler-broadened}} = 2 - \frac{8z^2d^2}{z_o^2 + z^2 + d^2}$$

showing that even at the centre of the region ($z = 0$) there is no advantage to be gained; there is in fact a disadvantage, as the total signal is down:-

$$\frac{\text{Doppler-free}}{\text{Doppler-free (d=0)}} = 1 - \frac{d^2}{z_o^2 + z^2 + d^2} \quad .$$

3.5 The Detection of the Fluorescence

The aperture through which the fluorescence was monitored subtended a solid angle at the interaction region of 0.132 sr, and so the fraction f of light collected by it is $f = 1.05 \times 10^{-2}$. The interaction region was imaged through this aperture onto the photocathode of an EMI 9635QA photomultiplier. This photomultiplier is of the bialkali type, and the wavelength to be detected (423 nm) is near the peak of its spectral response, with a quantum efficiency of 26%. The photocathode was covered with a Chance-Pilkington OB10 colour filter; this has a transmission of about 50% at 423 nm, but an extremely low transmission (less than 10^{-3}) at the laser wavelength of 600 nm.

Initially the imaging was done with a single lens; both this and the photomultiplier were mounted on an optical bench bolted to a plate which was hung from the frame on which the vacuum system was supported. This is the situation shown in Fig. 3.7; during a run all these components were carefully covered with a black cloth to exclude stray light, and the room containing the vacuum system was in darkness. Subsequently, as described in section 3.7, tests were done with an interference filter and for this purpose the single lens was replaced by two lenses, with a region of parallel light between them where the filter could be inserted.

We are now in a position to estimate the total signal to be expected. If I is the power per unit area in each of the two laser beams (assumed identical) then the theory of Chapter 2 gives the excitation rate per atom at any point as $R(\omega)I^2$, where R has the value 4.7×10^{-6} $s^{-1}mW^{2}mm^{-4}$ at the peak of the Doppler-free component. For each laser beam we take I to be a lowest order Gaussian beam

$$I = \frac{2P}{\pi}\frac{1}{w^2}\exp(-2r^2/w^2) \qquad (9a)$$

where we define the spot size w, which varies with z as

$$w^2 = w_o^2 (1 + z^2/z_o^2) \tag{9b}$$

and z_o, the confocal parameter, which is related to w_o by

$$z_o = \frac{\pi w_o^2}{\lambda} \quad . \tag{9c}$$

(The theory of Gaussian beams is presented in, for example, Kogelnik and Li, 1966). The physical interpretation of w and z_o is that w is the radius at which I has fallen to $1/e^2$ of its value at r = 0, and z_o is the distance from the waist at which the spot size has increased by a factor of $\sqrt{2}$.

The number density in the beam is Gn, where G is given by equation 5 and n in Fig. 3.1; the fraction of fluorescent photons in the detection solid angle is f, and the fraction that get detected is d, which, considering the quantum efficiency and the glass filter is about 10%. Then the counting rate for fluorescent photons is

$$\int R(\omega)\ I^2 G\ n\ f\ d\ d^3\underline{r} \ . \tag{10}$$

In equation 10, R, n and d are constant, but I^2, G and, in principle at least, f vary over the interaction region. It is a reasonable approximation to replace G by $\bar{G}$ (equation 6b) and take f as constant also, but to cut off the integral at the ends of the slit, z = ±L/2. This involves two approximations:

(i) Neglect of the region $|z| > L/2$ entirely - but unless z_o is quite large the values of I^2 as well as G are very small in this region (see Fig. 3.10). The effect of the aperture in front of the photomultiplier described in section 3.7 is to eliminate light from this region entirely.

(ii) Assumption of uniform G over the slit. This is a reasonable

approximation, and if anything leads to an underestimate, as the largest value of G is at z = 0 where I is also greatest.

The integral over I^2 between $z = \pm L/2$ is straightforward; the result for the counting rate C is

$$C = R(\omega)\ P^2\ \bar{G}\ n\ f\ d\ \frac{2z_o}{\pi w_o^2}\ \arctan\frac{L}{2z_o} \quad . \tag{11}$$

Comparing this with the calculations of sections 2.7 and 3.1, we see that, since in section 2.7 I used $P/\pi w_o^2$ as the effective power per unit area, the effective interaction volume is $(\pi w_o^2)2z_o\arctan(L/2z_o)$. This raises the question of the optimum value of w_o and z_o. From equations 11 and 9c we see that the only dependence of the rate C on w_o is through the inverse tangent, so that if $L \gg z_o$ the total counting rate is independent of waist size. The reason for this is that the rate per atom varies as w_o^{-4}, but the effective interaction volume varies as w_o^4, so that provided the whole interaction volume is within the region of the atomic beam, there is actually no gain in total signal from focussing to a smaller w_o.

There is in fact a penalty, since the effect of the finite time of interaction with the laser increases as w_o decreases. This leads to the phenomenon of transit time broadening discussed briefly in section 2.6. The diameter of the laser beam is $\sim 2w_o$, and so an atom crosses it in a time $\sim 2w_o/\bar{c}$, leading to a transit time linewidth $\Delta\nu_{tt} \sim \bar{c}/4\pi w_o$. Thus, in the limit $L \gg z_o$, the peak signal actually varies as w_o, and its width as w_o^{-1}, so that there is a disadvantage in focussing too tightly. In the opposite limit $z_o \gg L$, the effective interaction volume is $\pi w_o^2 L$, and so the peak signal varies as w_o^{-1}, and its width as w_o^{-1}.

To sum up, on the grounds of maximizing the signal there is little to be gained from making w_o smaller than the value for which, say,

$$4z_o \sim L$$

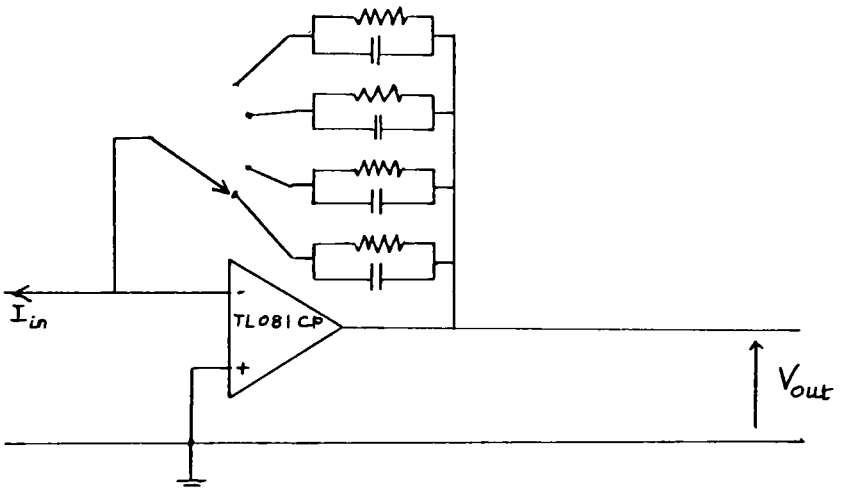


FIGURE 3.13 Smoothing Circuit for Photomultiplier Current.

$$V_{out} = \int_{-\infty}^{t} R\, I_{in}(t')P(t' - t)\, dt'$$

where the smoothing fuction is given by

$$P(t) = \frac{\exp(t/\tau)}{\tau}, \quad \tau = RC = 0.33\ s$$

Values of resistance and capacitance:

R	C
3.3 MΩ	100 nF
4.7 MΩ	68 nF
6.8 MΩ	47 nF
10 MΩ	33 nF

which, for L of 1 cm, gives

$$w_o \sim 22\ \mu m.$$

Considering the transit time width, there is little to be gained from making w_o smaller than the value for which

$$\Delta\nu_{tt} \sim \Delta\nu_{nat} + \Delta\nu_{\ell}$$

where $\Delta\nu_{nat}$ and $\Delta\nu_{\ell}$ are the natural width of the line and the laser spectral width, about 4 MHz in total. Substituting a reasonable value of $\bar{c}$ at around 600°C of 740 ms^{-1}, we find

$$w_o \gtrsim 15\ \mu m,$$

and so a reasonable value of w_o appears to be 20 μm.

Finally we consider the recording of the photomultiplier signal. The anode current of the photomultiplier was smoothed using the circuit of Fig. 3.13, with a time constant τ of 0.33 s. The output voltage of this circuit was digitized, on a scale 4096 ≡ 10 V, at intervals of 0.4 s, and the numbers punched onto paper tape for subsequent analysis. Typically, the maximum value of this voltage, at the peak of ^{40}Ca, was about 10 V, with the lowest gain setting on the smoothing box, that is R = 3.3 MΩ. If the charge delivered by the photomultiplier per photon is q, then the value we estimate for this voltage V is

$$V = R\,q\,C \tag{12}$$

where C, given by equation 11, has the value 1.5 x 10^6 s^{-1} at 600°C. If we estimate q = 3 x $10^7 |e|$, we find V = 23 volts, in excellent agreement with

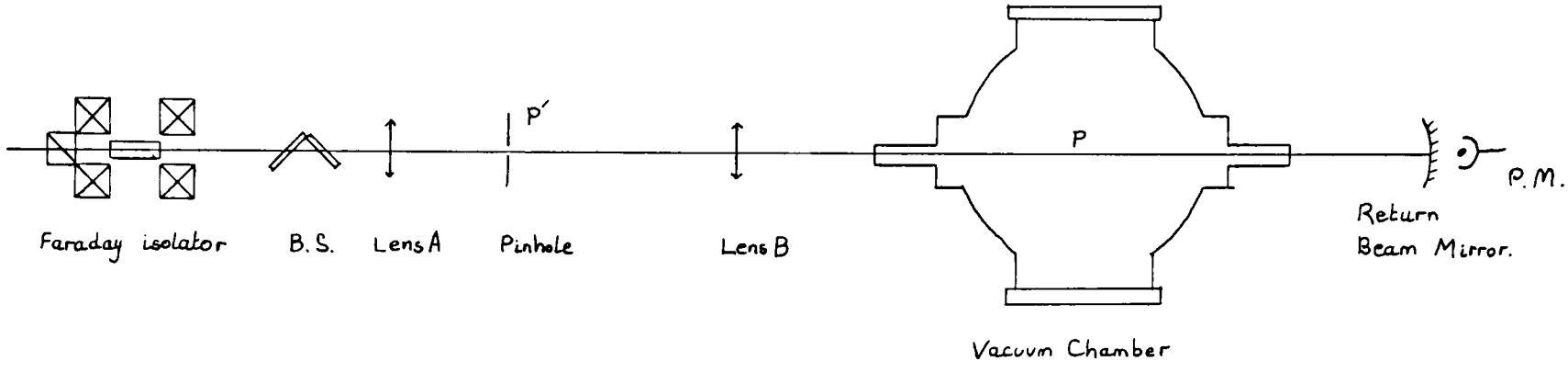


FIGURE 3.14 Additional Optical Components

the observed signal size, given the uncertainty in C.

3.6 The Focussing Lenses

In this section I shall describe the system of lenses used to focus the laser into the interaction region and the method used to position these components. The frame which supported the vacuum system was located next to a steel table which the laser beam crossed at a height of about one foot. The additional optical components described in this section, except for the mirror, were supported on magnetic mounts on this table, with vertical and horizontal translation mounts as necessary. The mirror was mounted on a dural plate on the frame; this mount is visible on the left of Fig. 3.7.

It is necessary to superpose the waists of the forward and return laser beams to a small fraction of their size both along the axis and transverse to it. Since the waists are each only about 40 μm in diameter, the transverse adjustment is the more critical. For this reason, we decided to form a waist of the required size outside the vacuum system, and form an image waist inside the vacuum system (see Fig. 3.14). When the mirror is so adjusted that the waists are co-incident at P in the beam, then they are also co-incident at P'. If a pinhole is placed at P' then the return laser beam will pass through the pinhole only when the waists are superposed at P. This condition can be seen by observing the reflected beam off the beam splitter B.S., made of two microscope slides at right angles. When the mirror is adjusted to maximise this return beam the beam splitter can be removed from the beam; because of its construction this will not translate the laser beam sideways and so the alignment will be preserved while the loss which the beam splitter causes is eliminated. In practice removal of the beam splitter did not preserve the alignment perfectly and so the procedure followed was to leave it in place until the two-photon absorption signal had been observed,

and then when it was removed the signal was usually still visible, although reduced in size, and the signal could be maximized by adjustment of the mirror. The pinhole was made by plunging a fine needle into a stack of thin copper foils, and selecting the best pinhole with the aid of a travelling microscope. The pinhole selected was circular, with a diameter of 113 μm.

We now consider the focal lengths required for the lenses, using the theory of Gaussian beams (e.g. Kogelnik and Li, 1966).

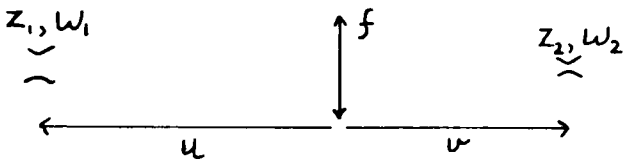


FIGURE 3.15

The result of this theory that we require is an imaging law in a lens for a waist size w_1 and confocal parameter z_1, with an "object distance" u, as shown in Fig. 3.15. This is

(13a) $$(v - f) = \frac{f^2(u-f)}{(u-f)^2 + z_1^2} \qquad (\underline{cf}.\ v - f = \frac{f^2}{u-f})$$

(13b) $$z_2 = \frac{f^2 z_1}{(f-u)^2 + z_1^2} = z_1\left(\frac{u-f}{v-f}\right)$$

(13c) or $$w_2 = \frac{fw_1}{\{(f-u)^2 + z_1^2\}^{\frac{1}{2}}} \qquad (\underline{cf}.\ \text{magnification} = \frac{f}{|u-f|})$$

where the equivalent results of Newtonian optics are given in brackets.

It is seen that the focal length f we require for lens A depends on the confocal parameter z_1 (or waist size w_1) of the laser beam. Now the laser has a waist at its end mirror, but its size, and hence z_1, depends on how the laser is adjusted. The beam divergence of the 580A laser was measured on two occasions, and found to be 0.55 ± 0.08 mrad and 1.1 ± 0.1 mrad

(semi-angle of divergence) which, with the results $w_1 = \lambda/\pi\alpha$, $z_1 = \lambda/\pi\alpha^2$ which are easily derived from equation 9, give

$$(14) \qquad \begin{aligned} w_1 &= 350\ \mu m \quad \text{or } 170\ \mu m \\ z_1 &= 63\ cm \quad \text{or } 16\ cm. \end{aligned}$$

The specification for the 580A laser quotes a typical value for the confocal parameter of 38 cm, giving a spot size of $w = 270\ \mu m$, but it is clear that there is considerable variation in these quantities as the laser is adjusted on different occasions, and so we should aim to make the final waist size and position independent of z_1. We can achieve this if $z_1^2 \ll (u-f)^2$; then the waist position is nearly independent of z_1, since then

$$(15) \qquad (v-f) = \frac{f^2}{(u-f)} - \frac{f^2 z_1^2}{(u-f)^3}$$

and so the second term is a small correction to the first term. If, in addition $u \gg f$, then the first term is very small also. The image spot size w_2 is, under these conditions, proportional to w_1, but w_1 is less sensitive to adjustment than z_1, as we can see from equation 14.

Thus we require the distance from the laser to lens A to be large compared with 40 cm; this was achieved by the location of the steel table and atomic beam in a room adjacent to the laser system, with $u \simeq 3.7$ m. With this value of u, and the required magnification $M = w_2/w_1$, we solve equation 13c for f

$$(16) \qquad f = \left(\frac{M^2}{1 - M^2}\right)\left[\left\{ u^2 + \left(\frac{1-M^2}{M^2}\right)(u^2 + z_1^2)\right\}^{\frac{1}{2}} - u\right] .$$

The range of values of w_1 and z_1 in equation 14, with $w_2 = 20\ \mu m$ and $u = 370$ cm, gives a range of values for f from 20 to 35 cm. We used a 20 cm lens, which errs, if anything, on the side of small w_2.

From this point on, the confocal parameter is very small (~2 mm) and we can use geometrical optics formulae to find waist positions and sizes. Lens B images the waist at P' onto P, the centre of curvature of the mirror M. The distance PP' was roughly $4f_B$ and so very little change in waist size occurred between P' and P. B was also a 20 cm lens. Two different mirrors were used, each coated for high reflectivity at 600 nm. The first had a radius of curvature of 25 cm; when the Babinet-Soleil compensators were introduced (as described in Chapter 4) there was insufficient space for the compensator between the window of the vacuum system and the mirror, and so the mirror was changed to one of 30 cm radius of curvature.

The lining up procedure is as follows. Initially all the magnetic bases are placed in position according to the nominal values of the focal lengths, and the laser adjusted so that it hits the centre of the mirror without passing through any components. Lens A is inserted and its transverse position adjusted until the laser beam again hits the centre of the mirror. The pinhole is then inserted and adjusted until the laser beam passes through it. The intensity transmitted by the mirror can be measured by a photomultiplier located behind it (this can be seen in Figs. 3.7 and 3.14) and so we can deduce, by taking measurements with the pinhole in and out, the fraction transmitted by the pinhole. I call this the "forward beam transmission"; when the pinhole is correctly located at the waist this is a maximum. Lens A is adjusted to maximize the forward beam transmission; the maximum value was unity, to within 2%.

By tracking lens A away from this position, the forward beam transmission can be measured as a function of distance. If we assume a Gaussian beam, and knowing the pinhole size, we can deduce the spot size. The intensity distribution is (from equation 9)

$$I \sim e^{-2r^2/w^2}$$

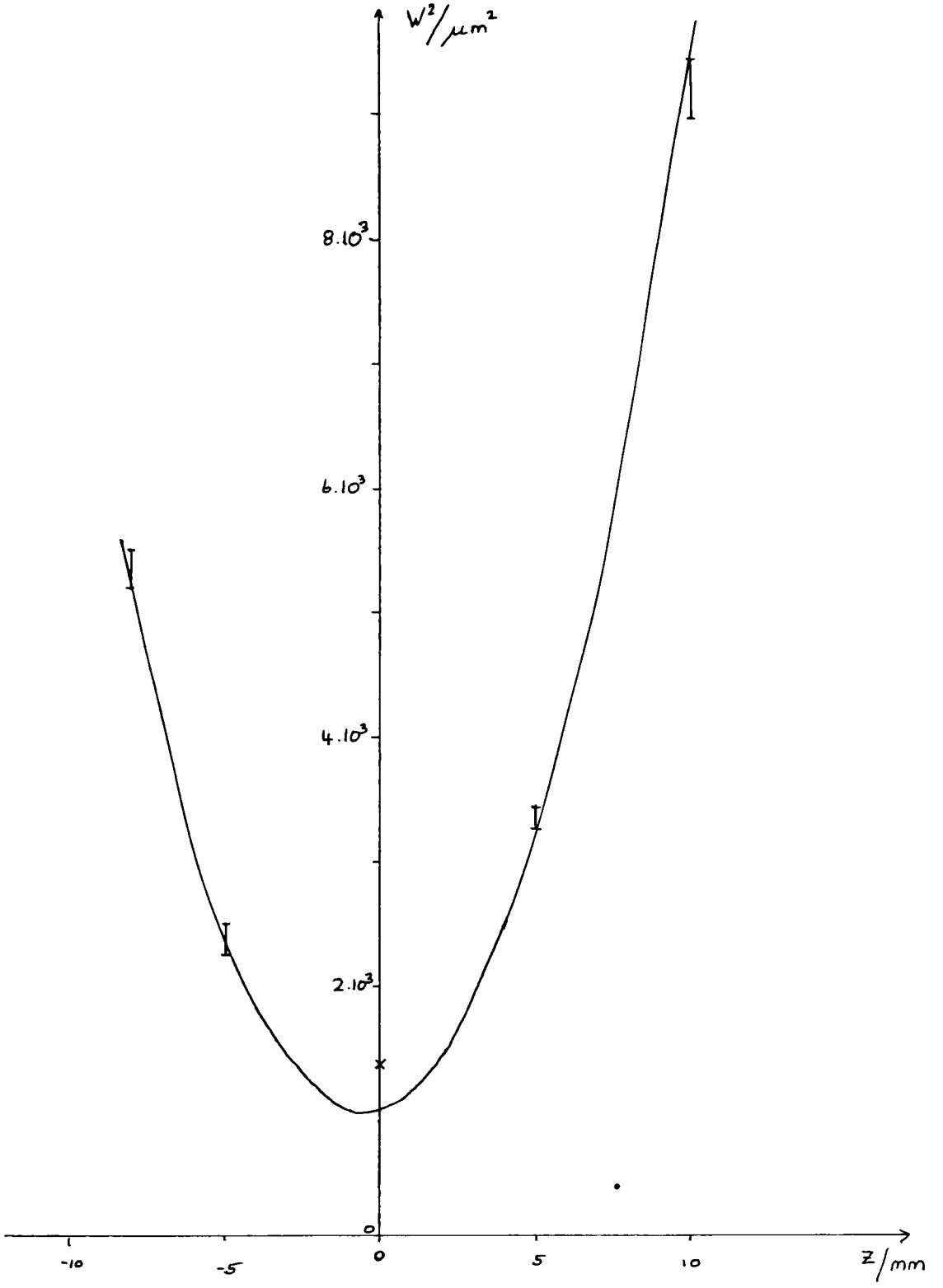


FIGURE 3.16 Laser beam Spot size near the waist

and so the fraction contained within a circle of radius R is

$$f \simeq \frac{\int_0^R e^{-2r^2/w^2} r\, dr}{\int_0^\infty e^{-2r^2/w^2} r\, dr} = 1 - e^{-2R^2/w^2}.$$

Thus

$$w = R \sqrt{\frac{2}{\ln(1/1-f)}} , \qquad R = 56.5\ \mu m.$$

$f > 0.99$ implies $w < 37\ \mu m$, which is thus the smallest value of w that can be measured using this method.

Position /mm	-8	-5	0	+5	+10
w /μm	73.1	48.8	37.4	57.9	96.0

(The origin is at 21.3 cm from lens A.) These values were measured, which are plotted in Fig. 3.16. As explained above the smallest w is probably an overestimate; the other four points are fitted to a parabola to compare with the theoretical relation

$$w^2 = w_2^2(1 + z^2/z_2^2) .$$

This gives

$$w_2 = 31\ \mu m$$
$$z_2 = 3.6\ mm.$$

These are not consistent - the measured value of the confocal parameter implies a spot size of 26 μm - but they do suggest that on this occasion at least the waist size was rather larger than the predicted value. This probably suggests that the output beam is not a perfect Gaussian lowest order

beam; any other beam will lead to a larger waist size.

The next part of the alignment is to put lens B in its correct position. The lens is required to image the waist at P' on the centre of curvature of the mirror, and so there are two locations of the lens which achieve this; we choose the position nearer the oven, which gives a magnification of less than one. The theoretical spot size is then even smaller than the w_2 ~ 15 μm predicted at P', but the actual spot size is probably nearer 20 μm, in the light of the above measurement of w_2.

The transverse position of lens B is determined by the requirement that the laser remain central on the mirror. The longitudinal position is fixed as follows: when the lens is at its correct position the returning beam is focussed to a waist in the plane of the pinhole, and if the mirror is correctly aligned it will pass through the pinhole, and part of its intensity is split off by the beam splitter and can be measured with a photodiode connected to a voltmeter. At any other position the returning beam is not correctly focussed, and less will get back through the pinhole. If we measure the ratio of the intensities of the beam off the beam splitter with the pinhole in and out, we measure the product of the forward beam transmission and the return beam transmission. The forward beam transmission is, as explained above, nearly unity, and constant, and so this ratio is essentially the return beam transmission. The form of this transmission as lens B is tracked along the laser beam is shown in Fig. 13.17. The two image positions are clearly visible, and the lens can be correctly located to about 0.5 mm. This last stage must be done with the vacuum system in position because of the additional optical depth of the two windows. The magnification can be found using the distance between conjugate points and the focal length; it is found to be 0.78. At this stage the lenses are forming a waist of the required size at the centre of curvature of the mirror. The oven is located underneath this point by checking that an optical pin placed over it is in no parallax with its image in the mirror, and the pinhole image in lens B.

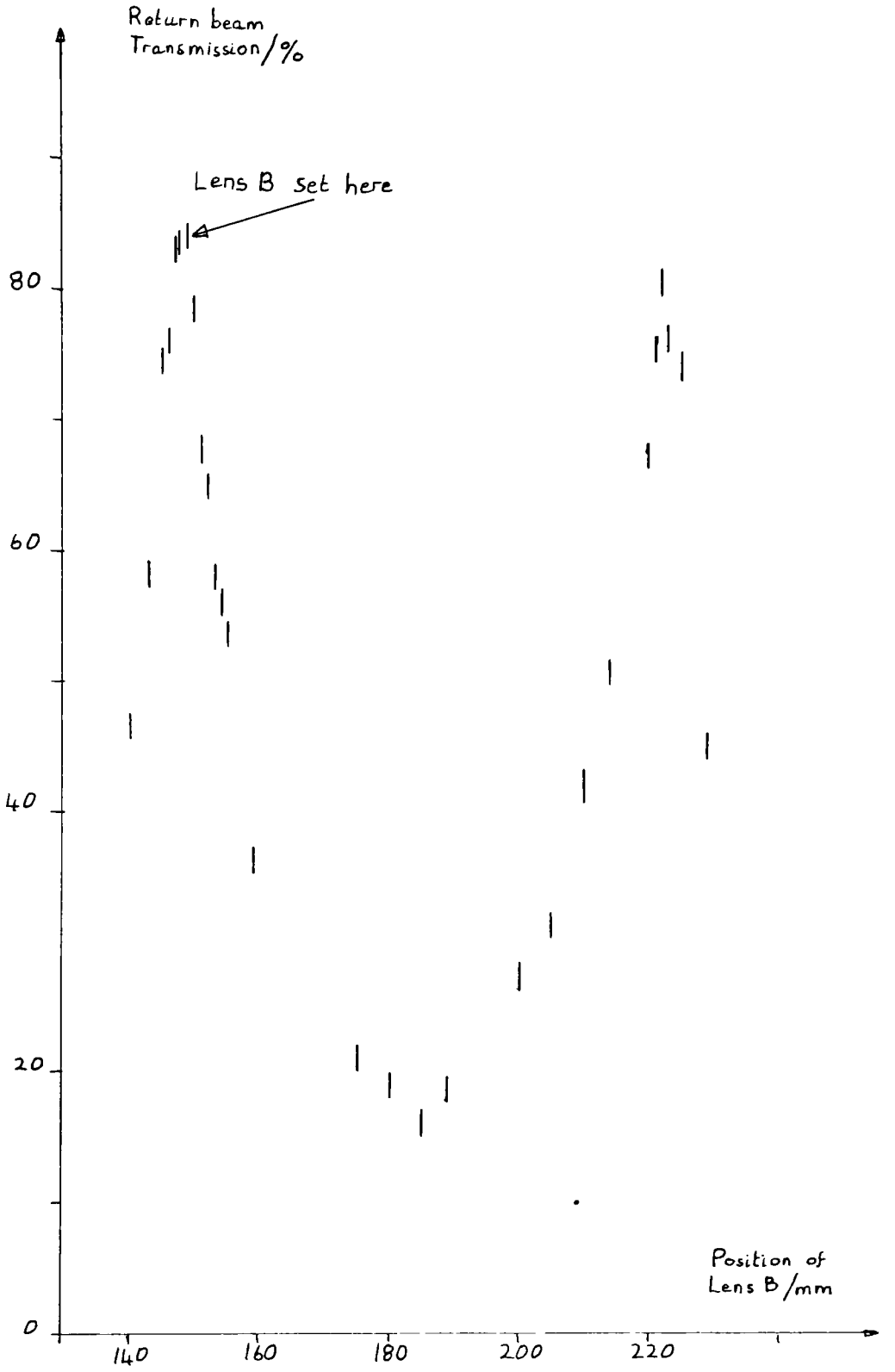


FIGURE 3.17 Return beam transmission as a function of the position of Lens B. This clearly shows the two positions of the lens at which the image of the pinhole is located at the centre of curvature of the return beam mirror. The chosen image position is marked.

I shall finally describe the procedure for loading the calcium into the oven. First the stainless steel vacuum can is placed in position and using the adjustments of tilt and rotation of the whole system, the laser beam is made to pass centrally through the two windows. As these are quite small this has to be done quite carefully. The can is then removed, the conical oven base is placed on its tripod support and the thermocouple located in its hole. The oven base is filled with calcium granules and the rest of the oven placed on top. The mirror is adjusted so that the return beam is lined up through the pinhole, and using only the vertical mirror adjustment the mirror is tilted down a small amount until the return beam touches the top of the oven. This line of light is used to line up the slit using the oven height and tilt adjustments, and a small amount of freedom to rotate the oven top on the conical base. The heater connections are then secured and the side and top heatshields put in place, taking care that the heatshield slit is lined up with the oven slit, and that the laser is passing close to the top heat shield, but not being obstructed by it. The heat shield was about 2 mm above the oven, and so the laser was usually at 3.5-4.5 mm above the slit. The can is then replaced, taking care not to knock the oven, and immediately evacuated so that the calcium does not oxidise in the air more than necessary. The vacuum system is then kept evacuated for the life-time of the charge of calcium, usually being about three working days at operating temperature.

3.7 Background Light

The first time the oven was heated to 600°C a blue glow was seen over the oven which saturated the photomultiplier. This was sufficiently bright to be seen in a spectrometer, which identified the light as the calcium resonance line. Subsequent examination showed that there had been

a discharge between the oven and the heatshield, because the heatshield had been at the potential of the positive heater connection. Thereafter the heatshield was separately earthed, and the heater negative connection earthed. When this earth connection was removed, or the positive connection earthed, the discharge could be switched on and off. I experimented with biassing the heatshield, but there was no further reduction in the background light. If the heaters were suddenly switched off, the remaining background light (or at least a significant part of it) decayed with a time constant of a few seconds, indicating that its origin was not electrical but due to stray light, either from the heaters or from the oven.

I compared the effect of three different methods of reducing this background light:

(i) A narrow band interference filter (20Å bandwidth) at 4227Å;

(ii) An extra OB10 colour filter;

(iii) Careful masking in front of the photomultiplier using an adjustable mask of two spectrograph slits at right angles, so that only the light from interaction region, and not the oven, reached the photomultiplier.

I found that at 600°C just (iii) produced the best signal-to-background noise ratio (I did the tests while the two-photon signal was displayed on an oscilloscope, measuring separately the two-photon signal and the background light under different combinations of (i), (ii) and (iii)). However, as noted above, at higher temperatures the background light rose faster than the signal, so that at a much higher temperature the conclusions would have been different; 600°C gave a sufficient signal for measuring all the stable isotopes in the natural mixture.

CHAPTER 4

THE LASER SYSTEM

4.1 Introduction

In this chapter I describe the laser system used in this work. Most of this system was designed and built by others and is described elsewhere (Brambley, 1978; Burnett, 1978). I shall therefore give only a brief description of the apparatus, emphasizing any changes that were made in the course of the work.

In section 4.2 I describe the dye lasers used in this work, and in section 4.3 the apparatus used to calibrate the laser scan. In section 4.4 I describe the remaining optical components, the Faraday effect isolator, and the Babinet-Soleil compensators used to eliminate the Doppler-broadened component, and the final section contains a description of the way the experiment was run, from setting the laser on wavelength to getting the data punched onto paper tape for computer analysis.

4.2 The Dye Lasers

Two dye lasers were used in the course of the experiment: a Spectra Physics 580-A dye laser, and a Coherent 699 ring dye laser. The ring laser became available after a lot of data had been taken with the 580-A laser, and with its increased power it enabled us to measure the isotope shift of ^{46}Ca, which because of its low abundance was not visible on the earlier runs.

Both dye lasers were pumped with a Spectra Physics 141 Ar^+ laser, operating at about 5 W output for the 580-A dye laser, and a rather higher

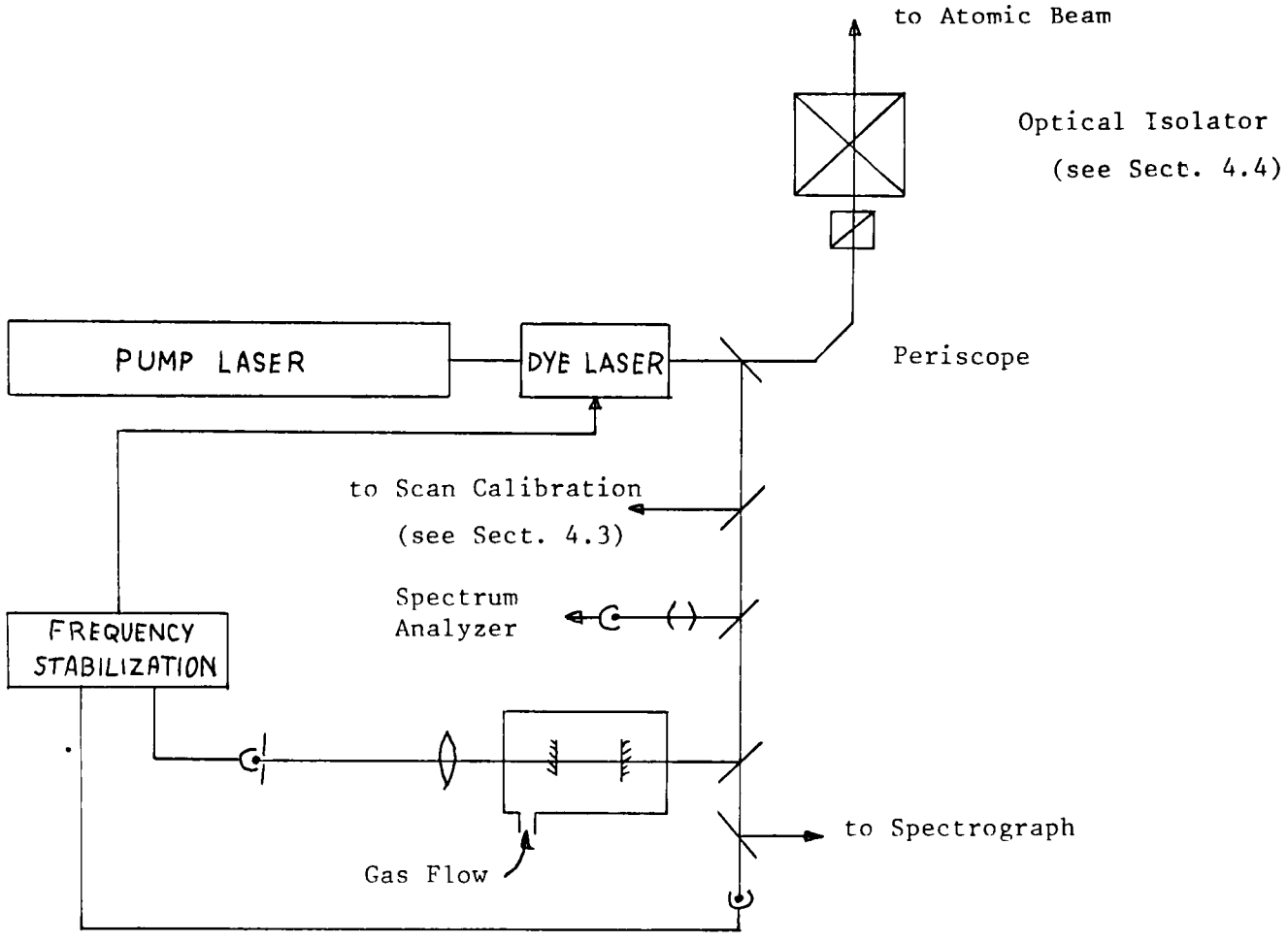


FIGURE 4.1 The Dye Laser System

power of 8-9 W for the ring laser. The dye lasers were operated with the dye Rhodamine 6G; the required wavelength of 600 nm is close to the peak of the R6G gain curve for a standing wave laser. Ring lasers have been found to have their gain curves "blue-shifted", and so for the ring laser the peak of the gain curve is around 570 nm; the output power at 600 nm is about 50% less than at the peak.

The 580-A laser is of the three-mirror, jet-stream type, with cavity modes separated by 390 MHz. An intra-cavity air-spaced etalon with free spectral range 75 GHz selects a single cavity mode for laser operation, and an external lock circuit controls the etalon spacing piezo-electrically to match this etalon mode correctly to the cavity mode. A solid etalon with free spectral range 1500 GHz selects a single air-spaced etalon mode; the solid etalon is tuned, to match its mode to the air-spaced etalon mode, by tilting. The correct solid etalon mode is selected by an interference filter of which the half-wavelength layer is in the form of a wedge so that the pass-band of the filter can be tuned by moving the filter transverse to the laser beam.

The equipment used to stabilize, monitor and scan the laser is shown in Fig. 4.1. The laser is locked to an external 12 cm plane etalon; this reduces the frequency jitter of the laser to give it a linewidth of about 4 MHz, by controlling the length of the laser cavity using the output mirror, which is mounted on a piezo-electric ceramic mount. • By pressure scanning the etalon the laser can be made to scan slowly in frequency up to 4 GHz. The etalon chamber was evacuated and air was admitted through a constant flow valve.

All these components were mounted on a marble table which could be floated on air bearings. However, when floated, the table gradually settled, and because the reflection of the laser back into the atomic beam is a very critical adjustment, owing to the very small size of the laser beam, any movement of the marble table would have to be compensated by continuous re-

adjustment of the mirror. For this reason the table was not floated, which meant that the laser was susceptible to vibration transmitted from the floor. There were three important sources of vibration:-

(i) The pumps which circulated cooling water to the pump laser and dye to the dye laser; these were mounted on foam or piles of cloth, and surrounded by cardboard baffles to reduce airborne noise.

(ii) The apparatus is situated in the basement of the Laboratory, and water used in the basement (including of course the laser cooling water) drains to a tank which is periodically emptied. The pump which does this is situated at the end of the corridor, and while the tank is being emptied there is significant vibration, which seriously affects the laser stability. Fortunately the tank empties only about twice a day (depending on water usage in the basement) and it takes only about ten minutes each time, so no data is taken during this period.

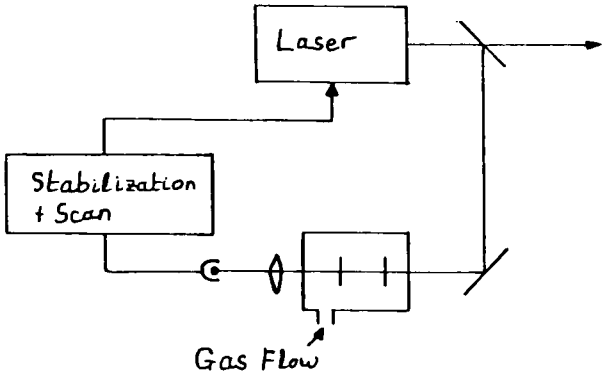
(iii) People moving about during a run were liable to cause the laser to "jump" out of its locked state. Most of the data was taken with only myself in the room, and always care had to be exercised during a run, and all movement had to be quiet.

The limitation on the power output of the standing wave laser is the suppression of the adjacent longitudinal cavity mode. This is because a standing wave does not deplete the gain in the dye uniformly along its path, but with a series of antinodes, where the gain is depleted, and nodes where the gain is not utilized. This means that some other mode whose nodes and antinodes do not coincide with those of the mode that is lasing has some gain available to it. However because all the etalons in the laser are lined up so that the lasing mode is at the peak transmission of all etalons, one might think that this would suppress all other cavity modes. In practice, modes a long way away in frequency are effectively suppressed, but suppression

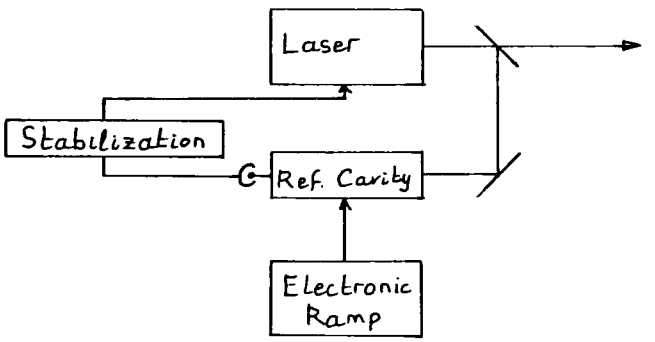
of the adjacent cavity modes comes only from the air-spaced etalon, since the other etalons have much larger transmission bandwidths. Thus the laser will start to operate on these modes when there is sufficient gain at the nodes of the lasing mode for it to do so. This limits the single mode power to about 30 mW.

The wave in the cavity of a ring laser is a travelling wave and so the problem is completely eliminated. Even with no tuning elements in a ring laser except a Lyot filter to select a particular part of the dye tuning range, a ring laser will still operate single mode, although in these conditions it will hop from mode to mode fairly quickly. This means that much higher power can be obtained because there is very little tendency for the adjacent mode to operate. We were able to get about 250 mW of single mode power, pumping at 9 W, using all the visible Ar^+ lines. The pumping is more efficient using just the green 514.5 nm line, but we were unable to get sufficient power on this line alone with our pump laser.

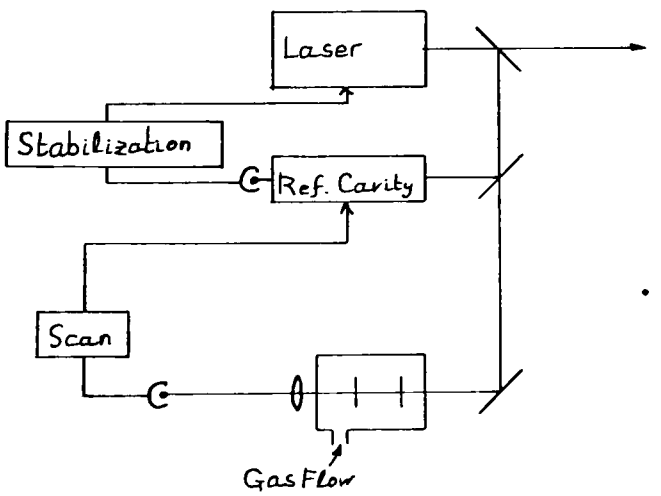
The Coherent 699 ring laser comes supplied with a temperature stabilized external cavity and control electronics which will lock the laser to a mode of this cavity; the length of the laser cavity is controlled by two elements: a parallel-sided glass plate mounted on a galvanometer, which can be tipped about Brewster's angle, providing large, slow (< 10 Hz) length changes, and a small, piezo-electrically mounted mirror which provides small high frequency (up to 2 kHz) length changes. There is also a facility for electronically scanning the laser by applying a ramp of adjustable size and speed to a similar plate mounted in the reference cavity. Thus unlike the Spectra Physics laser, the ring laser as supplied can be scanned while it is stabilized with reference to an external cavity. However we found that the available scan speeds were all too fast and so we used the same system of putting part of the laser light through the plane etalon and locking the laser to the etalon. Because the laser was already stabilized, this lock circuit was really being used simply to supply a slow ramp; the output of



Spectra-Physics 580 A Laser.



Coherent 699 Ring Laser. Electronic Scan.



Coherent 699 Ring Laser. Pressure Scan.

FIGURE 4.2 Comparison of the Stabilization and Scanning of the two Lasers.

the lock circuit was fed back to the tipping plate in the reference cavity of the ring laser. The stabilization and scanning of the two lasers are compared in Fig. 4.2.

4.3 Calibration of the Scan

As shown in Fig. 4.1, part of the output of the laser is split off for the purpose of calibrating the frequency scan, and it is to this that we now turn. The apparatus is shown in Fig. 4.3; light from the laser passes through a 2 m confocal cavity, and the transmission of the cavity is recorded by a photodiode. The output of the photodiode is smoothed and digitized before being recorded on paper tape in the same way as the photomultiplier signal described in section 3.5. The cavity is stabilized against drift and vibration by locking it to a helium-neon laser whose frequency is locked by the method of saturated absorption to a hyperfine component of the I_2 spectrum at 633 nm.

The scan calibration is of great importance in establishing the overall accuracy of measurement, and I shall discuss various aspects of this part of the apparatus in order to show that our calibration is correct. Firstly I consider the I_2-stabilized He-Ne laser. This is built to an N.P.L. design, and uses the third-derivative locking technique described by Wallard (1972). This involves modulating the length of the laser, and hence its frequency, at a modulation frequency ν. The intensity of the laser will also show modulation due to both the variation of the neon gain curve over the amplitude of modulation and, in the vicinity of one of the I_2 hyperfine components, the change in saturated absorption. The output of a phase-sensitive detector with a reference frequency of 3ν is proportional to the third derivative of the intensity with respect to frequency. This derivative contains very little contribution due to the gain curve, while having a large

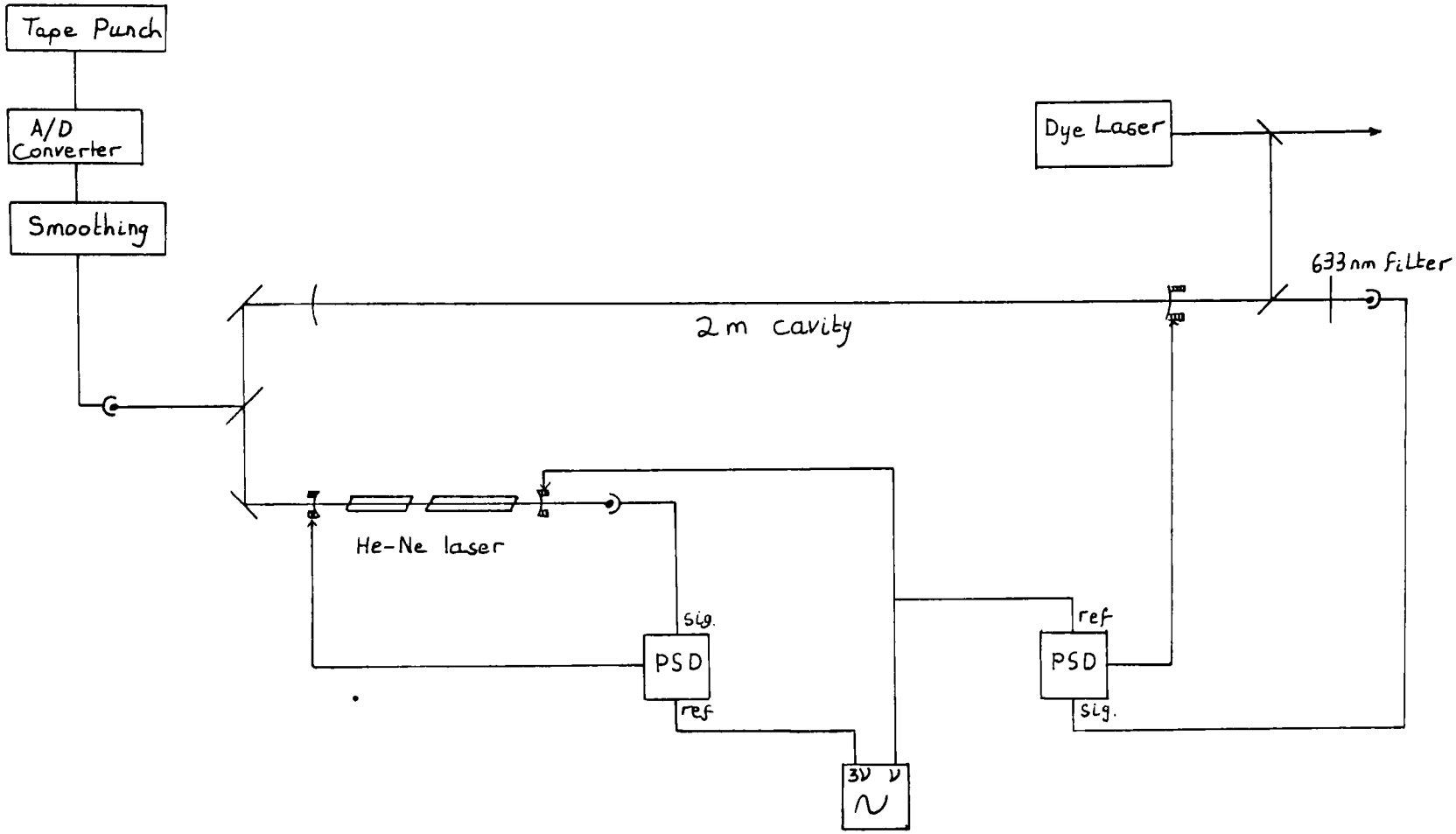
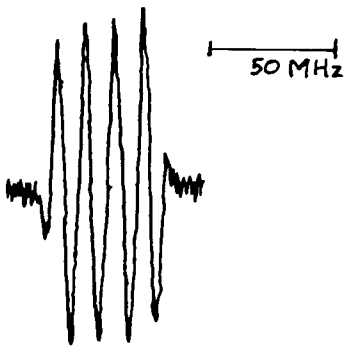


FIGURE 4.3 The Calibration of the Laser Scan.

contribution from the narrow absorption feature which crosses zero at line centre. It is to this zero that the laser is locked. In experiments at the N.P.L., two lasers locked to different hyperfine components showed a variance in their beat frequency, for integration times from 5 ms to 5 s, of around 100 kHz (Wallard, 1972) which is therefore an estimate of the frequency jitter of these lasers. We can estimate the jitter of our laser when locked by looking at the error signal in the feedback loop controlling the laser frequency, and comparing it with the third derivative signal when the unlocked laser is scanned between hyperfine components (see Fig. 4.4).

FIGURE 4.4



Third derivative of intensity

If the peak third derivative signal is $\pm V_o$, and the error signal when locked is of order $\pm V$, then the frequency jitter is

$$\Delta\nu \sim \frac{V}{V_o} \Delta\nu_I$$

where $\Delta\nu_I$, the separation of the hyperfine components, is 13 MHz. This formula also indicates that the frequency jitter is well under 1 MHz.

The optimum amplitude of frequency modulation was found by Wallard to be 6 MHz; we also used a modulation of about this size. Thus the output of the He-Ne laser is a frequency-modulated wave, whose centre frequency is stable to well under 1 MHz. It should be noted that the absolute frequency of the He-Ne laser is not important, only its frequency stability. In fact the absolute frequency is also well-known, and it shows pressure shifts, especially if water vapour is present with the iodine. However, this is of no concern in this application.

When this laser is directed into the 2 m cavity, unless the two cavities are very carefully isolated the error signal of the He-Ne frequency servo loop gets larger, indicating increased frequency jitter. For the first

two sets of runs, with the 580-A laser, isolation was achieved with a quarter-wave plate optical isolator. The theory of this isolator is as follows. Let the polarization of the laser beam, propagating in the z-direction, be $a\hat{x} + b\hat{y}$, which we write as a column vector $\begin{pmatrix} a \\ b \end{pmatrix}$. Then the action of any optical component on the polarization can be represented by a matrix (the Jones matrix) operating on this vector. (For a fuller description of the Jones matrices see, for example, Hecht and Zajac, 1974, Chapter 8). The isolator consists of a linear polarizer, which we can take as defining the x-axis, and a quarter-wave plate with its slow and fast axes at 45° to the x-axis, shown diagrammatically in the upper part of Figure 4.5.

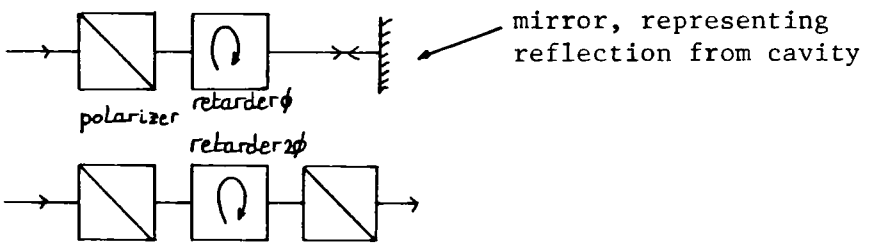


FIGURE 4.5

Thus the Jones matrices we require are those for polarizers and retarders, which are given in the Table below. A matrix for a rotated com-

TABLE 4.1. Jones Matrices for Polarizers and Retarders

Component	Jones Matrix
Polarizer, transmitting direction along x-axis	$\begin{pmatrix} 1 & 0 \\ 0 & 1 \end{pmatrix}$
Polarizer at angle α to x-axis	$\begin{pmatrix} \cos^2\alpha & -\cos\alpha\sin\alpha \\ -\cos\alpha\sin\alpha & \sin^2\alpha \end{pmatrix}$
Retarder, angle ϕ, fast axis along x-axis	$\begin{pmatrix} e^{-i\phi/2} & 0 \\ 0 & e^{i\phi/2} \end{pmatrix}$
Retarder, angle ϕ, fast angle at α to x-axis	$\begin{pmatrix} \cos\phi/2-i\cos2\alpha\sin\phi/2 & i\sin2\alpha\sin\phi/2 \\ i\sin2\alpha\sin\phi/2 & \cos\phi/2+i\cos2\alpha\sin\phi/2 \end{pmatrix}$

ponent $M(\alpha)$ is found from the matrix for the unrotated component $M(0)$ using

$$M(\alpha) = R(\alpha)\, M(0)\, R(-\alpha)$$

where $R(\alpha) = \begin{pmatrix} \cos\alpha & \sin\alpha \\ -\sin\alpha & \cos\alpha \end{pmatrix}$ is a rotation matrix.

The sign of α is such that a rotation from the y-axis to the x-axis is positive. We have also to establish a convention for reflection, which is that the x and y axes, and hence the polarization vector, remain unchanged. This convention means that the matrices for birefringent materials are the same for light propagating in the +z and -z directions. (The same is not true for the Faraday effect, because the optical properties then depend on the direction of propagation along a given line.)

Hence the two passages through retarder ϕ at angle α are equivalent to a single passage through a retarder 2ϕ at angle α, and so the components shown in the upper part of Fig. 4.5 are equivalent to those shown in the lower part of Fig. 4.5. Thus the matrix for two passes through the isolator is

$$\begin{pmatrix} \cos\phi - i\cos 2\alpha \sin\phi & 0 \\ 0 & 0 \end{pmatrix}$$

and so if the initial polarization vector is $\begin{pmatrix} a \\ b \end{pmatrix}$, the fraction of the intensity transmitted by the isolator is

(1) $$|a|^2(1 - \sin^2 2\alpha \sin^2\phi).$$

The output of the laser is linearly polarized, so if the transmission axis of the polarizer is parallel with this axis, $|a|^2 = 1$. Putting $\alpha = \pi/4 + \delta\alpha$, $\phi = \pi/2 + \delta\phi$, we find the fractional transmission is $4\delta\alpha^2 + \delta\phi^2$.

If we take into account the imperfection of the polarizer, which trans-

mits a fraction f of the polarization it is meant to block, the fractional transmission of the isolator is

$$4\delta\alpha^2 + \delta\phi^2 + f \quad . \tag{2}$$

Various sorts of imperfection will be represented by this expression - for example, incorrect thickness of the retarder, and the optic axis of the quartz not lying exactly in the surface. The quarter-wave plate is of the temperature-compensated type, consisting of two plates of quartz with the fast axis of one aligned with the slow axis of the other, the difference of whose retardation is $\lambda/4$ at the required wavelength. Imperfect alignment of the fast and slow axes of the two plates is also represented by equation 2, but any stray reflections which happen to lie along the same axis are not.

For a good crystal polarizer $f \sim 10^{-6}$ and the specification for the quarter-wave plate was $\delta\phi < 0.01\pi/2$ so that provided we can set α to about $\frac{1}{2}°$ we can get rejection of one part in 10^3.

In fact the isolator never performed as well as this, and after it became clear that the calibration of the laser scan was limiting the accuracy of determination of the isotope shifts, due to instability of the long cavity, this was further investigated. We found that the optical isolation of the 2 m cavity was inadequate, and optical feedback from this cavity to the He-Ne laser was causing increased jitter. This was found to be due to destruction of the circular polarization of the laser in the 2 m cavity, most of which was due to internal reflections in the 2 m cavity end mirror. When a beam expander was placed between the He-Ne laser and the isolator, the expanded beam in the cavity had a pattern of parallel fringes across it due to these internal reflections, and the same fringes could be seen in the light transmitted by the polarizer back to the laser. Thus the destruction of circular polarization was preventing the isolator from achieving the required rejection, and this feedback, by perturbing the He-Ne laser, was affecting the calibra-

tion of the dye laser scan.

It was found that the solution to this problem was to leave the beam expander situated between the He-Ne laser and the optical isolator. The effect of this change was to make the return beam from the optical isolator to the laser very diffuse, and thus to minimize further the perturbation to the laser. The calibration of the third set of runs, taken with the ring laser, is substantially better than that of the earlier runs taken with the 580-A laser; some of this improvement is undoubtedly attributable to the improved dye laser stability, but some may also be due to the improved stability of the He-Ne laser as a result of this change.

The 2 m cavity was locked to the He-Ne laser by using the laser's frequency modulation. This modulation produces modulation in the transmitted intensity of the He-Ne laser through the cavity, which is detected by a photodiode. Phase-sensitive detection, using the modulation frequency as a reference produces an error signal which is zero when the mean laser frequency is at a maximum of transmission of the 2 m cavity. The same sort of estimate as for the jitter of the He-Ne laser, based on the error signal in the feedback loop, can be made for the vibration of the long cavity; it is found to correspond to a vibration of one fringe with an amplitude of about 0.3 MHz at about 100 Hz, and so, when the integration over the time between measurements of the transmission of the cavity (0.4 s) is taken into account, the effective jitter is very small.

We have assumed, up till now, that the only change in the dye laser beam entering the 2 m cavity, as the laser is scanned, is its frequency, and so the time between maxima of transmission of the cavity is an accurate measure of the time taken for the laser to scan its mean frequency by one free spectral range. In fact the laser beam could also change the angle at which it enters the cavity, and this could also lead to a change in fringe number. For a plane etalon followed by a lens, provided that all the light in the focal plane is detected, the number of fringes N observed while the

laser frequency changes by $\Delta\nu$ and the square of the angle between its propagation direction and the normal to the plates changes by $\Delta\theta^2$, is

$$N = \frac{\Delta\nu}{\nu_{fsr}} - \frac{\Delta\theta^2}{\theta^2_{fsr}}$$

where $\nu_{fsr} = c/2L$ and $\theta^2_{fsr} = \lambda/2L$. For a symmetric confocal cavity however (that is one for which the mirror radii and the length satisfy $R_1 = R_2 = L$) this second order effect is zero, or θ^2_{fsr} is infinite, and it is easy to show that any fourth order effect, given the sizes of the input and output apertures of the cavity (2 mm diameter) would be negligibly small. The other special property of the symmetric confocal cavity is that its free spectral range is given by $\nu_{fsr} = c/4L$, due to the fact that a geometrical ray makes two round trips before returning to its original position. (For a discussion in terms of Gaussian optics see, for example, Kogelnik and Li, 1966.) This property is shared by a more general class of confocal cavities for which $R_1 = L$ but $R_1 \neq R_2$. These cavities do not, however, show the vanishing second order effect of the symmetric confocal cavity. It is however smaller than that for the plane etalon by a factor of order $(R_1-R_2)/L$, which is sufficient to make it negligible.

Other departures from the symmetric confocal condition would lead to asymmetry of every other fringe, and shift of their centre of gravity. Such an effect is certainly less than the random scatter of fringes, which is about 50 kHz on the best runs. The centres of gravity of the calibration fringes can thus be taken as a true measure of the frequency of the laser. The question of how we interpolate between fringes to find the frequency of the laser at all times is taken up in Chapter 5.

4.4 Other Optical Components

In the same way that reflection from the 2 m cavity would affect the

locking of the helium-neon laser, if the two were not isolated, the reflection from the return beam mirror will perturb the dye laser if the atomic beam part of the experiment is not isolated from the laser. In fact this isolation is even more critical than the former, since the laser beam is reflected and re-focussed by the return beam mirror, and so when the alignment is perfect the laser beam is actually re-focussed back into the laser. A quarter-wave plate isolator of the type described in section 4.3 is not applicable here, since the circularly polarized beams would give rise to no signal, as described in Chapter 2. An optical isolator based on the Faraday effect is therefore used.

This consists of a polarizer followed by a cylinder of glass suspended in a magnetic field, in which the plane of polarization of the light is rotated by 45° by the Faraday effect. On return the polarization is rotated by a further 45° and stopped by the polarizer. We found that the ends of the glass rod, as supplied, were accurately parallel, leading to etalon-type interference effects, which reduced the effectiveness of the isolator, because the polarization was no longer uniform over the laser beam, and so a good extinction of the return beam could not be obtained. To counteract this the rod was tilted so that the reflections from the end faces did not overlap the beam, and so could not interfere with it. This further reduced the aperture of the rod, which had a diameter of only 8 mm, so that the alignment of the laser beam such that it passed cleanly through the isolator required care. The laser beam was raised by a periscope from the level of the laser to that of the Faraday isolator and the atomic beam, and it was necessary to have both tilt and vertical translation adjustments on the periscope mirrors in order to achieve the correct alignment.

A magnet current of about 2.1 A was required to give 45° rotation of the polarization; this was set by adjusting the current while observing the beam transmitted by the polarizer on a card. As the magnet coils heated up slowly their resistance changed, and it was necessary to check the extinction

of the return beam periodically.

The two-way beam splitter described in section 3.6, because it is an off-axis optical element, introduces slight elliptical polarization, and also some non-uniformity of polarization due to interference. The magnet current was therefore set with the beam splitter removed; when it was re-inserted in order to line up the return beam mirror, the isolation was thereby reduced, but the laser stability was not affected sufficiently to prevent the signal being found. When the signal had been found the beam splitter could be removed again, thus restoring the isolation.

The elimination of the Doppler-broadened component of the two-photon absorption by circularly polarizing the laser beams was described in Chapter 2. This was not done in the initial stages of the experiment, but after the installation of the ring laser it became necessary in order to observe the rare isotope ^{46}Ca, as explained in section 4.5 below. This was effected by installing two Babinet-Soleil compensators (BSCs) set to be quarter-wave plates, one between the pinhole and lens B, and one between the atomic beam and the return beam mirror. I shall now describe the method of alignment used for these BSCs.

We recall from section 4.3 that if linearly polarized light is put into a retarder ϕ with the fast axis at an angle α to the axis of polarization, a fraction $(1 - \sin^2 2\alpha \sin^2 \phi/2)$ emerges with the initial polarization, and a fraction $\sin^2 2\alpha \sin^2 \phi/2$ with the orthogonal polarization, and that if the retarder is placed in front of a mirror so that the light passes through it twice, the effect is just to double the retardation. Thus if the Faraday isolator is set to extinguish the return beam with no retarder, and then a BSC is inserted, the extinction will not be complete, but a fraction $\sin^2 2\alpha \sin^2 \phi$ will be transmitted, and so for any rotation angle α, nulls will be observed when the retardation angle is 0, π, 2π, etc., i.e. when the retardation is zero, $\lambda/2$, λ, etc. By noting the micrometer readings for these nulls, the $\lambda/4$ position that is required can be estimated by interpolation. This was

done for both BSCs separately.

The BSCs were of different manufacture; one was manufactured by Melles Griot and had a micrometer adjustment to set the retardation and a continuous rotation adjustment with no angular scale. The second was manufactured by Special Optics; it also had a micrometer adjustment for retardation and continuous rotation adjustment, but it had in addition a facility for rotating the compensator in steps of 45° once the continuous adjustment had been set.

With both BSCs approximately set as $\lambda/4$ plates at the appropriate wavelength, the final setting was found as follows. The magnet of the Faraday isolator was switched off and the Special Optics BSC inserted. This, together with the polarizer of the Faraday isolator, make up a quarter-wave plate isolator of the type discussed in section 4.3, and for this the fast axis is required to be at ±45° to the incident plane of polarization; thus by rotation of the BSC we find nulls at these positions. The transmission of the isolator, as discussed above, is $4\delta\alpha^2 + \delta\phi^2$, and so by iterative adjustment of the rotation and retardation separately, the best null was found. The Faraday rotator was then switched on; when the rotation is 45° we find another null, because then the incident plane of polarization is parallel to the fast or slow axis of the BSC, which thus has no effect on the polarization, and we see the usual Faraday isolator operation. The first BSC was finally rotated by 45°, using the stepped rotation mount, and was then correctly set both in rotation and retardation.

The second BSC, set approximately as a quarter-wave plate, was then inserted between the vacuum system and the return beam mirror. The rotation of this BSC is not significant (it simply rotates the plane of polarization of the beam on the mirror) and so the only remaining adjustment is to make any small necessary changes to the retardation of the second BSC to produce extinction of the return beam. This procedure ensures that the polarization of the laser beams in the interaction region is accurately circular, and that

the isolation is maintained.

After this alignment procedure the longitudinal positions of the lenses were adjusted to focus the laser correctly, as described in section 3.6. The effect of the Babinet-Soleil compensators used in this way was to reduce the intensity of the Doppler-broadened background by a factor of about 70; this will be shown in Chapter 6.

4.5 The Method of Running

In this section I shall describe the procedure that was used for the taking of data. Here, and subsequently, a set of runs refers to a number of runs taken over a period of a few weeks with little change to the apparatus during that time. Three such sets were taken, in January-March 1980, June-July 1980 and January 1981; the first two used the 580-A laser and the third set the ring laser.

Before each set of runs the lenses were aligned as described in section 3.6; the data shown in Fig. 3.17 were taken during one such alignment, on 17th January 1980. This alignment was checked each day before taking data by measuring the return beam ratio, which checks the entire longitudinal alignment, apart from the location of oven slit under the beam waist. No change was usually necessary, unless an optical component had been accidentally moved.

The oven was loaded with calcium and aligned under the laser beam as described in section 3.6, and the vacuum system left pumping overnight. The following morning the oven heaters were started; the oven took about an hour to reach operating temperature, during which time the laser was switched on and set on wavelength.

The setting of the laser on wavelength was of crucial importance. In outline, the method used was first to set the laser wavelength as close as

possible to the required wavelength using a spectrograph, and then systematically scan the laser until fluorescent light, indicating two-photon absorption, was seen. The spectrograph had a grating with 600 lines mm^{-1}, and was used in a 3 m autocollimation mounting, giving a dispersion of 1.5 Å mm^{-1} in the focal plane. This was calibrated using neon spectral lines, and the required wavelength found by calculating the offset from a spectral line of caesium at 6010 Å. By this means the laser could be set to within about 0.2 Å of the required wavelength, or about 20 GHz.

At this point it was necessary to scan the laser repeatedly, using an electronic scan while observing the output of the photomultiplier on a synchronously triggered oscilloscope. With the ring laser this was comparatively straightforward, since its power was sufficient to give rise to a detectable signal on a single scan, lasting 250 ms, over its full scan range of 30 GHz from the Doppler-broadened component of the signal. This meant that the laser could be set to the required wavelength before the careful alignment of the return beam mirror, which alignment was then made very easy, as the laser could be set to scan repeatedly over the region of the Doppler-broadened component, and the return beam mirror adjusted to maximise the Doppler-free component, seen as a sharp spike at line centre on an oscilloscope next to the atomic beam displaying the photomultiplier output.

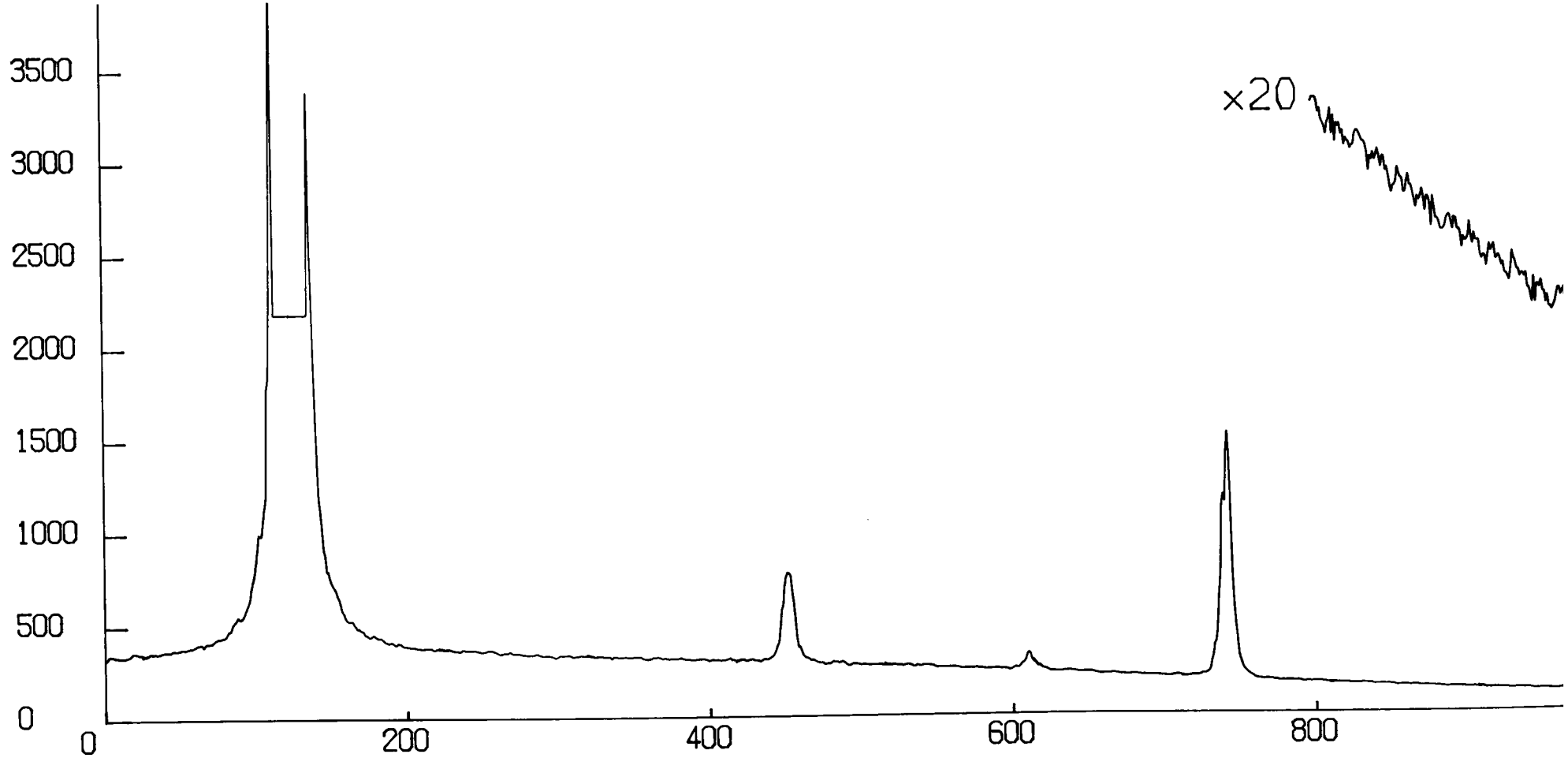
However, with the 580-A laser, the signal was not large enough to be found in this way. The Doppler-broadened component was too broad and of too small an amplitude to be easy to observe on an oscillosope, in comparison with the background noise. It was therefore necessary for the return beam to be correctly aligned without the signal present, using the pinhole as described in section 3.6. The Doppler-free signal is, by comparison, very narrow, and so if the laser scans too rapidly over it, there is not sufficient scattered light to be detected against the background noise. It is convenient to observe a stable oscilloscope trace, which requires a scan repetition rate of at least 5 s^{-1}, and it was found that the requirement that the scan be

not too rapid limited the scan width at this repetition rate to about 1 GHz. The central frequency of the scan window is changed in steps of one cavity f.s.r. or about 0.4 GHz, and so the scan window must be larger than this to prevent the possibility of stepping over the signal without observing it. Thus the scanning conditions were constrained by these considerations, and the 1 GHz scan window had to be moved slowly through the 20 GHz uncertainty in frequency in order to find the signal.

Once the signal had been found the pinhole and two-way beam splitter were removed, and the signal maximized by careful adjustment of the return beam mirror. After a few scans to establish gain settings, the data could be taken onto paper tape. After one or two runs, the laser was re-adjusted to maximize its power, and various consequential adjustments to the optical alignment made. One day's running usually amounted to 6-10 runs.

Typical data recorded on paper tape are shown in Figs. 4.6 - 4.8. In each case the upper curve is the intensity transmitted by the 2 m cavity, and the lower curve the fluorescent light recorded by the photomultiplier. The horizontal axis is labelled with channel numbers; that is the n^{th} data point of the scan is labelled by channel number n. Fig. 4.6 shows a run taken with the 580-A laser, and Figs. 4.7 and 4.8 runs taken with the ring laser. These latter runs illustrate two points about data taken with the ring laser. Fig. 4.7 was taken before the installation of the circular polarizers, and shows that the noise due to the Doppler-broadened component (originating ultimately in intensity fluctuations of the laser) is sufficient to swamp the isotope ^{46}Ca, with a predicted intensity of about 1/60 of the ^{48}Ca peak at the extreme lefthand end of the trace. (This was an early trial run and the 2 m cavity was not being used and so there are no calibration fringes.) The effect of eliminating the background is shown in Fig. 4.8, where the expanded section shows the noisy but quite definite peak of ^{46}Ca.

The second point is that it would be impossible to observe ^{40}Ca on


3500
3000
2500
2000
1500
1000
500
0
0
200
400
600
800
×20

the same run as ^{46}Ca because of their very different intensities (the truncated peak of ^{40}Ca is visible on the righthand end of the trace.) In fact, because of the necessity of measuring the smaller isotopes ^{43}Ca and ^{48}Ca, and in particular ^{46}Ca, which are all noisy or invisible on runs taken with the 580-A laser, none of the third set of runs, taken with the ring laser, includes a measurement of the position of ^{40}Ca. The isotope shift of ^{40}Ca from the other isotopes is thus entirely determined from the earlier runs taken with the 580-A laser.

CHAPTER 5

COMPUTER ANALYSIS OF RESULTS

5.1 Introduction

The data was recorded on punched paper tape as a sequence of numbers; in this chapter I describe how this sequence of numbers was turned into isotope shifts. Much similar computer analysis has been done in this research group in recent years (see e.g. Thompson, 1981, Brambley, 1978, Burnett, 1978, Malvern, 1974) and I benefitted greatly from the experience gained by these workers. However all the programs described in section 5.3 onwards were written by myself; this was because all the previous work had been done on the University's ICL 1906A computer, which was being withdrawn from service at about the time this work started. I used the ICL 2980 computer which replaced the 1906A, and all the programs were re-written for this computer in FORTRAN. I shall tend in what follows to emphasize what is new in my method of analysis and so stress the differences between it and previous work done here.

A small number of runs were analysed by Richard Thompson using a modified form of the program he wrote for fitting spectra of neon and so I shall describe in section 5.2 the fitting procedure he used, and in section 5.3 discuss why it was thought desirable to modify it. In section 5.4 I describe the plotting and calibration programs and in section 5.5 how the revised fitting procedure was implemented. For reasons discussed there I also had to use a different fitting routine, which I compare with other routines that have been used. In section 5.6 I describe the function generating subroutine used in the fitting program.

The running of all the programs to be described in this chapter was

made very easy by utilizing 'macros'. These are essentially files which are read by the computer when their name is given to it, which contain all the system control commands necessary to run a program. At the time at which the macro is called it can be given values (numerical or otherwise) of parameters needed either in the system control commands, or by the program.

For example, to run the calibration program for a run with index number 228, a card CACAL(228) is typed, where CACAL is the macro name. In this example, several other parameters apart from the run number will be given default values, which could be changed by adding more numbers after the first. The run number is a mandatory parameter, that is, it has no default value.

Apart from convenience, the major benefit of using macros is to remove the risk of a certain type of human error. To continue the above example, the output of the program, to be used to calibrate run 228, will be automatically stored in a file called CAL.CA228, with the same reference number, and this file can only be used to calibrate this run. If the names of the data file and calibration file had to be given in separate instructions, a typing error could lead to a serious mistake. Most typing errors in calling macros were detected by various error traps in the fitting program, or led to obviously nonsensical results.

5.2 Analysis of the first fitting program

The method of reading in the data to the computer will be described in section 5.3; the method formerly used on the 1906A, and hence by Thompson in his analysis was somewhat different, but this difference is not of any significance. We shall assume, therefore, that the data is stored in the computer in pairs of numbers (S^{μ}, C^{μ}), where S^{μ} represents the fluorescent light intensity and C^{μ} the 2 m cavity transmission, measured at the same

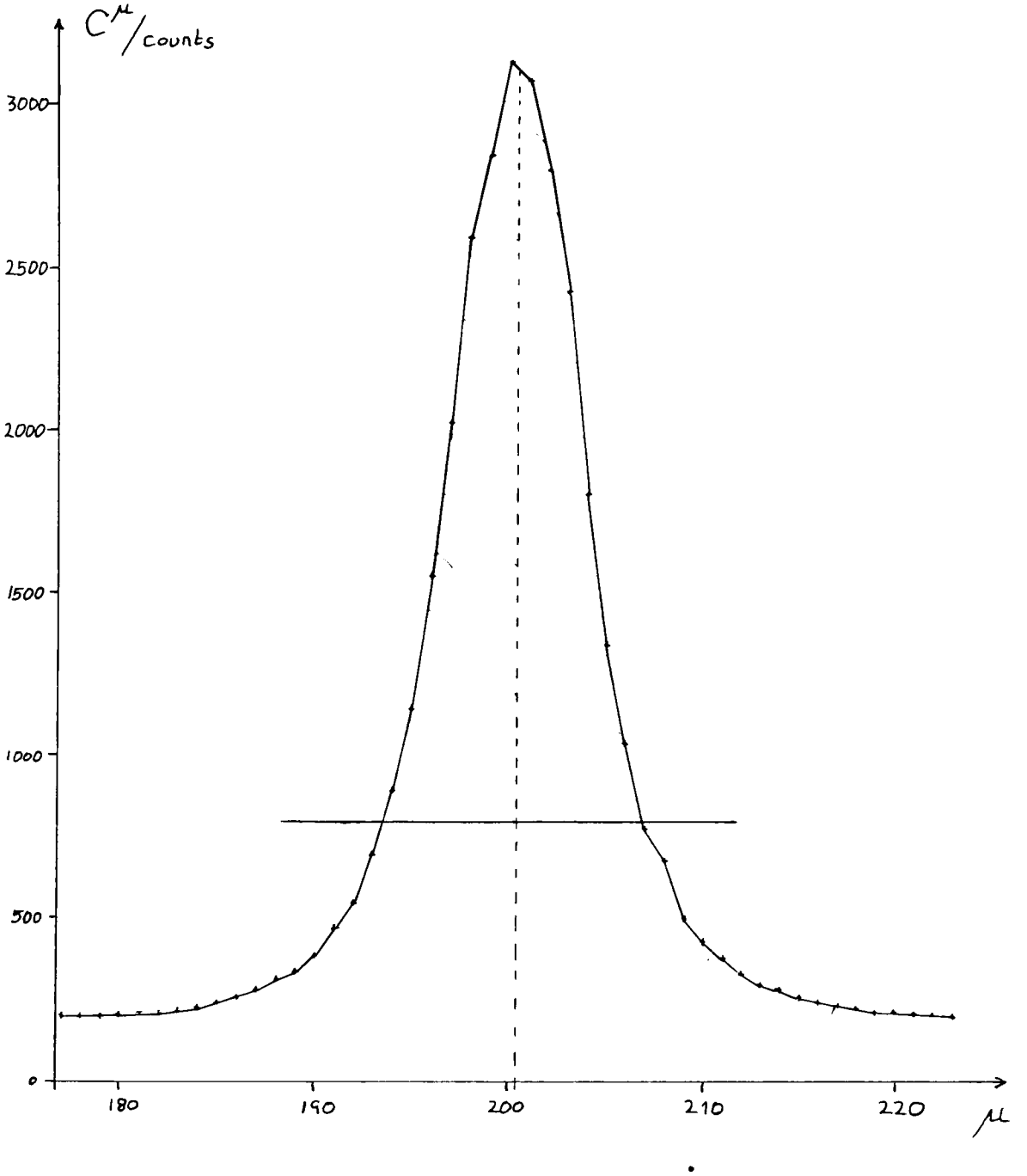


FIGURE 5.1 A Typical Calibration Fringe. The reference level is marked; the centre of gravity of the shaded region above the reference level is shown by the broken line.

time. The order number, μ, of the pair from the beginning of the run is referred to as the channel number.

The first stage of the analysis is to establish a frequency scale; that is, to use the calibration fringes to assign a frequency to each channel number. A typical fringe is shown in Fig. 5.1; the channel number of the fringe is defined to be the centre of gravity of the shaded region, and the centre of gravity of the i^{th} fringe, μ_i, is taken to have frequency

$$\nu_i = i\,\nu_{fsr} \tag{1}$$

where ν_{fsr} is the free spectral range of the 2 m cavity. Thus we have a set of points (ν_i,μ_i) on the calibration curve $\mu(\nu)$, and by fitting a smooth curve through them a channel number can be assigned a frequency and <u>vice versa</u>. This curve was taken to be a cubic

$$\mu(\nu) = c_1 + c_2(\nu/\nu_{fsr}) + c_3(\nu/\nu_{fsr})^2 + c_4(\nu/\nu_{fsr})^3 \; . \tag{2}$$

It can be seen from equation 1 that the zero of the frequency scale is at the last calibration fringe before the calibrated region of the laser scan.

The second stage of the analysis is to transfer the information about the laser scan to the data points; this is done by establishing a new set of data points with equal frequency spacing (which was taken to be 2 MHz) and transferring the old data points on to the new. The method of doing this is shown in Fig. 5.2. The old data point μ falls between the new data points m and m+1, dividing the interval in the ratio α:1-α. If the value of the data point is S^{μ}, it contributes $(1-\alpha)S^{\mu}$ to the new data point S^{m}, and αS^{μ} to the new data point S^{m+1}. S^{m} also receives contributions from old data points μ-1, μ-2 and μ-3, in this example; in general, provided all intervals between new data points contain at least one old point, this procedure smooths the data while transferring it to a linear scale.

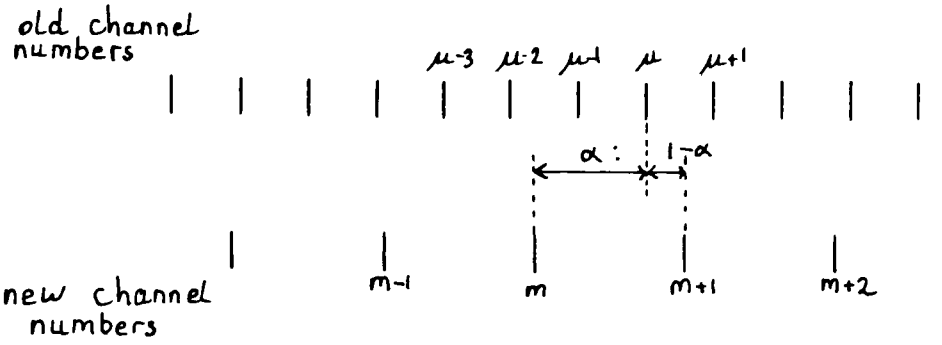


FIGURE 5.2. Transferring the Data (see text)

The third stage of the analysis is to fit the data with a theoretical spectrum. This is made up of a constant background intensity plus spectral lines; each line has the same profile but scaled by an isotope ratio. The profile is the sum of a Voigt profile, representing the Doppler-free component, and a Gaussian of large width representing the Doppler-broadened component. In practice only the Doppler-broadened component of ^{40}Ca is significant. The fitting program calculates the theoretical spectrum for a given set of parameters, and finds the differences between the theoretical and experimental data points (the residuals). By varying the parameters the program minimizes the sum of the squares of the residuals.

The total number of parameters is 14; these are

1) Constant background intensity

2) Position of ^{40}Ca

Isotope shifts:

3) Isotope shift of ^{42}Ca

4) Isotope shift of ^{43}Ca

5) Isotope shift of ^{44}Ca

6) Isotope shift of ^{48}Ca

Line Profile parameters:

7) Gaussian width

8) Lorentzian width

9) Intensity

10) Gaussian width of Doppler background

Isotope Ratios

11) $^{42}Ca:^{40}Ca$

12) $^{43}Ca:^{40}Ca$

13) $^{44}Ca:^{40}Ca$

14) $^{48}Ca:^{40}Ca$

It is not possible to vary all these parameters together because of the very different sizes of the isotopes. Thus if, at some stage of the fitting process, the position and lineshape of ^{40}Ca were wrong this would lead to very large residuals compared with any movement of the smaller isotopes. Thus the movement of the small isotopes at this stage of the fitting procedure might be almost random, and by the time the line profile parameters of ^{40}Ca were correctly determined, the positions of the smaller isotopes might have drifted away from their starting values too far for the fitting program to find the correct values. The fitting therefore proceeded in several stages; first the background, lineshape parameters and position of ^{40}Ca were determined, keeping the small isotopes fixed at an estimate of their correct position and intensity. Secondly, the small isotopes were fitted, keeping fixed the background, lineshape and position of ^{40}Ca.

It will be noted that the size of the Doppler-broadened component relative to the Doppler-free component is not given as a parameter. This is because there is insufficient information to determine it since the scan goes over less than one full width at half the maximum intensity of the Doppler-broadened component. This means that the value of the flat background in the absence of the Doppler-broadened component is not known. The combination of a flat background with a Gaussian of variable width but having an area under it a fixed fraction of the area under the Doppler-free component is sufficient to fit the observed background. If the area-ratio is allowed to vary there is not a unique solution to the fitting problem, and the program oscillates between different solutions. One parameter therefore has to be fixed; the area ratio was chosen, and this was fixed at its theoretical value of 0.5. An alternative procedure would have been to determine the background

intensity, and fix it at that value while allowing the area ratio to vary.

This fitting procedure was carried out for a small number of early runs, one of which is shown in Fig. 6.5. It was important in that it demonstrated that the sloping background which we observed under the small isotope peaks was indeed due to the Doppler-broadened component of ^{40}Ca, and so we were justified in fitting a sloping background beneath each isotope peak, as described below, in sections 5.3 and 5.5. However the results were not used in the final evaluation of isotope shifts; the runs were re-analysed with the revised fitting procedure.

5.3 Discussion of Fitting Procedure

The fitting procedure described in section 5.2 has been developed over a number of years for two different applications. One was the fitting of spectral line profiles from a cooled discharge source in a study of pressure broadening (see, e.g. Thompson, 1981); the other was the fitting of spectra of the barium resonance line in an experiment to measure isotope shifts and hyperfine structure (Brambley, 1978; Baird et al., 1979). In the former case there is a single spectral line, and in the latter case a partially resolved spectrum; thus in both these cases the information is distributed throughout the spectrum. Also there are no very narrow structures, and so the linearized data set can have a spacing of several MHz, while the original data set has a spacing which, although smaller, could still be over 1 MHz.

The spectra of calcium isotopes produced in this work are quite different; the spectrum is completely resolved, as can be seen from Figs. 4.6 - 4.8, and so only a small fraction of the data points contain useful information, since between isotope peaks only the calibration signal is important. However, the peaks are very narrow, and so in order to get an adequate number of data points over a peak, twelve for example, the point

spacing needs to be small, about 0.8 MHz. Furthermore, it is not desirable to transfer this data to a linearized data set with a very similar point-spacing, as this introduces noise rather than smoothing, nor with a larger point spacing, as this effectively convolves into the line profile a contribution from the linearization.

One strategy that could be adopted is to scan the laser at a variable rate, slowly over the isotope peaks and rapidly between them, while taking data at a constant rate. This would be undesirable because of the uncertainty it introduces about the laser scan. The only way we can assign a frequency to a point between two calibration fringes is to use neigh-bouring fringes to estimate the non-linearity of the scan. Thus a minimum of four fringes is required to determine the frequency of an isotope peak, and if the scan speed is changed, time for the scan to settle down must be allowed. The frequency separation of the isotope peaks is insufficient to permit a variable scan speed, as can be seen from Fig. 4.6.

Another strategy is to take data points at a variable rate, slowly between peaks and more rapidly over isotope peaks. However, as can also be seen from Fig. 4.6, the calibration fringes are roughly the same width as the isotope peaks, and so a scan rate giving an adequate number of points over an isotope peak will also give an adequate number of points over a calibration fringe. Thus, since all calibration fringes are required to establish the frequency scale, as we saw above, it is not possible to vary the rate of taking data.

Thus we are bound to take more data points than we need on some parts of the laser scan. Fitting a theoretical spectrum to all these points (which we might term global fitting) simply uses up computer time to no good purpose, and also requires the linearization of the scan, which, as we noted above, either broadens the spectral lines, or introduces noise. Global fitting has another, more serious, disadvantage, which is that a single function $\mu(\nu)$ is required to describe the whole laser scan. The function that was used in the

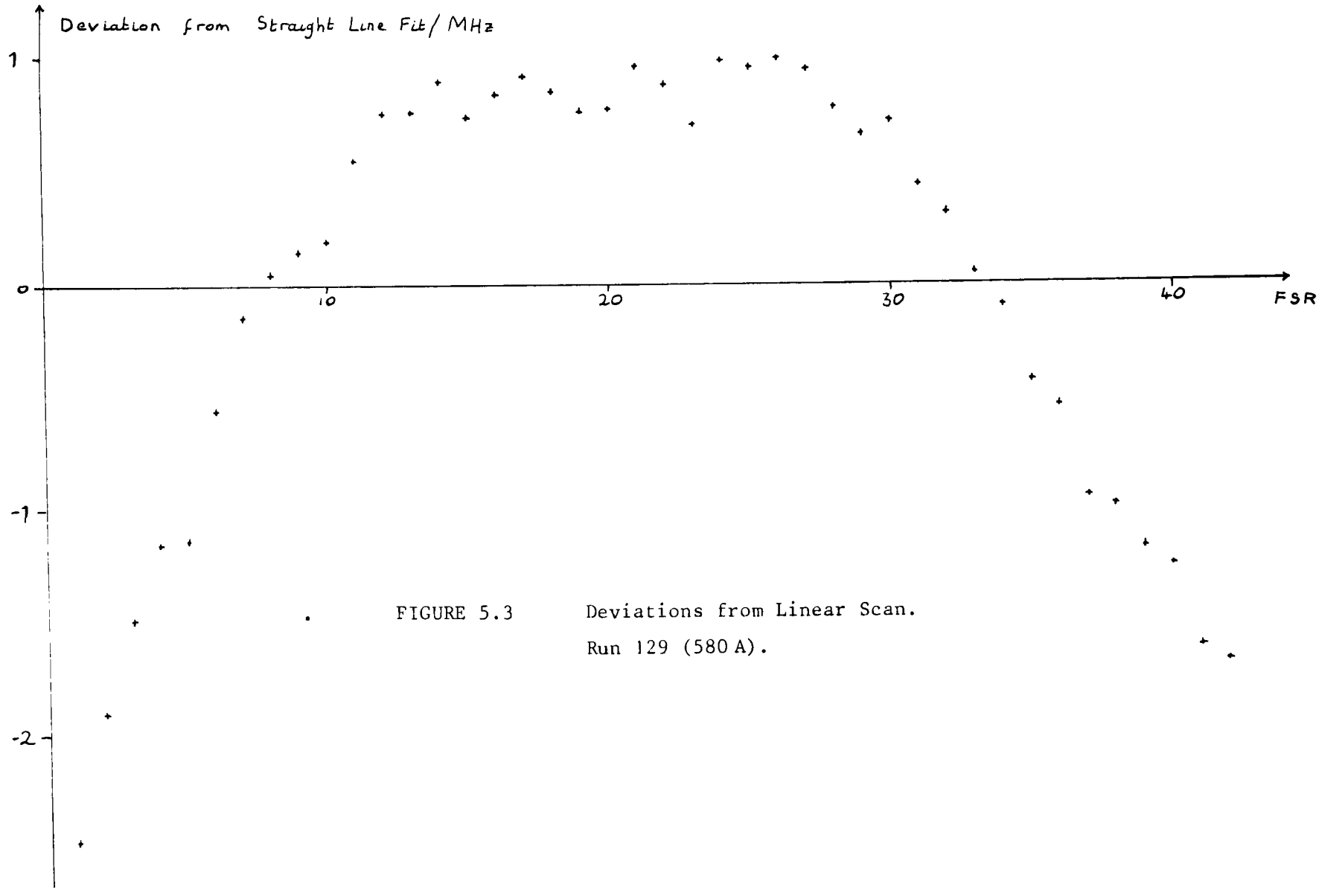


FIGURE 5.3 Deviations from Linear Scan.
Run 129 (580 A).

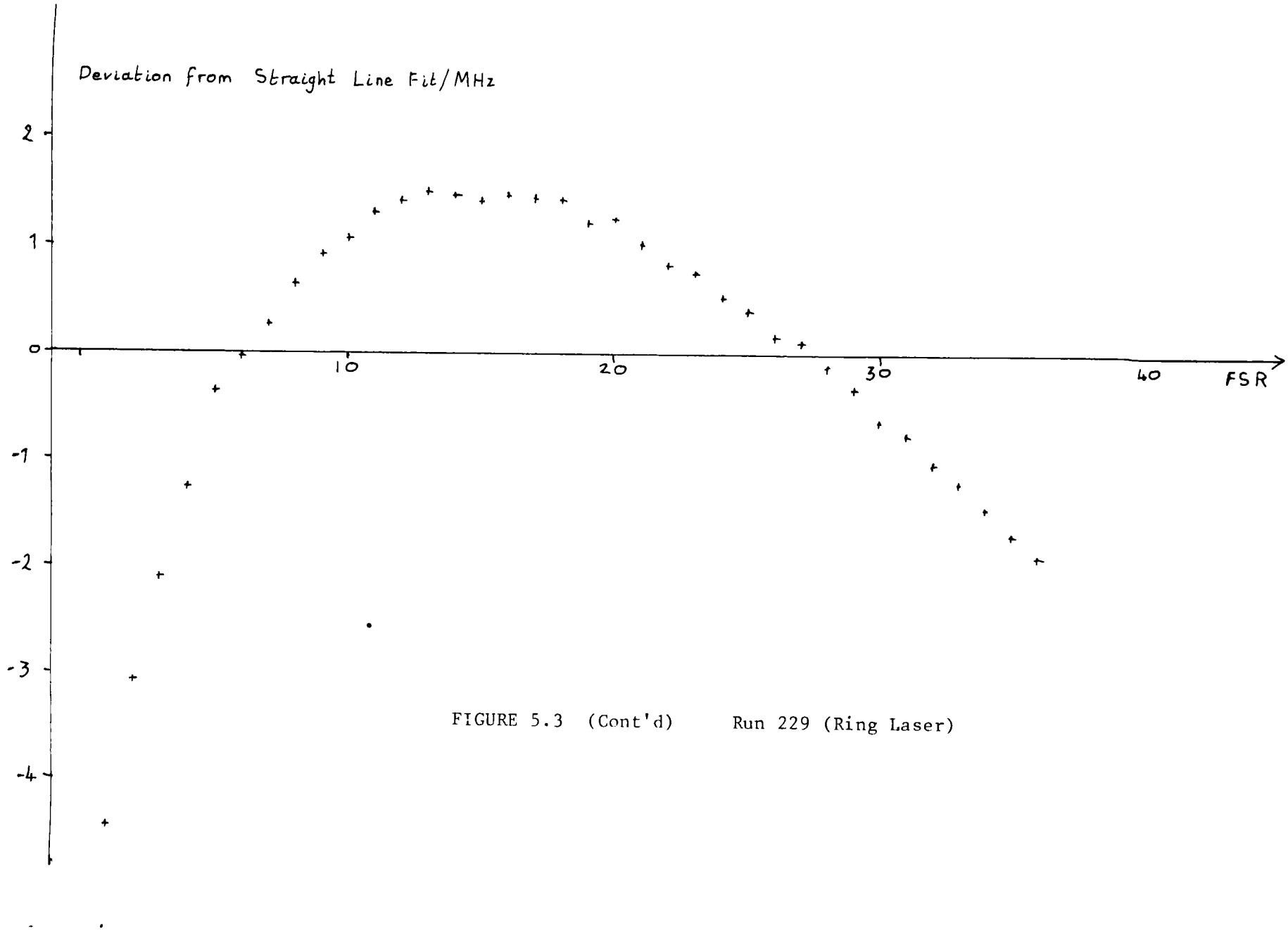


FIGURE 5.3 (Cont'd) Run 229 (Ring Laser)

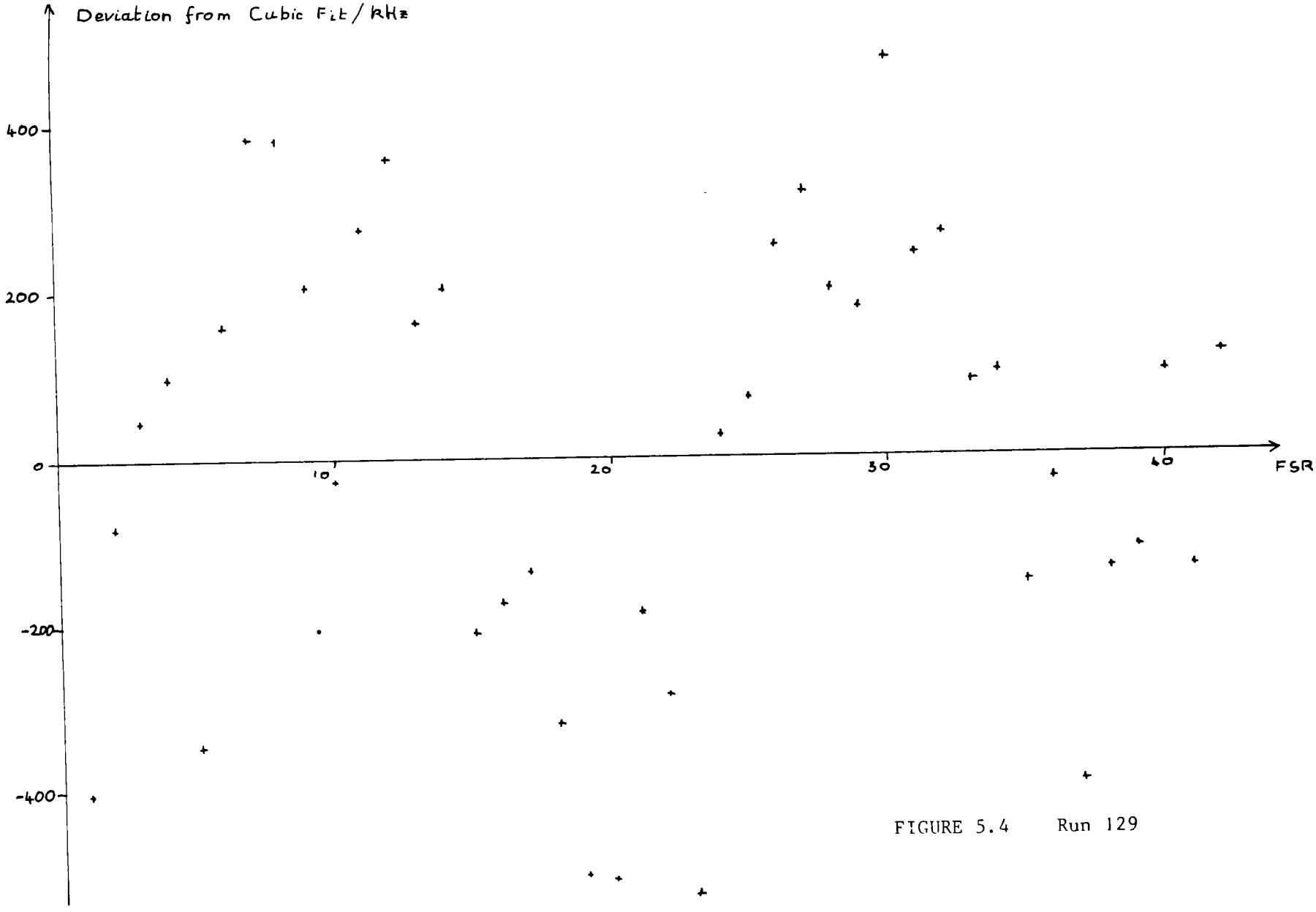


FIGURE 5.4 Run 129

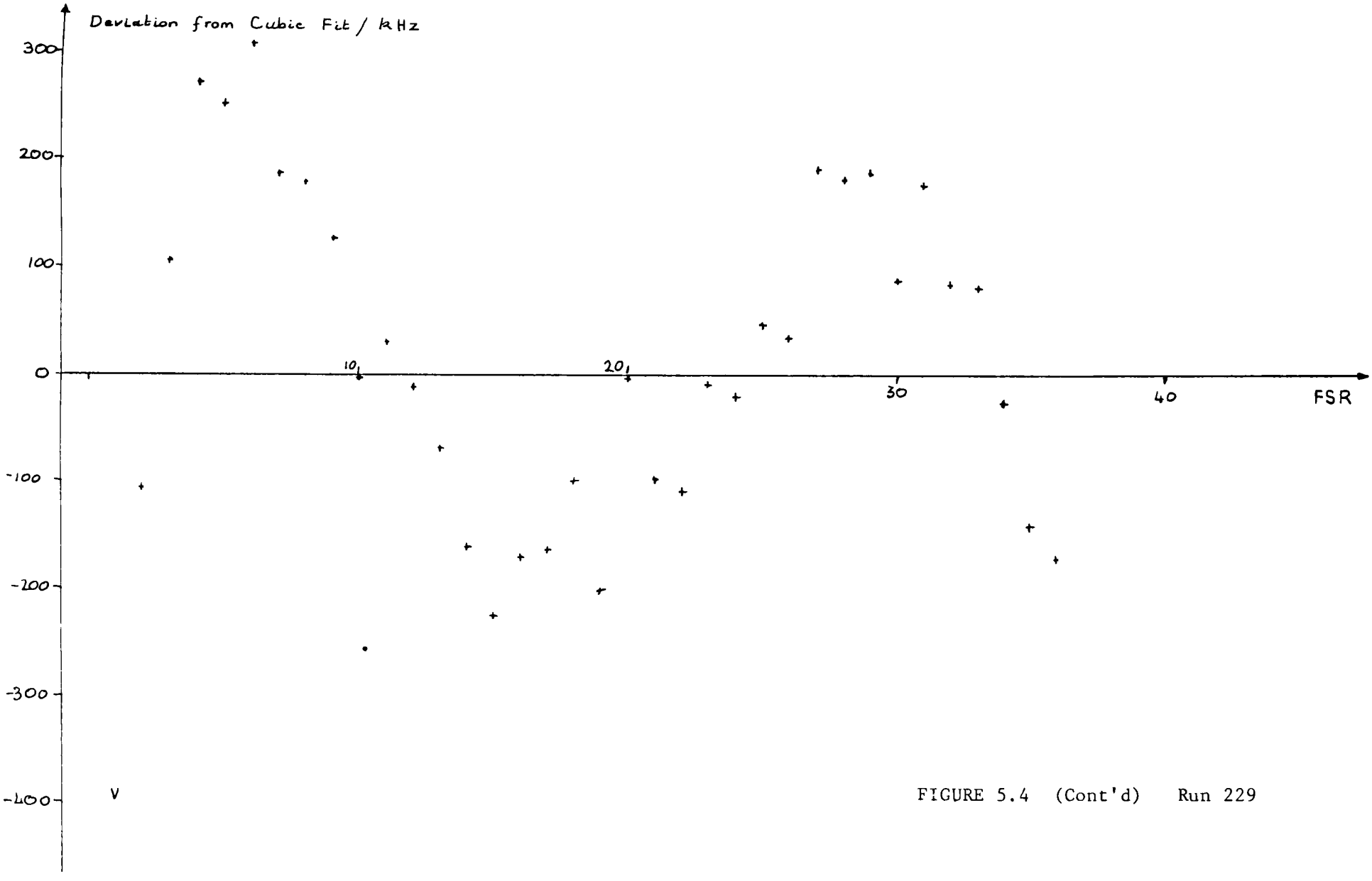


FIGURE 5.4 (Cont'd) Run 229

global fitting described in section 5.2, namely a cubic, did not adequately describe the laser scan over more than 800 MHz, as I shall now show. Since the scan is in fact highly linear, the deviations from a linear scan give the best idea of the form of the required function. These are plotted for two runs in Fig. 5.3, one run taken with the 580-A laser and one with the ring laser. It can be seen that the form of the scan is very similar in the two cases; since in both cases the scan is controlled by the flow of air into the etalon, this is to be expected. The deviations from a cubic scan are shown in Fig. 5.4; while on scans shorter than these, the deviations appear random, it is clear on these longer scans that much of the deviation is systematic. However, over a very short region of the scan it is clear that a low order polynomial would be a very good fit.

Thus the strategy we adopted was to fit only short regions around each isotope peak, each region being separately calibrated using the calibration fringes around each peak. A region of 100 channels was selected around each isotope peak; at a typical scan rate this corresponds to 80-100 MHz, or about ten times the full width at half maximum height of the peaks. A particular fringe, usually the one just to the low frequency side of the largest peak on the run, was chosen to have frequency zero, and so the i^{th} fringe in the direction of decreasing channel number (since the laser scans towards lower frequency) has frequency i fsr. All the isotope shifts are calculated in terms of free spectral ranges of the 2 m cavity; the conversion to absolute frequency is performed in section 6.3. A small number of fringes, usually six or seven, symmetrically placed about the region of 100 channels to be fitted, is used to establish the local conversion from channel numbers to frequency. This is done by fitting the six or seven points (ν=i, $\mu=\mu_i$) to a parabola

$$\mu = A\nu^2 + B\nu + C \tag{3}$$

using a least squares fit. The coefficients A, B, C obtained from this fit are used in two ways.

(i) Over the 100 channels to be fitted the scan is highly linear, and over this short region the original data set can be taken to be a linear data set, with point spacing given by $|B^{-1}|$. This is clear from Fig. 5.3; we can also see from this Figure that we cannot take the whole trace as a linear data set. Thus a Voigt profile can be fitted to the signal over this region using the original data set as one linear in frequency.

(ii) The fitting routine then finds the channel number μ_c of the line centre. This is converted to a frequency using the inverse of equation 3

$$\nu = -\frac{B}{2A} \pm \left\{ \frac{B^2}{4A^2} + \frac{\mu_c - C}{A} \right\}^{\frac{1}{2}} \quad . \tag{4}$$

This gives the frequency of the isotope peak, relative to the chosen fringe of zero frequency, in free spectral ranges.

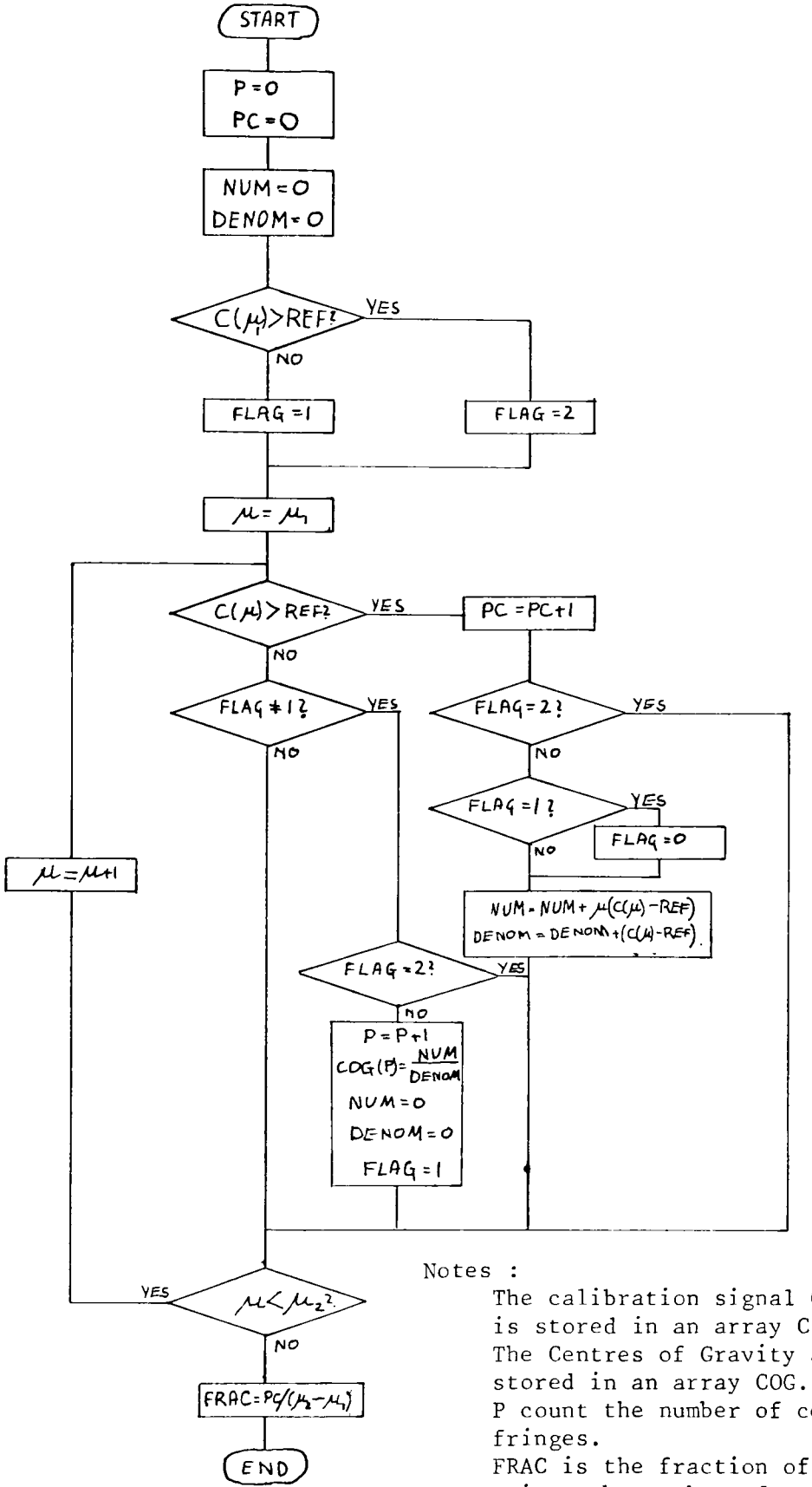
In sections 5.4 and 5.5 we discuss how this procedure was implemented.

5.4 The Calibration and Plotting Programs

The format of the data punched onto the paper tape is a string of groups of twelve characters, each group containing a four-digit integer between 0000 and 4096 representing the fluorescent light intensity, and a similar integer representing the calibration signal. This tape is read into the computer using the Clarendon Laboratory Data Transfer System, and stored in the computer's disc store in a file labelled with a three-digit integer which is called the run number. As explained in section 4.5, three sets of runs were made; these have run numbers commencing with 0, 1 or 2 respectively.

Having read the data into the computer, the first operation is to plot it so that it can be seen what portions of the trace, if any, should be neglected in the subsequent fitting, due to, for example the helium-neon laser losing its lock to the I_2 absorption feature. This was done by a program PLOT, run by a macro CAPLOT. The program reads in the data, up to a maximum of 5000 points which represents a scan of over half an hour, about 50% longer than the longest scan ever taken. If the last line of data is incomplete it is lost: a maximum of seven points can therefore be lost in this way. The program then, using the GHOST graphical output system, creates a plotting file showing the calibration fringes and fluorescent signal separately. Up to two sections of the fluorescent signal, between specified channel numbers, can be shown on an expanded scale. This plotting file can then be plotted on any device supported by the Computing Service; the standard plot was in biro on a 10" Calcomp plotter. Some of the pictures in this thesis (Figs. 4.6 - 4.8) were produced by this program, but plotted in ink.

When the data has been plotted it is examined by eye; the points to be noted are the general appearance of the fringes, for example the smoothness of the trough between the fringes, and the symmetry of the fringes, and, in particular, whether or not there are any 'glitches'. (For example, the fourth fringe of Fig. 4.8 has a glitch in it.) These are caused by some sudden effect during the scan - a sharp change in laser intensity due to an air bubble passing through the jet, or a large frequency excursion of the dye laser, or a jolt to the 2 m cavity would all cause glitches. A lot of the early scans had glitches in them, and all that can be done is to arrange that the reference level does not pass through any; if it does it will count the fringe twice because the signal dips below the reference level and then returns above it. It is not usually possible to arrange that the reference level passes above all glitches, and so some peaks will have glitches in them, and thus their centres will be subject to a random error. Later scans were much better in this respect.



Notes :

The calibration signal C^{μ} is stored in an array C.
The Centres of Gravity are stored in an array COG.
P count the number of complete fringes.
FRAC is the fraction of the points above the reference level REF.
The first and last channel numbers of the calibrated region are μ_1, μ_2.

FIGURE 5.5 The Calibration Algorithm.

A reference level and range of calibration (e.g. all the scan) are selected and the calibration program CALIBRATE is run by calling the macro CACAL. This reads in the calibration signal (up to a maximum of 3000 points) and finds the centres of gravity of all the complete fringes between the specified start and end channel numbers. The algorithm used is shown below in Fig. 5.5.

According to the strategy outlined in section 5.3, all that is now required is to list the centres of gravity and store them for use by the fitting program. However, in order that we could compare the relative merits of the local calibration and the global calibration, the centres of gravity were fitted to a cubic and the coefficients displayed. It requires very little extra calculation, once the required sums have been computed, to fit to a straight line and a quadratic as well, so these coefficients and the sum of the squared deviations (SUMSQ) from the least squares fit are tabulated also. A deviation $\delta\mu$ in channel numbers can be converted to a frequency by multiplying by the slope of the line, and so the sum of the squared deviations from the fit is also given as a root mean square deviation in frequency units. Finally the fit to the cubic is displayed in a table of centres of gravity and a rough plot of the deviations from the fit. A typical output from the program is shown in Fig. 5.6.

The program was written independently of the calibration program of Richard Thompson's analysis, but gave exactly the same results when calibrating the same trace; this therefore checks the correctness of the program.

The output was used as follows:

(i) If the reference level hit a 'glitch' this immediately showed itself by large rms deviation and a minimum fringe spacing of about five channels.

(ii) The fraction of all points above the reference level was constrained to be 25-30%.

(iii) It was apparent whether the calibration was good or not

from the deviations - on the best traces these are mainly systematic, that is the smooth laser scan is not well-described by a cubic, while on others they appear random. These systematic deviations from a cubic were referred to above, and are shown in Fig. 5.4 for two runs.

(iv) When the channel numbers at which isotope peaks appear have been read off from a listing of the file, or the plot, the reference numbers of nearby calibration fringes can be read off from the list; these are then used as input data to the fitting program.

5.5 The Fitting Programs

In this section I describe the fitting program I wrote to calculate the isotope shifts from the digital data. In order to compare this fitting program with earlier programs used in this group it is necessary first to consider generally the problem of fitting an experimental spectrum with a theoretical one.

We have an experimental spectrum defined by a series of numbers S^{μ}, where $\mu = 1,2,...M$, and a theoretical spectrum depending on N parameters X_i, $T^{\mu}(\underline{X})$. We define the residuals to be $R^{\mu} = S^{\mu} - T^{\mu}$; the best fit is that which minimizes the sum of squares of the residuals, F:

$$F = R^{\mu} R^{\mu} \qquad \text{(Einstein summation convention).} \tag{5}$$

Strictly speaking the function F should be a weighted sum in many cases; we have never used a weighted sum however, and the weighting would not affect the discussion of different fitting methods below, only complicate it. For use in the discussion, we define the following:

(6a) Gradient vector $G_i = \frac{\partial F}{\partial X_i}$

(6b) Hessian matrix $H_{ij} = \frac{\partial^2 F}{\partial X_i \partial X_j}$

(6c) Jacobian matrix $J_i^\mu = \frac{\partial R^\mu}{\partial X_i}$.

By carrying out the differentiations for the form of F given in equation 5 we find that

(7a) $G_i = 2J_i^\mu R^\mu$

(7b) $H_{ij} = 2R^\mu \frac{\partial^2 R^\mu}{\partial X_i \partial X_j} + 2J_i^\mu J_i^\mu$.

In what follows I shall find it useful to refer to the "residual surface"; this is a surface in N+1-dimensional space of which N co-ordinates are the N parameters X_i, and one is the value of F. What we are searching for, then, is the overall lowest point on the residual surface.

Having established the notation we can proceed to the discussion. The earliest fitting program in this research group was written by Malvern (1974). The method used is to approximate the residual surface to a surface of the second degree, with the minimum at the best fit position $\underline{X}_o$:-

(8) $F(\underline{X}) = F_o + \tfrac{1}{2}H_{ij}(X_i - X_i^o)(X_j - X_j^o)$.

If the current estimate of the minimum position is $X_i^{(k)}$, we can rewrite equation 8

(9) $$F(\underline{X}) = [F_o + \tfrac{1}{2}H_{ij}(X_i^o - X_i^{(k)})(X_j^o - X_j^{(k)})] + [(X_j^{(k)} - X_j^o)H_{ji}](X_i - X_i^{(k)}) + \tfrac{1}{2}H_{ij}(X_i - X_i^{(k)})(X_j - X_j^{(k)}) .$$

The first factor in square brackets is the value $F(\underline{X}^{(k)})$, the second is the local value of the gradient vector $G_i(\underline{X}_j^{(k)})$ and the Hessian matrix H is assumed to be the same everywhere. The method used is to find an approximation to the local values of G and H; according to the model we see from equation 9 that

$$G_i^{(k)} = H_{ij}(X_j^{(k)} - X_j^o)$$

and so

$$X_i^o = X_i^{(k)} - (H^{-1})_{ij}G_j \quad . \tag{10}$$

This value of X_i^o is taken as the new estimate of the minimum position $X_i^{(k+1)}$.

The local values of $G^{(k)}$ and H are found by evaluating F at the current best estimate $X_i^{(k)}$ and at points $(\underline{X}^{(k)} \pm \Delta j)_i$ where the notation indicates a vector equal to $X_i^{(k)}$ except that the j^{th} component has been stepped to $X_j^{(k)} \pm \Delta j$. For example

$$G_j = \frac{F(\underline{X} + \Delta j) - F(\underline{X} - \Delta j)}{2\Delta j} \quad .$$

In the first iteration the step lengths Δi are set by the user; in subsequent iterations they are reset by the program. This method has been found to converge in a very small number of iterations to the minimum sum of squares, but in terms of computer time it is quite slow because of the large number of function evaluations - the residuals are evaluated N^2+N+1 times per iteration cycle, in order to evaluate the $\frac{1}{2}N^2+\frac{3}{2}N+1$ coefficients of the model - roughly two function evaluations per coefficient, as illustrated by the gradient vector G.

The fitting program used by Richard Thompson in his analysis of some of the calcium spectra (see section 5.2) and also in the line-broadening work,

and also that used by Brambley for fitting barium spectra, was based on a routine supplied by the Numerical Algorithms Group, NAG routine E04FAF. This differs from Malvern's approach in several respects. A rather complete description is given by Peckham (1970); I shall give a brief description here.

This method models the residual surface in a rather different way, by making a linear approximation to each residual

$$R^{\mu}(\underline{X}) = E^{\mu} + J^{\mu}_{i} X_{i} \tag{11}$$

where J^{μ}_{i} is the Jacobian matrix, and E^{μ} is a constant vector. This linear approximation to each residual gives rise to a quadratic form for the residual surface, with gradient vector

$$G^{(k)}_{i} = 2J^{\mu}_{i}(E^{\mu} + J^{\mu}_{j} X^{(k)}_{j}) \tag{12a}$$

and

$$H_{ij} = 2J^{\mu}_{i} J^{\mu}_{j}. \tag{12b}$$

Thus another way of looking at this model is to say that it neglects the first term of equation 7b compared to the second, which one might call the small residual approximation. The advantage of this is that J, the matrix of first derivatives of the residuals, can be found with many fewer function evaluations. For example in the first iteration the program will evaluate the residuals at the point supplied by the user $R^{\mu}(\underline{X})$ and this will give the vector

$$E^{\mu} = R^{\mu}(\underline{X}) - J^{\mu}_{i} X^{\mu}_{i}$$

The Jacobian will be given by evaluating the residuals at the N points $(\underline{X} + \Delta i)$:-

$$(13) \qquad J_i^\mu = \frac{R^\mu(\underline{X} + \Delta i) - R^\mu(\underline{X})}{\Delta i} \quad .$$

Then by substituting equation 12 into equation 10 we find the next estimate of the minimum to be

$$(14) \qquad X_i^o = -(J_i^\mu J_j^\mu)^{-1} J_j^\nu E^\nu \quad .$$

At this and each subsequent iteration the new estimate of the minimum replaces the point with largest F of the current set, and the new set of N+1 points is used to find the model coefficients J and E. If at some stage the set of points fails to span the N-dimensional parameter space, a new point in the vicinity of the point of lowest F is generated randomly. The maximum distance the best estimate of the minimum can move along each axis in one iteration is set by a step length along that axis (these could be the same as the Δi used in the first iteration).

Comparing this with the Malvern method we see that by neglecting part of the expression for the Hessian matrix it is in principle not as good. It does however make use of the structure of F as a sum of squares, and by this means greatly reduces the number of function evaluations required - N+1 for the first iteration, and one for each subsequent iteration. This is also partly due to the fact that Malvern throws away all previous function evaluations at each stage, while E04FAF only throws away the worst point, and uses the rest in the next iteration. (The reason for this is that the Hessian matrix is found, in Malvern's method, by fitting the points to a surface of the second degree, which is very difficult unless the points are situated in a highly symmetrical fashion.) The E04FAF method carries a penalty however: its storage requirement is larger; fortunately, though, on the 2980 storage is not really a problem for typical numbers of data points and parameters. In practice Malvern found that while each iteration of E04FAF was very much faster than with his program, convergence, in terms of number of iterations,

was slower. He does not state which program was actually faster in computer time.

At about the time when the programs for the calcium experiment were being written, NAG announced that the routine E04FAF would shortly be withdrawn, to be replaced by E04FCF. I therefore decided that I would write my fitting program around this new routine in order to see if it would be more satisfactory than either of the former routines. It is, like E04FAF, specially written for the case of minimizing a sum of squares, but it uses more sophisticated techniques to try to estimate the additional term in the Hessian matrix neglected in E04FAF, and so obtain quicker convergence. It is described by Gill and Murray (1978). My conclusion is that for many purposes it is less satisfactory than E04FAF, although it was adequate for this experiment.

The program works as follows. (I shall give much less detail for this program because of its much greater complexity.) From the current best estimate of the minimum $\underline{X}$, the program generates a new estimate $\underline{X} + \alpha\underline{p}$, where $\underline{p}$ is a direction of search, and α is the distance along this direction giving the minimum residuals. Now the algorithm for finding $\underline{p}$ described by Gill and Murray assumes that the Jacobian matrix is available, and so in the NAG routine it is found using equation 13 but with Δi set very small; exactly how small will be specified later. Thus the direction of search $\underline{p}$ is susceptible to local "roughness" of the residual surface, which is almost certainly present, which is averaged over in the finite difference methods of the former two routines. The effect of this is as follows:-

(i) with two parameters to be varied the program almost invariably finds a true minimum, and will stop when all the gradients are sufficiently small;

(ii) with more than two parameters the program will get important parameters having a large effect on the residuals correctly - such as line centres and halfwidths. Parameters having smaller or more

localized effects on the residuals, such as the Lorentzian/Gaussian decomposition, cannot be determined.

In fact after a few iterations the vector of search will be pushed by some local roughness of the surface to a direction such that no minimum is found in that direction significantly different from the current point. The program will then terminate with the message "Not all conditions for a solution have been met, but no better point can be found". In a typical case, the fitting routine, trying to fit a "large" isotope - say ^{40}Ca - will decide on the best value of the line centre in one or two iterations, and if the sum of initial Lorentzian and Gaussian widths does not give the correct half-width, the Lorentzian will be changed to give the correct half-width. The vector of search in subsequent iterations is bound to be orthogonal to these directions, and if little improvement is found, which is usually the case, the program will stop, without making any significant change to the Gaussian width or the height of the peak.

The fitted line centre of ^{40}Ca was found to depend on the initial value of the Lorentzian and Gaussian widths at the level of a few kHz, and so it was to be expected that the line centres of smaller isotopes might do so to a greater, and possibly significant extent. In order to get the best possible fit, it was necessary to determine in advance the best values of the Lorentzian and Gaussian widths. This was done by a program FIT40, which I shall now describe.

This program worked with the same 100 channels as the fitting program, and was used only for the largest isotope peak on the trace; that is ^{40}Ca, or ^{44}Ca on ring laser runs. First the centre of gravity of the peak was found, and this was used for the line centre subsequently in the program. Then, between specified limits of Gaussian and Lorentzian width, the program calculated the best fit, for each Gaussian and Lorentzian width, of the height of the peak and the background. This turns out to be a straight line fit:- let V^{μ} be a Voigt profile with unit height at line centre; then the

best fit is that for which $HV^{\mu} + B$ is closest to S^{μ} over the whole trace; but this is just a straight line, if S^{μ} is plotted against V^{μ}, with slope H and intercept B. Thus the height and background are determined, and the sum of residuals F calculated and displayed in a table. A typical output is shown in Fig. 5.7.

Fig. 5.7 gives a series of spot heights on a two-dimensional residual surface and we can see its form quite clearly. To aid this, contours for $\sqrt{F/100}$ = 20, 50 and 100 have been sketched on. We see that the surface is a long narrow valley; moving across the valley we change the half-width, and moving along the valley we change the Lorentzian/Gaussian decomposition. This illustrates why the fitting program finds the latter more difficult to determine than the former.

This program was run three times, successively expanding the region around the lowest point on the residual surface each time. Thus the next time the program was run for this particular run the limits of the Gaussian width would be set at (4.2,4.8) and the limits of the Lorentzian at (3.9,4.5).

After three calls of FIT40, the lowest point on the final output tells us the Lorentzian and Gaussian widths, the height and background level, and the centre of gravity gives us the line centre. These are used as input data to the fitting program; all are floated, and so we see the behaviour described in (ii) above, that is the line centre and Lorentzian width only are significantly changed. It is to this program that we now turn.

The main program, FITMAIN, is very short; it simply reads the run and isotope numbers, prints a title block and calls three subroutines, testing an error flag on return from each to ensure that various error conditions have not been encountered. If the error flag is changed by the subroutine, FITMAIN prints an appropriate error message and terminates immediately.

The first subroutine is CALIB, which establishes the calibration around the region to be fitted. This is done in three ways: the local quadratic fit and the global cubic fit have already been described; in addition

the program finds the coefficients for linear interpolation between the peaks on either side of the estimated line centre.

The second subroutine is PARAM, which reads in the estimated parameter values and the 100 channels to be fitted. This brings us to another drawback to this fitting routine. As we saw above, E04FAF has step lengths on each axis that determine how far the best estimated position may move between iterations, and also the initial stepping to calculate model parameters in the first iteration. E04FCF dispenses with a step length for both these purposes. The step length limit is on the total distance $\delta X_i \delta X_i$ moved between iterations. Now clearly a unit change of parameter value has a very different effect on a line centre and on intensity, for example. Some scaling is therefore necessary. The subroutine PARAM reads in the estimated parameter values PE_i and step lengths L_i. The actual parameter values used in any function evaluation are $P_i = PE_i + X_i L_i$ where X_i are the parameters varied by the fitting routine, initially set to zero. If the number of parameters to be varied is N, the maximum step length is set to $\sqrt{N}$. If a step length is set to zero, the parameter is not varied.

I should mention here the step length used in E04FCF to evaluate gradients, which I referred to above as "very small". With two parameters varying, and so the maximum step per iteration being $\sqrt{2}$, the step length was found to be 1.5×10^{-8}.

The eight parameters available are

1) Line centre
2) Intensity
3) Isotope ratio

(height in counts at line centre is intensity/isotope ratio)

4) Gaussian width
5) Lorentzian width
6) Flat background
7) Sloping background
8) Curved background.

The final subroutine is FIT, which calls the NAG subroutine E04FCF. On exit from E04FCF, a error flag IFAIL is tested. This gives information about how the fitting has proceeded; the most common results were

IFAIL = 0: all conditions for finding the minimum have been met. This is common when only two parameters are varied, but not otherwise.

IFAIL = 3: not all the conditions for a successful exit have been met, but no better solution can be found. This is common when more than two parameters are floated, for reasons discussed above.

IFAIL < 0: this means that on entering the function-generating subroutine one of the parameters fell outside its allowed range, e.g. Lorentzian width < 0. This rarely occurred, and only when one parameter was close to its limit; then there is a risk that some step length from the current position will take the parameter outside its allowed region and cause the program to fail.

Finally the centre channel number is converted to a frequency using the three different calibrations. For the cubic calibration, this requires solving a cubic equation, for which a separate subroutine, CUBIC, was written, which used the method of comparing the reduced cubic equation with trigonometric or hyperbolic identities.

This completes the description of the method used for the fitting of the largest isotope of each run. The values found for the Lorentzian and Gaussian widths, and the intensity of this isotope, are used to fit the smaller isotopes on that run. The background under these isotopes is also separately determined, by fitting a straight line to the region of the scan on either side of the isotope peak, as shown in Fig. 5.8. In this way, allowance is made for the slope of the Doppler-broadened component of ^{40}Ca, which is just visible as a perceptible slope in Fig. 5.8. A correction is made to

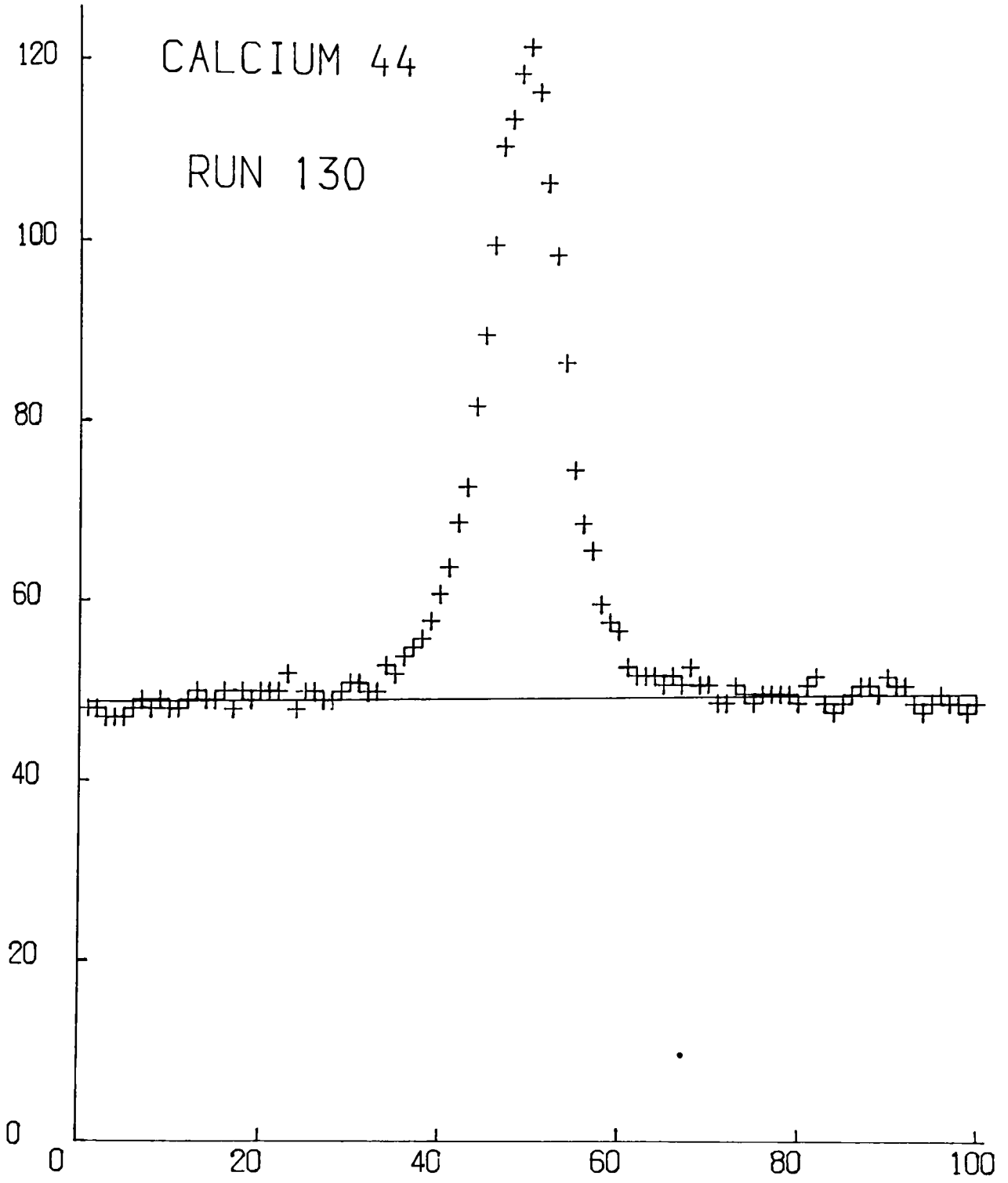


FIGURE 5.8 A Typical Isotope Peak, showing the fitted sloping background found using the program LINE.

the value of the flat background to allow for the Lorentzian wing of the small isotope, using its known Lorentzian width. The flat background and slope are then fixed at these values; thus in the final fit to the smaller isotopes, only the line centre and isotope ratio are varied.

5.6 The Function-generating subroutine

The fitting routine E04FCF requires a subroutine, LSQFUN, which calculates the residuals for any set of parameter values. The subroutine is given the parameters X_i which are varied by E04FCF, and the initial estimates PE_i and step widths L_i. Using these it calculates the 'physical' parameters:-

$$P_i = PE_i \qquad \text{for a fixed parameter}$$

$$P_i = PE_i + X_i L_i \qquad \text{(no sum) for a variable parameter.}$$

The residuals R^μ are defined by

$$R^\mu = S^\mu - T^\mu \tag{15}$$

where the theoretical spectrum T^μ is given by

$$T^\mu = \left(\frac{P_2}{P_3}\right) \frac{V(x,P_4,P_5)}{V(0,P_4,P_5)} + P_6 + P_7(\mu-PE_1) + P_8(\mu-PE_1)^2 \tag{16}$$

where $V(x,\nu_G,\nu_L)$ is a Voigt profile, $x = (P_1-\mu)/|B|$ is the distance from line centre, and the parameters P_i are described in section 5.5. PE_1 is the initial estimate of P_1, the line centre, and so the sloping and curved backgrounds are zero at this channel number.

In fact the curved background parameter P_8 was always fixed at zero. It was included in the theoretical spectrum because it was thought that in the same way that it is necessary for the sloping background under smaller

isotopes due to the Doppler-broadened component of ^{40}Ca to be allowed for, the curvature of this component under ^{40}Ca itself might also be significant. In practice, however, the systematic differences between the Doppler-free component and a Voigt profile were sufficiently large to make this refinement inappropriate.

We now turn to the problem of evaluating the Voigt profile in equation 16. The function V is the convolution of a normalized Lorentzian (FWHM = ν_L) and a normalized Gaussian (FWHM = ν_G):

$$V(x,\nu_G,\nu_L) = \frac{b}{a\pi^{3/2}} \int_{-\infty}^{\infty} \frac{\exp(-y^2/a^2)}{(x-y)^2 + b^2}\, dy \tag{17a}$$

where

$$a = \nu_G/2\sqrt{\ln 2}, \qquad b = \nu_L/2. \tag{17b}$$

This integral can be expressed in terms of error functions of complex argument, or the function w(z) (see, for example, Abramowitz and Stegun, 1964):

$$V(x,\nu_G,\nu_L) = (2a\sqrt{\pi})^{-1}\left(w\left(\frac{x+ib}{a}\right) + w\left(\frac{-x+ib}{a}\right)\right. \tag{18a}$$

where w is related to the error function by

$$w(z) = e^{-z^2}\,\mathrm{erfc}(-iz) \tag{18b}$$

and

$$\mathrm{erfc}(z) = 2/\sqrt{\pi} \int_z^{\infty} e^{-z^2}\, dz\ . \tag{18c}$$

This is not directly of any help as the w function is not available on the 2980 computer. I used instead a subroutine written by Reichel, and described by Chiarella and Reichel (1968), for evaluating the integral in equation 17. This subroutine actually calculates the function

$$H(A,U) = \frac{A}{\pi} \int_{-\infty}^{\infty} \frac{\exp -(y^2/A^2)}{(U-y)^2 + A^2}\, dy \tag{19}$$

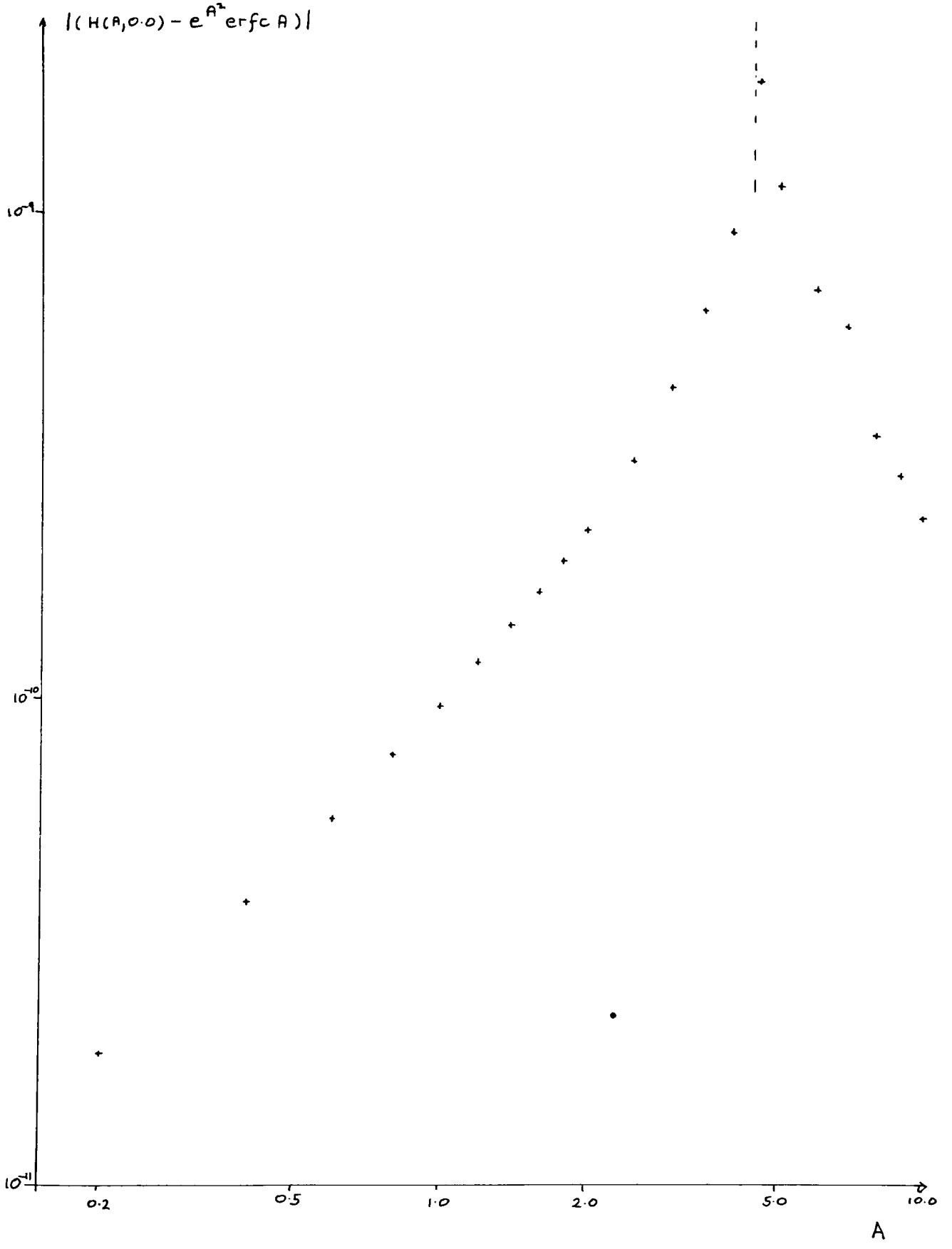


FIGURE 5.9 The Graph shows the difference between H(A,0.0) calculated using the subroutine VOIGT and the exact result. The subroutine uses different approximations for $A > 4.49$ and $A < 4.49$; the dividing line is marked.

and so

$$V(x,\nu_G,\nu_L) = \frac{1}{a\sqrt{\pi}} H(b/a,\ x/a). \tag{20}$$

Hence the ratio in equation 16 is given by

$$\frac{V(x,\nu_G,\nu_L)}{V(0,\nu_G,\nu_L)} = \frac{H(b/a,\ x/a)}{H(b/a,\ 0)} \quad , \tag{21}$$

and using this equation the whole of the expression in equation 16 can be calculated.

We note that at line centre (x=0) equation 18 simplifies to

$$V(0,a,b) = \frac{1}{a\sqrt{\pi}} \exp(-b^2/a^2)\mathrm{erfc}(b/a) \tag{22a}$$

or in terms of H

$$H(A,0) = \exp A^2\ \mathrm{erfc}\ A \quad . \tag{22b}$$

The complementary error function for real arguments is available on the 2980 computer and, using equation 22, the subroutine VOIGT can be tested. The difference (H(A,0) - $\exp A^2 \mathrm{erfc} A$) is plotted in Fig. 5.9 for a range of values of A. It can be seen that the subroutine gives an excellent approximation to the function H.

CHAPTER 6

RESULTS

6.1 Introduction

In this chapter the results obtained from the fitting procedure described in Chapter 5 are presented. In section 6.2 the values found for the line profile parameters, that is Lorentzian width, Gaussian width, isotope ratios etc, are briefly described and discussed. In section 6.3 the isotope shifts and their errors are fully described. The interpretation of these shifts, and the results of other experiments, is deferred to Chapter 7.

6.2 The Line Profile

The purpose of this section is to show that we have a good overall understanding of the line profile, despite the fact that, for the reasons discussed in Chapter 2, a detailed theoretical description of the line-shape of the Doppler-free component is not possible. It is necessary to establish this because the isotope shifts have been determined to a small fraction of a line width.

The first thing to establish about the observed spectrum is that we can correctly identify the isotope peaks. The peak due to ^{40}Ca is obvious because of the very large abundance of this isotope; the identification of the other peaks is straightforward when we recall that we expect the mass shift to be very much greater than the field shift, and so the peaks will spread out in mass-number order, with separations

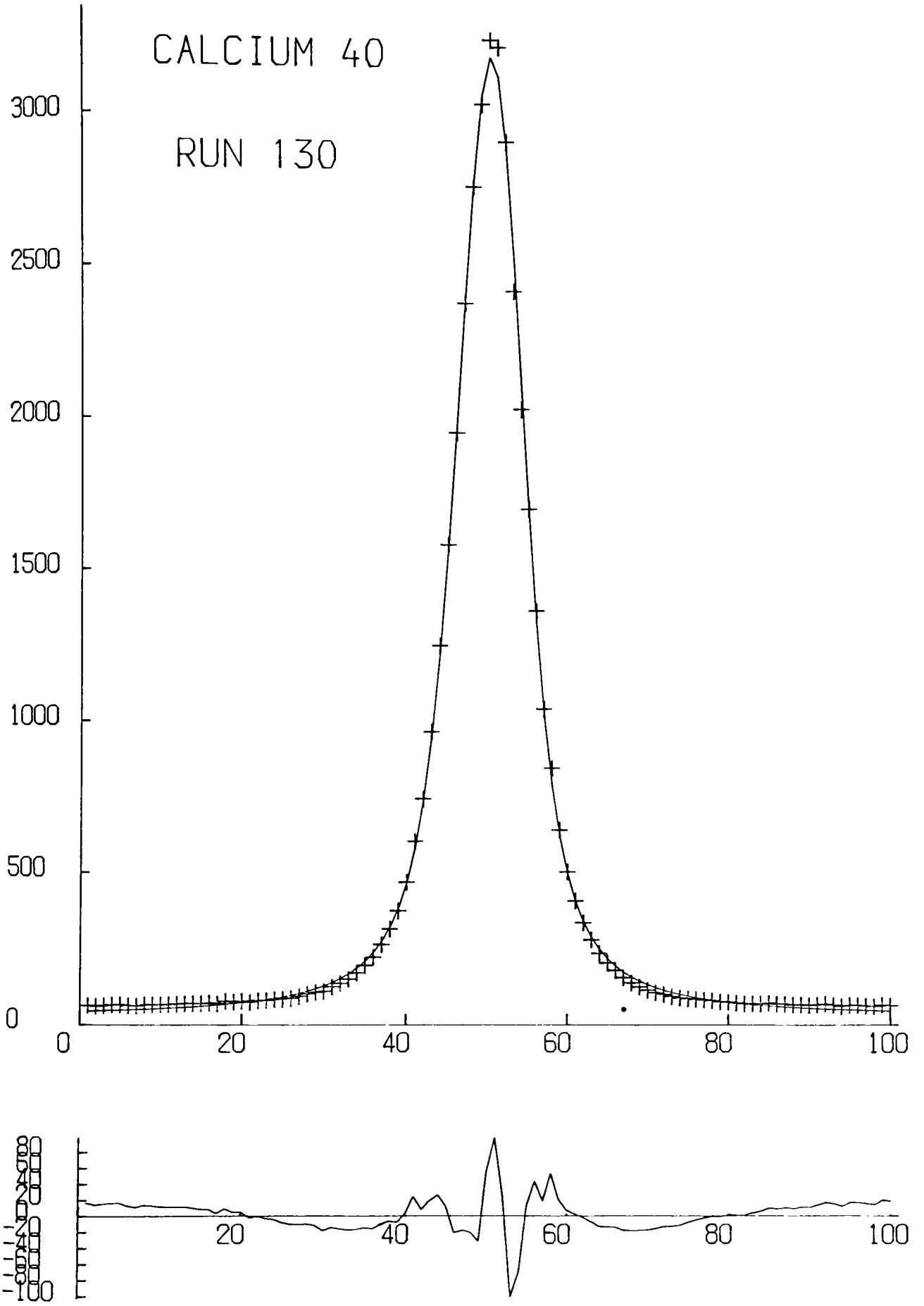


FIGURE 6.1 The upper curve shows the fitted profile and the crosses mark the data points. The residuals are shown below on an expanded scale.

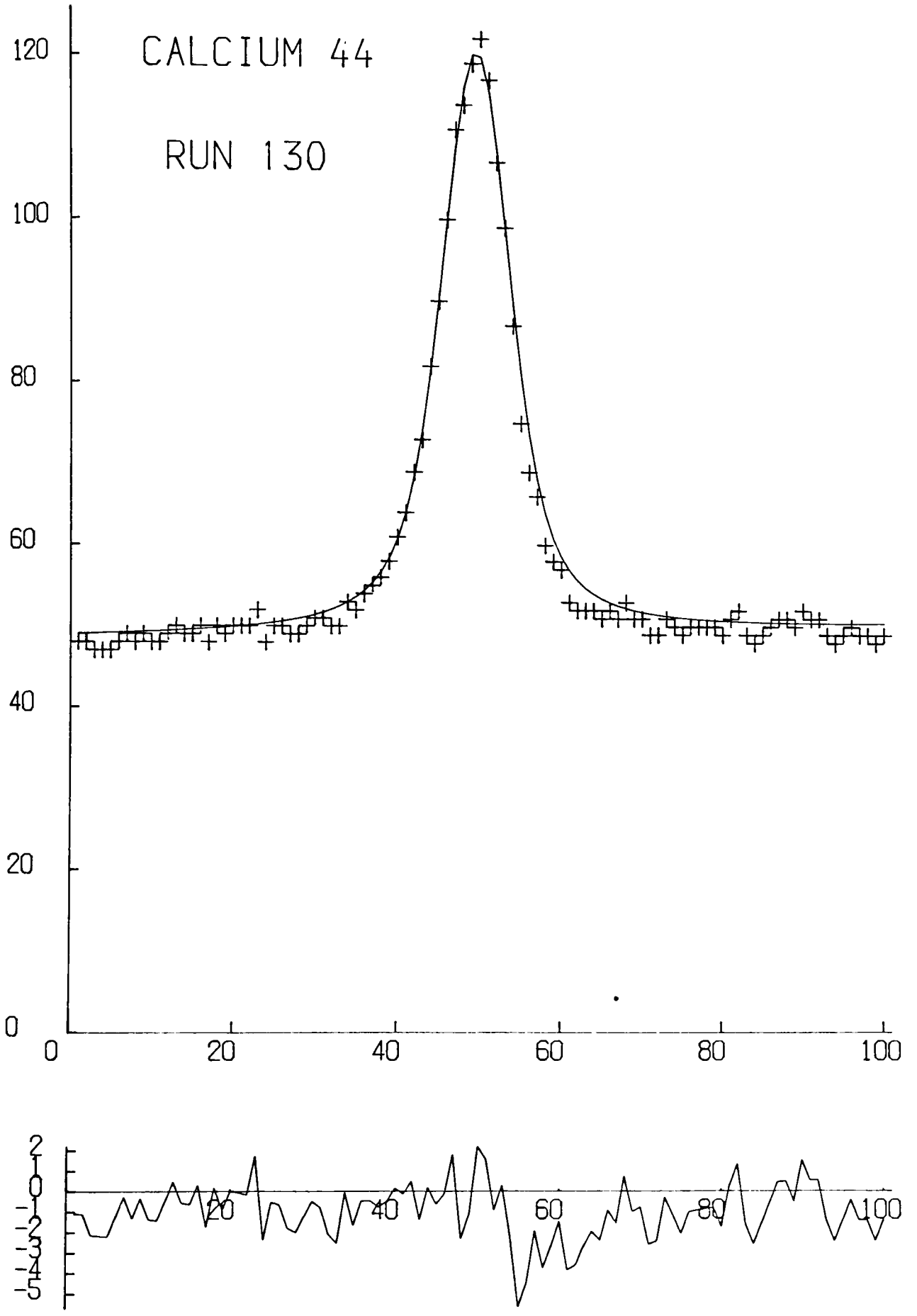

CALCIUM 44
RUN 130
120
100
80
60
40
20
0
0
20
40
60
80
100
2
1
0
-1
-2
-3
-4
-5
20
40
60
80
100

FIGURE 6.2

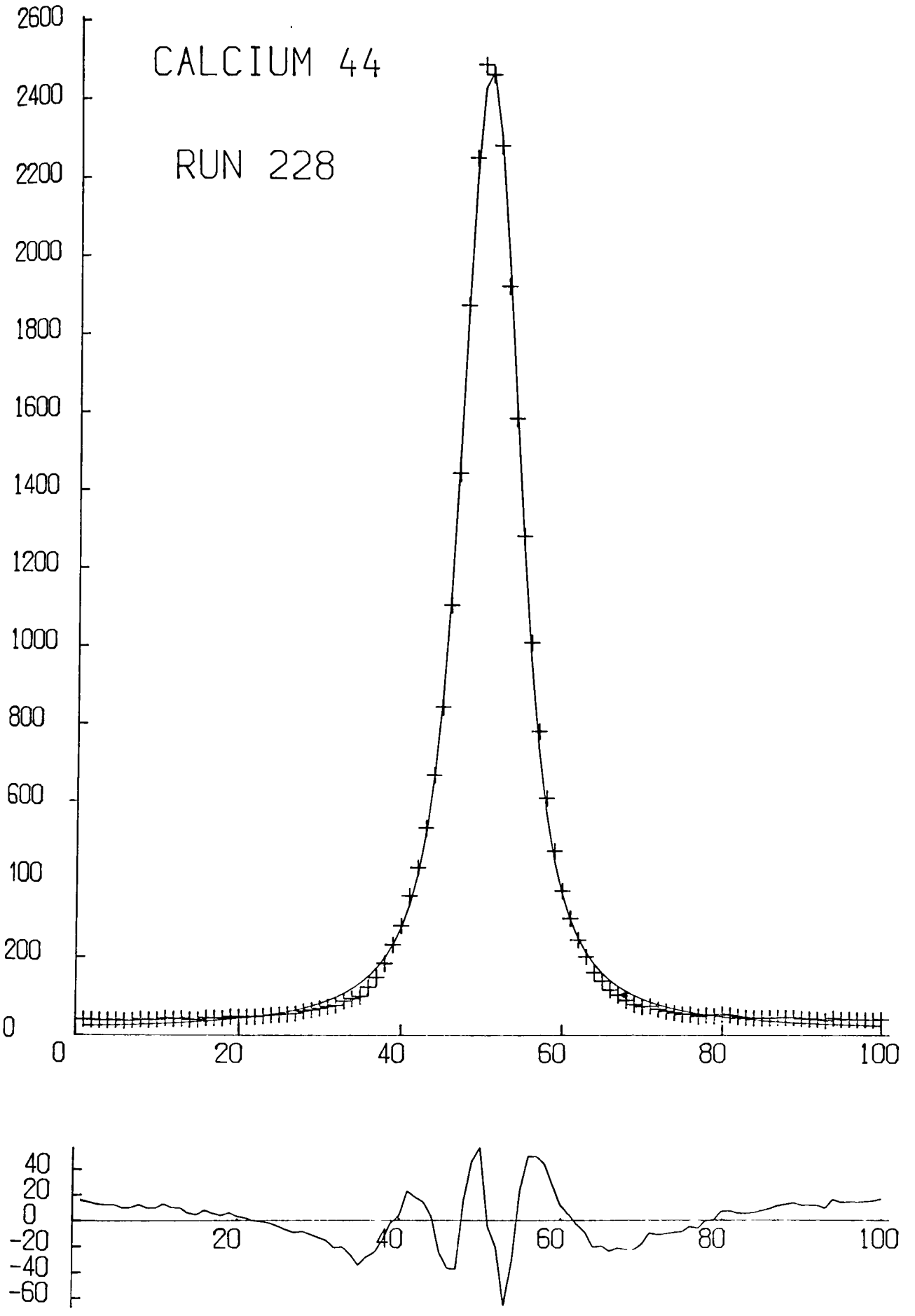

CALCIUM 44
RUN 228
2600
2400
2200
2000
1800
1600
1400
1200
1000
800
600
100
200
0
0
20
40
60
80
100
40
20
0
-20
-40
-60
20
40
60
80
100

FIGURE 6.3

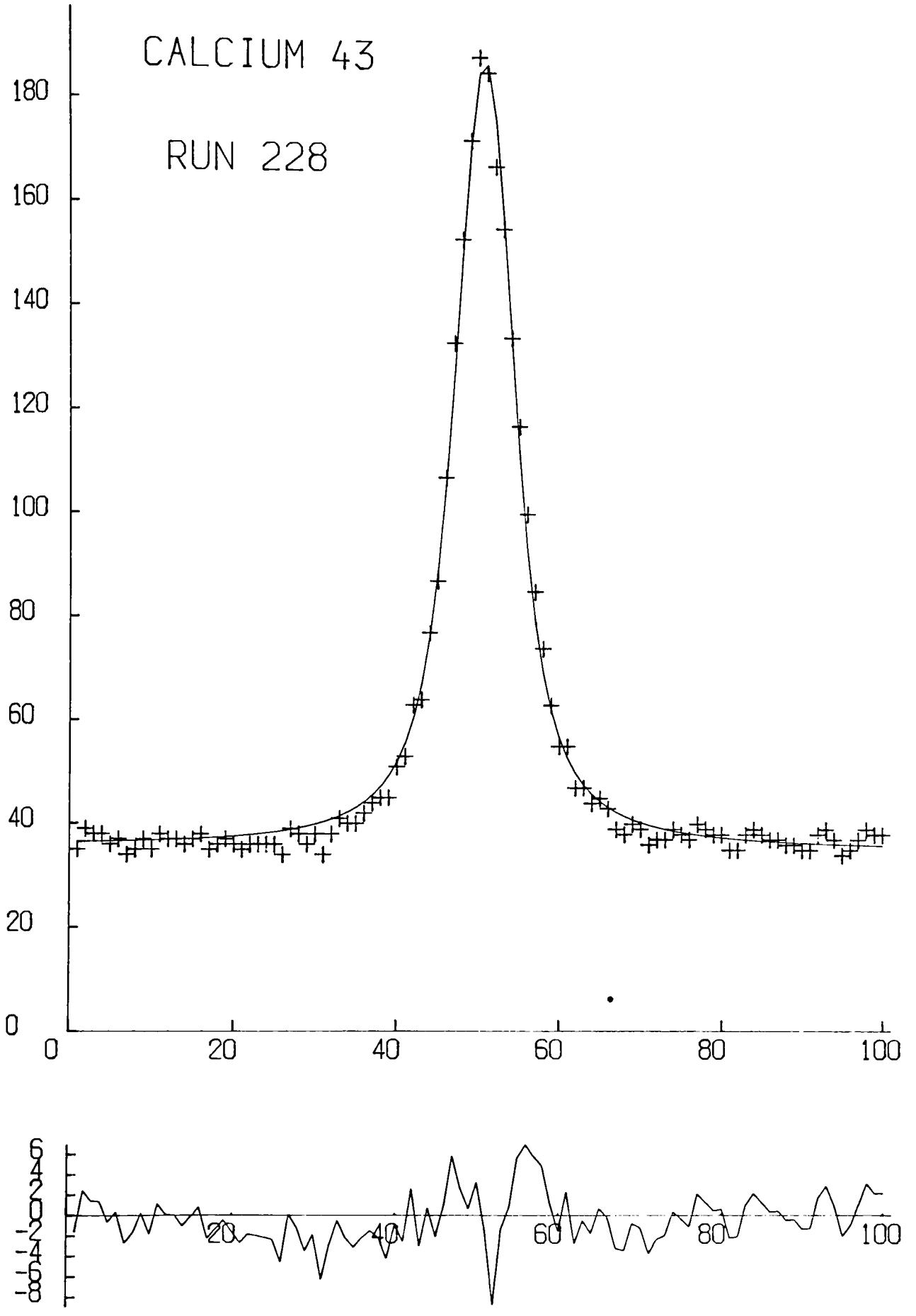

CALCIUM 43
RUN 228
180
160
140
120
100
80
60
40
20
0
0
20
40
60
80
100
6
4
2
0
-2
-4
-6
-8
20
40
60
80
100

FIGURE 6.4

roughly proportional to δA. This is exactly what we observe, as shown in, for example, Fig.4.6. A cross-check on this identification is provided by the peak heights, which should be proportional to the isotope abundances; this is dealt with below.

We now turn to the line profile. The least-squares fit of a Voigt profile to some typical peaks is shown in Figs 6.1 - 6.4. From these it is clear that the actual profile is not well described by Voigt profile, that is, for much of the profile the differences between the theoretical and experimental curves are systematic. It is also clear that the values obtained for the Lorentzian and Gaussian widths are influenced by the size of the fitted region, since at the edges of the fitted region the data lies above the theoretical curve, and the theoretical curve has too great a slope at this point. If we had fitted a larger region, then the least-squares fit would have fitted the wings of the line better, giving a smaller Lorentzian width and a larger Gaussian width, with consequential changes to the flat background. This effect can be seen in the original, global fitting shown in Fig. 6.5, where the wings of the line are correctly fitted, while the curvature in the places of greatest positive curvature (the 'shoulders' of the line) is greater in the data than in the fitted profile. Thus we can describe the deviation from a Voigt profile by saying that the curvature at the shoulders is greater than that of a Voigt profile with the same full width at half maximum, and slope of sides, as the actual profile.

Thus the separation into Lorentzian and Gaussian widths, in our analysis, is devoid of physical meaning, and simply provides a convenient two-parameter description of the line profile. It is important to have a reasonably good description of the central part of the profile for two reasons. Firstly the residuals provide a check on the symmetry of the line, which is very important since the primary aim of the experiment is to determine line separations, and the line position is ill-defined if the

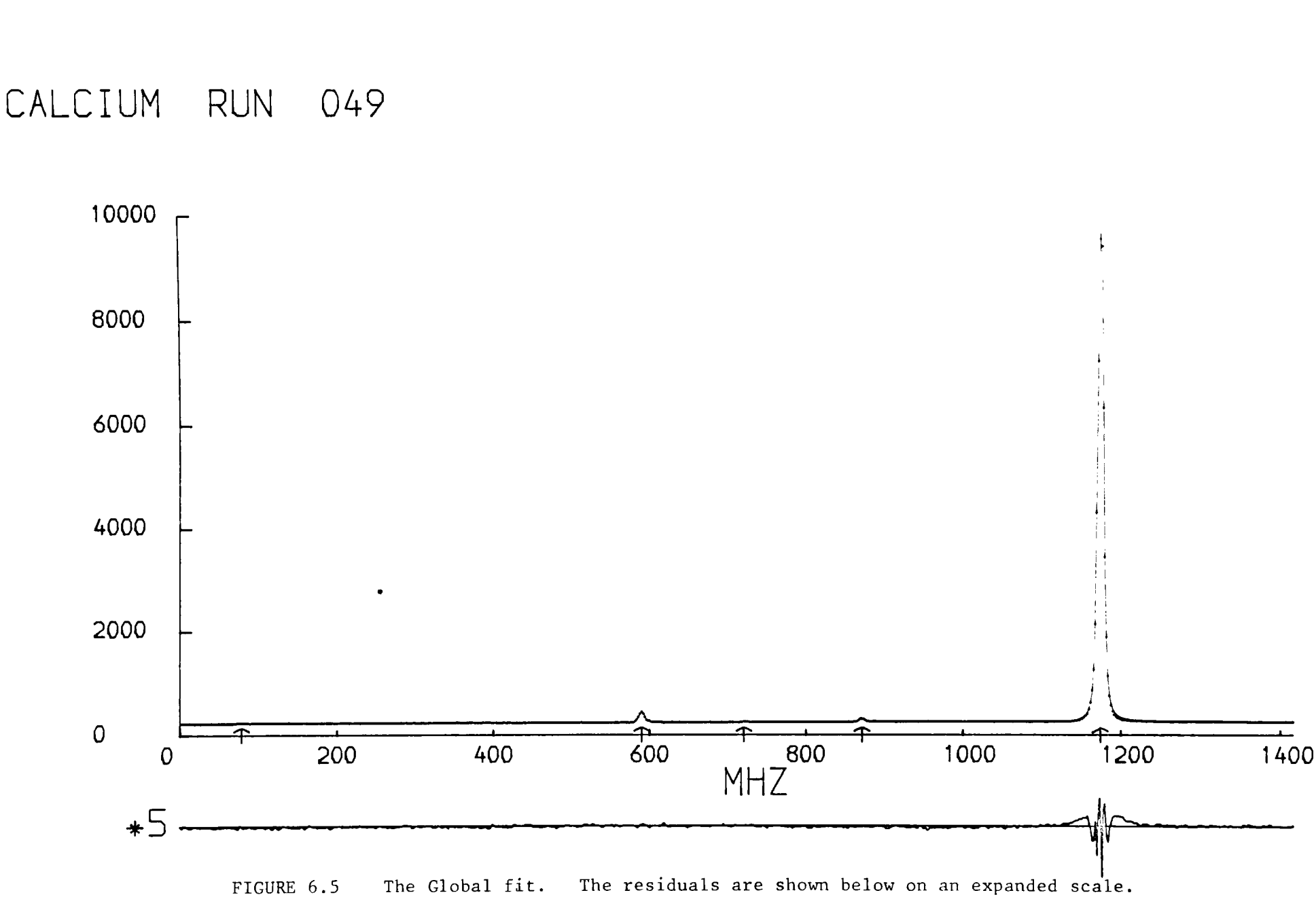


FIGURE 6.5 The Global fit. The residuals are shown below on an expanded scale.

line is asymmetrical. In addition to the appearance of the residuals an objective criterion was used as a test for significant asymmetry; if the centre of gravity of the line (calculated by the program FIT 40) differed by more than about 80 kHz from the fitted centre, the run was rejected. Secondly, we are using the fitted profile to interpolate between the data points to find the line centre, using the data from the whole profile, and this requires some curve to be fitted to the data points.

Fig. 6.6 shows the Lorentzian and Gaussian widths of all runs used in the determination of isotope shifts; with the above considerations in mind we note that the total linewidth is really the only significant quantity. Lines of constant FWHM are sketched on the diagram also. There are several points to be noted: except for run 014, a very early run, the first data set (first digit zero) have lines narrower than the second data set by about 1 MHz. These two sets were both taken with the same laser, but there was a change of focussing lens B between them. This would produce a change in the size of the laser waist, and so lead to a change in transit time broadening. On the other hand, the change between runs 128 - 131 and run 136 is almost certianly due to a change in laser adjustment, since runs 128 - 131 were taken on one day, and run 136 about a week later. The third data set, taken with the ring laser, have lines 1.5 - 2 MHz narrower than the second set. The optical system was unchanged between these two sets of runs, and so the change in laser is responsible. The ring laser is believed to have a rather narrower spectral width than the 580 A laser: its specification gives a width of 1 MHz, whereas we estimate the 580 A laser to have a spectral width of 3 - 4 MHz.

In the fitting procedure we assume that all the isotopes have the same profile, but scaled by an isotope ratio; thus in fitting a smaller isotope the line profile parameters are fixed at the values determined for the main isotope, and the isotope ratio allowed to vary. These ratios

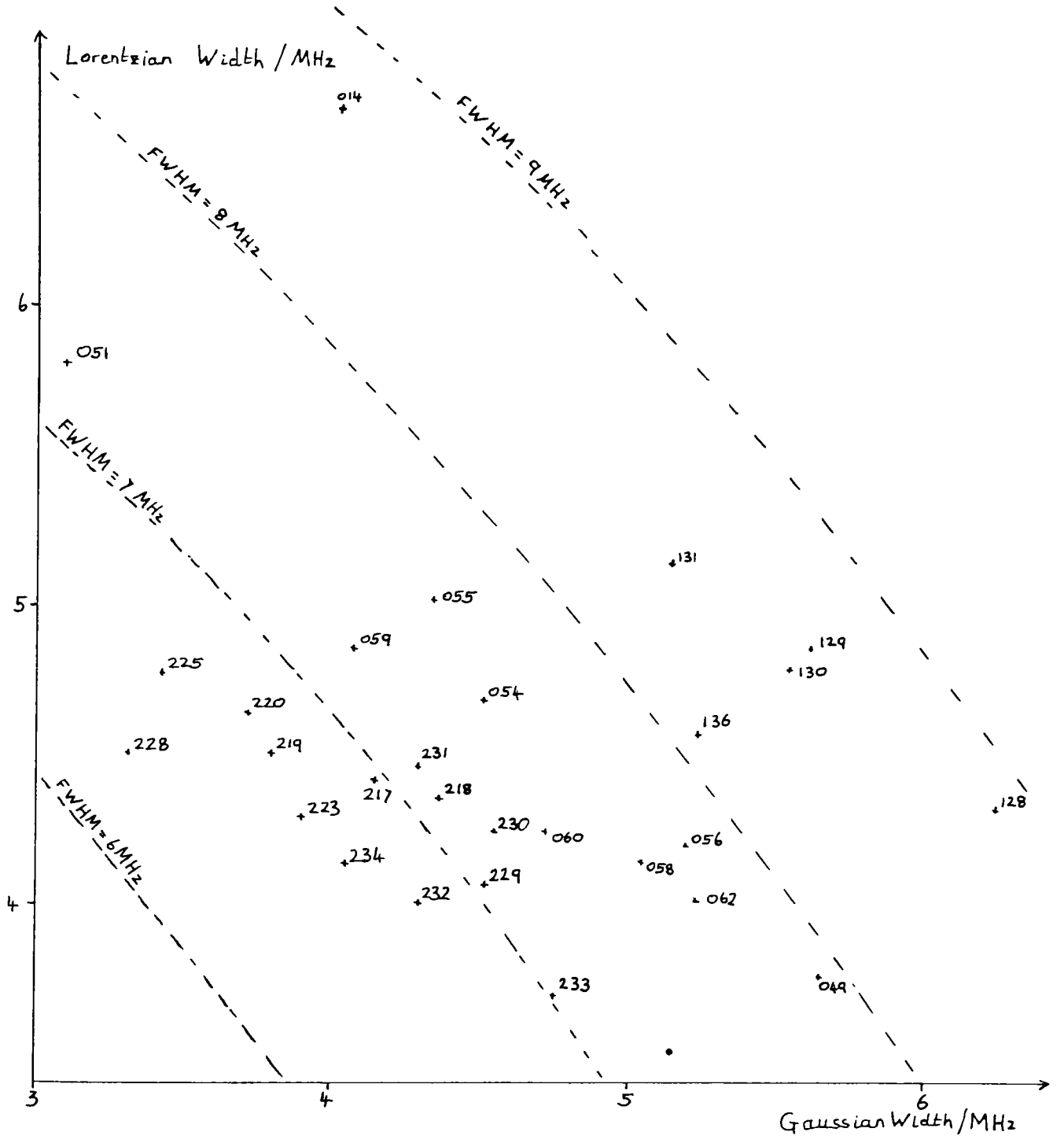


FIGURE 6.6 Gaussian and Lorentzian Widths of all runs used to determine Isotope Shifts, with contours of constant full width at half maximum intensity.

should therefore be consistent with the known isotopic abundances of the calcium isotopes. The isotope ratios and the resulting abundances are shown in Table 6.1, together with the abundances taken from the 1974 Chart of the Nuclides given earlier in Table 1.1. The agreement is very satisfactory.

Table 6.1 Isotope Ratios of Calcium Isotopes

The second column gives the ratio found in this work, and the third column the resulting percentage abundance. The abundances given in the fourth column are taken from the 1974 Chart of the Nuclides, published by Kernforschungszentrum, Karlsruhe.

A'/A	Isotope Ratio A'/A	Abundance (A)/%	
$40/40$	1.0	96.92	96.94
$40/44$	45.5(0.8)	2.13	2.08
$44/42$	3.45(6)	0.62	0.65
$44/43$	16.08(16)	0.132	0.14
$44/48$	10.65(50)	0.200	0.19

Finally we must consider the Doppler-broadened background. The overall fit of the background to a Gaussian can be seen by looking at Fig. 6.5; the total height of the Doppler-broadened component beneath ^{40}Ca is about 35 counts above the edge of the trace, while the residuals (shown below the main curve on an expanded scale), although showing some systematic behaviour, remain less than about 4 counts over the whole background. The Doppler-broadened component in this fit has an area of 0.5 x area of the Doppler-free component, and a full width at half maximum of 1500 MHz, showing a good agreement with the theory of Chapters 2 and 3. The factor by which the Doppler-broadened component is reduced in set 3 was estimated by finding the difference in the backgrounds between

isotopes ^{42}Ca and ^{48}Ca for sets 2 and 3, as a proportion of the total intensity. By this means the factor was found to be 71 ± 15.

6.3 Isotope Shifts

We now turn to the primary results of this experiment, the isotope shifts. The total number of runs taken onto paper tape was about 150, but the number of runs used to determine isotope shifts, after runs with poor calibration fringes, laser mode hops or line asymmetry were rejected, was 28. Runs from sets 1 and 2 were used to determine the isotope shift 40 - 44, and from set 3 the other isotope shifts. Although the smaller isotopes are visible on the earlier runs, the signal to noise ratio on ^{43}Ca and ^{48}Ca was poor, and since the calibration on these runs was generally worse then set 3 anyway it was felt that it would not be worthwhile analyzing these isotopes. On the better runs ^{42}Ca was measured, and this provides a second, less accurate, determination of the isotope shift 42 - 44.

The measurements were combined together using weights derived from a standard deviation assigned to each; we must now consider how these were obtained. The standard deviation is, of course, an estimate of the likely error in each measurement; part of this error comes from the limited accuracy with which we can assign a frequency, on the scale of calibration fringes, to a specified channel number. The deviation of the six or seven calibration fringes of the 2 m cavity from the local calibration parabola gives an estimate of this contribution to the error. We define this standard deviation to be $\Delta\nu_c$. Of course the centres of gravity of the fringes will be perturbed by a variety of effects, and not just interruptions of the smooth change of laser frequency: for example, sudden changes in laser intensity during the scan over a given fringe. It is

important to note, however, that such effects will also affect the centres of the isotope peaks, and by a similar extent, because the isotope peak has almost the same width as the calibration fringes, and so a similar averaging over a number of data points is involved in finding the centre of each. There will be other sources of error - jitter in the Helium-Neon laser, or in the length of the 2 m cavity, for example - which would mean that even if the fringes lay exactly on the parabola fitted to them, there would still be some uncertainty in assigning a frequency to a given channel number.

In addition to the error in assigning a frequency to a specified channel, there is the error in finding the centre channel number of the spectral line. The error in this is difficult to quantify, although we note that a similar error exists in finding the centre of the calibration fringes. However the fluorescent signal is much more sensitive to laser fluctuations, both in intensity and beam position. Tests done by fitting a particular ^{40}Ca peak with different Lorentzian and Gaussian widths and intensities showed that there is a small dependence (of order 10 KHz) of the channel number found for the line centre on the starting values of these parameters. Similar behaviour is expected for smaller isotope peaks also, and so we can say that the line centres are probably only defined to within 10 KHz. Because, with the exception of ^{46}Ca, only peaks with good signal to noise ratio are fitted there is no reason to suppose that what we might term the fitting error varies from isotope to isotope. Also, because the residuals are dominated by systematic deviations from a Voigt profile, the sum of the squares of the residuals is not a measure of the signal to noise ratio, only the total intensity, and so is not a suitable parameter to use in weighting.

To sum up then, we have a measure of the standard deviation of any isotope peak , except ^{46}Ca, in the deviation of the calibration fringes from the fitted parabola ($\Delta\nu_c$). However it is not unlikely, for various

causes, some physical and some associated with the fitting, that the true standard deviation is larger than this, but we have no a priori information as to how it varies from run to run or from isotope to isotope. The correct procedure is thus to take as standard deviation for each isotope peak

$$\sigma = (\Delta\nu_c^2 + \Delta\nu_e^2)^{\frac{1}{2}} \tag{1}$$

where the extra standard deviation, $\Delta\nu_e$, is adjusted to match the observed scatter in a way to be described below, and is the same for all runs taken with that laser; that is we have one value of $\Delta\nu_e$ for the 580 A laser, and another value for the ring laser. $\Delta\nu_c$ is found from the information supplied by the fitting program, namely S, the sum of squared deviations from the calibration parabola, and the number of fringes used to determine the parabola N. Since the deviations are subject to three constraints, the estimate of the mean square deviation is

$$\Delta\nu_c^2 = S/(N-3) \tag{2}$$

Equation 2 gives the standard deviation of the position of 1 peak relative to the fringes; for the standard deviation of a shift we use

$$\Delta\nu_c^2 = \frac{S_1 + S_2}{N_1 + N_2 - 6} \tag{3}$$

where S_1, S_2, N_1, N_2 are the values of S and N for the two peaks; in both cases the standard deviation of the measurement is derived from equation 1, although the value of $\Delta\nu_e$ is also different in the two cases.

I should insert here a note about units. The isotope shifts are calculated in units of the free spectral range of the 2 m cavity; however certain quantities, for example Lorentzian and Gaussian widths, and standard

deviations, are expressed in frequency units (MHz, kHz) in order to make their magnitude more readily apparent to the reader. For this purpose the rough conversion 1 fsr = 38.75 MHz was used. Weights are multiplied by $k = 0.01\,\mathrm{MHz}^2$ to make them dimensionless; a weight of 1 is then equivalent to a standard deviation of 100 kHz.

We first present results for the isotope shift $\delta\nu^{40-44}$ using 15 runs from data sets 1 and 2. The shifts are found by taking the difference of the frequencies assigned to the two isotope peaks, and the weight for the i th run is given by

$$w_i = k/\sigma_i^2 \tag{4}$$

where σ_i is given by equation 3 and $k = 0.01\,\mathrm{MHz}^2$ as explained above. The weighted mean is given by

$$\bar{\nu} = \sum_i w_i\nu_i \Big/ \sum_i w_i \tag{5}$$

and its standard deviation by

$$\sigma_m = \left[\sum_i w_i(\nu_i - \bar{\nu})^2 \Big/ \sum_i w_i\,(N-1)\right]^{\frac{1}{2}} \tag{6}$$

where N is the number of runs. However we can also calculate the standard deviation of the mean by combining the standard deviations of the runs in the usual way:-

$$\sigma'_m = \left[\sum 1/\sigma_i^2\right]^{-\frac{1}{2}} = \left[k/\sum w_i\right]^{\frac{1}{2}} \tag{7}$$

Equations 6 and 7 tell us what value of $\Delta\nu_e$ to use - it is that value which makes $\sigma_m = \sigma'_m$. The ratio of the two is found to be

Table 6.2 Isotope Shifts from Data Sets 1 and 2

The column headed CAL S.D. gives $\Delta\nu_c$, and that headed O/A S.D. gives σ from equation 1, using $\Delta\nu_e$ = 0.47 MHz, except that for Data set 1 the standard deviation has been increased (see text).

Calcium 40-44

RUN	CAL.S.D. (MHz)	O/A S.D. (MHz)	WEIGHT	SHIFT (fsr)
014	0.411	0.659	0.023	-15.10704
049	0.082	0.523	0.037	-15.09742
051	0.138	0.535	0.035	-15.10910
054	0.089	0.524	0.036	-15.10174
055	0.091	0.525	0.036	-15.10694
056	0.122	0.531	0.035	-15.10337
058	0.168	0.543	0.034	-15.10155
059	0.082	0.523	0.037	-15.08330
060	0.161	0.541	0.034	-15.11249
062	0.224	0.563	0.032	-15.10473
128	0.188	0.506	0.039	-15.13878
129	0.089	0.478	0.044	-15.09733
130	0.232	0.524	0.036	-15.12292
131	0.481	0.672	0.022	-15.11847
136	0.136	0.490	0.042	-15.12225
			Sum = 0.522	Mean = -15.10840
				Rms.dev. = 0.01329
				S.D. of mean = 0.00355

Table 6.2 Continued

Calcium 42-44

RUN	CAL.S.D. (MHz)	O/A S.D. (MHz)	WEIGHT	SHIFT (fsr)
049	0.144	0.502	0.040	-7.27445
054	0.176	0.512	0.038	-7.28078
128	0.250	0.532	0.035	-7.27996
129	0.152	0.494	0.041	-7.25952
130	0.154	0.495	0.041	-7.27825
131	0.353	0.588	0.029	-7.29540
136	0.186	0.505	0.039	-7.26703
		Sum =	0.263	Mean = -7.27557
				Rms.dev. = 0.01011
				S.D. of mean = 0.00413

$$(8) \qquad \frac{\sigma_m^2}{(\sigma'_m)^2} = \frac{1}{N-1} \sum \frac{(\nu_i - \bar{\nu})^2}{\sigma_i^2}$$

which is χ^2 per degree of freedom. Thus in effect we are adjusting the standard deviation of the runs to make χ^2 per degree of freedom equal to one.

For data from the first set there is one slight complication - in between the two sets of measurements, one of the 2 m cavity mirror mounts was altered, which had the effect of changing the cavity length slightly. The two values were measured to be

$$(9) \qquad \text{Data set } 1 \qquad L_1 = 1934.3(0.5) \text{ mm}$$
$$\text{2 \& 3} \qquad L_2 = 1935.1(0.5) \text{ mm}$$

The values of the shifts from data set 1 were accordingly multiplied by $L_2/L_1 = 1 + 4.14 \times 10^{-4}$ and their standard deviation increased by the error, that is 3.5×10^{-4} of the shift.

To sum up:

$$(10) \qquad \text{Data set 2} \qquad \sigma^2 = \Delta\nu_c^2 + \Delta\nu_e^2$$
$$\text{Data set 1} \qquad \sigma^2 = \Delta\nu_c^2 + \Delta\nu_e^2 + 0.046 \text{ MHz}^2$$

In order to make χ^2 equal to one it was necessary to have $\Delta\nu_e = 0.47$ MHz. The results are presented in Table 6.2; it can be seen that a typical value of $\Delta\nu_c$ is 0.2 MHz.

Table 6.3 contains a similar analysis for data set 3. The improved performance of the ring laser over the 580 A laser can be seen from the fact that a typical $\Delta\nu_c$ is 70 kHz, and $\Delta\nu_e$ is found to be 80 kHz. The values of the isotope shifts given in table 6.3 are not, however, the best possible values from this set of data because of the problem of coupled errors, which

Table 6.3 Isotope Shifts from Data Set 3

Calcium 42-44

RUN	CAL. S.D. (MHz)	O/A S.D. (MHz)	WEIGHT	SHIFT (fsr)
217	0.193	0.021	0.228	-7.27697
218	0.107	0.013	0.562	-7.28548
220	0.289	0.030	0.111	-7.28276
228	0.105	0.013	0.572	-7.27577
229	0.065	0.010	0.943	-7.28298
230	0.048	0.009	1.151	-7.27659
231	0.063	0.010	0.960	-7.27582
232	0.080	0.011	0.785	-7.28010
233	0.059	0.010	1.010	-7.28033
234	0.077	0.011	0.809	-7.28045
			Sum = 7.132	Mean = -7.27943
				Rms. dev. = .00305
				S.D. of mean = .00102

Table 6.3 Continued

Calcium 43-44

RUN	CAL.S.D. (MHz)	O/A S.D. (MHz)	WEIGHT	SHIFT (fsr)
217	0.086	0.021	0.475	-3.40457
218	0.050	0.011	0.880	-3.40418
219	0.074	0.019	0.538	-3.40291
220	0.082	0.019	0.527	-3.40780
225	0.073	0.016	0.612	-3.39997
228	0.068	0.015	0.664	-3.40258
229	0.044	0.010	0.969	-3.40581
230	0.035	0.009	1.153	-3.40772
231	0.046	0.010	0.970	-3.40756
232	0.038	0.009	1.095	-3.40403
233	0.047	0.011	0.949	-3.40521
234	0.044	0.010	1.003	-3.40351
		Sum =	9.835	Mean = -3.40488
				Rms.dev. = .00214
				S.D. of mean = .00065

Table 6.3 Continued

Calcium 48-44

RUN	CAL.S.D. (MHz)	O/A S.D. (MHz)	WEIGHT	SHIFT (fsr)
219	0.085	0.014	0.738	13.22452
223	0.120	0.021	0.481	13.21410
225	0.145	0.027	0.364	13.21938
228	0.106	0.018	0.566	13.21675
229	0.066	0.011	0.935	13.21123
230	0.063	0.010	0.968	13.21789
231	0.080	0.013	0.785	13.21799
232	0.063	0.010	0.968	13.21691
233	0.056	0.010	1.043	13.21714
234	0.058	0.010	1.026	13.21613
		Sum =	7.873	Mean = 13.21704
				Rms.dev. = .00321
				S.D. of mean = .00107

did not arise in the case of data sets 1 and 2 because only one isotope shift is measured on each run (except for ^{42}Ca, which is measured on a few runs as well.) The coupled error problem can be visualized in the following way; imagine the isotope positions found on each run marked on separate strips of paper. The analysis of Table 6.3 is equivalent to the situation shown in Fig. 6.7 where all the ^{44}Ca peaks are lined up, and

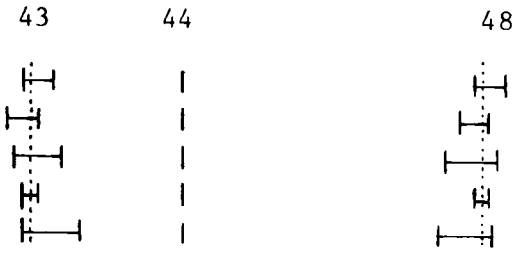


Fig. 6.7 The diagram shows the measured positions of 3 isotopes on a number of runs. The measurement of ^{44}Ca is assumed infinitely accurate, with all the error attributed to the other isotope positions.

isotope positions and errors worked out from the scatter of the corresponding marks. Thus an error in a ^{44}Ca position contributes to all the shifts measured on that run. However information in this case is not being used - the isotope shifts 43 - 48 for example - which could be used to estimate the error of the ^{44}Ca position. The better way to proceed is to move the pieces of paper to minimize the scatter on each isotope separately and then determine the shifts. The theory of this is worked out in Appendix B, and a computer program was written to implement this procedure. The output of this program is presented and explained in the Appendix; here we give the results with their errors in Table 6.4. Fig. 6.8 shows the results pictorially; the solid vertical lines show the 4 isotopes in their correct relative positions. The vertical dashed lines show one standard deviation about each isotope position, multiplied by 200. Each run is labelled with its index number, and is shown as a number of bars of length ± 1 standard deviation for each peak, also multiplied by 200.

FIGURE 6.8

The vertical lines show the isotope positions on a frequency scale; the dashed lines show standard deviations of these positions, increased by a factor of 200. The bars show individual measurements, with their uncertainty also increased by 200.

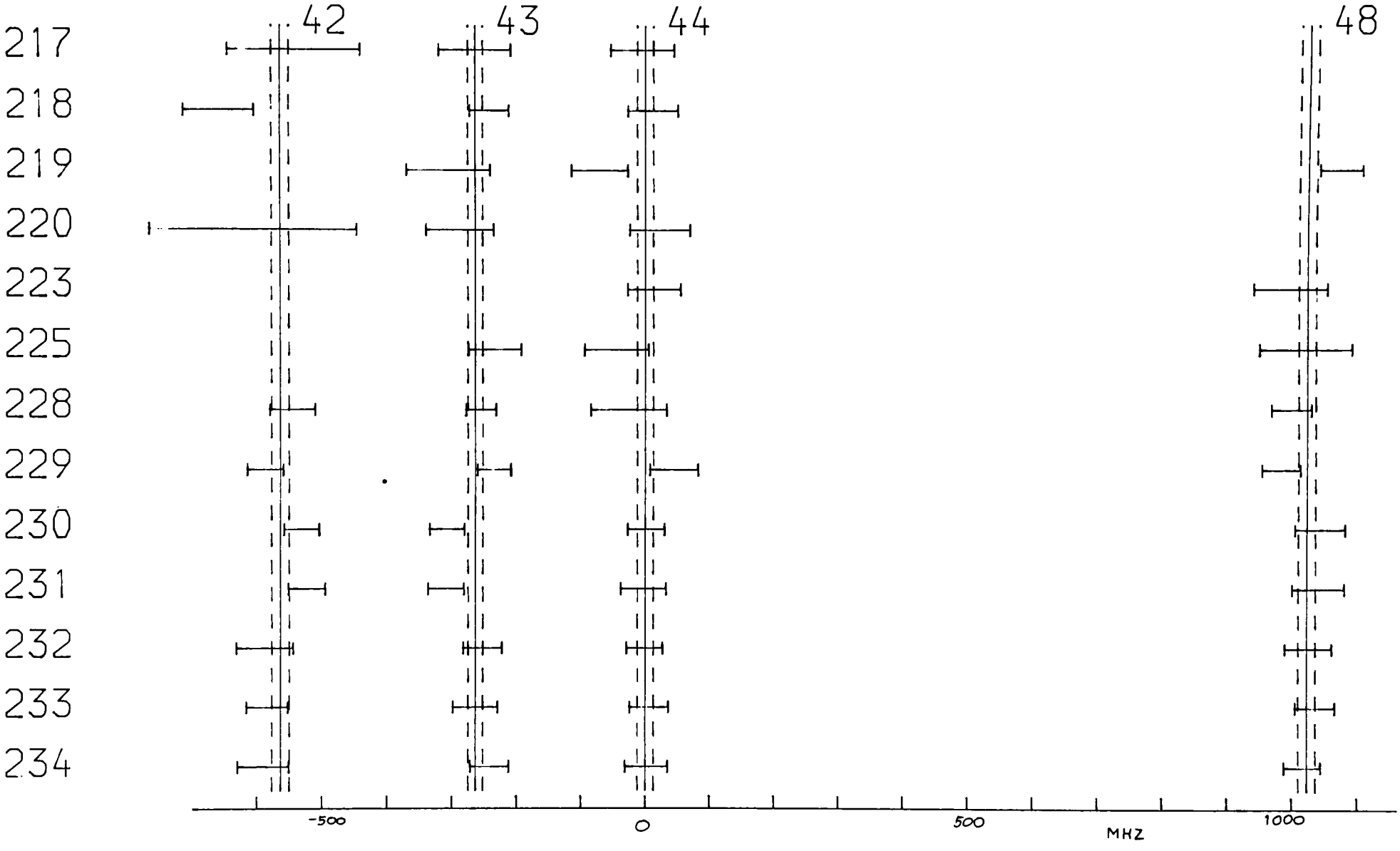


TABLE 6.4 Isotope Shifts from Data Set 3

A	Isotope shift A-44/fsr	standard deviation/fsr
42	-7.27861	0.00087
43	-3.40481	0.00075
48	13.21667	0.00085

TABLE 6.5 Isotope Shift $\delta\nu^{46-44}$

run	signal found on trace/counts	rms noise on trace	(s/n)	shift 46-44 /fsr
217	3.38	2.028	2.8	6.88501
220	3.61	1.255	8.3	6.89472
228	5.25	1.620	10.5	6.90499
229	3.67	2.333	2.5	6.91408
230	3.89	2.395	2.6	6.97293
233	4.13	1.617	6.5	6.88340
234	6.62	2.964	5.0	6.88321
			mean =	6.90000
			rms dev. =	0.02209
			s.d. of mean =	0.00902

Finally we must consider ^{46}Ca. Fig.6.9 shows this isotope on a number of runs, and we note that the accuracy in determining the line centre is dominated by the signal to noise ratio, and so the calibration accuracy is of negligible importance. Only those runs were used for which the (peak height)^2 was greater than 2.5 times the mean square residual, and for which the signal found was roughly consistent with the signal expected on the basis of the sizes of the other isotope peaks and the isotope ratio. The runs were weighted by the signal to noise ratio squared. In this case the differences of the frequencies of the two peaks was not used to find the shift $\delta\nu^{46-44}$, but fitted position of ^{44}Ca using all the other isotopes and the isotope shifts was used in place of the measured line centre of ^{44}Ca. A table of these positions is produced by the above mentioned computer program, as explained in Appendix B. The results are given in Table 6.5.

All the results quoted so far have been in units of free spectral ranges of the long cavity, and refer to the frequency change of the dye laser between isotope peaks; the shift in the atomic transition is exactly twice as large, because of the two-photon absorption. Using the length

$$L_2 = 1935.1(0.5)\ \text{mm}$$

and $c = 2.99793\ 10^8\ ms^{-1}$, refractive index of air $\mu = 1 + 2.77 \times 10^{-4}$ we find the free spectral range to be

$$\Delta\nu_{fsr} = c/4\mu L = 38.720(10)\ \text{MHz}.$$

We here summarize in Table 6.6 the results of this section, multiplying each shift by $2\Delta\nu_{fsr} = 77.440\ \text{MHz}$. We have not, however, increased the quoted error, because the uncertainty in the free spectral range is an error of a quite different sort from the errors in the shifts themselves. It is an

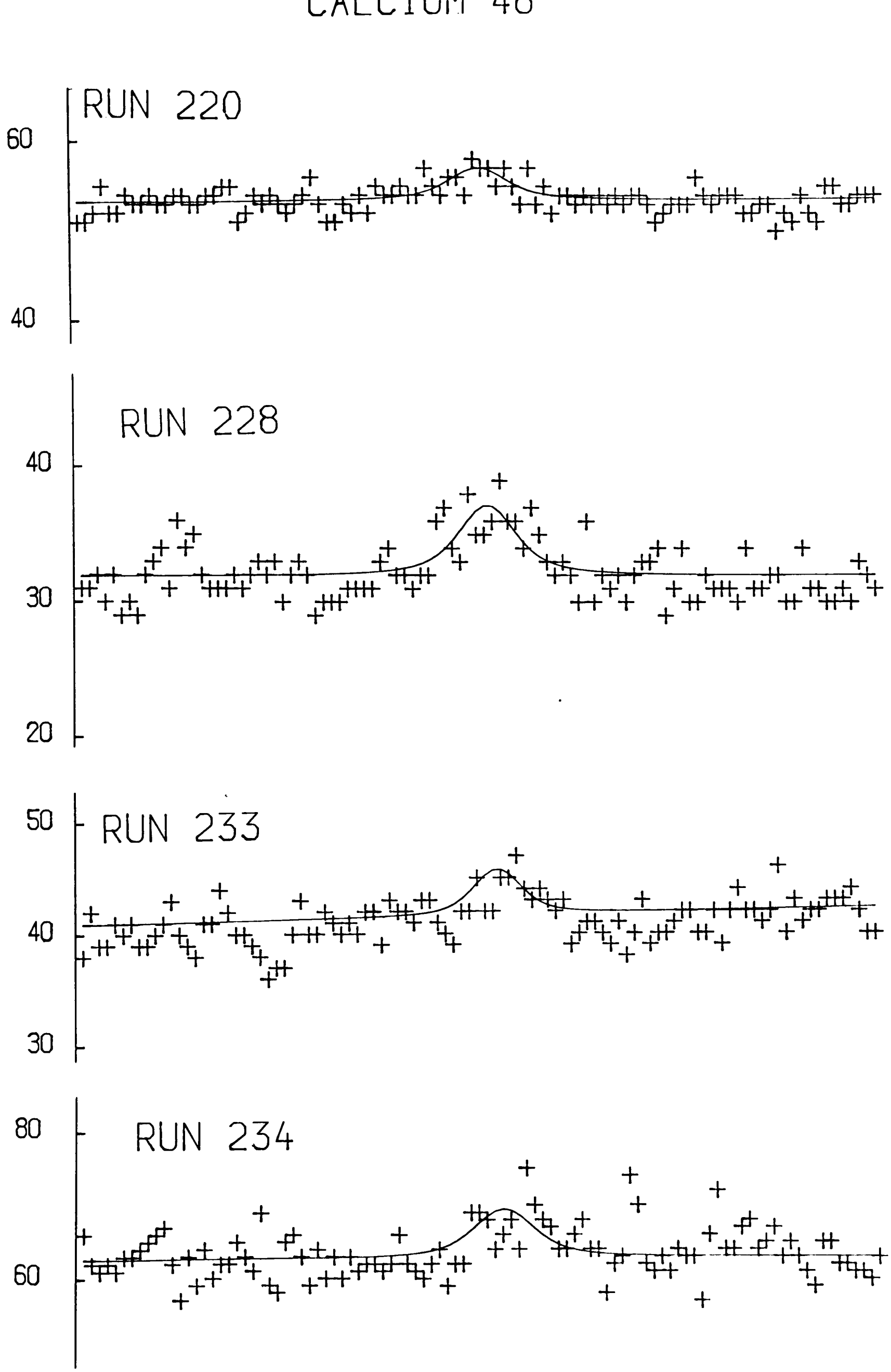


FIGURE 6.9 ^{46}Ca on four runs.

The solid line shows the fitted spectrum.

uncertainty of scale, and does not affect the relative sizes of the shifts. Thus all the shifts are subject to an uncertain scale factor of $1 \pm 2.6 \times 10^{-4}$.

Table 6.6

A	Isotope Shift A-44 / MHz	Standard deviation /MHz
40	-1169.99	0.28
42	-563.66	0.07
43	-263.67	0.06
46	534.34	0.70
48	1023.50	0.07

CHAPTER 7

DISCUSSION OF RESULTS

7.1 Introduction

In this Chapter the results presented in Chapter 6 are interpreted, together with other experimental results, within the framework of the theory of isotope shifts presented in Chapter 1. In section 7.2 I compare the accurate isotope shift measurements in three spectral lines by means of the King plot, and derive the best consistent values of the isotope shifts in these transitions. This requires a correction to be made for the additional isotope shift due to the hyperfine interaction; the theory of this effect, and a calculation for the levels of interest, is presented in section 7.3. These isotope shifts are then used, in section 7.4, together with measurements of $\delta\langle r^2\rangle$ by muonic atom isotope shifts, to derive values for $\delta\langle r^2\rangle$ of increased precision. These results are then briefly discussed, and the experimental situation with regard to the determination of $\delta\langle r^2\rangle$ of calcium isotopes summarized.

7.2 Comparison of Isotope Shifts using the King Plot

In this section I shall compare sets of isotope shifts, measured in different transitions, using the King Plot (equation 13 of Chapter 1). As we anticipated in Chapter 1, the three sets of isotope shifts to be compared are the results of this work (Table 6.6), the results of Bergmann et al. (1980) in the intercombination line and preliminary results from the experiment at Kernforschungszentrum Karlsruhe (Schatz, 1981, private communication)

in the resonance line. These results are given in Table 7.1. The standard deviations of Bergman et al. include an error of 4×10^{-4} of the shift added quadratically to the experimental standard deviation, to allow for the uncertainty in the free spectral range of their calibration etalon. This is similar to the 2.6×10^{-4} uncertainty which I have not included in our results because it is a scaling factor, and so does not affect the linearity of King plots. Thus for consistency this should be subtracted off the quoted standard deviations of Bergmann et al. Because the difference of the two squares is rather sensitive to rounding in the quoted standard deviations (which are rounded to the nearest 100 kHz), 50 kHz was added linearly to each standard deviation before the subtraction of the squares. These reduced standard deviations are also given in Table 7.1.

It is very important that the comparison of these results is performed in such a way as to use all the information contained in them. Since they do not all refer to the same isotope pairs, and also have very different errors associated with them, due to the particular problems of each experiment, this is not straightforward to do without introducing coupling between the errors, which ought to be avoided if possible. Furthermore, comparisons of these lines in pairs in the form of equation 13 of Chapter 1 does not lead to a single set of isotope shifts which is the most consistent with all the measured data. It is thus necessary to compare all the data simultaneously; the method adopted is described in Appendix C section 2, and I shall give a brief description of it here.

We are comparing the isotope shifts of the stable calcium isotopes in three transitions, and so we consider the vector of measured isotope shift values $\underline{z}$ (a 15-vector for three transitions) and a set of values $\underline{x}$ which exactly satisfy the King relations (equation 1.13) between the isotope shifts in the different spectral lines. The solution we seek is that which minimizes

$$\chi^2 = \sum_i (z_i - x_i)^2 / \sigma_i^2 \quad .$$

TABLE 7.1. Isotope Shifts in Calcium Measured by Laser Spectroscopy.

λ 423nm G. Schatz (1981, private communication).

λ 657nm Bergmann et al. (1980). The second error is the reduced standard deviation (see text).

A	λ 423 nm $\delta\nu^{A-40}$ / MHz	λ 657 nm $\delta\nu^{A-40}$ / MHz
42	391.1 (0.78)	509.5 (3) (0.28)
43	611.0 (0.98)	782.2 (7) (0.68)
44	770.8 (0.80)	996.2 (5) (0.38)
46	1158.9 (0.74)	1481.1 (7) (0.46)
48	1510.7 (0.84)	1922.5 (8) (0.36)

TABLE 7.2. Nuclear Masses of Calcium Isotopes.

The atomic masses are in amu and are taken from Wapstra and Bos (1977). The nuclear masses are given by $M_N = M_A - 20m_e + m_B$, where m_B, the binding energy, is 17.74 keV. The quantity $\alpha_{AA_o} = AA_o/(A-A_o)$ is given for A_o = 40 and 44.

A	Atomic Mass	Nuclear Mass	α_{AA_o} A_o = 44	A_o = 40
40	39.9625907(9)	39.9516381(9)	-439.69512(20)	-
41	40.9622776(9)	40.9513250(9)	-659.85990(30)	1636.5849(21)
42	41.9586218(15)	41.9476692(15)	-923.1333 (10)	839.6052 (8)
43	42.9587704(15)	42.9478178(15)	-1893.543 (4)	572.6745 (3)
44	43.9554848(15)	43.9445322(15)	-	439.69512(20)
45	44.9561894(16)	44.9452368(16)	1973.707 (4)	359.58753(14)
46	45.953689 (4)	45.942736 (4)	1010.373 (2)	306.36915(24)
47	46.954543 (4)	46.943590 (4)	687.8541(9)	268.23316(18)
48	47.952532 (4)	47.941579 (4)	527.0817(5)	239.71950(15)

The results of the program are the values of $\underline{x}$, the King parameters ζ and μ and a variance/covariance matrix allowing the error in any fitted shift to be determined. The goodness of fit is indicated by the minimum value of χ^2, which should be roughly equal to the number of degrees of freedom (three for a comparison of two spectral lines, six for a comparison of three spectral lines, with five isotope shifts per line). The program requires values of

$$\alpha_{AA_o} = AA_o/(A - A_o) ,$$

where the A's are nuclear masses in amu, for pairs with $A_o = 40$ and $A_o = 44$. These were taken from the 1977 Atomic Mass Evaluation (Wapstra and Bos, 1977) with the mass of the electrons subtracted off and their binding energy added. The values used are given in Table 7.2.

Firstly the program was used to compare the isotope shifts of this experiment with those of Bergman et al., using the quoted standard deviations. The minimum χ^2 was 3.16, indicating a satisfactory fit. However when the reduced standard deviations referred to above were used the χ^2 increased to 3.81, a slightly high value, and from the differences between fitted and experimental shifts it was clear that the major discrepancy was in the shift $\delta\nu^{43-40}$ of the intercombination line, for which the fitted shift lay 1.3 standard deviations (0.9 MHz) away from the measured shift.

This discrepancy was slightly reduced when the isotope shift due to the second-order effect of the hyperfine interaction was subtracted. This is calculated in section 7.3, where it is found that the only significant shift is in the 4s4p $^3P_1$ state, where it has the value of 0.14 MHz. The correction of the measured isotope shift for this effect reduced the χ^2 to 3.31, with the largest discrepancy still in the shift $\delta\nu^{43-40}$ of the intercombination line.

When the preliminary data for the isotope shifts in the resonance line are included, the value of χ^2 increases to 9.48, a distinctly high value.

Again the largest discrepancy is in the shift $\delta\nu^{43-40}$, but this time in the resonance line; the fitted value lies 2.2 standard deviations, or 2.2 MHz, away from the measured value, in the same direction as the discrepancy in the intercombination line, that is the fitted value is smaller than the measured value. If the comparison is repeated with both isotope shifts $\delta\nu^{43-40}$ given a very large standard deviation, so that these shifts are freely floating in the fit, the χ^2 falls to 2.24 (four degrees of freedom) indicating that the shifts of the even-even isotopes are all consistent within their quoted errors, and that the only discrepancy lies in the shifts of ^{43}Ca. However the values of the fitted shifts change very little compared with their estimated errors when this is done; the largest change is, of course, the shift $\delta\nu^{43-40}$, which decreases by 0.8 of the standard deviation of the fitted shift when the two isotope shifts $\delta\nu^{43-40}$ are floated freely.

Thus, to conclude this comparison, Table 7.3 contains the fitted shifts for the intercombination line from the fit using the quoted standard deviations, reduced in the case of the intercombination line , with their estimated standard deviations. These standard deviations have not been multiplied by $\sqrt{\chi^2/N}$ for N degrees of freedom; this procedure indicates a re-scaling of all standard deviations, but this is not appropriate here, since it does not appear that the differences between fitted and measured shifts are entirely random. The King parameters relating these shifts to those in the $4s^2$-4s5s $^1S_0$ transition are

$$\phi = 0.4985(46) \qquad \mu = 296.2(2.1)\ \text{GHz}$$

and to the shifts in the $4s^2$-4s4p $^1P_1$ transition

$$\phi = 1.016(16) \qquad \mu = -105.8(7.0)\ \text{GHz}.$$

7.3 The Second-Order Hyperfine Shift

The shift of an hyperfine sublevel $|\gamma JF\rangle$ due to the hyperfine operator

TABLE 7.3. Fitted Values of Isotope Shifts in $4s^2$-$4s4p\ ^3P_1$ of Calcium.

The isotope shifts have been adjusted for maximum consistency with shifts measured in the $4s^2$-$4s4p\ ^1P_1$ and $4s^2$-$4s5s\ ^1S_0$ transitions.

A	$\delta\nu^{A-40}$ / MHz
42	509.37 (22)
43	781.37 (22)
44	996.49 (29)
46	1481.07 (40)
48	1922.51 (35)

in second order perturbation theory has been calculated by Woodgate (1966), in the approximation that the dependence of the energy denominator on F can be neglected, that is that other levels are distant compared with the hyperfine structure. If this is not the case, then second-order perturbation theory is not sufficient, and this condition is well satisfied for the levels of interest in calcium.

The hyperfine operator is given by equation 12 of Chapter 1:

$$H_{hf} = \sum_{k=1}^{2I} T_n^k . T_e^k$$

where only the k=1 and 2 terms are usually significant. Then the shift calculated by Woodgate (his equations B4 and B5 of Appendix B) is:

$$(1) \qquad \Delta E(\gamma JF) = \sum_K (-)^{1+J+F} \begin{Bmatrix} F & J & I \\ K & I & J \end{Bmatrix} D_K(J)$$

where

$$(2) \qquad D_K(J) = \sum_{k_1 k_2} (-)^{2I+2J+k_1+k_2+K} (2K+1) \begin{Bmatrix} k_1 & k_2 & K \\ I & I & I \end{Bmatrix} \langle I \| T_n^{k1} \| I \rangle \langle I \| T_n^{k2} \| I \rangle$$

$$\times \sum_{\gamma' J'} \begin{Bmatrix} k_1 & k_2 & K \\ J & J & J' \end{Bmatrix} \frac{\langle \gamma J \| T_e^{k1} \| \gamma' J' \rangle \langle \gamma' J' \| T_e^{k2} \| \gamma J \rangle}{E(\gamma J) - E(\gamma' J')} .$$

Consider one term in the summation over K in equation 1. The dependence on F is the same as the rank K term of the hyperfine structure operator taken in first order perturbation theory; thus, for example, D_1 is a second order contribution to the A-factor, which is given by Woodgate as

$$(3) \qquad \delta A = \begin{pmatrix} I & 1 & I \\ -I & 0 & I \end{pmatrix} \begin{pmatrix} J & 1 & J \\ -J & 0 & J \end{pmatrix} \frac{D_1}{IJ} .$$

However these terms do not shift the centre of gravity of the hyperfine structure. Therefore, the shift of the centre of gravity, $\Delta E_c(\gamma J)$, is given by the K = 0 term of equation 1

$$(4) \qquad \Delta E_c(\gamma J) = \frac{D_o(J)}{[(2I+1)(2J+1)]^{\frac{1}{2}}} \quad .$$

Evaluating the 6-j symbols in D_o we find

$$(5) \qquad \Delta E_c(\gamma J) = \sum_k \frac{|\langle I \| T_n^k \| I \rangle|^2}{(2I+1)(2J+1)(2k+1)} \sum_{\gamma' J'} \frac{|\langle \gamma J \| T_e^k \| \gamma' J' \rangle|^2}{E(\gamma J) - E(\gamma' J')} \quad .$$

We now proceed to apply this result to the levels of interest in calcium. We first note that in all the low lying levels of ^{43}Ca the k=1 term (magnetic dipole hyperfine interaction) is very much larger than the k=2 term (electric quadrupole) and all others are negligible. The measurements of hyperfine constants A and B for various levels in calcium are given in Table 7.4.

TABLE 7.4. Hyperfine Structure Constants for ^{43}Ca

State	A / MHz	B / MHz	Reference
$4s4p\ ^1P_1$	-15.46(15)	-9.70(70)	Schatz (1981), private communication
$4s4p\ ^3P_1$	-198.890(1)	2.300(2)	Bergmann et al.[a]
$4s4p\ ^3P_2$	-171.962(2)	5.451(8)	Grundevik et al., 1979[b]
$4s5s\ ^3S_1$	-463.3(1.0)		Grundevik et al., 1979
CaII $4s\ ^2S_{\frac{1}{2}}$	-817(15)		Kelley et al., 1954

[a] Presented at 12th EGAS, Pisa (1980)
[b] B-value corrected at ECAP 1981

If we retain just the k=1 term in equation 5 we can substitute for $\langle I \| T_n^1 \| I \rangle$ in terms of A:-

$$(6) \qquad A(\gamma J) = \frac{\langle I \| T^1_n \| I \rangle \langle \gamma J \| T^1_e \| \gamma J \rangle}{[I(I+1)(2I+1)J(J+1)(2J+1)]^{\frac{1}{2}}}$$

to give

$$(7) \qquad \Delta E_c(\gamma J) = \frac{I(I+1)J(J+1)}{3} A^2(\gamma J) \sum_{\gamma' J'} \frac{1}{E(\gamma J) - E(\gamma' J')} \left| \frac{\langle \gamma J \| T^1_e \| \gamma' J' \rangle}{\langle \gamma J \| T^1_e \| \gamma J \rangle} \right|^2 .$$

We should note two things about the use of equation 6; firstly it is only valid for a state with $J \neq 0$, although the second order shift given by equation 5 will not vanish for a state of zero J, and secondly it indicates that the A-factors in equation 7 are 'theoretical', that is, they should be corrected for second order effects. Such corrections to an A-factor are in fact not large, and I shall use the experimental A-factors.

We first consider the shift of the 4s4p $^3P_1$ state due to the close lying $^3P_0$ and $^3P_2$ states. The operator T^1_e in equation 7 is a sum of three terms, the contact, orbital and spin-dipole terms; however we anticipate that in a 4s4p configuration the dominant term will be the contact term due to the 4s electron. This is verified by the A-factors in Table 7.4; if the hyperfine constant of the 4s electron, as measured in the CaII 4s $^2S_{\frac{1}{2}}$ state, is a_{4s}, then the contribution of this electron to the A-factor in the 4s4p $^3P_{2,1}$ states (assuming the same 4s wavefunction) will be $\frac{1}{4}a_{4s}$ (see, e.g. Woodgate, 1980, Chapter 8), and the contribution to the singlet states will be zero. Thus the rough equality of $A(^3P_2)$ and $A(^3P_1)$, the very small value of $A(^1P_1)$ and the fact that

$$A(^3P_1) \approx \frac{1}{4} a_{4s}$$

all support the hypothesis that the contact term of the 4s electron gives the major contribution to T^1_e.

Because the matrix elements are within an L-S term, the contact term of the 4s electron is proportional to $\underline{S}$, the total spin, and so (using

Sobel'man equation 14.70)

$$\left| \frac{\langle \gamma J \| T_e^1 \| \gamma' J' \rangle}{\langle \gamma J \| T_e^1 \| \gamma J \rangle} \right|^2 = \frac{\begin{Bmatrix} J' & J & 1 \\ S & S & L \end{Bmatrix}^2}{\begin{Bmatrix} J & J & 1 \\ S & S & L \end{Bmatrix}^2} \frac{(2J'+1)}{(2J+1)} \quad .$$

Evaluating the 6-j symbols, and putting I = 7/2, J = 1, we find

$$\Delta E_c(4s4p\ ^3P_1) = \frac{21}{2} A^2(^3P_1)\left(\frac{4}{3} \frac{1}{E(^3P_1) - E(^3P_0)} - \frac{5}{3} \frac{1}{E(^3P_2) - E(^3P_1)} \right)$$

which with

$$A(^3P_1) = 199 \text{ MHz}$$

$$E(^3P_1) - E(^3P_0) = 52 \text{ cm}^{-1}$$

$$E(^3P_2) - E(^3P_1) = 106 \text{ cm}^{-1}$$

gives

$$\Delta E_c(4s4p\ ^3P_1) = +0.14 \text{ MHz},$$

and this shift should be subtracted from the isotope shift $\delta\nu^{43-40}$ before it is used in a King plot.

We now consider the second order shift in the 4s5s configuration. Because equation 7 does not apply to levels with J = 0 we cannot use it for the $^1S_0$ level; we therefore calculate the shift of the $^3S_1$ level due to the $^1S_0$ level which, from the symmetry of equation 5 is equal to the shift of the $^1S_0$ level with the opposite sign.

Because the reduced matrix element couples states of different S, and the operator T_e^1 is thus no longer proportional to $\underline{S}$, it is easier to evaluate two matrix elements explicitly in order to deduce the reduced matrix elements.

The operator is

$$\underline{T}_e^1 = f_1 \underline{S}_1 + f_2 \underline{S}_2$$

where f is the radial part of the operator and $\underline{S}_i$ is the spin of the i^{th} electron. The 1-electron states we consider are $|4s,m_s\rangle$ and $|5s,m_s\rangle$ and the

radial part defines the interaction constants

$$\langle ns,m_s|fs_z|ns,m_s\rangle = m_s a_{ns}, \quad n = 4 \text{ or } 5.$$

The states we shall require are

$$|^1S_0\rangle = \frac{1}{\sqrt{2}}(\{4\overset{+}{s}, 5\overset{-}{s}\} - \{4\overset{-}{s}, 5\overset{+}{s}\})$$
$$|^3S_1\ M_s=1\rangle = \{4\overset{+}{s}, 5\overset{+}{s}\}$$
$$|^3S_1\ M_s=0\rangle = \frac{1}{\sqrt{2}}(\{4\overset{+}{s}, 5\overset{-}{s}\} + \{4\overset{-}{s}, 5\overset{+}{s}\})$$

where the notation $\{4\overset{+}{s}, 5\overset{-}{s}\}$ denotes a Slater determinant. Then, taking the matrix element of $(T_e)^1_q$ we find

$$\langle ^1S_0|T^1_0|^3S_1\ M_s=0\rangle = \frac{1}{2}(a_{4s} - a_{5s}) = \begin{pmatrix} 0 & 1 & 1 \\ 0 & 0 & 0 \end{pmatrix} \langle ^1S_0 \| T^1_e \| ^3S_1\rangle$$

$$\langle ^3S_1\ M_s=1|T^1_1|^3S_1\ \ M_s=0\rangle = \frac{1}{2}(a_{4s} + a_{5s}) = \begin{pmatrix} 1 & 1 & 1 \\ -1 & 1 & 0 \end{pmatrix} \langle ^3S_1 \| T^1_e \| ^3S_1\rangle$$

and so

$$\left| \frac{\langle ^1S_0 \| T^1_e \| ^3S_1\rangle}{\langle ^3S_1 \| T^1_e \| ^3S_1\rangle} \right|^2 = \frac{1}{2}\left(\frac{a_{4s} - a_{5s}}{a_{4s} + a_{5s}}\right)^2 .$$

The A-factor for the 4s5s $^3S_1$ state is given by $\frac{1}{2}(a_{4s} + a_{5s})$ and so, if we take $a_{4s} = 800$ MHz as before, $a_{5s} \simeq 100$ MHz, and so the ratio has a value of roughly $\frac{1}{2}\cdot(\frac{7}{9})^2 \simeq 0.3$. The energy denominator is

$$E(^3S_1) - E(^1S_0) = -1778 \text{ cm}^{-1}$$

giving

$$\Delta E_c(^3S_1) = -0.013 \text{ MHz}$$

and so

$$\Delta E_c(^1S_0) = +0.013 \text{ MHz}.$$

This is almost negligible, and so we estimate that the correction for the $4s4p\ ^1P$ state (energy denominator = 8000 cm^{-1}) will be quite negligible.

7.4 Values of $\delta\langle r^2\rangle$ for the stable Calcium Isotopes

In this section I shall calculate the final values of $\delta\langle r^2\rangle$ for the stable calcium isotopes, using a combined analysis of optical and muonic data. The method makes use of equation 13 of Chapter 1

$$\delta\nu^{A-A'} = M/\alpha_{AA'} + F\delta\langle r^2\rangle^{A-A'} \tag{8}$$

which, in terms of the scaled isotope shifts

$$\delta\sigma^{A-A'} = \alpha_{AA'}\delta\nu^{A-A'}$$

gives

$$\delta\sigma^{A-A'} = M + F(\alpha_{AA'}\delta\langle r^2\rangle^{A-A'}). \tag{9}$$

The values of the $\delta\langle r^2\rangle$ from the combined analysis of muonic atom shifts and electron scattering are given in Table 7.5; using these, and the values of α given in Table 7.2, $\alpha_{AA'}\delta\langle r^2\rangle^{A-A'}$ can be calculated. Compared with the errors in these quantities, the errors in the $\delta\sigma$ are negligible, and so the coefficients M and F can be determined by a weighted straight line fit of $(\alpha\delta\langle r^2\rangle)$ against $(\delta\sigma)$ in the form

$$\alpha_{AA'}\delta\langle r^2\rangle^{A-A'} = \frac{1}{F}\delta\sigma^{A-A'} - \frac{M}{F} \tag{10}$$

which is a straight line with slope 1/F, y intercept -M/F and x intercept

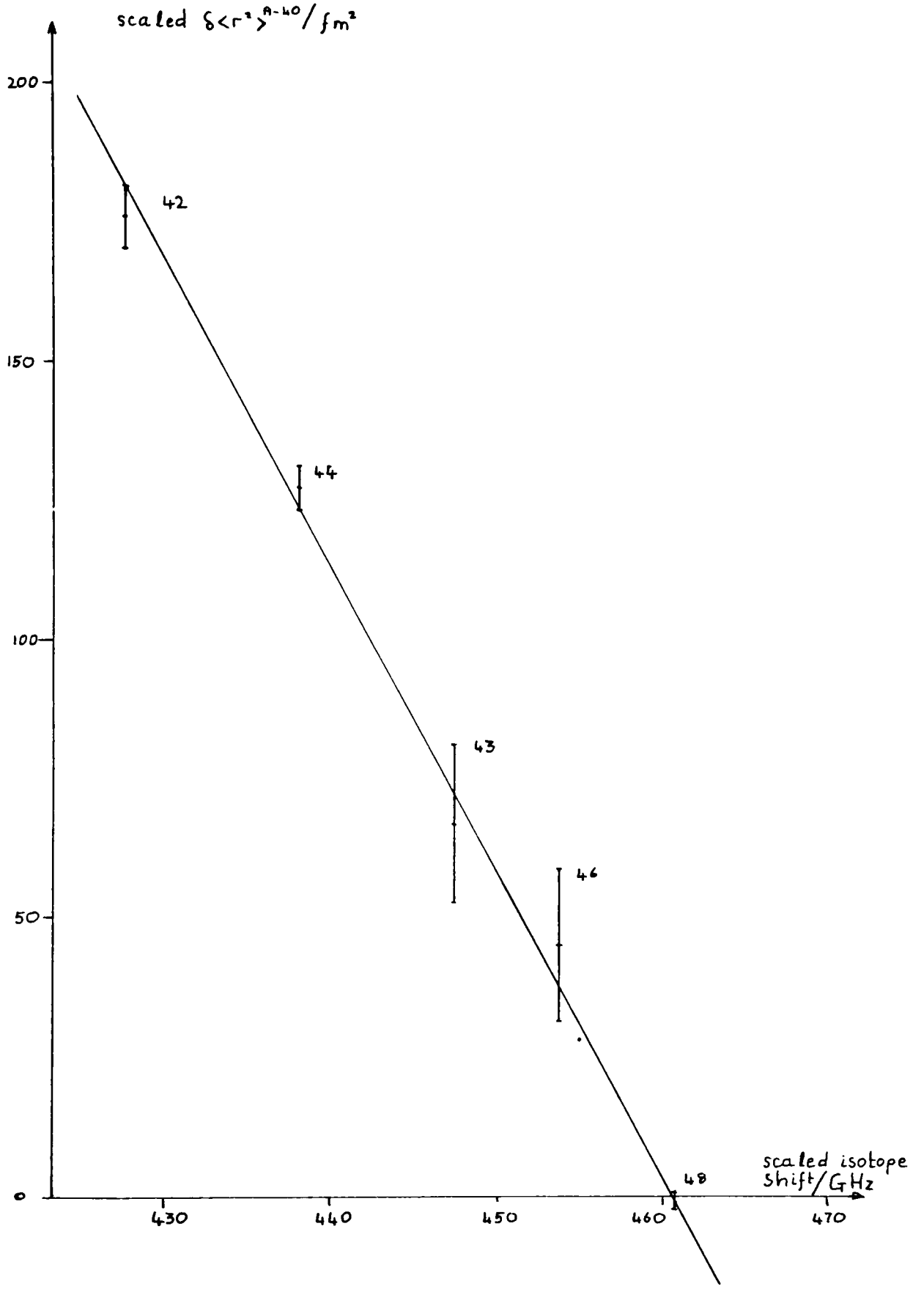


FIGURE 7.1 Separation of mass and field shifts using muonic isotope shifts. The x intercept is the mass shift constant, and the slope is the field shift constant.

TABLE 7.5. Values of $\delta\langle r^2\rangle$ for Stable Calcium Isotopes.

The first column gives the values of $\delta\langle r^2\rangle$ measured by muonic atom isotope shifts (Wohlfahrt et al., 1978 and 1981). The second column gives the values deduced from optical isotope shifts.

A	Muonic $\delta\langle r^2\rangle^{A-40}$ /fm^2	Optical $\delta\langle r^2\rangle^{A-40}$ /fm^2
42	0.210(7)	0.2162(42)
43	0.117(25)	0.1268(29)
44	0.290(9)	0.2818(55)
46	0.147(45)	0.1243(42)
48	-0.005(6)	-0.0043(51)

M. This is shown in Fig. 7.1; the slope and intercept give

$$M = 460.68(21)\ \text{GHz}$$
$$F = 0.1818(37)\ \text{GHz fm}^{-2}.$$

Using these values, $\delta\langle r^2\rangle$ can be calculated from equation 8:-

$$\delta\langle r^2\rangle^{A-A'} = \frac{1}{F}\left(\delta\nu^{A-A'} - M/\alpha^{AA'}\right). \tag{11}$$

The error in $\delta\langle r^2\rangle$ is found by combining quadratically the errors in F, M and $\delta\nu$; the error in $\delta\nu$ is generally rather smaller than the combined errors in F and M, and so the final values are limited in their precision by the precision of the muonic $\delta\langle r^2\rangle$. The final values are given in Table 7.5; the improvement in the overall precision compared with the muonic data is illustrated by Fig. 7.2.

I shall briefly describe the different approaches that have been made in the interpretation of these $\delta\langle r^2\rangle$, in the papers by Wohlfahrt et al. (1981) and Trager (1981). Wohlfahrt et al. give diagrams of charge distribu-

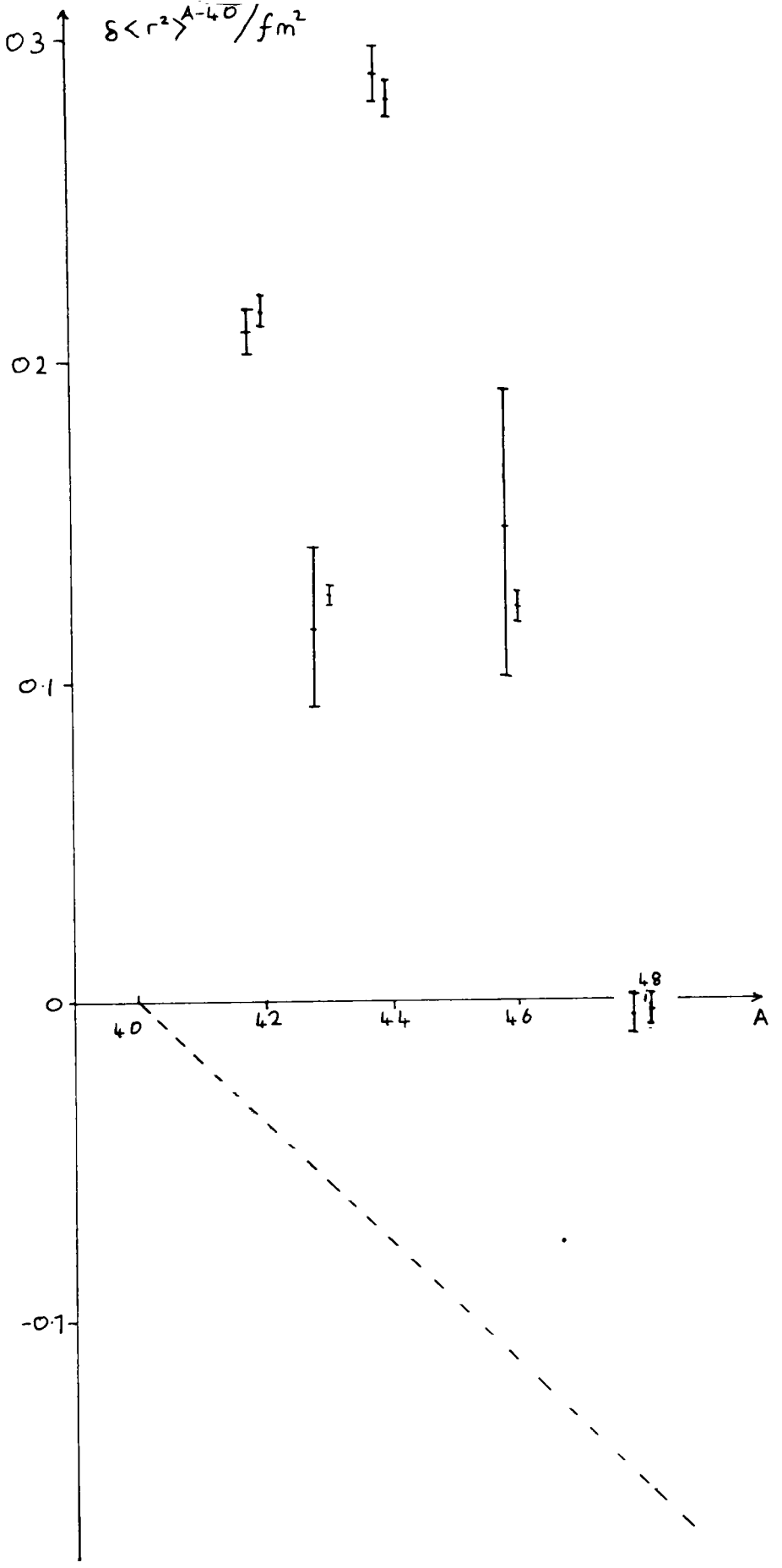


FIGURE 7.2 $\delta\langle r^2\rangle$ for stable Ca Isotopes
The left-hand bar is from muonic isotope shifts; the right-hand bar is from optical spectroscopy. The contribution of the neutrons is shown by the dashed line.

tion differences between calcium isotopes from the combined analysis of muonic and electron scattering data; these are shown in Fig. 7.3. We can see that between ^{40}Ca and ^{44}Ca charge moves from the region 0-3 fm to the region 3-5 fm, and between ^{44}Ca and ^{48}Ca charge moves from the region 5-7 fm to the region 3-5 fm, and the net effect on $\delta\langle r^2\rangle^{48-40}$ is roughly zero. The latter type of charge distribution change is the one produced by the effects of the neutrons' charge distribution, as described in section 1.2; however the total decrease in $\langle r^2\rangle$ between ^{44}Ca and ^{48}Ca is some four times larger than the decrease due to the neutrons (the $\delta\langle r^2\rangle$ due to the neutrons is also sketched on Fig. 7.2). Thus, speaking purely phenomenologically, one could describe the variation in $\langle r_p^2\rangle$ as an increase from ^{40}Ca to ^{48}Ca, combined with an additional contribution that vanishes for a full or empty neutron sub-shell.

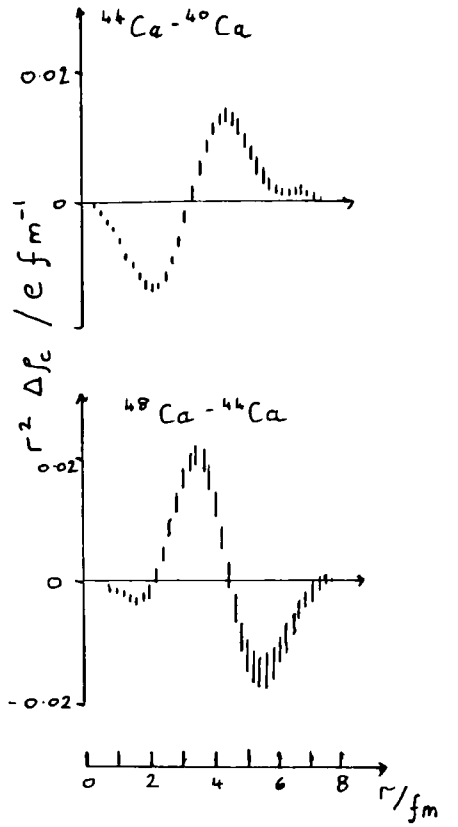
This sort of behaviour could be explained by supposing that there is a change in proton wavefunction, leading to an increase in $\langle r_p^2\rangle$, between ^{40}Ca and ^{48}Ca, and that in addition the proton distribution is polarized or deformed by a partly filled neutron sub-shell. Some of this physical interpretation is contained in a parameterization of the $\delta\langle r^2\rangle$ due to Zamick (1971). By assuming that the charge radius operator is a sum of one-body and two-body operators (the origin of the two-body operator is not physically obvious) he obtains the following formula, which is exact within the basis of the $1f_{7/2}$ configuration:-

$$\delta\langle r^2\rangle^{A-40} = nC + \frac{1}{2}n(n-1)\alpha + [n/2]\beta \qquad (12)$$

where $[x]$ = largest integer $\leq x$

and $n = N - 20.$

Wohlfahrt et al. found quite good agreement between this formula and the $\delta\langle r^2\rangle$ for changes in neutron number, and they extended it to include changes in proton number also. However the improved precision of these measurements



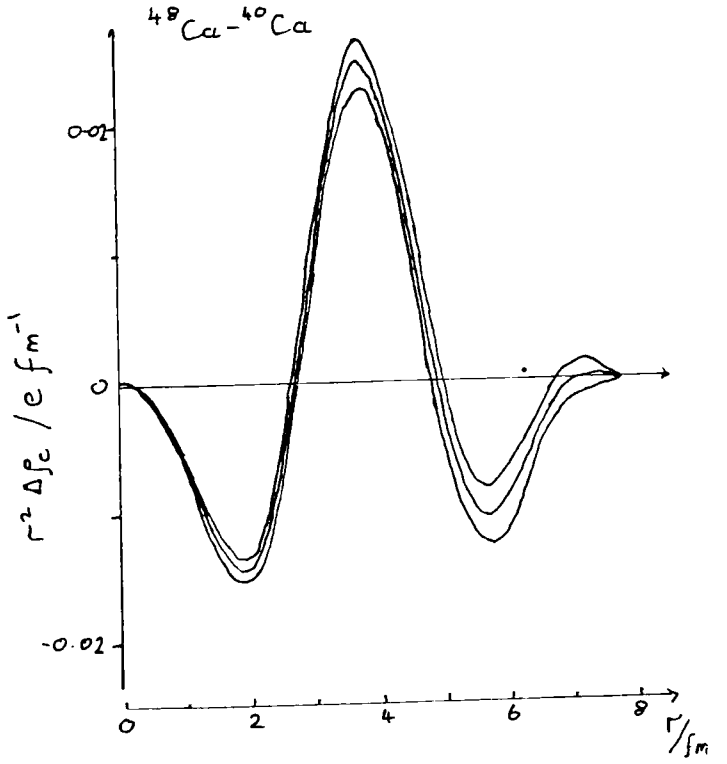


FIGURE 7.3 Charge Distribution Differences of Calcium Isotopes deduced from a combined analysis of Electron Scattering and Muonic Atom Isotope Shifts (from Wohlfahrt et al 1981)

reveals a discrepancy, which is apparent from the results in Table 7.5 - equation 12 is quadratic in neutron number and so, by symmetry, if

$$\langle r^2 \rangle^{40} = \langle r^2 \rangle^{48}$$

then equation 12 predicts

$$\langle r^2 \rangle^{42} = \langle r^2 \rangle^{46}$$

which is clearly not true. However, in the physical picture outlined above, the equality of $\langle r^2 \rangle^{40}$ and $\langle r^2 \rangle^{48}$ is fortuitous, arising from a coincidental equality of the effect of the neutrons and the effect of the changes in the proton distribution. The former effect is a one-body effect and clearly included in equation 12; however the latter effect is a sort of configuration interaction due to the added neutron sub-shell, in the sense that to describe the proton wavefunction of ^{48}Ca in terms of eigenstates of the central field of ^{40}Ca requires the admixture of other configurations. An alternative way of describing this would be to say that ^{48}Ca has a different central field, and such an effect is not included in the above parameterization, except in the sense that it causes $\mathcal{C}$, α and β to depend on neutron number. Thus the three-parameter fit of equation 12 is notably less successful for $\langle r^2 \rangle$ than it is for binding energies (see Talmi, 1961) where the parameterization works very well. We thus see very clearly how these experimental results provide a test of our understanding of the shell closure at N = 28, and the effect of a partly filled shell of neutrons on the proton core.

Träger (1977) also refers to the Zamick parameterization, including in it the unstable odd isotopes ^{41}Ca, ^{45}Ca and ^{47}Ca. It appears that, with the exception of ^{46}Ca a reasonable fit to all the mean square radii can be obtained using equation 12. However, the discrepancy between ^{46}Ca and equation 12 is unlikely to be resolved in a way specific to this isotope; in the light of the above discussion it is more likely that equation 12 is an over-simplification, and it would therefore be unwise to place too much reliance on the good agreement between it and the $\delta\langle r^2 \rangle$. Träger also discusses the mean square radii in terms of changes in the deformation and volume of a

uniformly charged ellipsoid, a model which has given many useful insights into nuclear shapes and sizes at large values of A. It is clear, however, from Fig. 1.1, that ^{40}Ca has no uniformly charged region at all. Furthermore, the charge density change between ^{40}Ca and ^{48}Ca, shown in Fig. 7.3, is of the same order of magnitude as that between ^{40}Ca and ^{44}Ca. Since $\delta\langle r^2\rangle^{48-40} \simeq 0$, then according to the model these isotopes have the same charge distribution (since, being doubly magic, they are not expected to show deformation). Thus the charge density changes that are interpreted by the model are no larger than those which cannot be, and so this model is unlikely, in this low-A region, to give useful insights.

Finally I shall summarize the experimental position with regard to the determination of $\delta\langle r^2\rangle$ in calcium. The even-even shifts have been determined in three separate transitions with high precision, and the resulting $\delta\langle r^2\rangle$ are limited in their precision by the muonic data. The situation with the odd isotopes is less satisfactory; the situation would be clarified slightly if a more accurate measurement were made on the shift $\delta\nu^{43-40}$ in the two-photon transition, since the substantially lower precision of the shift $\delta\nu^{44-40}$ at present limits the usefulness of the high precision obtained for the shift $\delta\nu^{43-44}$. It is hoped that this measurement will be undertaken in the near future. There is some evidence of systematic error in the measurements on odd isotopes in the two transitions with hyperfine structure. Since these experiments are at present the only ones with the sensitivity to do measurements on unstable isotopes, it is necessary for these effects to be investigated in order to obtain the highest possible precision for these isotopes also. This re-emphasizes the importance of the isotope shift of the only stable odd isotope ^{43}Ca, since this is the only shift which permits a comparison between transitions with and without hyperfine structure.

CHAPTER 8

ANOMALOUS ISOTOPE SHIFTS IN SAMARIUM

8.1 Introduction

Experimental work performed at Birmingham University (first reported by Griffith et al., 1979, hereafter referred to as G79) using the method of laser heterodyne spectroscopy, showed that isotope shifts in a number of transitions did not obey the King relations (equation 14 of Chapter 1). As we have noted, these do not include any second-order effects, and significantly non-linear King plots due to the second order effect of the hyperfine interaction have been known for some years (e.g. Gerstenkorn and Vergès, 1975, Gerstenkorn et al., 1977). However, in this case, the isotope shifts were measured only between even-even isotopes, for which there is no hyperfine interaction. G79 considered other small, isotope-dependent effects and concluded that they were too small to account for the anomalies, the origin of which was therefore not understood. It was first pointed out by D.N. Stacey that the upper level of the perturbed transitions lay in close proximity with another level of the same J and parity, and he suggested that these anomalies might be due to the second order effect of the operators of mass and field shift coupling the levels. As a result, further experimental work was undertaken, reported by Griffith et al. (1981), hereafter referred to as G81. This paper also contains a qualitative analysis of such second-order isotope shifts, and they conclude that such effects could produce anomalies of the observed magnitude, and suggest that further, quantitative analysis is precluded by uncertainties in the mean square radii $\langle r^2 \rangle$.

In this Chapter I present a quantitative analysis of these anomalies in terms of two-level mixing which relies only on isotope shift measurements and,

at a later stage, on the values of $\delta\langle r^2\rangle$. Some of this work is to be published (Palmer and Stacey, 1982). In section 8.2 the experimental results of G79 and G81 are described, and the deviations from a King plot examined. In section 8.3 the analysis of these deviations in terms of mixing of two levels by the isotope shift operators is presented, and the results of this analysis are discussed in section 8.4.

8.2 Description of the Experimental Results

In G79 and G81, isotope shifts are presented for 15 transitions in the SmI spectrum for the isotope pairs 148-144, 150-148, 152-150 and 154-152. These have an estimated uncertainty of 200 kHz; one shift (148-144 of 597.94 nm) is not given because it is too large to be measured with their apparatus. These 15 transitions all connect levels of the ground term $4f^6 6s^2\ ^7F$ with excited odd-parity levels which are primary composed of the sub-configurations $4f^5(^6H \text{ and } ^6F)5d6s^2$ and $4f^6(^7F)6s6p$ (Carlier et al., 1968). The 15 transitions are shown in a term diagram in Fig. 8.1 and the wavelengths and term energies are given in Table 8.1.

Since this set of data all have the same error we can compare them using the multi-dimensional King plot described in Appendix C, section 1. A computer program was written to perform this comparison; a typical output is shown in Fig. 8.2. When all 14 transitions for which the four isotope shifts were measured are compared it is clear that the four lines connecting to the levels at 19174.84 cm^{-1} and 19191.64 cm^{-1} do not satisfy the King relations with the other lines, by many times the estimated uncertainty.

If these four spectral lines, marked in red on Fig. 8.1 and in Table 8.1, are excluded from the comparison, the remaining ten lines show reasonable agreement. If, however, the "estimated uncertainty" of 200 kHz is interpreted as a standard deviation, the comparison is still poor, with χ^2/degree of freedom

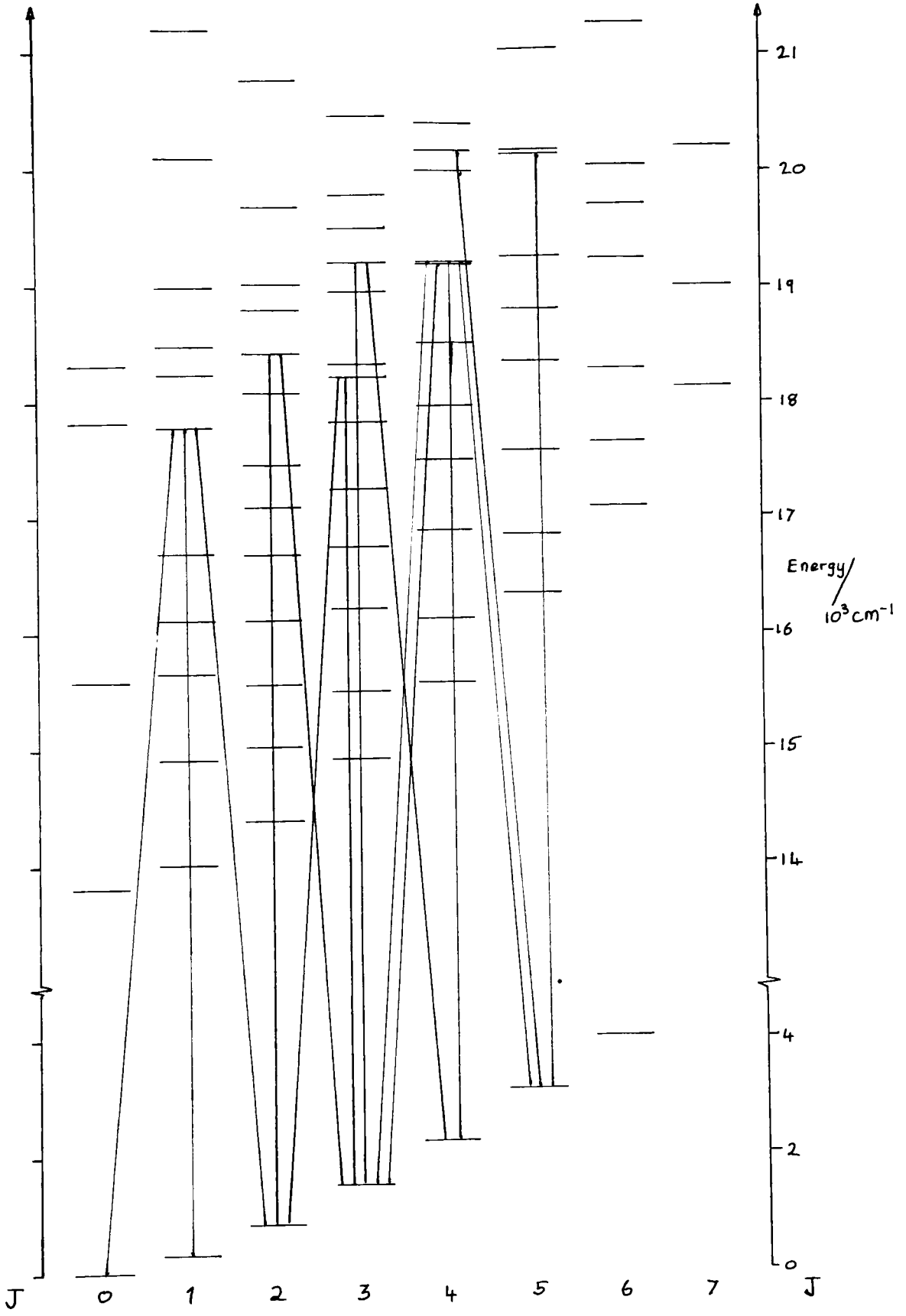


FIGURE 8.1 Term Diagram of excited, odd parity levels in Sm, showing the transitions studied by G79 and G81.

TABLE 8.1. Isotope Shift Data in Sm.

List of spectral lines and term energies for the transitions for which data are available (G79 and G81).

	Upper level		Lower level	
λ/nm	J	Energy/cm^{-1}	J	Energy/cm^{-1}
564.16	3	19210.09	3	1489.55
590.26	3	19210.09	4	2273.09
567.87	2	18416.62	2	811.92
590.62	2	18416.62	3	1489.55
574.65	3	18209.04	2	811.92
*597.94	3	18209.04	3	1489.55
565.28	4	19174.84	3	1489.55
564.75	4	19191.64	3	1489.55
590.90	4	19191.64	4	2273.09
622.26	4	19191.64	5	3125.46
562.60	1	17769.71	0	0.00
572.02	1	17769.71	1	292.58
589.54	1	17769.71	2	811.92
587.11	5	20153.47	5	3125.46
586.78	4	20163.00	5	3125.46

* Incomplete set of data.

7.8. Furthermore some spectral lines have much larger deviations from the King plot line than others, and these deviations have the same pattern as the much larger deviations in the spectral lines already excluded, being largest for the shift 154-152, and rather smaller with the opposite sign for the shift 148-144. If the three spectral lines having as upper level the level at 17769.71 cm^{-1}, and the two lines having upper levels at 20153.47 cm^{-1} and 20163.00 cm^{-1} are also excluded from the fit the remaining five spectral lines do lie on a single straight line within their errors (χ^2/degree of freedom 0.86). This set of five spectral lines, referred to subsequently as set A, are marked in black on Fig. 8.1 and in Table 8.1, while the five lines showing smaller deviations are shown in green.

In order to establish the form of the deviations from the King plot line a set of comparisons was performed of the set A with each of the apparently 'non-linear' spectral lines separately, with the non-linear lines given a very low weight so that they did not perturb the fit to the set A. The deviations of the four highly perturbed lines from the best line through set A are shown in Table 8.2. It is clear that the deviations of the three lines connecting to the level at 19191.64 cm^{-1} are all equal, to within errors; this is only to be expected, since the differences between the isotope shifts in these transitions are just the isotope shifts of transitions within the ground term. However the ground term is very well separated from other terms, whereas the terms in the excited configurations are strongly mixed, and so isotope-dependent perturbations are much more likely in the excited state. This expectation is confirmed by Table 8.2.

It is also clear that, within the errors, the deviations in the transition connecting to the level at 19174.84 cm^{-1} are equal in magnitude with the opposite sign. This strongly suggests that the dominant perturbation of these levels arises from interaction of these two levels, of the same J and separated by only 16.80 cm^{-1}, with each other. Any two-level mixing, in any order of perturbation theory, will result in equal but opposite shifts in the

TABLE 8.2. Deviations from King Plots.

The tabulated quantity is (measured isotope shift - nearest point on straight line) for the four spectral lines marked in red in Table 8.1. The final column gives the total squared deviation / σ^2 where σ = 200 kHz.

	Isotope Pair				
λ nm	148-144 MHz	150-148 MHz	152-150 MHz	154-152 MHz	χ^2
565.28	12.03	1.54	-1.27	-26.73	2.16×10^4
564.75	-12.01	-1.59	1.28	26.73	2.16×10^4
590.90	-11.88	-1.97	1.40	26.73	2.15×10^4
622.26	-11.79	-1.99	1.40	26.54	2.12×10^4

TABLE 8.3. Deviations from King Plots.

The tabulated quantity is as in Table 8.2, for the five lines marked in green in Table 8.1. The first three spectral lines have a common upper level.

	Isotope Pair				
λ nm	148-144 MHz	150-148 MHz	152-150 MHz	154-152 MHz	χ^2
562.60	0.47	-0.22	0.04	-0.85	24.9
572.02	0.64	-0.84	0.22	-0.98	56.5
589.54	0.44	-0.11	0.01	-0.85	23.1
587.11	0.83	-0.28	0.04	-1.55	62.5
586.78	0.13	-0.54	0.16	0.12	8.7

LAMBDA	NU	FIT	ERR/S.D	NU	FIT	ERR/S.D	NU	FIT	ERR/S.D	NU	FIT	ERR/S.D
565.00	0.99806	0.99805	0.06	0.72286	0.72289	-0.16	1.28076	1.28075	0.05	0.42989	0.42989	-0.02
574.65	-2.77604	-2.77647	0.20	-1.63004	-1.62993	-0.54	-2.28937	-2.28940	0.16	-1.23443	-1.23442	-0.03
590.26	-1.01975	-1.01967	-0.38	-0.56129	-0.56127	-0.09	-0.71704	-0.71605	0.05	-0.45694	-0.45712	0.89
564.14	-1.00167	-1.00163	-0.33	-0.55055	-0.55055	-0.02	-0.70075	-0.70076	0.03	-0.44895	-0.44910	0.73
590.62	-1.14276	-1.14287	0.53	-0.63961	-0.63993	1.58	-0.83229	-0.83220	-0.47	-0.51418	-0.51418	-0.02
567.87	-1.13143	-1.13155	0.62	-0.62993	-0.62991	-0.09	-0.81920	-0.81820	-0.01	-0.50681	-0.50656	-1.25

CHI-SQUARED(1)= [illegible]
CHI-SQUARED(2)= [illegible]
DEG.OF FREEDOM= 10

EIGENVALUES FIRST EIGENVECTOR XX

[illegible]	[illegible]	[illegible]
[illegible]	[illegible]	[illegible]
[illegible]	[illegible]	[illegible]
[illegible]	[illegible]	[illegible]
[illegible]	[illegible]	[illegible]
[illegible]	[illegible]	[illegible]

FIGURE 8.2 Multi-dimensional King Plot of the set $A + \bar{\lambda}$

energies of the levels, and so the sum of the isotope shifts in the two levels, for a pair of transitions connecting to the same lower level, should obey the King relations. One such pair of spectral lines in which isotope shifts have been measured is λλ 564.75 nm, 565.28 nm. The sum of the isotope shifts in these lines was entered as the shift in a fictitious spectral line $\bar{\lambda}$ = 565.00 nm, and compared with set A. The agreement is excellent, χ^2/degree of freedom falling to 0.69; this is the comparison shown in the sample computer output in Fig. 8.2.

The remaining five spectral lines, showing smaller perturbations, were treated in the same way, that is compared one at a time with the linear set, except that the fictitious spectral line $\bar{\lambda}$ was included with set A in the comparison. The deviations of these transitions from the King plot line through set A plus $\bar{\lambda}$ are shown in Table 8.3. We note that the level at 17769.71 cm^{-1} is significantly perturbed with the same general pattern of deviation as the strongly perturbed lines but about 30 times smaller. The level at 20153.47 cm^{-1} is also perturbed at about the same level. However the deviations in the isotope shifts of λ 586.78 nm are only on the borderline of significance, and we see that deviation from the King plot is concentrated in the shift 150-148, which is about two and a half standard deviations from the line. This is comparable with the scatter in the deviations of the three lines connecting to the level at 17769.71 cm^{-1}, one of which (the shift 150-148 in λ 572.02 nm) is about three standard deviations away from the other two values of that deviation.

To sum up, of the 14 spectral lines for which all four even-even isotope shifts have been measured only five (set A) obey the King relations with each other to within a standard deviation of 200 kHz, with a further one on the borderline of consistency. The deviations of the remaining eight lines from the King plot line through set A all have the same characteristic form, with the largest deviation being in the shift 154-152. Of these, four lines connecting to two closely spaced levels of the same J show evidence of two-

level mixing.

8.3 Two-level Mixing

In this section we consider the mixing of two levels by an isotope-dependent operator, and calculate the effect on isotope shifts, first in second order perturbation theory, then to all orders, by diagonalizing the 2x2 matrix. We then compare this theory with the observed shifts to establish what size of matrix element would be required to produce the observed deviations. The applicability of the two-level approximation, and the sizes of matrix elements one could expect, are considered in the following section.

We first consider what isotope-dependent operator is likely to couple the levels. All the isotopes involved have zero spin, and so the discussion of section 1.4 would lead us to suppose that the usual isotope shift operator was the only one possible. However, it is necessary to consider also small effects which were mentioned there in passing. The first is nuclear polarization, or the influence of nuclear states other than the ground state, which was dismissed as negligible in section 1.2. Reiner and Wilets (1962) showed that the shift due to this effect is proportional to the field shift constant F and so it will not affect the linearity of the King plot, but only the interpretation of the field shifts in terms of mean square radii. A more important possibility is the presence of a significant fourth moment term, that is that the field shift is given by (cf. equation 11 of Chapter 1):

$$(1) \qquad FS^{A'-A} = F(\delta\langle r^2\rangle^{A'-A} + \frac{C_2}{C_1}\delta\langle r^4\rangle^{A'-A}).$$

If the factor C_2/C_1 varies from transition to transition then the King relations will not be satisfied. According to G79 the second term is about 4% of the first, that is comparable with the anomalies. However C_2/C_1 is expected to

vary by no more than a few per cent for different transitions, and so it is unlikely to be responsible for the deviations in the highly perturbed lines. However it is large enough to be responsible for deviations at the level of a few hundred kHz.

Given that the deviations in the highly perturbed lines cannot be explained by these mechanisms, while level mixing due to the ordinary isotope shift operator is strongly suggested as a cause for these deviations, the question naturally arises as to which perturbation is responsible for the smaller deviations. If there were a large number of spectral lines having isotope shifts that obeyed the King relations, and a small number that did not, then the likelihood would be that level mixing was responsible, since if the electronic factor C_2/C_1 is making some King plots non-linear, it is very likely to make most, if not all, King plots non-linear. However the five lines of set A connect to only three upper levels, and the five lines showing small deviations connect to a further three, so the position is unclear. Provided that the sizes of the matrix elements are not unreasonably large, as I hope to show that they are not, then the existence of the strongly perturbed levels indicates the presence of level mixing due to the isotope shift operator as a physical mechanism causing non-linear King plots in this region of the samarium spectrum. This suggests that other levels will show smaller effects from the same cause. There is, on the other hand, no evidence requiring us to postulate that the fourth-moment term is causing non-linear King plots at this level of precision, and so I shall ignore it. However this question can only be settled by the analysis of a very much larger set of accurate isotope shift data for all levels in this region of the spectrum.

It is natural, within the theoretical framework set up in section 1.4. to take the levels of one isotope, A_o, as our basis set of wavefunctions. The Hamiltonian of another isotope, A, differs from that of A_o by the addition of the perturbation

(2) $$H_{is}^{A-A_o} = \hat{f}\,\delta\langle r^2\rangle^{A-A_o} + \hat{m}/\alpha_{AA_o}$$

where $\alpha_{AA_o} = AA_o/A\text{-}A_o$, and $\hat{f}$ and $\hat{m}$ are electronic operators. However this step is a very important one; G81 take as their basis set the levels of an infinitely massive point nucleus, with the perturbing Hamiltonian

$$H_{is}^{A} = \hat{f}\langle r^2\rangle^{A} - \hat{m}/A ,$$

a special case of equation (2) with $A_o = \infty$, $\langle r^2\rangle^{A_o} = 0$. However it is a very inappropriate special case, since the reference basis is taken an artificially long way away from the actual isotopes in question. To all orders of perturbation theory the results will be the same; however while second-order perturbation theory may be sufficient to go from $A_o = 144$ to $A = 154$, it may very well not be sufficient to go from $A_o = \infty$ to $A_o = 154$. In other words the isotope shift is given by the difference of two perturbation expansions, and the difference of the two second order expansions need not be the same as the second order theory using $A_o = 144$. Thus their results are not equivalent to mine, although their Hamiltonian, in a mathematical sense, is.

If first order perturbation theory is sufficient, then the isotope shift of a level i is given by the expectation value of $H_{is}^{AA_o}$:

(3) $$\langle i|H_{is}^{AA_o}|i\rangle = f_i\delta\langle r^2\rangle^{A-A_o} + m_i/\alpha_{AA_o}$$

and, taking the difference of two such equations for the upper (f) and lower (i) states of a transition we obtain equation 13 of Chapter 1, since

(4) $$F_{if} = f_f - f_i \quad \text{and} \quad M_{if} = m_f - m_i .$$

We now consider the effect of the perturbation H_{is} on two levels, which are isolated from other levels. In isotope A_o these states are separated by E,

and so their Hamiltonian matrix is $\begin{pmatrix} E & 0 \\ 0 & 0 \end{pmatrix}$. We denote the upper state by 1 and the lower state by 2. Then in isotope A the states and level energies are given by the eigenvectors and eigenvalues of

$$M_{AA_o} = \begin{pmatrix} E + f_1\delta\langle r^2\rangle^{A-A_o} + m_1/\alpha_{AA_o} & f_{12}\delta\langle r^2\rangle^{A-A_o} + m_{12}/\alpha_{AA_o} \\ f_{12}\delta\langle r^2\rangle^{A-A_o} + m_{12}/\alpha_{AA_o} & f_2\delta\langle r^2\rangle^{A-A_o} + m_2/\alpha_{AA_o} \end{pmatrix} \tag{5}$$

in an obvious notation. We make frequent use of the off-diagonal matrix element, and the difference of diagonal matrix elements, and so we here define

$$\varepsilon_{AA_o} = f_{12}\delta\langle r^2\rangle^{A-A_o} + m_{12}/\alpha_{AA_o} \tag{6}$$

$$\beta_{AA_o} = (f_1 - f_2)\delta\langle r^2\rangle^{A-A_o} + (m_1 - m_2)/\alpha_{AA_o} \, . \tag{7}$$

The eigenvalues of M are given by

$$\begin{aligned} E_1(A) &= \tfrac{1}{2}E + \tfrac{1}{2}[(f_1+f_2)\delta\langle r^2\rangle^{A-A_o} + (m_1+m_2)/\alpha_{AA_o}] \\ &\quad + \tfrac{1}{2}[(E + \beta_{AA_o})^2 + 4\varepsilon^2_{AA_o}]^{\frac{1}{2}} \\ E_2(A) &= \tfrac{1}{2}E + \tfrac{1}{2}[(f_1+f_2)\delta\langle r^2\rangle^{A-A_o} + (m_1+m_2)/\alpha_{AA_o}] \\ &\quad - \tfrac{1}{2}[(E + \beta_{AA_o})^2 + 4\varepsilon^2_{AA_o}]^{\frac{1}{2}} \, . \end{aligned} \tag{8}$$

We first find the sum of the isotope shifts in two transitions connecting the two levels with a common lower level i. We find

$$\delta\nu_{i1}^{A-A_o} + \delta\nu_{i2}^{A-A_o} = (f_1+f_2-2f_i)\delta\langle r^2\rangle^{A-A_o} + (m_1+ m_2-2m_i)/\alpha_{AA_o} \, , \tag{9}$$

and since this is of the form of equation 13 of Chapter 1 these shifts will obey

the King relations, as stated in section 8.2. Although it is straightforward to find the eigenvalues of M (equation 8 above) the expression for the isotope shift is rather complicated, and involves all the matrix elements of M. To second order, however, the shifts of level 1 are independent of m_2 and f_2, and so the four measured isotope shifts just determine two King parameters ϕ and μ relating a perturbed to a non-perturbed line, and the two off-diagonal matrix elements m_{12} and f_{12}, and so I next describe how this is done. It turns out that for the highly perturbed lines the second order theory is inadequate, and so it is necessary to use the full expression for the isotope shift.

However, we first suppose that the values of ε_{AA_o} and E are such that second order perturbation theory is a good approximation. Then the isotope shifts in a spectral line connecting level j (= 1 or 2) with lower level i are

$$\nu_{ij}^{A-A_o} = (f_j-f_i)\delta\langle r^2\rangle^{A-A_o} + (m_j-m_i)/\alpha_{AA_o} \pm \varepsilon_{AA_o}^2/E \tag{10}$$

where the + sign goes with level 1 and vice versa (that is, the levels repel each other). Here and subsequently isotope shifts are denoted by ν and not $\delta\nu$. In order to make a comparison with the observed shifts we must eliminate the factors $\delta\langle r^2\rangle$ in equation 10, and we do this by comparing them with an unperturbed spectral line, whose isotope shifts ν_u are given by

$$\nu_u^{A-A_o} = F_u\delta\langle r^2\rangle^{A-A_o} + M_u/\alpha_{AA_o} \quad . \tag{11}$$

Eliminating $\delta\langle r^2\rangle$ between equations 11 and 6 gives

$$\varepsilon_{AA_o} = \phi_{12}\nu_u^{A-A_o} + \mu_{12}/\alpha_{AA_o} \quad , \tag{12}$$

where $\phi_{12} = f_{12}/F_u$ and $\mu_{12} = m_{12}-\phi_{12}M_u$, and eliminating $\delta\langle r^2\rangle$ from equation 10 gives

(13a) $$\nu_{ij}^{A-A_o} = \phi\nu_u^{A-A_o} + \mu/\alpha_{AA_o} \pm (\psi\nu_u^{A-A_o} + \theta/\alpha_{AA_o})^2$$

where $$\phi = (f_j - f_i)/F_u, \qquad \mu = (m_j - m_i) - \phi M_u,$$

(13b)

$$\psi = \phi_{12}/\sqrt{E}, \qquad \theta = \mu_{12}/\sqrt{E}.$$

The equations 13a form a set of four equations in the four unknowns ϕ, μ, ψ and θ. Of these ϕ and μ are the usual King plot parameters, while ψ and θ are related by equation 13b to ϕ_{12} and μ_{12}, which are quantities analogous to the usual parameters, but involving the off-diagonal matrix elements. Thus the method involves decomposing the isotope shift into a part which would make a linear King plot with the unperturbed isotope shift ν_u, and a part whose square root would make a linear King plot with ν_u.

The four equations 13a, for the different values of A, form coupled quadratic equations in the four unknowns, and their solution is rather tedious but straightforward. We write the subscript or superscript AA_o as a number of primes, from zero to three, e.g.

(13a)' $$\nu' = \phi\nu_u' + \mu/\alpha' \pm (\psi\nu_u' + \theta/\alpha')^2.$$

Multiply by α' and subtract the unprimed equation from the other three:-

(14) $$\alpha'\nu' - \alpha\nu = \phi(\alpha'\nu_u' - \alpha\nu_u) \pm \alpha'(\psi\nu_u' + \theta/\alpha')^2 \mp \alpha(\psi\nu_u + \theta/\alpha)^2$$

with two similar equations with two or three primes. If we now eliminate ϕ from these three equations we obtain two equations of the form

(15) $$a_i\psi^2 + 2h_i\psi\theta + b_i\theta^2 = c_i, \quad i = 1,2$$

where the coefficients a_i, b_i, c_i and h_i are complicated functions of the α, ν and ν_u. The solution of these equations is

$$\psi^2 = \frac{A_b C_b + 2H_b(-C_h \pm [C_h^2 - C_a C_b]^{\frac{1}{2}})}{A_b^2 + 4H_a H_b} \qquad (16)$$

$$\theta = \frac{C_b - A_b \psi^2}{2H_b \psi}$$

where

$$A_b = a_2 b_1 - a_1 b_2 \qquad H_a = h_2 a_1 - h_1 a_2$$
$$C_a = c_2 a_1 - c_1 a_2 \qquad H_b = h_2 b_1 - h_1 b_2$$
$$C_b = c_2 b_1 - c_1 b_2 \qquad C_h = c_2 h_1 - c_1 h_2.$$

A program was written to perform this solution for any pair of spectral lines, using values of α_{AA_o} calculated from Wapstra and Bos (1977) given in Table 8.4, and $A_o = 144$.

The results of this are given in Table 8.5; rather than give the coefficients θ and ψ I have tabulated the values of the off-diagonal matrix element required to fit the data for the four isotope pairs, calculated using equations 12 and 13b. The value of E, the separation of the two perturbing levels, is also given in the Table; in each case it is the distance of the nearest level of the same J and parity, and the calculation is carried out for an upper or lower level, depending as to whether the presumed perturbing level is below or above the upper level of the transition. The signs of θ and ψ are of course not determined, since they enter equation 13 as squares; ψ is arbitrarily chosen to be positive.

The striking thing about the values of ε in Table 8.5 is that all the values are of the same order of magnitude as the isotope shifts, and thus not obviously unreasonable. The scatter of values between the four strongly perturbed lines, and the three lines connecting to the level at 17769.71 cm^{-1}

TABLE 8.4. Nuclear Masses of Sm Isotopes.

(Wapstra and Bos, 1977). $A_o = 144$, $62m_e = 0.034012$ amu.

	144	148	150	152	154
Atomic mass / amu	143.912009	147.914832	149.917285	151.919741	153.922218
Nuclear mass/ amu	143.877997	147.880820	149.883273	151.885729	153.888206
$AA_o/(A-A_o)$		5315.45	3590.99	2728.99	2211.85

TABLE 8.5. Results of Second-Order Perturbation Theory.

The first column gives the wavelength of the 'perturbed' line and the second column that of the 'unperturbed' line. The third column indicates whether the upper level is assumed to be level 1 or 2 (upper or lower) and the fourth gives the energy separation of the two levels. The remaining columns give the off-diagonal matrix element required to give the observed deviations for the four isotope pairs.

				Isotope Pair			
λ	λ_u		E	148-144	150-144	152-144	154-144
nm	nm		GHz	GHz	GHz	GHz	GHz
565.28	567.87	2	503.1	-2.87	-4.61	-7.18	-8.45
564.75	564.16	1	503.1	-2.80	-4.51	-7.05	-8.29
590.90	590.26	1	503.1	-2.76	-4.49	-7.11	-8.32
622.26	574.65	1	503.1	-2.77	-4.49 •	-7.11	-8.33
562.60	574.65	2	13654.1	3.39	4.76	5.49	7.06
572.02	567.87	2	13654.1	6.75	7.91	4.15	7.42
589.54	590.26	2	13654.1	3.22	4.81	6.47	7.93
587.11	590.62	2	896.1	2.10	2.51	1.49	2.51

indicates the likely errors in these values of ε.

In the case of the strongly perturbed lines the second order shifts deduced from this treatment are too large for third-order shifts to be neglected - this is clear since the largest off-diagonal matrix element is ~8 GHz, while the energy denominator is ~500 GHz. For this pair of levels it was necessary to go to a higher approximation, and this is most easily achieved by using the result of exact diagonalization. The eigenvalues of M are given by equation 8; the difference between them is

$$[(E + \beta_{AA_o})^2 + 4\varepsilon^2_{AA_o}]^{\frac{1}{2}}.$$

We consider a second fictitious transition (though a physically realizable one this time), the transition between the levels themselves which I denote λ_p. The isotope shifts in λ_p are given by

$$\nu_p^{A-A_o} = [(E + \beta_{AA_o})^2 + 4\varepsilon^2_{AA_o}]^{\frac{1}{2}} - E \; ; \tag{17}$$

these shifts can be found by subtracting shifts connecting levels 1 and 2 to a common lower level. Hence one set of values for ν_p exists, from the two spectral lines $\lambda\lambda$ 564.75 nm, 565.28 nm. We note from equation 17 that β_{AA_o} is the value the isotope shift in λ_p would have if ε_{AA_o} were zero. Thus β_{AA_o} gives a linear King plot with shifts in an unperturbed line. From equation 17 we deduce

$$(\nu_p^{A-A_o} + E)^2 = (E + \beta_{AA_o})^2 + 4\varepsilon^2_{AA_o} \; . \tag{18}$$

If we substitute for the $\delta\langle r^2\rangle$ in β and ε using an unperturbed spectral line ν_u we find

$$\varepsilon_{AA_o} = \phi_{12}\nu_u^{A-A_o} + \mu_{12}/\alpha_{AA_o} \tag{19a}$$

(19b) $$\beta_{AA_o} = \Delta\phi\nu_u^{A-A_o} + \Delta\mu/\alpha_{AA_o}$$

where ϕ_{12} and μ_{12} have been given above, and

$$\Delta\phi = (f_1-f_2)/F_u, \qquad \Delta\mu = (m_1-m_2) - \Delta\phi M_u \ ;$$

that is, they are the usual King parameters for the transition λ_p.

Equations 18 and 19 are more complicated than the corresponding equations 13a and 13b in the second order calculation, and they were solved iteratively, by taking values for ϕ_{12} and μ_{12}, calculating ε from equation 19a, β from equation 18 and then finding the correlation coefficient for a King plot of β against ν_u. When the correct values of ϕ_{12} and μ_{12} are found this King plot has a correlation coefficient of unity, and its slope and intercept give $\Delta\phi$ and $\Delta\mu$. Since we have only one set of values of ν_p we can only do the calculation once, and so we use the best possible values of ν_u. These are found from the multi-dimensional King plot to the set A plus $\bar{\lambda}$. The fitted values of the shifts in λ 567.87 nm were chosen; that is those values lying on the King plot line nearest to the measured values. The values of ν_p and ν_u are given in Table 8.6. (It might be objected that since the shifts in $\lambda\lambda$ 564.75 nm, 565.28 nm are used to derive both the ν_p and the shifts in $\bar{\lambda}$, it is incorrect to use $\bar{\lambda}$ in the multi-dimensional King plot to determine the shifts ν_u. However this is not the case, since ν_p and the shifts in $\bar{\lambda}$ are statistically independent.)

The results of this calculation give

$$\phi_{12} = 4.11(23) \qquad \mu_{12} = 10.0(1.7) \text{ THz}$$
$$\Delta\phi = 5.154(13) \qquad \Delta\mu = 12.47(8) \text{ THz},$$

which, using equations 19, give the values of ε and β in Table 8.7. The errors were estimated by repeating the calculation several times with values of ν_u offset from the values in Table 8.6 by amounts comparable with the uncertainties. The extent to which the off-diagonal terms in M_{AA_o} modify the shifts can be seen by comparing the ν_p (Table 8.6) with β (Table 8.7).

TABLE 8.6. Isotope Shifts in λ_p, λ_u.

The shifts in λ_p are the differences of the corresponding shifts in λλ 564.75, 565.28 nm. The errors are derived from the uncertainty of 200 kHz quoted for adjacent even-even shifts; they are rounded to the nearest 50 kHz. The shifts in λ_u = 567.87 nm have been adjusted for maximum consistency with results in other lines of class A (see text); the error limits are thus lower than those quoted with the original measurements, and are estimated to be 100 kHz for adjacent even-even shifts.

A,A_o	$\nu_p^{A-A_o}$ GHz	$\nu_u^{A-A_o}$ GHz
148,144	-3.45550 (30)	-1.13155 (10)
150,144	-5.52646 (40)	-1.76146 (14)
152,144	-8.53172 (50)	-2.57966 (17)
154,144	-9.99851 (55)	-3.08622 (20)

TABLE 8.7. Results of Diagonalization.

β_{AA_o} is the first-order contribution to the shifts in λ_p. ε_{AA_o} is the off-diagonal matrix element; it is the sum of two terms, m_{12}/α_{AA_o} and $f_{12}\delta\langle r^2\rangle^{A-A_o}$, due to mass and field effects respectively.

A,A_o	β_{AA_o} GHz	ε_{AA_o} GHz	m_{12}/α_{AA_o} GHz	$f_{12}\delta\langle r^2\rangle^{A-A_o}$ GHz
148,144	-3.4862 (14)	-2.77(4)	0.61 (24)	-3.38 (21)
150,144	-5.6062 (17)	-4.45 (5)	0.91 (35)	-5.36 (33)
152,144	-8.7264 (50)	-6.94 (8)	1.19 (47)	-8.13 (49)
154,144	-10.2689 (51)	-8.16 (8)	1.47 (58)	-9.63 (59)

8.4 Discussion

In section 8.3 the shifts in the perturbed levels were analysed in two ways using only comparisons with other isotope shift measurements. The accuracy of the results is limited only by the experimental error and the limitations of the theoretical model used. In order to get a clearer picture of the perturbations it is helpful to separate the mass and field contributions to the matrix element ε; this requires, of course, information in addition to isotope shifts themselves.

Brand et al. (1980) have measured isotope shifts in a number of transitions in this region of the samarium spectrum, and have, using established methods to estimate the mass shift, separated the mass and field shifts and also deduced a value of F for one transition. Hence, using the King plot we can find values for F and M for any transition. For the reference transition λ_r = 591.64 nm, they give

$$M_r = 280\ (140)\ \text{GHz} \qquad F_r = -5.50\ (22)\ \text{GHz fm}^{-2}.$$

The isotope shifts in λ_r were compared with set A plus $\bar{\lambda}$, using the multi-dimensional King plot, and from the vectors $\underline{y}_o$ and $\underline{m}$ the values of F_u and M_u for the transition λ_u = 567.87 nm were deduced using the known values of M_r and F_r:

$$M_u = -1.642\ (40)\ \text{THz} \qquad F_u = -1.59\ (6)\ \text{GHz fm}^{-2}.$$

Substituting these values into the definitions of ϕ_{12}, μ_{12}, $\Delta\phi$ and $\Delta\mu$ we find

$$m_{12} = 3.3\ (1.7)\ \text{THz} \qquad f_{12} = -6.53\ (45)\ \text{GHz fm}^{-2}$$

$$m_1 - m_2 = 4.01\ (22)\ \text{THz} \qquad f_1 - f_2 = -8.19\ (33)\ \text{GHz fm}^{-2}.$$

The errors in f_{12} and m_{12} are dominated by the experimental uncertainty in ϕ_{12} and μ_{12}, rather than the uncertainty in F_u and M_u, whereas for m_1-m_2 and f_1-f_2 the converse is true. We see that the subdivision of ε_{AA_o} into mass and field effects, given explicitly in Table 8.7, is less precise than the determination of ε_{AA_o} itself. Nevertheless it appears that both terms are needed to account for the observed shifts, although the field term is much the larger

of the two contributions to ε_{AA_o}.

The non-relativistic field shift operator $\hat{f}$, derived in section 1.4, is a sum of single electron scalar operators, while the mass-shift operator $\hat{m}$ is a sum of scalar products of single electron vector operators. Thus if two states have a non-zero matrix element of $\hat{f}$ between them there is no obvious reason why there should not also be a non-zero matrix element of $\hat{m}$; the converse, however, is not true. For example $\hat{m}$ can couple two configurations, while $\hat{f}$ cannot even couple two different terms of the same configuration. My purpose in the remainder of this section is to show that values of off-diagonal matrix elements of the size we observe are not unreasonable, and it is much simpler to discuss the case of field shift. Given a certain off-diagonal field shift matrix element, the only thing one can say simply about the mass shift matrix element is that one might expect it to be smaller by roughly the same sort of factor by which the first order mass shift is smaller than the first order field shift. This factor varies over a wide range for different excited states, and this range includes the value of about five for the ratio of off-diagonal mass shift and field shift matrix elements. In the remainder of this section, therefore, I shall discuss only field shift matrix elements.

The levels we are concerned with are largely composed of the configurations $4f^6 6s6p$, which I denote a, and $4f^5 5d6s^2$, which I denote b. The ground configuration $4f^6 6s^2$ I denote g. Then, in the central field approximation, $\hat{f}$ is a constant in any configuration, and has only diagonal matrix elements:-

$$(20) \qquad \langle a\gamma J|\hat{f}|a\gamma' J'\rangle = f_a \delta_{\gamma\gamma'}\delta_{JJ'}$$

where γ denotes a term of configuration a. Let $|i\rangle$ be a level made up of various terms from the two configurations; all these levels must have the same value of J, so this label will not be given. Thus

$$(21) \qquad |i\rangle = \sum_{\gamma} a_{\gamma}(i)|a\gamma\rangle + \sum_{\gamma'} b_{\gamma'}(i)|b\gamma'\rangle$$

where the coefficients $a_\gamma(i)$ and $b_{\gamma'}(i)$ are constrained by orthogonality and normalization of the levels $|i>$ to obey

$$\sum_\gamma |a_\gamma(i)|^2 + \sum_{\gamma'} |b_{\gamma'}(i)|^2 = 1 \tag{22a}$$

$$\sum_\gamma a_\gamma(i)a^*_\gamma(j) + \sum_{\gamma'} b_{\gamma'}(i)b^*_{\gamma'}(j) = 0. \tag{22b}$$

The value of f_i, the diagonal matrix element of $\hat{f}$, is easily found, using equations 20 and 21, to be

$$f_i = f_a \sum_\gamma |a_\gamma(i)|^2 + f_b \sum_{\gamma'} |b_{\gamma'}(i)|^2 \tag{23}$$

which is the well-known sharing rule for f. The off-diagonal matrix element between i and j can also be found

$$f_{ij} = f_a \sum_\gamma a_\gamma(i)a^*_\gamma(j) + f_b \sum_{\gamma'} b_{\gamma'}(i)b^*_{\gamma'}(j). \tag{24}$$

However this expression simplifies, using equation 22b, to

$$f_{ij} = (f_a - f_b) \sum_\gamma a_\gamma(i)a^*_\gamma(j) . \tag{25a}$$

Alternatively we can write

$$f_{ij} = (f_b - f_a) \sum_{\gamma'} b_{\gamma'}(i)b^*_{\gamma'}(j). \tag{25b}$$

If we introduce the fractional composition of configuration a in level i

$$A(i) = \sum_\gamma |a_\gamma(i)|^2$$

and similarly for B(i), so that A(i) + B(i) = 1, then using the Schwartz

inequality we deduce from equations 25

$$|f_{ij}| \leq |f_a - f_b|\sqrt{A_i A_j} \tag{26}$$

and

$$|f_{ij}| \leq |f_a - f_b|\sqrt{(1-A_i)(1-A_j)}$$

where the equality holds if $a_\gamma(i) = \alpha a_\gamma(j)$ for all γ. We can estimate the values of A_i using equation 23, which we can re-write as

$$f_i = A(i)f_a + B(i)f_b$$

and hence

$$F_{gi} = A(i)(f_a - f_g) + B(i)(f_b - f_g) \ , \tag{27}$$

where we shall neglect the small dependence of f_g on which level of the ground term is involved in the transition.

Values of $(f_a - f_g)$ and $(f_b - f_g)$ were given by Brand et al. (1980)

$$f_a - f_g = -5.50\ (20)\ \text{GHz fm}^{-2}$$
$$f_b - f_g = +10.6\ (1.0)\ \text{GHz fm}^{-2}$$

and hence

$$f_a - f_b = -16.1\ (1.2)\ \text{GHz fm}^{-2}.$$

We can determine F_{g1} and F_{g2} for the two perturbed levels using the value of $f_1 - f_2$ quoted above, and the value of $(f_1 + f_2 - 2f_g)$ which we can determine from the multi-dimensional King plot of set A including $\bar{\lambda}$, using the known value of F for λ 567.87 nm. This gives

$$f_1 + f_2 - 2f_g = +4.48\ \text{GHz fm}^{-2}$$

and so

$$F_{g1} = -1.86 \text{ GHz fm}^{-2}$$

$$F_{g2} = +6.34 \text{ GHz fm}^{-2}.$$

Then using equation 27 we find the composition of the two levels:-

$$A(1) = 0.77$$

$$A(2) = 0.26$$

Thus the level at 19191.64 is composed of roughly three-quarters of the configuration $4f^{6}6s6p$, and the level at 19174.84 of about the same fraction of $4f^{5}5d6s^{2}$. The compositions given by Carlier et al. (1968) based on a theoretical calculation containing parameters determined by a fit to energies and g-values, indicate rather greater purity, about 95% for level 2 and 80% for level 1.

The inequalities of equation 26 then give

$$|f_{12}| \leq 6.64 \text{ GHz fm}^{-2} .$$

Thus the observed value of f_{12} is not inconsistent with this analysis, but it does require that the terms admixed into level 1 of configuration b are in roughly the same proportions as those terms appear in level 2, and vice versa.

In conclusion, then, I have shown that quantitative analysis of the deviations from King plots is possible, using other isotope shift data only, and not any information about nuclear sizes. The separation of the non-linear effects into mass and field effects then follows once this separation has been performed for isotope shifts in an unperturbed line, and in this respect there is no essential difference between linear and non-linear isotope shifts. If we use the separation of mass and field effects of Brand et al. (1980), we find that the non-linear effects in the strongly perturbed levels are primarily due to the field effect, and the value of the off-diagonal field shift matrix

element, while roughly as large as it can be, is not so large as to make this interpretation of the deviations untenable. As for the levels showing smaller deviations, quantitative analysis is at present precluded by the experimental accuracy. However it is interesting to note that, according to the compositions of Carlier et al. (1968) the levels at 17769.71 cm^{-1} and 20153.47 cm^{-1} occupy positions in the J=1 and J=5 level lists analogous to the positions of the strongly perturbed levels in the J=4 level list. In particular, all the lower levels are nearly pure $4f^{6}6s6p$ configurations, and the levels of higher energy contain significant or dominant admixtures of $4f^{5}5d6s^{2}$. Thus our model would predict that the lower levels will be found to give linear King plots, and these borderline levels will only be perturbed by higher levels.

A more detailed interpretation of all these non-linear effects in isotope shifts will therefore require a new study of this entire region of the samarium spectrum, which in turn will require further experimental investigation of isotope shifts for many levels in this region.

APPENDIX A

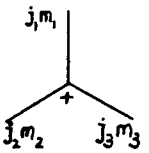
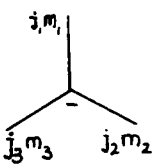
ANGULAR MOMENTUM DIAGRAMS

1. Elementary Rules

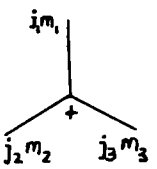
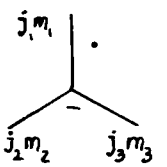
The rules I shall give for defining angular momentum diagrams are those given by Brink and Satchler (1968) Chapter 7, which is a general reference for this Appendix. In this section I shall very quickly give a few definitions and elementary applications sufficient for understanding the following two sections, where some rules used in Chapter 2 are presented.

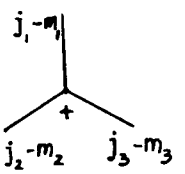
Any sum of products of 3-j symbols can be represented by a diagram or sum of diagrams. There are three elements in such diagrams:

(a) Node, which represents a 3-j symbol.

(1) $$\begin{pmatrix} j_1 & j_2 & j_3 \\ m_1 & m_2 & m_3 \end{pmatrix} =$$  $=$ 

We note here two symmetry properties of 3-j symbols:

(2)  $= (-)^{j_1+j_2+j_3}$ 

$= (-)^{j_1+j_2+j_3}$ 

(b) Line which represents a Kronecker delta

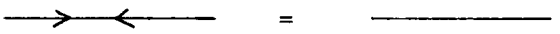
(3) $$j_1 m_1 \text{———————} j_2 m_2 = \delta(j_1, j_2)\delta(m_1, m_2) \ .$$

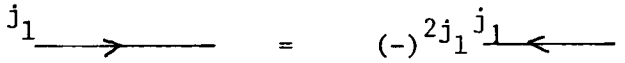
(c) Line with Arrow which represents the "1-j" symbol or metric tensor

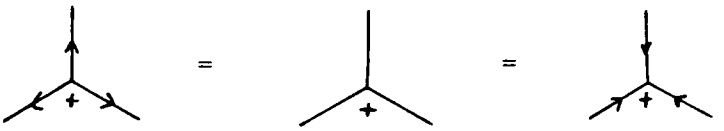
(4) $j_1 m_1 \longrightarrow j_2 m_2 = \delta(j_1, j_2)\delta(m_1, -m_2)(-)^{j_1 - m_1}$.

Joining two such elements represents summing over the corresponding m, which need not then be written on the diagram.

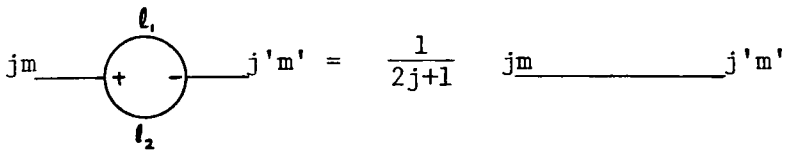
Simple rules for transforming diagrams follow straightforwardly from these definitions:-

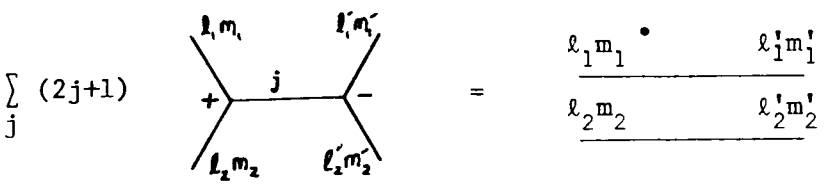
(5) 

(6) 

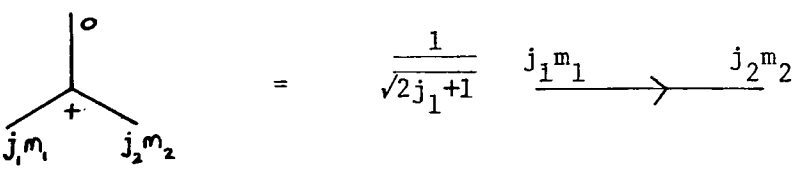
(7) 

Two further rules are derived from the two 3-j symbol sum rules:-

(8) 

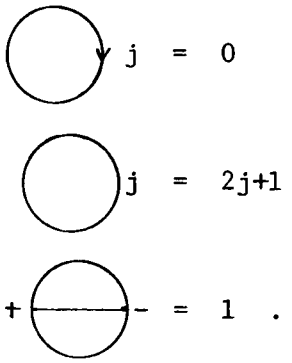
(9) 

A useful identity for a 3-j symbol with one j equal to zero is

(10) 

and three simple rules follow from equation 8 and the definitions

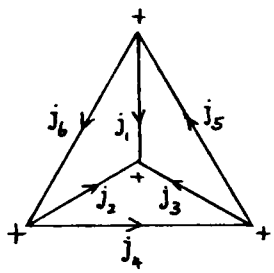
(11)



All the above transformations are very straightforward, and are used frequently here and in Chapter 2 without comment. Also used frequently is the definition of the 6-j symbol in terms of 3-j symbols:-

(12)

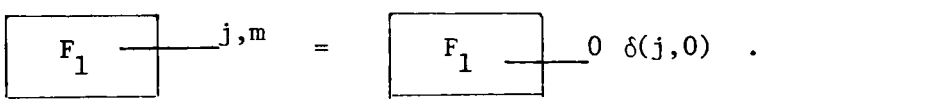
$$\left\{ \begin{matrix} j_1 & j_2 & j_3 \\ j_4 & j_5 & j_6 \end{matrix} \right\} =$$



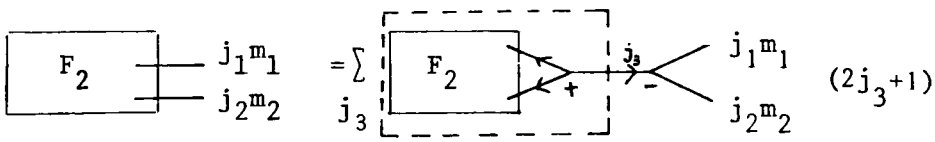
Note that the central three arrows, by equation 7, can point in or out or be absent, but the outside three must go round anticlockwise.

An important theorem concerns diagrams or parts of diagrams in "normal form": these are defined as diagrams in which every internal line (that is, one connecting two nodes) has an arrow and every external line (that is, one connected to a node at one end only) has no arrow. The theorem concerns a diagram in normal form with one external line, shown here as a box, labelled F_1 for one external line:-

(13)

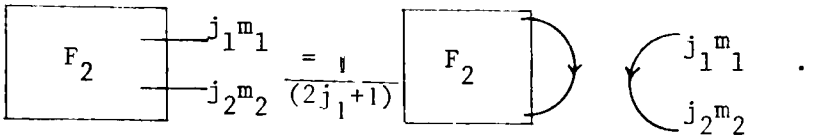


We can easily generate corollaries of this using equation 9; consider an F_2 box



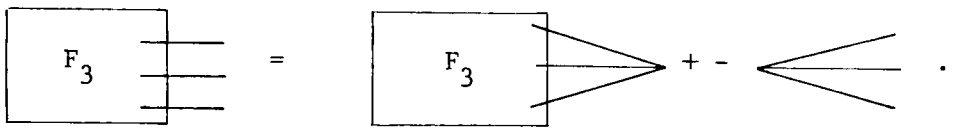
The dotted line encloses an F_1 box, and so using (13) we find

(14)

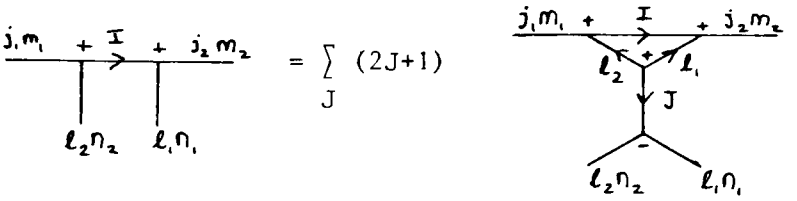


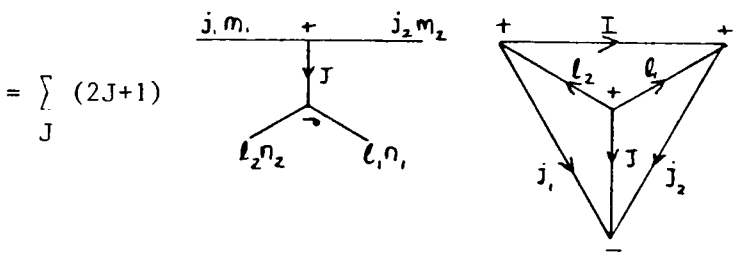
Similarly

(15)



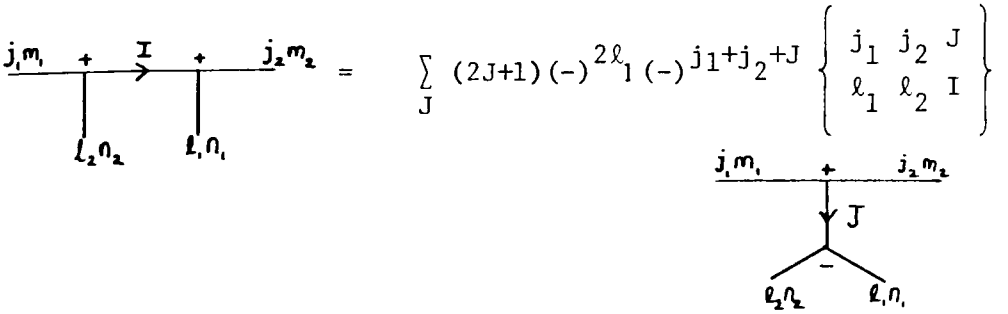
We now derive an elementary recoupling which is used a number of times in Chapter 2. Consider the diagram below and use equation 9





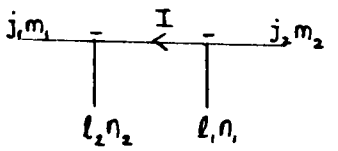
where the second step used the F_3 box rule, equation 15. Checking the sign of the 6-j symbol we find

(16)

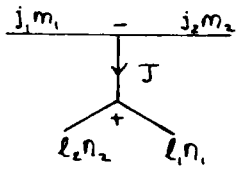


This can easily be transformed into two other forms used in Chapter 2:-

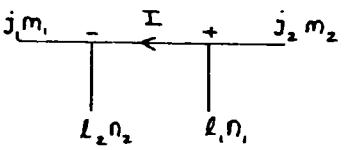
(17)



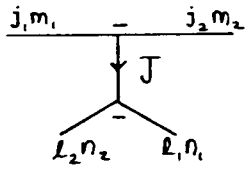
$$= \sum_J (2J+1)(-)^{2\ell_2}(-)^{j_1+j_2+J} \begin{Bmatrix} j_1 & j_2 & J \\ \ell_1 & \ell_2 & I \end{Bmatrix}$$



(18)



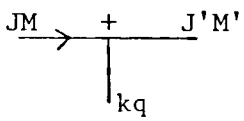
$$= \sum_J (2J+1)(1)^{2\ell_1}(-)^{j_1+\ell_2-I} \begin{Bmatrix} j_1 & j_2 & J \\ \ell_1 & \ell_2 & I \end{Bmatrix}$$



2. Graphical Representation of the Wigner-Eckart Theorem

I shall not follow the convention of Brink and Satchler for reduced matrix elements, but the more usual one of Edmonds. In this convention, the Wigner-Eckart theorem for a tensor operator of rank k, A^k_q, states:

(19) $$\langle \gamma\, JM | A^k_q | \gamma' J' M' \rangle = \langle \gamma J \,\|A^k\|\, \gamma' J' \rangle$$



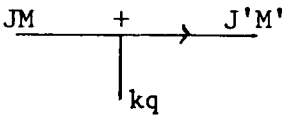
.

The matrix elements we require are of the scalar product of a tensor operator A^k_q with a "c-number" tensor E^k_q (e.g. a polarization vector $\underline{\varepsilon}$):

(20) $$A^k . E^k = \sum_q (-)^q A^k_q E^k_{-q} \; .$$

These matrix elements can easily be expressed using equations 19 and 20:

$$(21)\qquad \langle\gamma JM|A^k.E^k|\gamma'J'M'\rangle = (-)^k\langle\gamma J\,||A^k||\,\gamma'J'\rangle E^k$$

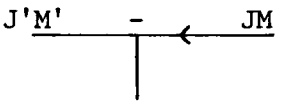


where, as in Chapter 2, the subscript q and the summation are understood. For the purpose of writing down diagrams for complex conjugate matrix elements, it is useful to have a different form of equation 21, using the result for a c-number tensor that

$$(E^k_q)^* = (-)^q(E^*)^k_q.$$

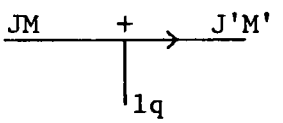
Then we find

$$(22)\qquad \langle\gamma JM|A^k.E^k|\gamma'J'M'\rangle^* = \langle\gamma J\,||A^k||\,\gamma'J'\rangle^*(E^*)^k$$

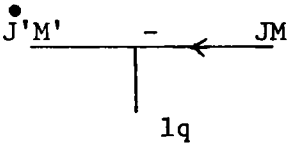


Equations 21 and 22 give the rules for turning matrix elements of the type required in Chapter 2 into diagrams; for reference I give the matrix elements explicitly here:

$$(23)\qquad \langle\gamma JM|\underline{R}.\underline{\varepsilon}|\gamma'J'M'\rangle = -\langle\gamma J\,||R||\,\gamma'J'\rangle\,\varepsilon$$



$$(24)\qquad \langle\gamma JM|\underline{R}.\underline{\varepsilon}|\gamma'J'M'\rangle^* = \langle\gamma J\,||R||\,\gamma'J'\rangle^*\varepsilon^*$$



.

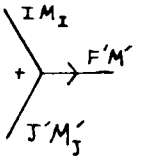
Secondly we require matrix elements in the case of hyperfine structure, that is, of the type

$$\langle JIFM|\underline{R}.\underline{\varepsilon}|J'IF'M'\rangle\ .$$

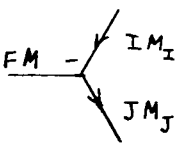
We could use the usual rule that expresses such matrix elements in terms of

a 6-j symbol, but if we do this in the full diagram of equation 20 in Chapter 2 we get eight 6-j symbols, many of which would vanish subsequently in summations. It is thus more convenient to keep the nuclear spin I coupled into the diagram. We must therefore uncouple the two states in the matrix element:-

$$|J'IF'M'> = \sum_{m'_J m_I} \sqrt{2F'+1}\ (-)^{2J'}\ |J'M'_J>|IM_I>$$

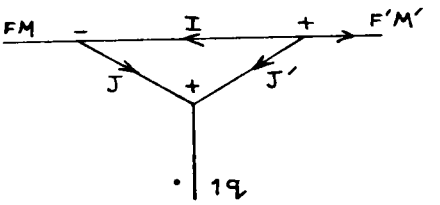


$$<JIFM| = \sum_{M_J M_I} \sqrt{2F+1}\ <JM_J|<IM_I|$$

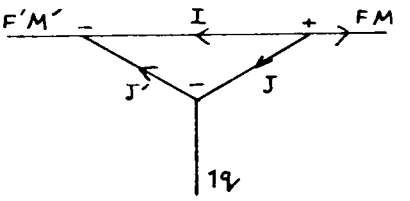


Using equations 23 and 24 we find

(25) $$<\gamma JIFM|\underline{R}.\underline{\varepsilon}|\gamma'J'IF'M'> = (-)\ \sqrt{(2F+1)(2F'+1)}\ <\gamma J\ ||R||\ \gamma'J'>\ \varepsilon$$



(26) $$<\gamma JIFM|\underline{R}.\underline{\varepsilon}|\gamma'J'IF'M'>^* = \sqrt{(2F+1)(2F'+1)}\ <\gamma J\ ||R||\ \gamma'R'>^*\ \varepsilon^*$$



3. Isotropic Diagrams

We here consider the properties of a class of diagrams that occur several times in Chapter 2. I define an n^{th} order isotropic diagram as a diagram with n external lines with angular momentum 1 and no arrows, and on which all internal lines have arrows (that is, the graph is in normal form). Since the external lines can be coupled to n c-number vectors - e.g. polarization vectors - the diagram must represent an n^{th} rank isotropic tensor. There are two fundamental isotropic tensors, the metric tensor δ_{ij} (in Cartesian co-ordinates) and the antisymmetric third rank tensor ε_{ijk}, and all isotropic tensors of higher rank can be decomposed into sums and products of these. The number of independent n^{th} order isotropic diagrams can thus be deduced by finding the number of different ways n indices can be divided into pairs (if n is even) or one set of three and the rest into pairs (if n is odd). This gives the number of independent diagrams N(n)

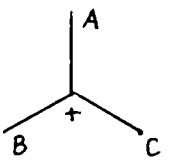
$$N(n) = (n-1)(n-3) \ldots\ldots 1 \quad \text{if n is even}$$

$$N(n) = \frac{1}{6} n(n-1)(n-2)N(n-3) \quad \text{if n is odd.}$$

The total number of apparently different ways of coupling together n vectors is larger than this - at least N^2 - but these are not all independent. This is because the N independent ways of coupling them may be generated by either taking one diagram and coupling the vectors onto its external lines in N different ways, or by keeping the same association of vectors with external lines and changing the values of angular momenta of the internal lines. There will be other variants, differing in sign of nodes, for example, and there may also be diagrams of a different shape, although these will be reducible to the simplest possible shape by some of the elementary transformations of section 1. We now consider specific diagrams of low order.

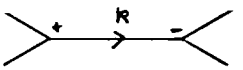
n=2 There is just one diagram A—→—B. (We here use an even more abbreviated notation for the vectors, where a q on the vector, a q on the external line adjacent to it and a summation over the q are all understood.) This diagram represents δ_{ij} and so its value when coupled to the vectors is $-\underline{A}.\underline{B}$.

n=3 Again there is just one diagram:

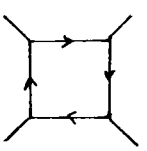


$$= \frac{i}{\sqrt{6}}\,\underline{A}\times\underline{B}.\underline{C}$$

n=4 This exemplifies the point I just made concerning the number of possible diagrams; N(4) is 3, and there is one shape of diagram with fewest lines on it as shown:

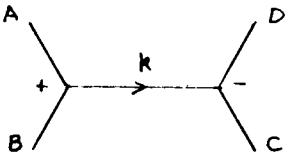


The internal line can have k = 0, 1 or 2, and this generates the three independent diagrams; alternatively one value of k can be chosen and $\underline{A}$ coupled with $\underline{B}$, $\underline{C}$ or $\underline{D}$ on the same node. These three diagrams are also independent. There are also more complicated diagrams such as



but these can be reduced to sums of the simpler diagrams. Because it applies to the work of Chapter 2 I shall consider only the first way of generating the N diagrams, that of allowing the internal lines to take all possible values of their angular momenta.

Note that the direction of the arrow is irrelevant, since 2k = even. This is always true, since all angular momenta will be integral in these diagrams for all n. In this case we find

$D_4(k) =$ 

(27a) $$D_4(0) = \frac{1}{3}\, \underline{A}.\underline{B}\ \underline{C}.\underline{D}$$

(27b) $$D_4(1) = \frac{1}{6}\, (\underline{A}\times\underline{B}).(\underline{C}\times\underline{D})$$

(27c) $$D_4(2) = \frac{1}{5}\, T_{ij}(A,B)\ T_{ij}(C,D)$$

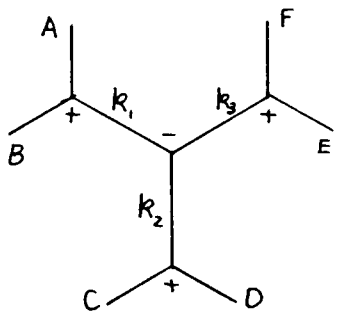
where $$T_{ij}(A,B) = \frac{1}{2}\,(A_iB_j + A_jB_i) - \frac{1}{3}\,\underline{A}.\underline{B}\ \delta_{ij}\ .$$

Expanding the product in the case k = 2 we find

$$D_4(2) = \frac{1}{5}\,[\frac{1}{2}\,\underline{A}.\underline{C}\ \underline{B}.\underline{D} + \frac{1}{2}\,\underline{A}.\underline{D}\ \underline{B}.\underline{C} - \frac{1}{3}\,\underline{A}.\underline{B}\ \underline{C}.\underline{D}]\ .$$

The form of these results is very reasonable, since $D_4(0)$ is the product of two scalar products, $D_4(1)$ is the product of two vector products and $D_4(2)$ is the product of two tensor products.

n=6 In this case there are 15 independent diagrams, but fortunately some of them have the same structure with a different coupling of the vectors. They are all of the form

$D_6(k_1,k_2,k_3) =$ 

with k_1, k_2 and k_3 equal to 0, 1 and 2 independently, except that (0,1,2), (0,0,1) and (0,0,2), and permutations, vanish, reducing the number of diagrams

to 15. However these are of seven different sorts only:

(i) (0,0,0),

(ii) (1,1,1),

(iii) (2,2,2),

(iv) (0,1,1) and permutations,

(v) (0,2,2) and permutations,

(vi) (1,2,2) and permutations,

and (vii) (2,1,1) and permutations

and so only one diagram from each class need be given explicitly.

Consider first $k_3 = 0$ (classes (i), (iv) and (v)). From equation 10 we have

$$D_6(k,k,0) = \frac{(-)^{1+k}}{\sqrt{3(2k+1)}} D_4(k)\ \underline{E}.\underline{F}. \tag{28}$$

Secondly, class (iii):

$$D_6(2,2,2) = \frac{2}{25}\sqrt{\frac{3}{7}}\ T_{ij}(A,B)T_{jk}(C,D)T_{ki}(E,F). \tag{29}$$

Thirdly, class (vi):

$$D_6(2,2,1) = \frac{1}{15\sqrt{5}}\ T_{il}(A,B)T_{lj}(C,D)\varepsilon_{ijk}(\underline{E}\times\underline{F})_k. \tag{30}$$

Diagrams of class (ii) and (vii) are not required in Chapter 2 and have not been calculated. Presumably they are proportional to

$$\varepsilon_{ijk}(\underline{A}\times\underline{B})_i(\underline{C}\times\underline{D})_j(\underline{E}\times\underline{F})_k$$

and

$$T_{ij}(\underline{A}\times\underline{B},\ \underline{C}\times\underline{D})T_{ij}(E,F) \quad \text{respectively.}$$

APPENDIX B

EXTRACTION OF ISOTOPE SHIFTS FROM MEASURED POSITIONS

In this Appendix I give the correct solution to the coupled error problem referred to in Section 6.3, when more than two isotope positions are measured on the same spectrum. Although the mathematics is straightforward, the solution has not, so far as I know, been given explicitly before. The problem is, given sets of numbers x_i^A representing the measured positions of isotopes A relative to an arbitrary origin on each set, find the best values of the 'true' positions consistent with constant values of the isotope shifts. We write the 'true' position as $x_i^o + \nu^A$, where x_i^o is the arbitrary origin on each spectrum, and ν^A are the isotope positions. Thus we must minimize, to find the least squares solution,

$$R = \sum_{i,A} (x_i^A - x_i^o - \nu^A)^2 \, w_i^A, \tag{1}$$

where $w_i^A = 1/(\sigma_i^A)^2$ is the weight attached to the measurement of isotope A on run i, σ_i^A being the standard deviation, calculated using equations 1 and 2 of Chapter 6.

In minimizing R we can vary the origins x_i^o, and the isotope positions ν^A. Consider first the origins:

$$\frac{\partial R}{\partial x_i^o} = \sum_A - 2w_i^A (x_i^A - x_i^o - \nu^A)$$

and so the best value for x_i^o is

$$x_i^o = \sum_A \frac{w_i^A (x_i^A - \nu^A)}{S_i} \tag{2}$$

where

$$S_i = \sum_A w_i^A \quad (3)$$

We now adopt a vector and matrix notation: singly (doubly) underlined quantities are column vectors (matrices) labelled by isotope mass number A. Thus, for example, $\nu^A \rightarrow \underline{\nu}$. $\underline{\nu}^T$ denotes the transposed (row) vector. Substituting equation 2 into equation 1 then gives

$$R = A - 2\underline{B}^T\underline{\nu} + \underline{\nu}^T\underline{\underline{C}}\,\underline{\nu} \quad (4)$$

where

$$\underline{\underline{C}} = \sum_i \underline{\underline{C}}_i \quad \text{and} \quad C_i^{AA'} = W_i^A \left(\delta^{AA'} - \frac{W_i^{A'}}{S_i}\right),$$

$$\underline{B} = \sum_i \underline{\underline{C}}_i \underline{x}_i \quad (5)$$

$$A = \sum_i \underline{x}_i^T \underline{\underline{C}}_i \underline{x}_i \quad .$$

($\delta^{AA'}$ denotes the components of $\underline{\underline{I}}$, the unit matrix.) It is then straightforward to show that R is stationary when ν satisfies

$$\underline{\underline{C}}\nu = \underline{B} \quad . \quad (6)$$

Call the vector satisfying equation 6 $\underline{\nu}_o$; then we can easily demonstrate the nature of the stationary point by re-writing equation 4 as

$$R = (A - \underline{B}^T \underline{\nu}_o) + \delta\underline{\nu}^T \underline{\underline{C}}\,\delta\underline{\nu} \quad (7)$$

where $\delta\underline{\nu} = \underline{\nu} - \underline{\nu}_o$. The first, bracketed, term is the value of R at the stationary point, which is therefore a minimum provided that the second term is

positive definite. However, since R is a sum of squares, the second term must be at least positive semi-definite.

We now consider how to solve equation 6, which determines the minimum. The matrix C is, in fact, singular but the reason for this is physically obvious: if we add some constant onto all the ν^A, and subtract the constant from all the arbitrary origins x_i^o then the value of R is unchanged. Suppose we have n isotopes, so that sums over A have n terms. We define

$$\underline{u}_1 = (n^{-\frac{1}{2}}, n^{-\frac{1}{2}} \ldots\ldots, n^{-\frac{1}{2}})^T ;$$

the reason for this notation will become clear in a moment. Then, using equations 1 and 2, $\underline{\nu}$ and $\underline{\nu} + \alpha \underline{u}_1$ have the same value of R for all α. This implies, as easily verified from equations 5, that

$$\underline{\underline{B}}^T \underline{u}_1 = 0$$

and

$$\underline{\underline{C}}\, \underline{u}_1 = 0 ;$$

that is, $\underline{u}_1$ is an eigenvector of $\underline{\underline{C}}$ with zero eigenvalue, but $\underline{\underline{B}}$ is orthogonal to $\underline{u}_1$ and hence equations 6 are consistent but not independent. Thus we cannot directly solve equation 6 by multiplying by $\underline{\underline{C}}^{-1}$, since $\underline{\underline{C}}$ has no inverse.

We therefore consider the expression for the inverse of a matrix in terms of its eigenvalues and eigenvectors, in order to see how it can be modified in this case. Consider a non-singular symmetric matrix $\underline{\underline{M}}$, and consider the solution of the equations analogous to equations 6:

$$\underline{\underline{M}}\, \underline{x} = \underline{L} \tag{8}$$

The eigenvalues and eigenvectors of $\underline{\underline{M}}$ are λ_i, $\underline{u}_i$, and they satisfy

$$\underline{\underline{M}}\,\underline{u}_i = \lambda_i \underline{u}_i ,$$

(9)

$$\underline{u}_i^T \underline{u}_j = \delta_{ij} ,$$

and

$$\sum_i \underline{u}_i \underline{u}_i^T = \underline{\underline{I}}$$

Using equations 9 it is easy to verify that the solution to equation 8 is

$$\underline{x} = \sum_i (\underline{u}_i^T \underline{L})\, \lambda_i^{-1}\, \underline{u}_i ,$$

that is M^{-1} is given by

$$\underline{\underline{M}}^{-1} = \sum_i \underline{u}_i \underline{u}_i^T \lambda_i^{-1} .$$

This suggests that a solution of equation 6 is

(10)

$$\underline{\nu}_o = \sum_{i \neq 1} (\underline{u}_i^T \underline{B})\, \lambda_i^{-1}\, \underline{u}_i$$

and that the general solution is

(11)

$$\underline{\nu}_o = \alpha \underline{u}_1 + \sum_{i \neq 1} (\underline{u}_i^T \underline{B})\, \lambda_i^{-1} \underline{u}_i .$$

This is easily verified to be the case, and so the differences between the components of $\underline{\nu}_o$ in equation 11 provide the required best values of the isotope shifts, and the 'true' value of the position on any run is given by $x_i^o + \nu^A$, where x_i^o is given by equation 2.

I shall now briefly describe the output of the computer program that was written to implement this procedure which is shown in Fig. B.1. The computer first calculates A, $\underline{B}$ and $\underline{\underline{C}}$, and uses a NAG routine to find the eigenvalues and eigenvectors of $\underline{\underline{C}}$. The smallest eigenvalue, which is mathematically zero, is then printed, and the difference between the exact

COMBINED ANALYSIS OF ALL DATA

ZERO EIGENVALUE= 0.0E-01
RMS ERROR OF EIGENVECTOR=8.48E-16

EIGENVALUE	ST.DEV.	EIGENVECTOR
11.362	0.00077	(0.791,-0.012,-0.202,-0.577)
12.827	0.00072	(0.273,-0.192,-0.706, 0.625)
16.226	0.00064	(0.223,-0.844, 0.459, 0.162)

BEST FIT POSITION	ST.DEV.
-7.27861	0.00087
-3.40481	0.00075
0.00000	0.00081
13.21667	0.00085

CHI-SQUARED= 29.1660
DEGREES OF FREEDOM= 29.
CHI-SQUARED/DEG.OF FREEDOM= 1.00572

	CALCIUM 42				CALCIUM 43				CALCIUM 44				CALCIUM 48			
RUN	* WEIGHT	DATA	FIT	ERR/S.D*	WEIGHT	DATA	FIT	ERR/S.D*	WEIGHT	DATA	FIT	ERR/S.D*	WEIGHT	DATA	FIT	ERR/S.D
217	*0.15	1.41293	1.41157	0.21*0.52	5.28533	5.28537	-0.01*0.66		8.68990	8.69018	-0.09*0.00		0.00000	21.90685	0.00	
218	*0.54	0.33178	0.33787	-1.73*1.74	4.21308	4.21167	0.72*1.06		7.61726	7.61649	0.31*0.00		0.00000	20.83316	0.00	
219	*0.00	0.00000	-3.15614	0.00*0.38	0.71499	0.71766	-0.64*0.83		4.11790	4.12247	-1.62*1.48		17.34242	17.33915	1.54	
220	*0.06	6.66590	6.66859	-0.26*0.58	10.54086	10.54239	-0.45*0.73		13.94866	13.94720	0.48*0.00		0.00000	27.16387	0.00	
223	*0.00	0.00000	-6.47166	0.00*0.00	0.00000	-2.59786	0.00*0.94		0.80784	0.80695	-0.33*0.50		14.02194	14.02363	-0.46	
225	*0.00	0.00000	-1.88913	0.00*0.97	1.98664	1.98467	0.75*0.65		5.38661	5.38948	-0.89*0.31		18.60599	18.60615	-0.03	
228	*1.32	0.14848	0.14727	0.54*2.98	4.02167	4.02108	0.40*0.46		7.42425	7.42589	-0.43*1.68		20.64100	20.64256	-0.78	
229	*2.08	0.52438	0.52586	-0.83*2.36	4.40155	4.39966	1.13*1.14		7.80736	7.80447	1.19*1.83		21.01859	21.02114	-1.34	
230	*2.22	0.58161	0.57949	1.22*2.24	4.45048	4.45329	-1.63*1.93		7.85820	7.85811	0.05*1.08		21.07609	21.07478	0.53	
231	*1.99	0.58694	0.58432	1.43*2.08	4.45520	4.45813	-1.64*1.28		7.86276	7.86294	-0.08*0.99		21.08075	21.07961	0.44	
232	*0.84	0.05563	0.05519	-0.55*1.78	3.92970	3.92899	0.37*2.03		7.33373	7.33381	-0.04*1.23		20.55064	20.55048	0.07	
233	*1.57	1.05497	1.05631	-0.65*1.33	4.93009	4.93011	-0.01*1.74		8.33530	8.33492	0.19*1.71		21.55244	21.55159	0.43	
234	*1.02	1.05396	1.05569	-0.68*1.79	4.93090	4.92950	0.73*1.44		8.33441	8.33431	0.05*2.01		21.55054	21.55098	-0.24	

eigenvalue, which is $(\frac{1}{2},\frac{1}{2},\frac{1}{2},\frac{1}{2})^T$ for n = 4, and the computed eigenvalue is computed, that is $\delta\underline{u}^T\,\delta\underline{u}$, where $\delta\underline{u}$ is the appropriate difference vector. Both of these are zero to machine accuracy (about 15 decimal places.)

R is of course equivalent to χ^2, and so the remaining eigenvectors give directions in A-space in which χ^2 increases most rapidly from the minimum; the distance for χ^2 to increase by a factor $(1 + 1/N)$, where N is the number of degrees of freedom, is then calculated. This is a standard deviation of the minimum position in that direction. The number of degrees of freedom is P - n - k + 1 where P is the total number of peaks on all runs, and k is the number of runs. The program next prints the isotope positions using equation 11, with α determined by $\nu^{44} = 0$, and standard deviations in these positions, which are found in the same way as the standard deviations from the eigenvalues, using C^{AA} instead of the eigenvalues.

Finally the program prints the value of R and the table of measured and 'true' positions. We expect R to be approximately equal to N, and so the program was re-run using different values of $\Delta\nu_e$ to achieve this. The value giving R = N was 51 kHz per peak - which is consistent with the 80 kHz per shift found for the analysis described in Chapter 6, being about $\sqrt{2}$ smaller.

APPENDIX C

METHODS FOR COMPARING ISOTOPE SHIFTS IN SEVERAL TRANSITIONS

C.1 King Plots in N dimensions

In this Appendix I extend the idea of comparing isotope shifts in two spectral lines by means of the King plot, described in Section 1.4. The aims of this are two-fold: firstly to compare all spectral lines simultaneously, so that all the data contributes to the best values for mean square radii, and secondly to avoid coupling of the errors. This will occur if isotope shifts have been measured in two different spectral lines, and values are quoted for different isotope pairs in the two lines, if the two sets of data are first made to refer to the same isotope pairs before comparing them in a King plot in the usual way. In this section I consider the extension of the King plot to N spectral lines, where the same isotope pairs are measured in each; it is also necessary that the standard deviation satisfy a certain criterion. In the next section these two conditions are relaxed; however the comparison is then more abstract, and the idea of a King plot as a line in N-dimensional space is lost, and one is left with just isotope shifts satisfying the King relations.

It was shown in section 1.4 that the scaled isotope shifts $\delta\sigma^{A-A'}$, defined by

$$\delta\sigma_i^{A-A'} = \alpha_{AA'}\ \delta\nu_i^{A-A'}$$

where

$$\alpha_{AA'} = AA'/(A-A')$$

and the A's are nuclear masses in amu, lie on a straight line, when the

shifts for each isotope pair in the two spectral lines are plotted against each other. We now consider the extension of this to the case where measurements are available for N spectral lines. Initially we shall restrict ourselves to the case where the measurements are for the same isotope pairs, and I shall label the istotope pairs AA' by a Greek superscript such as μ.

The equation for the isotope shift in spectral line i is then

$$\delta\nu_i^\mu = M_i/\alpha^\mu + F_i\ \delta\langle r^2\rangle^\mu \quad . \tag{1}$$

Introduce an N-dimensional space with axes labelled by $\delta\sigma_i$, the scaled isotope shifts, and let $\underline{x}$ be a vector in this space, i.e. $x_i = \delta\sigma_i$. Then, multiplying equation 1 by α^μ, we obtain

$$\underline{x}^\mu = \underline{M} + \underline{F}\,\delta^\mu \tag{2}$$

where $\underline{M}$ is the vector of M_i's, similarly for $\underline{F}$, and

$$\delta^\mu = \delta\langle r^2\rangle^\mu\alpha^\mu \quad .$$

But equation 2 states that the points $\underline{x}^\mu$ lie on a straight line passing through the point $\underline{M}$, with $\underline{F}$ a vector lying along the line. This we call the multi-dimensional King plot. All that can be done by measurement of optical isotope shifts is to find the line in N-dimensional space; we cannot establish which point corresponds to the point $\underline{M}$ (this would separate the mass and field shift) or the length of vector $\underline{F}$ (this gives the conversion from field shift to $\delta\langle r^2\rangle$). It is clear that knowing M_i for any transition establishes the point $\underline{M}$, and knowing F_i for any transition gives the length of $\underline{F}$. Thus we cannot determine all the coefficients in equation 2, but we can in equation 3

(3) $$\underline{x}^{\mu} = \underline{x}_o + \lambda^{\mu}\underline{n}$$

because the coefficients are subject to two constraints:

(4a) $$\underline{n}.\underline{n} = 1$$

(4b) $$\underline{n}.\underline{x}_o = 0 \ .$$

Given isotope shifts in the form of points $\underline{x}^{\mu}$, the problem is to find the best values of λ^{μ}, $\underline{n}$ and $\underline{x}_o$. The advantage of working with multi-dimensional King plots, rather than comparing all spectral lines in pairs in a conventional King plot, is that we can find the most consistent values of the isotope shifts for all the spectral lines at once.

We first consider the simple case of equal standard deviations for all measurements of scaled shifts. Then the best staight line is that which minimizes the squared distance from the points $\underline{x}^{\mu}$ to the line. The squared distance from a point $\underline{x}^{\mu}$ to a point on a line of the form

$$\underline{x} = \underline{x}_o + \lambda\, \underline{n}$$

is given by

(5) $$d^2 = (\underline{x}^{\mu} - \underline{x}_o - \lambda\,\underline{n})^2 = (\underline{x}^{\mu} - \underline{x}_o)^2 - 2\lambda\underline{x}^{\mu}.\underline{n} + \lambda^2$$

This has a minimum when $\lambda = \lambda^{\mu}$, where

(6) $$\lambda^{\mu} = \underline{x}^{\mu}.\underline{n}$$

and

(7) $$d^2 = (\underline{x}^{\mu} - \underline{x}_o)^2 - (\underline{x}^{\mu}.\underline{n})^2$$

Thus we require to minimize

(8) $$R = \sum_{\mu} (\underline{x}^{\mu} - \underline{x}_o)^2 - (\underline{x}^{\mu}.\underline{n})^2$$

with respect to $\underline{x}_o$ and $\underline{n}$, subject to the constraints of equation 4.

Differentiating equation 8 with respect to the components of $\underline{x}_o$ and $\underline{n}$ we obtain the set of equations

(9) $$\sum_{\mu} (\underline{x}^{\mu} - \underline{x}_o) = M\xi\underline{n}$$

(10) $$\sum_{\mu} \underline{x}^{\mu}\underline{n}.\underline{x}^{\mu} = M\eta\underline{n} + M\xi\underline{x}_o$$

where η and ξ are Lagrange multipliers derived from the constraint equations 4, and M is the number of points labelled by μ. Forming the scalar product of equation 9 with $\underline{n}$ we obtain, using equations 4a and 4b,

(11) $$\xi = \bar{\underline{x}}.\underline{n}$$

and hence

(12) $$\underline{x}_o = \bar{\underline{x}} - \bar{\underline{x}}.\underline{nn}$$

where here and subsequently the bar notation denotes the usual average,

$$\bar{\underline{x}} = \frac{\sum_{\mu} \underline{x}^{\mu}}{M} \quad .$$

Forming the scalar product of equation 10 with $\underline{n}$ we obtain

(13) $$\eta = n_i n_j \overline{x_i x_j} \qquad \text{(Einstein summation convention on subscripts)}$$

Substituting equations 11 to 13 in equation 10 yields

(14a) $$C_{ij}\, n_j = \gamma n_i$$

where the matrix C is given by

(14b) $$C_{ij} = \overline{x_i x_j} - \bar{x}_i \bar{x}_j = \overline{(x_i - \bar{x}_i)(x_j - \bar{x}_j)}$$

(14c) and $$\gamma = n_i n_j C_{ij} \ .$$

There are N solutions to equation 14, when $\underline{n}$ is any one of the N eigenvectors of C, and γ is then the corresponding eigenvalue. The reason for this multiplicity of solutions can be seen by considering the case N = 3. Suppose that the points are uniformly distributed through an ellipsoid; then there are three lines - three axes of the ellipsoid - for which the value of R is locally stationary with respect to nearby lines. If there is a real linear dependence, then the ellipsoid will be a very long prolate ellipsoid, with one eigenvalue very different from the others. We can re-express R in terms of C (equation 8)

(15) $$R = M(C_{ii} - n_i n_j C_{ij})$$

and so when $\underline{n}$ is an eigenvector of C, with eigenvalue γ,

(16) $$R = M(\mathrm{Tr}C - \gamma) \ .$$

Thus the least squares solution is that for which $\underline{n}$ is the eigenvector of C with largest eigenvalue, $\underline{x}_o$ is given by equation 12 and the λ^μ by equation 6. The most consistent values of the isotope shifts are given by

$$\bar{x} + (\underline{x}^\mu - \underline{\bar{x}}).\underline{n}\ \underline{n}$$

Secondly we consider the case of unequal standard deviations, so that the standard deviation of x_i^μ is σ_i^μ. (Note that this will in general be the

case, even if the $\delta\nu$ are all measured with the same accuracy because of the different values of α^{μ}.) Thus, in the minimization we must weight the distance along each axis from the points $\underline{x}^{\mu}$ to the line with weight $w_i^{\mu} = (\sigma_i^{\mu})^{-2}$. If we do this, we find the results analogous to equations 6 and 7 are

$$\lambda^{\mu} = \frac{n_i w_i^{\mu} (\underline{x}^{\mu} - \underline{x}_o)_i}{n_j w_j^{\mu} n_j} \tag{17}$$

$$d^2 = (\underline{x}^{\mu} - \underline{x}_o)_i \, w_i^{\mu} \, (\underline{x}^{\mu} - \underline{x}_o)_i - \frac{\left[(\underline{x}^{\mu} - \underline{x}_o)_i \, w_i^{\mu} n_i\right]^2}{n_j \, w_j^{\mu} \, n_j} \tag{18}$$

The corresponding equation for R is a sum of terms like equation 18 for the different values of μ. However there is no corresponding solution for the minimization problem in terms of an eigenvalue equation. This problem will be taken up below. However the equations 17 and 18 reduce to the form of equations 6 and 7 if w_i^{μ} factorizes

$$w_i^{\mu} = w_i w^{\mu} \quad \text{or} \quad \sigma_i^{\mu} = \sigma_i \sigma^{\mu} \tag{19}$$

This case is important in Chapter 8, because the isotope shifts we are concerned with there all have the same uncertainty σ, and so $w_i = 1$, $w^{\mu} = (\alpha^{\mu}\sigma)^{-2}$.

Then we consider a different space, with axes labelled by the scaled isotope shifts divided by the corresponding σ_i,

$$y_i^{\mu} = \alpha^{\mu} \delta\nu_i^{\mu} / \sigma_i \quad .$$

Since this is a linear scaling of each axis, the points $\underline{y}^{\mu}$ will lie on a straight line $\underline{y} = \underline{y}_o + \lambda^{\mu} \underline{m}$.

Note that in this space, the vector $\underline{M}$ does not lie on the line, but the vector $\underline{M}'$, with $M'_i = M_i/\sigma_i$, does. Similarly $\underline{m}$ is not parallel to $\underline{F}$ but to $\underline{F}'$, $F'_i = F_i/\sigma_i$. Equations 17 and 18 then reduce to

$$\lambda^{\mu} = \underline{m}.\underline{y}^{\mu} \tag{20}$$

$$d^2 = w^{\mu} \left[(\underline{y}^{\mu} - \underline{y}_o)^2 - (\underline{y}.\underline{m})^2 \right] . \tag{21}$$

Apart from the w^{μ}, these are of the same form as equations 6 and 7, and so the rest of the treatment will follow with $\underline{x}$ replaced by $\underline{y}$, provided the bar notation is re-defined to represented weighted means

$$\bar{\underline{y}} = \frac{1}{W} \sum_{\mu} w^{\mu} \underline{y}^{\mu} \qquad \text{where} \quad W = \sum_{\mu} w_{\mu}$$

and M in equations 9, 10, 15 and 16 is replaced by W.

C.2 The King Relations in N Dimensions

In this section we consider the case when the standard deviations cannot be represented by equation 19, and also allow for the possibility that different isotope pairs have been measured in each spectral line. In this case we cannot represent the experimental results by a set of points in N-dimensional space with a certain "error volume" around each one, as we did with the simpler cases above, because in converting the isotope shifts as measured to a common set of isotope pairs we introduce coupling between the errors. In this case there is no King plot as such, but there are still relations between isotope shifts in different lines, which we may term the King relations. For example if an isotope pair AA' in spectral line i has been measured, and pairs AA_o, $A'A_o$ in line j, then

there is a King relation

$$\delta\nu_i^{A-A'} = \phi(\delta\nu_j^{A-A_o} - \delta\nu_j^{A'-A_o}) + \mu/\alpha_{AA'} \quad . \tag{22}$$

Thus the problem is to find a set of isotope shifts in one line, and values of ϕ and μ for all the other lines, which minimize the squared differences between these consistent values and the measured values.

A very general algorithm for solving problems of this type has been given by Britt and Luecke (1973). They give an iterative technique for solving the following problem. Given an m-vector of experimental results $\underline{z}$, find the best values $\underline{x}$, i.e. those values which minimize $(\underline{z} - \underline{x})^T \underline{\underline{R}}^{-1} (\underline{z} - \underline{x})$ where $\underline{\underline{R}}$ is the variance/covariance matrix of $\underline{z}$, subject to k constraints $\underline{f} = 0$, where $\underline{f}$ depends on $\underline{x}$ and on n parameters $\underline{\theta}$. For this problem we can introduce two simplifications:

(i) We assume all the measured isotope shifts are independent; hence R is diagonal

$$\underline{\underline{R}} = \begin{pmatrix} \sigma_1^2 & & 0 \\ & \ddots & \\ 0 & & \sigma_m^2 \end{pmatrix} , \qquad \underline{\underline{R}}^{-1} = \begin{pmatrix} w_1 & & 0 \\ & \ddots & \\ 0 & & w_m \end{pmatrix} = \underline{\underline{w}}$$

(ii) The number of constraint equations k = m, and each is of the form

$$f_i = x_i - g_i(\theta) = 0 \qquad i = 1 \ldots\ldots m$$

This means that the matrix $\dfrac{\partial f_i}{\partial x_j}$ has the simple form

$$\frac{\partial f_i}{\partial x_j} = \delta_{ij} \quad .$$

This leads to the important simplification that whereas in the full

algorithm an nxn and an mxm matrix have to be inverted in each iteration, in the simplified algorithm, only the nxn matrix requires inversion, and, of course, the number of parameters, n, is less than the number of measurements m. For this reason I shall derive the simplified algorithm.

We require to minimize

$$(\underline{z} - \underline{x})^T \underline{\underline{w}}(\underline{z} - \underline{x}) \tag{23a}$$

with respect to $\underline{x}$ and $\underline{\theta}$, subject to the m constraints

$$\underline{x} - \underline{g}(\underline{\theta}) = 0 \ . \tag{23b}$$

The equations to be solved are thus

$$-\underline{\underline{w}}(\underline{z} - \underline{x}) + \underline{\lambda} = 0 \tag{24a}$$

$$-\underline{\underline{G}}_{\theta}^T \ \underline{\lambda} = 0 \qquad \text{where } \left[G_{\theta} \right]_{ij} = \frac{\partial g_i}{\partial \theta_j} \tag{24b}$$

and $\underline{\lambda}$ is an m-vector of Lagrange multipliers. Equations (23b) and (24) form a set of 2m + n equations in the unknowns $\underline{\theta}$, $\underline{\lambda}$ and $\underline{x}$; although they are linear in $\underline{x}$ and $\underline{\lambda}$ they are non-linear in $\underline{\theta}$, and we must solve them iteratively. First we eliminate $\underline{\lambda}$ between equations 24

$$\underline{\underline{G}}_{\theta}^T \ \underline{\underline{w}}(\underline{z} - \underline{x}) = 0 \ , \tag{25}$$

and then eliminate $\underline{x}$ between equations 25 and 23b

$$\underline{\underline{G}}_{\theta}^T \ \underline{\underline{w}}(\underline{z} - \underline{g}(\theta)) = 0 \ . \tag{26}$$

Suppose we have a set of values of $\underline{\theta}$, $\bar{\underline{\theta}}$, which are near the solution of

equation 26. Then we can approximate $\underline{\underline{G}}$ by its value at $\bar{\underline{\theta}}$, and $\underline{g}(\theta) = \underline{g}(\bar{\underline{\theta}}) + \underline{\underline{G}}_\theta(\underline{\theta} - \bar{\underline{\theta}})$. Denoting $\underline{g}(\bar{\underline{\theta}})$ by $\bar{\underline{g}}$ and $\underline{\underline{G}}_\theta(\bar{\theta})$ by $\bar{\underline{\underline{G}}}_\theta$, equation 26 reduces to

$$\bar{\underline{\underline{G}}}_\theta^T \; \underline{\underline{w}} \; \bar{\underline{\underline{G}}}_\theta \; (\underline{\theta} - \bar{\underline{\theta}}) = \bar{\underline{\underline{G}}}_\theta^T \; \underline{\underline{w}} \; (\underline{z} - \bar{\underline{g}}) \tag{27}$$

and so, defining $\underline{\underline{B}} = \bar{\underline{\underline{G}}}_\theta^T \; \underline{\underline{w}} \; \bar{\underline{\underline{G}}}_\theta$, we find

$$\underline{\theta} - \bar{\underline{\theta}} = \underline{\underline{B}}^{-1} \; \bar{\underline{\underline{G}}}_\theta^T \; \underline{\underline{w}} \; (\underline{z} - \bar{\underline{g}}) \; . \tag{28}$$

Thus equation 28 gives us the correction to the current value of $\underline{\theta}$; this can then be used as $\bar{\underline{\theta}}$ for the re-evaluation of $\bar{\underline{g}}$ and $\underline{\underline{G}}_\theta$ in the next iteration. The process can be stopped when the value of $\bar{\underline{\theta}}$ has stopped changing significantly; then the final value of $\bar{\underline{g}}$ gives the best consistent values of the measurements $\underline{z}$, and it can be shown that $(\underline{z} - \underline{x})^T \; \underline{\underline{w}} \; (\underline{z} - \underline{x})$ has a roughly χ^2 distribution with $(m - n)$ degrees of freedom, as we might expect. Finally, $\underline{\underline{B}}^{-1}$ gives the variance/covariance matrix of the parameters $\underline{\theta}$; if χ^2 differs greatly from $(m - n)$ a more realistic estimate of this matrix is probably

$$\frac{\chi^2}{(m - n)} \; \underline{\underline{B}}^{-1} \qquad \text{where } \chi^2 = (\underline{z} - \underline{x})^T \; \underline{\underline{w}} \; (\underline{z} - \underline{x})$$

APPENDIX D

COMPUTER PROGRAMS

All the computer programs referred to in the thesis are listed on the enclosed microfiche. The programs are in alphabetical order on the fiche; I list them below in the order in which they are referred to in the thesis.

PLOT — plots signal and calibration fringes (see Fig. 4.6)

CALIBRATE — calibrates a trace (see Fig. 5.5)

FIT40 — finds lineshape parameters of main peak (see Fig. 5.6)

FITMAIN — Fitting program. It calls the following subroutines:-

- CALIB — does local calibration
- PARAM — reads in parameter values
- FIT — calls the fitting routine E04 FCF.
- VOIGT — calculates Voigt profile - see section 5.6
- LSQFUN — calculates theoretical profile - see section 5.6
- LSQMON — see implementation documents for E04 FCF.
- CUBIC — solves a cubic equation.

LINE — finds parameters of sloping background

CARS — finds best values of isotope shifts from the results - see Appendix B.

CAFF — compares isotope shifts in three spectral lines - see Appendix C.2

PICTURE, DISPLAY — draw data and fitted curve - Fig. 6.1

SMPLOT — multidimensional King plot - see Appendix C.

SECOND — compares two spectral lines using second order theory of deviations - see section 8.3

SMFIT — compares two spectral lines using diagonalization - see section 8.5



BIBLIOGRAPHY

References to journals are given in the form Volume Number (Page) Date.

Abbreviations

A.D. & N.D.T.	Atomic Data and Nuclear Data Tables.
Ann. Phys.	Annals of Physics (New York).
J.E.T.P.	Soviet Physics (Journal of Experimental and Theoretical Physics).
J. de Phys.	Journal de Physique (Paris).
J. Phys. B	Journal of Physics B; Atomic and Molecular Physics.
J. Phys. E	Journal of Physics E; Scientific Instruments.
Nucl. Phys.	Nuclear Physics.
Phys. Lett.	Physics Letters.
Phys. Rev.	Physical Review.
Phys. Rev. Lett.	Physical Review Letters.
Proc. Phys. Soc.	Proceedings of the Physical Society.
Proc. Roy. Soc.	Proceedings of the Royal Society.
Z. Phys. A	Zeitschrift für Physik A; Atoms and Molecules.

Abramowitz M and Stegun I (Editors): "Handbook of Mathematical Functions" (NBS Applied Mathematics Series: Washington DC) 1964.

Baird P, Brambley R, Burnett K, Stacey D, Warrington D, and Woodgate G: Proc. Roy. Soc. A365 (567) 1979.

Barrett R : Phys. Lett. 33B (388) 1970.

Bashkin S and Stoner J : Atomic Energy-Level and Grotrian Diagrams, Vol. II. (North Holland : Amsterdam) 1978.

Bauche J and Champeau R-J : Advances in Atomic and Molecular Physics 12 (39) 1976.

Ben-Reuven A, Jortner J, Klein L and Mukamel S : Phys. Rev. A13 (1402) 1976.

Bergmann E, Bopp P, Dorsch Ch, Kowalski J and Träger F : Z. Phys. A 294 (319) 1980. Earlier work is reported in Z. Phys. A 279 (249) 1976, Z. Phys. A 290 (143) 1979, Z. Phys. A 290 (345) 1979 and Z. Phys. A 292 (401) 1979.

Bergman P : Phys. Rev. A13 (2191) 1976.

Bertozzi W, Friar J, Heisenberg J and Negele J : Phys. Letts. 41B (408) 1972.

Bodmer A : Proc. Phys. Soc. A66 (1041) 1953

Brambley R : Thesis (unpublished) Oxford 1978.

Brand H, Seibert B and Stuedel A : Z. Phys. A 296 (281) 1980.

Brandt H-W, Heilig K, Knöckel H and Steudel A : Z. Phys. A 228 (241) 1978.

Brink D and Satchler G : "Angular Momentum" (Clarendon Press : Oxford) Second Edition 1968.

Britt H and Luecke R : Technometrics 15 (233) 1973.

Bruch R, Heilig K, Kaletta D, Steudel A and Wendlandt D : J. de Phys. (Colloque) 30 (C1) 1969.

Bunkin F : J.E.T.P. 23 (1121) 1966.

Burnett K : Thesis (unpublished) Oxford 1978.

Cagnac B, Grynberg G and Biraben F : J. de Phys. 34 (845) 1973.

Carlier A, Blaise J and Schweighoffer M-G : J. de Phys. 29 (729) 1968.

Chandra H and Sauer G : Phys. Rev. C13 (245) 1976.

Chiarrella C and Reichel A : Mathematics of Computation 22 (137) 1968.

Cohen-Tannoudji C : "Atoms in Strong Resonant Fields" in "Frontiers in Laser Spectroscopy," Les Houches Lectures Session XXVII, edited by Balian R, Harouche S and Liberman S, (North Holland : Amsterdam) 1977.

de Clercq E, Biraben F, Giacobino E, Grynberg G and Bauche J : J. Phys. B 14 (L183) 1981.

Dreher B, Friedrich J, Merle K, Rothhaas H and Lührs G : Nucl. Phys. A235 (219) 1974.

Epstein G and Davis S : Phys. Rev. A4 (464) 1971.

Flusberg A, Mossberg T and Hartmann S : Phys. Rev. A14 (2146) 1976.

Gerstenkorn S and Vergès J : J. de Phys. 36 (481) 1975.

Gerstenkorn S, Labarthe J and Vergès J : Physica Scripta 15 (167) 1977.

Gill P and Murray W : SIAM Journal on Numerical Analysis 15 (977) 1978.

Goldstein H : "Classical Mechanics" (Addison-Wesley : Massachusetts) 1950.

Griffith J, Isaak G, New R, Ralls M and van Zyl C : J. Phys. B 12 (L1) 1979.

Griffith J, Isaak G, New R, and Ralls M : J. Phys. B 14 (2769) 1981.

Grundevik P, Gustavsson M, Lindgren I, Olsson G, Robertsson L, Rosén A and Svanberg S : Phys. Rev. Lett. 42 (1528) 1979.

Grynberg G and Cagnac B : Reports on Progress in Physics 40 (791) 1977.

Hecht E and Zajac A : "Optics" (Addison-Wesley : Massachusetts) 1974.

Heilig K and Steudel A : A.D. & N.D.T. 14 (613) 1974.

Jackson D : "Nuclear Radii" in Proceedings of the International Discussion Meeting "What do we know about the Radial Shape of Nuclei in the Ca-Region?", edited by Rebel H, Gils H and Schatz G (Kernforschungzentrum, Karlsruhe) 1979.

Kelly F, Kuhn H and Pery A : Proc. Phys. Soc. A67 (450) 1954.

King W : Journal of the Optical Society of America 53 (638) 1963.

Kogelnik H and Li T : Applied Optics 5 (1550) 1966.

Loudon R : "The Quantum Theory of Light" (Clarendon Press : Oxford) 1973.

Malvern A : Thesis (unpublished) Oxford 1974.

Mollow B : Phys. Rev. 175 (1555) 1968.

Palmer C and Stacey D : J. Phys. B 1982 (to be published).

Peckham G : Computer Journal 13 (418) 1970.

Pery A : Proc. Phys. Soc. A67 (181) 1954.

Ramsey N : "Molecular Beams" (Clarendon Press : Oxford) 1956.

Reiner A and Wilets L : Nucl. Phys. 36 (457) 1962.

Rinker G and Steffen R : A.D. & N.D.T. 20 (143) 1977.

Rosenthal J and Breit G : Phys. Rev. 41 (459) 1932.

Salomaa R and Stenholm S : J. Phys. B 8 (1795) 1975.

Salomaa R and Stenholm S : J. Phys. B 9 (1221) 1976.

Salomaa R : J. Phys. B 10 (3005) 1977.

Salomaa R : J. Phys. B 11 (3745) 1978.

Salour M : Ann. Phys. 111 (364) 1978.

Seltzer E : Phys. Rev. 188 (1916) 1969.

Shera E, Ritter E, Perkins R, Rinker G, Wagner L, Wohlfahrt H, Fricke G and Steffen R : Phys. Rev. C14 (731) 1976.

Sick I : Nucl. Phys. A218 (509) 1974.

Sick I, Bellicard J, Cavedon J, Frois B, Huet M, Leconte P, Nakade A, Phan Xuan Hô, Platchkov S, de Witt Huberts P and Lapikás L : Phys. Rev. Lett. 38 (1259) 1977.

Sick I, Bellicard J, Cavedon J, Frois B, Huet M, Leconte P, Phan Xuan Hô and Platchkov S : Phys. Lett. 88B (245) 1979.

Sobel'man I : "Introduction to the theory of Atomic Spectra" (Pergamon Press) 1972.

Stone A : Proc, Phys. Soc. 77 (786) 1961.

Stone A : Proc. Phys. Soc. 81 (868) 1963.

Talmi I : Reviews of Modern Physics 34 (704) 1962.

Thompson R : Thesis (unpublished) Oxford 1980.

Träger F : Z. Phys. A 299 (33) 1981.

Vasilenko L, Chebotaev V and Shishaev A : J.E.T.P. Letters 12 (113) 1970.

Wallard A : J. Phys. E 5 (926) 1972.

Wapstra A and Bos K : A.D.& N.D.T. 19 (177) 1977.

Wiese W, Smith M and Miles B : "Atomic Transition Probabilities; Vol II" (NSRDS : Washington DC) 1969.

Wohlfahrt H, Shera E, Hoehn M, Yamazaki Y and Steffen R : Phys. Rev. C23 (533) 1981. Preliminary results are given in Phys. Lett. 73B (131) 1978.

Woodgate G : Proc. Roy. Soc. A293 (117) 1966.

Woodgate G : "Elementary Atomic Structure" (Clarendon Press : Oxford) 1980.

Zamick L : Ann. Phys. 66 (784) 1971.